Alma Mater Studiorum – Università degli Studi di Bologna

DOTTORATO DI RICERCA IN

DISEGNO E METODI DELL'INGEGNERIA INDUSTRIALE

Ciclo XXIV

Settore scientifico-disciplinare di afferenza: ING-IND/05

INNOVATIVE ARCHITECTURES OF ON-BOARD AND ON-GROUND RADIO SYSTEMS FOR SPACE COMMUNICATION

Presentata da: Ing. Davide Cinarelli

Coordinatore Dottorato

Prof. Vincenzo Parenti Castelli

Relatore

Prof. Paolo Tortora

anno 2012

ABSTRACT

The radio communication system is one of the most critical system of the overall satellite platform: it often represents the only way of communication, between a spacecraft (S/C) and the Ground Segment (GS) or among a constellation of satellites. In light of this, starting in the 60's, satellite radio communication systems have been characterized by a large effort in research and development, in order to design even more reliable and efficient systems.

This thesis is not intended to give an overview of the state-of-the-art of space communication techniques, but it focuses on specific innovative architectures for on-board and on-ground radio systems. In particular, this work is an integral part of a space program started in 2004 at the University of Bologna, Forlì campus, which led to the completion of the microsatellite ALMASat-1, successfully launched on-board the VEGA maiden flight. The success of this program led to the development of a second microsatellite, named ALMASat-EO, a three-axis stabilized microsatellite, operating in Low Earth Orbit (LEO) and able to capture images of the Earth surface. Therefore, the first objective of this study was focused on the investigation of an innovative, efficient and low cost architecture for on-board radio communication systems. The TT&C system and the high data rate transmitter for images downlink design and realization are thoroughly described in this work, together with the development of the embedded hardware and the adopted antenna systems. Moreover, considering the increasing interest in the development of constellations of microsatellite, in particular those flying in close formations, a careful analysis has been carried out for the development of innovative communication protocols for inter-satellite links.

Furthermore, in order to investigate the system aspects of space communications, a study has been carried out at the European Space Operations Center (ESOC) having as objective the design, implementation and test of two experimental devices for the enhancement of the European Space Agency (ESA) Ground Stations. Thus, a significant portion of this thesis is dedicated to the description of the results of a method for improving the phase stability of GS radio frequency (RF) equipments by mean of real-time phase compensation and a new way to perform two antennas arraying tracking using already existing ESA tracking stations (ESTRACK) facilities.

Overview

List of Figures

List of Tables

List of Acronyms

A list of the acronyms used in the thesis is listed below.

ACK   Acknowledge
ADEV   Allan DEViation
AFC   Automatic Frequency Control
AMSC   ALMASat MultiSpectral Camera
AOS   Advanced Orbiting Systems
BEB   Binary Exponential Back-Off
BER   Bit Error Rate
BOT   Back-Off Time
BWG   Beam Wave Guide
CA   Collision Avoidance
CCSDS   Consultative Committee for Space Data System
COTS   Commercial Of The Shelf
CSMA   Carrier Sensing Multiple Access
CW   Contention Window
DAC   Digital to Analog Conversion
DC   Direct Current
DCE   Diversity Combiner Estimator
DCF   Distributed Coordination Function
DPU   Digital Processing Unit
DS   Deep Space
DSA   Deep Space Antenna
ECSS   European Cooperation for Space Standardisation
EIRP   Equivalent Isotropic Radiated Power
EO   Earth Observation
ESA   European Space Agency
ESOC   European Space Operative Centre
ESTRACK   ESA Tracking Stations
FFRF   Formation Flying Radio Frequency
FPGA   Field Programmable Gate Array
FSK   Frequency Shift Keying
GFSK   Gaussian FSK
GNSS   Global Navigation Satellite System
GPS   Global Positioning System
GS   Ground Segment
GSRF   Ground Segment Reference Facility
GTO   Geostationary Transfer Orbit
HPA   High Power Amplifier
JUICE   JUpiter ICy moon Explorer

IEEE	Institute of Electrical & Electronics Engineers
IF	Inter Frequency
IFMS	Intermediate Frequency and Modem System
KPA	Klystron Power Amplifier
LEO	Low Earth Orbit
LHCP	Left Hand Circular polarization
LNA	Low Noise Amplifier
LPA	Low Power Amplifier
MAC	Medium Access Control
MER	Main Equipment Room
MORE	Mercury Orbiter Radio science Experiment
NASA	National Aeronautics and Space Administration
OBRAS	On-Board RAdio Science experiments
PA	Power Amplifier
PCB	Printable Circuit Board
PCF	Point Coordination Function
PLL	Phase Locked Loop
PSS	Portable Satellite Simulator
QPSK	Quadrature Phase Shift Keying
RF	Radio Frequency
RHCP	Right Hand Circular Polarization
RSSI	Received Signal Strength Indicator
SAR	Synthetic Aperture Radar
S/C	Spacecraft
SDR	Software Defined Radio
SFF	Satellite Formation Flying
SMT	Surface Mount Technology
SNR	Signal to Noise Ratio
SPI	Serial Peripheral Interface
SSL	Satellite to Satellite Link
SSPA	Solid State Power Amplifier
SST	Satellite to Satellite Tracking
TRP	Token Ring Protocol
TT&C	Tracking Telemetry and Command
TXBE	Transmitter Back-End
UART	Universal Asynchronous Receiver-Transmitter
USO	Ultra Stable Oscillator
VCPS	Voltage Controlled Phase Shifter
VIL-1	Villafranca antenna 1
VIL-2	Villafranca antenna 2
VSWR	Voltage Standing Wave Ratio

1 Introduction

In a satellite platform the radio communication system is one of the most critical ones to guarantee the mission performance and overall success. It presents the preferable way of communication, and often the only way of communication, between a S/C and the GS or among a constellation of satellites. So, it is easy to understand how vital for a satellite the radio system is, and how catastrophic a failure on this system could be.

The topic of space communication has been deeply analyzed during the recent years [1] [2]. Historically, the concept of satellite communication is accredited to A. C. Clarke, thanks to his famous paper published in 1945 [3]. Starting in the 60's, satellite radio communication systems were characterized by a large effort in research and development, in order to design even more reliable and efficient systems.

The main requirements for a satellite communication systems are:

- Reliability: considering that a failure on this system can preclude any communication with an orbiting satellite platform, the radio system should offer the higher reliability. Often, this system is designed in redundancy, with the possibility to switch the main system to a backup one in case of irreversible failure;

- Power efficiency: being the total available power on-board a spacecraft limited the communication system should be as more efficient as possible. In particular, in a radio communication system the RF Power Amplifier (PA) introduces the higher power consumption and particular attention must be kept designing this device. The total available RF power directly affects the maximum distance that could be covered with the radio communication between the orbiting platform and the GS;

- Available data rate: the trend of future mission data demand is constantly increasing and the radio system should offer even greater data rate exploiting the same resources, i.e. the available frequency bandwidth and the received power.

The satellite communication system consists of a Space Segment, a Control Segment and a Ground Segment.

- The Space Segment contains one or several spacecrafts organized into a constellation. On-board radio system consists of one or more antennas, inter frequency (IF) modulator, frequency up-converter and RF high power amplifier (HPA) for the transmitting path and IF

demodulator, frequency down-converter and RF low noise amplifier (LNA) for the receiving chain.

- The Control Segment consists of all ground facilities for the control and monitoring of the satellites, also named TT&C stations (tracking telemetry and command). The TT&C station provides constant checking of the spacecraft subsystems' status, monitors outputs, provides ranging data and updates the satellite configuration via telemetry links.

- The Ground Segment consists of all the communicating Earth station which access the operational satellite. Depending on the type of service considered, these stations can be of different size.

Radio systems for space communication can also be divided with respect to the final purpose of the communication itself. Typically, radio communication can be divided in:

- TT&C link: this radio link is used for downlink communication, that is transmitting from the S/C and receiving at GS, of telemetry data in order to monitoring the behavior of the spacecraft, its position and orientation. In addition, uplink communication, that is transmitting from the GS and receiving on-board, is used for sending commands to the orbiting platform in order to start some procedure or correct the attitude and orientation of the satellite if possible. Furthermore, it is used to collect range and range-rate data to track the satellite. The TT&C system is required to offer a very high reliable link at the expense of low data rate. As a matter of fact, information that are communicated through this link are vital for the spacecraft correct behavior and communications error must be reduced to a minimum.

- High data rate link: typically, this radio link is used to transmit to the GS data collected by on-board payload, such as sensor or multispectral camera. The error rate requirement on this link could be less stringent than the one for the TT&C system, but the amount of data collected by the spacecraft could reach remarkable sizes so it is important to offer a very high data rate.

- Radio science link: radio link used for radio science mission is typically characterized by very narrowband channel (from 1-2 KHz up to 8 KHz), with carrier-only signal transmitted. Since spacecrafts need to be equipped with radio subsystems for carrying out communication with the Earth and execute orbit determination measurements, the opportunity arose to exploit instrumentation already present on-board to perform radio science experiments. As a matter of fact, most of radio science subsystems are not

independent instruments and experiments are executed using the radio carrier links of the spacecraft TT&C subsystem, by analysing the dual-frequency one-way or two-way radiometric tracking data. More advanced spacecraft have filtering and polarization capabilities added to the telecommunications receiver/transmitter.

The research of innovative solution of on-board and on-ground radio systems for space communication have reached nowadays their maximum effort. In particular, the ever more growing trend of development of LEO micro- and nano-satellite has shift the attention to the design of low power, low volume on-board communication system. Moreover, on the GS side, the small antenna array technique is became very attractive as an alternative to the classical solution of a single antenna, forced by physical and technical limitation on keep increasing antenna dimension, RF output power.

1.1   Objectives of the study

The work described in this thesis has been carried out at the University of Bologna, Forlì campus, in the Microsatellite laboratory of the engineering aerospace faculty. In this laboratory, a space program started in 2004 led to the completion of the microsatellite ALMASat-1, the first microsatellite entirely designed and realized at the University of Bologna. ALMASat-1 was successfully launched on-board the VEGA maiden flight, the new ESA launcher for small satellite. The success of this program led to the development of a second microsatellite, called ALMASat-EO, a three-axis stabilized microsatellite, operating in LEO orbits and able to capture images of the Earth surface.

As a consequence, the first objective of this study was focused on the investigation of an innovative, efficient and low cost architecture for on-board radio communication systems. The TT&C system and a downlink high data rate transmitter were entirely designed and realized taking into account the typical microsatellite requirements, such as low mass, low volume and low power consumption. Both hardware and software were designed and developed and thoroughly described in Section 2 and 3.

In addition, the increasing interest in the development of constellation of microsatellite and in the definition of reliable communication protocol for maintaining the constellation attitude has then given the input to the study of low delay and low error protocol based on terrestrial one for inter-satellite link, as described in Section 4.

Finally, in order to investigate the system aspects of space communications a parallel work has been carried out concerning ESA Ground Stations. Two different solutions for the enhancement of GS were designed, implemented and tested at ESOC, one of the ESA headquarters, sited in Darmstadt, Germany. In detail, a method for improving the phase stability of HPA by mean of voltage controlled phase shifter and an innovative way to perform two antennas arraying tracking using existing ESTRACK facilities have been carried out. ESTRACK represents ESA's capability to provide links between in orbit spacecrafts and the Operations Control Centre at ESOC, and consists of a large range of GS all around the world with state-of-the-art equipment. ESTRACK is designed to provide global space link connectivity coverage for a wide range of space missions [4]:

- The Deep Space missions;
- The Near Earth missions: e.g. Geostationary Transfer Orbits, Medium Earth Orbits, Highly Eccentric Orbits, Lunar Orbits, Lagrangian orbits;
- The Low Earth Orbit missions.

Motivation for the proposed studies are the development of technology both in the space and the ground segment that has recently resulted in the migration to higher frequency bands (i.e. Ka-band), to more sophisticated modulation and coding schemes and to very high data transfer. Furthermore, some characteristics that were improved in recent years to enhance GS capability, as the antenna dimension and the maximum available RF power, have now reach their physical and practical limitations, making the GS enhancement a hard challenge for the future.

1.2   Specific field of interest

1.2.1 Microsatellite platform

In the last three decades the advance of increasingly low-power, miniature electronic components combined with growing financial pressures, have focused attention on the use of small satellites to complement large satellite systems for many space applications. Usually large satellites take many years to mature from concept to useful orbital operation; furthermore, new ideas, technologies and scientific experiments find it difficult to gain timely access to space introducing lag in space technology demonstrator. The University of Surrey have pioneered microsatellites technologies since its beginning of UoSAT program in 1978, with the purpose of research cost-effective small satellite techniques and demonstrate the capabilities of micro/minisatellites [5].

Satellite platform are classified with respect to their size: even if the classification sometimes depends upon viewpoint and is not so clear, the classification shown in Table 1 has become widely adopted [2]. Although there have been many examples of large, small and even nanosatellite it is only relatively recently that capable microsatellites have shown that it is possible to perform different kind of mission very effectively, rapidly and at low cost and risk.

Class	Mass
Large satellite	> 1000 Kg
Small satellite	500-1000 Kg
Minisatellite	100-500 Kg
Microsatellite	10-100 Kg
Nanosatellite	< 10Kg

Table 1: Size classification for satellites

Microsatellite are currently used for the following applications:

- Low Earth Orbit communications: the close proximity of the satellites in LEO to the user and the consequent reduction in transmission loss and delay time is attractive when compared to traditional communications satellite in a geostationary orbit. Furthermore, the possibility of less expensive GS and of a higher frequency reuse are main advantages for microsatellite. However, the use of a constellation such a space platform introduces different problems, such as varying communications path and links and high Doppler shift.

- Space radio-science: microsatellite can offer very quick turnaround and inexpensive means of exploring well focused, small-scale science objectives or providing an early proof of concept prior to the development of large-scale instrumentation in a fully complementary manner to expensive space science missions.

- Technology demonstration and verification: microsatellite platform provides an attractive and low cost means of demonstrating, verifying and evaluating new technologies or services rapidly, and in realistic orbital environment and within acceptable risks. In recent years, starting from UoSAT-based platforms [6] [7] [8], microsatellite have supported a wide range of in-orbit technologies, such as:
  - New solar cell technology;
  - Demonstration of advanced communications;

- Attitude and orbital determination and control systems: e.g. Micropropulsion systems, momentum wheel, magnetometers, etc.

- Education and training: microsatellite platforms are particularly suitable for the education and training of scientists and engineers by providing a means for direct experience of all stages and aspects of satellite mission, from design, construction, test and launch to orbital operation. The very low cost, rapid timescale and manageable dimensions make this approach very attractive to university that wish to develop and establish a national expertise in space technology: the ALMASat-1 project is an example of this application field, being the first educational microsatellite designed, manufactured and assembled at the University of Bologna, Forlì aerospace campus [9] [10].

- Earth Observation (EO): microsatellite is an attractive solution for Earth Observation. The advantage of a low cost platform with restricted time of realization combined with the ever more increasing interest in Earth observation during the recent years for military and civil purposes have brought great interest in microsatellite development. The ALMASat-EO mission [11], described in paragraph 1.3.1 as reference mission for this study, is a clear example of microsatellite application.

1.2.2 Satellite to satellite link

In addition to the classical GS to S/C link configuration, an ever more increasing number of mission consist of multiple S/C cooperating to fulfil a common purpose. As a consequence, a new link configuration is established among different S/C, the so called satellite to satellite link (SSL). For instance, Satellite Formation Flying (SFF) missions deeply involve the use of SSL: SFF is the concept that multiple satellites can work together in a group to accomplish the objective of one larger, usually more expensive, satellite. Coordinating smaller satellites has many benefits over single satellites including simpler design, faster build time, cheaper replacement creating higher redundancy, unprecedented high resolution and the ability to view research targets from multiple angles or at multiple times.

For a better understanding, examples of current formation flying missions are here reported:

MISSION	DESCRIPTION
PRISMA	is a mission dedicated to formation flying using a Formation Flying Radio Frequency (FFRF) subsystem, an RF metrology package that is targeted as the metrology sensor for many future European formation flying missions, and GPS positioning. The range accuracy is in the order of millimetres. Using thrusters, several manoeuvres are performed with the small satellite moving around the larger [12].
TanDEM-X	is a pair of spacecraft equipped with SAR instruments, flying in a passive helix formation (two elliptical orbits with interchanged apogee and perigee with slightly different inclination) with active orbit control (hydrazine thrusters). The distance between the two satellites is estimated from their GPS positions with an (on-ground processing) accuracy in the order of a millimetre. A form of inter-satellite communication is applied for pulse synchronisation (needed for interferometry), which is done by steering the SAR beam towards the other satellite 5 times per second. The mission's objective is to provide a level-3 Digital Elevation Model (DEM) of the Earth [13].
GRACE	is a satellite-to-satellite tracking mission with an inclination of 89 degrees and an initial altitude of 450 - 500 km. It is intended to accurately define the gravitational field of the Earth (geoid). GRACE uses microwave ranging to assess the distance between two spacecraft (about 240 km). The range and range rate accuracy is at the micron level. Inter-satellite laser ranging system for even better accuracy is under study for use on a possible GRACE-2 mission [14].
THEMIS	a five-spacecraft constellation to study magnetospheric events leading to auroral outbursts—launched on February 17, 2007. Activities of the multi-mission operations team include mission and science operations, flight dynamics and ground station operations. Communications with the constellation are primarily established via the Berkeley Ground Station, while NASA's Ground Network provides secondary pass coverage. In addition, NASA's Space Network supports maneuver operations near perigee. Following a successful launch campaign, the operations team performed on-orbit probe bus and instrument check-out and commissioning tasks, and placed the constellation initially into a coast phase orbit configuration to control orbit dispersion and conduct initial science operations during the summer of

2007. Mission orbit placement was completed in the fall of 2007, in time for the first winter observing season in the Earth's magnetospheric tail. Over the course of the first 18 months of on-orbit constellation operations, procedures for instrument configuration, science data acquisition and navigation were refined, and software systems were enhanced. Overall, the implemented ground systems at the Mission Operations Center proved to be very successful and completely adequate to support reliable and efficient constellation operations. A high degree of systems automation is employed to support lights-out operations during off-hours [15].

Table 2: current SFF missions

Furthermore, advantages arising from SSL can also concern radio science missions. The satellite to satellite configuration is particularly interesting if we consider the possibility to receive radio signal on-board a S/C instead of at GS, as in the classical downlink configuration. Recent study committed by ESA [16] have pointed out a viable architecture for performing radio science experiments exploiting a satellite to satellite configuration, the so-called OBRAS (On-Board Radio Science experiments) architecture. SSL OBRAS offers a new perspective on atmospheric measurements which considerably extends the scientific merits of radio occultation experiments with respect to those carried out from the ground. The essential concept is that of radio occultations being carried out between two spacecraft in orbit around the same planet. The radio signal emitted by one spacecraft as it disappears behind the planet and its atmosphere is recorded by the other spacecraft, which samples Doppler frequency shift, phase, polarisation, propagation time and amplitude and allows inferring neutral and ionospheric gas densities as well as neutral pressures and temperatures. In particular, with respect to the classical downlink architecture error budget, this unexplored technique would allow to cancel out completely the error contributions due to the ground segment and to the media propagation. Moreover, if combined, also, with standard ground based radiometric tracking techniques (direct Doppler tracking with each S/C separately), a SSL Doppler link would allow to better constrain the orbital solutions for both S/C, eliminating possible degeneracies intrinsic to the S/C geometries and lines-of-sights.

1.2.3 Ground Segment enhancement

Satellite communications can be made available from almost any point on the Earth's surface to any other point, in both international and domestic environment and they are high in reliability and quality. These attributes have led to the popularity of space communications. The number of services exploiting satellite communications is even increasing and so also requirements for the design of future Ground Stations are even harder to accomplish.

In particular, deep space links offer the most challenging design of GS, requiring the state-of-the art equipments and the higher investment in terms of cost and time to be realized. The aforementioned ESTRACK complex, represents the highest technological level of ESA GS which most advanced stations are represented by the Deep Space Antenna (DSA) structures: two already built, at New Norcia (Australia) and Cebreros (Spain), and one under construction, at Malargue (Argentina). Despite the recent construction, the future trend in mission data demand and deep space exploration has highlighted the need for an enhancement of DSA, as the migration to higher frequency bands (i.e. K- and Ka bands) for both transmission and reception capability and the possibility of multifrequency link (i.e. X- and Ka-bands at the same time). Furthermore, in recent years major improvements have been involved the Equivalent Isotropic Radiated Power (EIRP) or the G/T factor increasing the antenna physical dimension, the HPA RF output power or the noise introduced by the receiver. These solutions have now reach their mechanical and practical limitations, making the GS enhancement a hard challenge for the future. Steps beyond the state-of-the-art are not without drawbacks: for instance 70-m or larger parabolic dishes are affected by additive losses due to mechanical errors or deformation of the structure and 20 KW or more powerful Klystron HPA (KPA) demand very expensive cooling system, implying a large amount of maintenance, to eliminate the considerable amount of phase instability that is generated because of the high temperature the device reaches during operation.

1.3 Reference missions of the study

In order to investigate the whole topic of radio system for space communications, both on-board and GS equipment were studied. In light of this, two reference missions were considered. Concerning the on-board segment, the whole hardware and software designed, realized and tested is referred to the ALMASat-EO microsatellite communication systems, as thoroughly described in

Section 2 and 3. Both the TT&C subsystem and the high data rate downlink transmitter were designed following the main requirements of microsatellite platform.

A radio science mission orbiting Jupiter, as the many proposed in the last years, was considered as main application for innovative solutions proposed in this study regarding GS enhancement. Initially conceived as an exploratory tool, radio science techniques have provided considerable knowledge of the atmosphere and gravity of planets, some of which was originally unanticipated. Furthermore, the number of radio science mission planned by ESA and National Aeronautics and Space Administration (NASA) is constantly increasing, together with the complexity of the mission. As a consequence, the radio link for this kind of mission has to satisfy ever more stringent requirements, and the GS in particular can contribute in order to open the door to a better understanding of the deep space.

1.3.1 Low Earth Orbit microsatellite ALMASat-EO

The Microsatellites and Space Microsystems Laboratory of the University of Bologna in Forlì is involved since 2004 in the design and development of microsatellite missions. While the precursor microsatellite, ALMASat-1, was successfully launched on-board the VEGA maiden flight, researchers and students are currently assembling the next generation of ALMASat satellite, ALMASat-EO whose project started in 2007 as a collaboration between the same laboratory of the University of Bologna and ALMASpace s.r.l..

The main purpose of the ALMASat-EO project is related to multispectral Earth observation mission: the microsatellite will carry on-board the ALMASat MultiSpectral Camera (AMSC) payload in which an high sensitivity CCD detector is coupled to a LCD tunable filter in order to achieve multispectral capabilities in the visible spectrum with ground resolution in the order of 35m. The S/C will be inserted in a circular sun synchronous LEO by the second VEGA flight, named VERTA-1. The satellite will be in the small-satellite range with a size of about 300x300x600 mm and a mass smaller than 35 kg. ALMASat-EO bus structure is shown in Figure 1. The microsatellite is a three axis stabilized spacecraft equipped with four redundant reaction/momentum wheels necessary for fine pointing and off-nadir maneuvers and a cold-gas micropropulsion system for orbital maneuvers. A set of 3 orthogonal magnetic coils will be used for attitude de-tumbling after launcher separation and coarse attitude pointing. Attitude determination is performed using two bi-axial sun sensors, a Thermal InfraRed based Earth sensor and two redundant three-axis magnetometers, while for orbit determination a Field Programmable Gate Array (FPGA)-based dual

frequency Global Navigation Satellite System/Global Positioning System (GNSS/GPS) receiver was specifically developed for this mission, to meet the images geo-referencing requirements. ALMASat-EO attitude during images acquisition is shown in Figure 2. Power will be supplied by body mounted solar panels with TJ solar cells fixed to an carbon fiber honeycomb substrate.

The communication system object of the thesis consists of the UHF bidirectional TT&C radio link, located in the closest tray to the top of the ALMASat-EO structure, and an S-band high data rate transmitter used to downlink the acquired images of the Earth surface, directly located together with the EO payload.
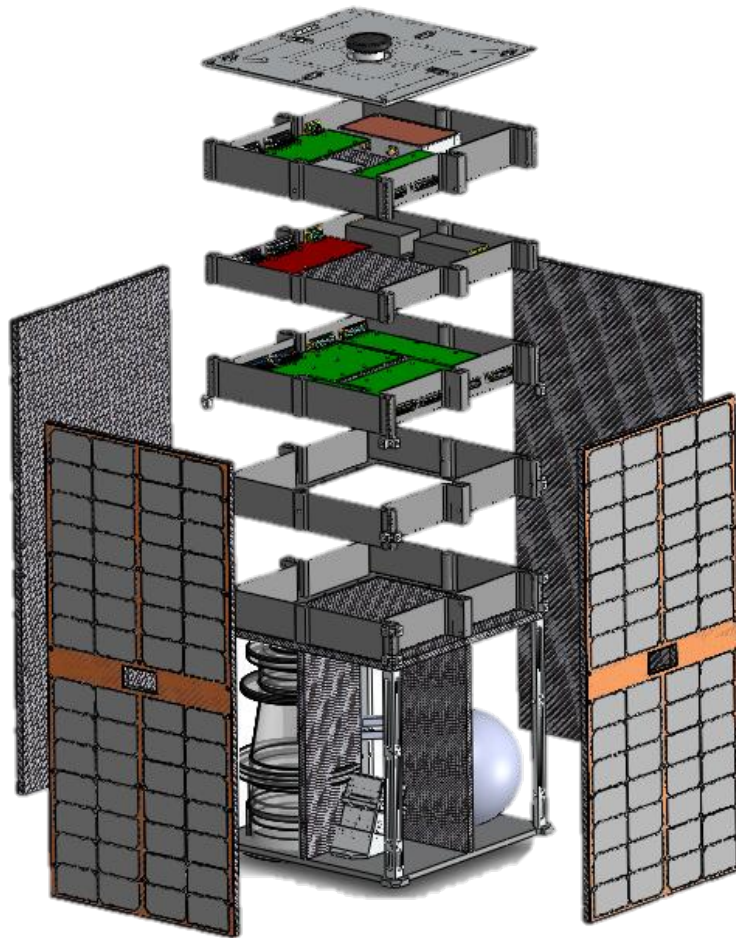
Figure 1: ALMASat-EO bus structure
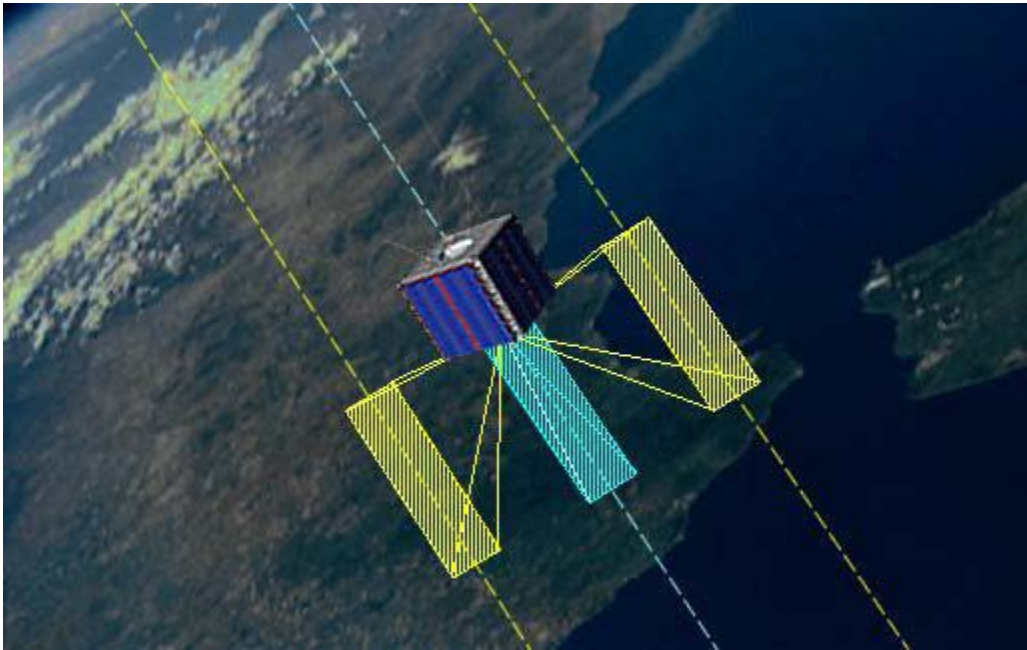
Figure 2: ALMASat-EO attitude during Earth images acquisition

1.3.2 Radioscience mission orbiting Jupiter

The deep space exploration is become of great interest in recent years as radio science techniques have provided considerable knowledge of the atmosphere and gravity of planets. Different techniques based on spacecraft radio signal interaction through layers of an atmosphere or against surface structures have been developed: atmospheric occultations (planetary neutral atmospheric science and planetary ionospheric science), solar corona and solar wind studies, planetary bistatic radar experiments and navigation experiments (gravity science, gravitational wave search) are the main used techniques.

Recently, different missions orbiting Jupiter and its satellites have been proposed by ESA and NASA. Among them, relevant is the JUpiter ICy moon Explorer (JUICE) mission [17]. The goal of JUICE is the study of the emergence of habitable worlds around gas giant planets. The mission will carry out an in-depth study of Europa and the Jupiter system, and will carry instruments to monitor dynamic phenomena (volcanoes, atmospheric changes), map the magnetospheres and characterise the water oceans beneath the ice shells. Moreover, being possible the presence of liquid water oceans under the icy crusts of Europa, Ganymede and Callisto, that is the key criterion for habitable worlds, JUICE will look to answer such questions about the conditions of formation of Jupiter and the habitability of Europa.

This kind of mission requires ever more high capability to the dedicated GS for the remote control and the signal acquisition. At present, very few deep space antennas are able to accurately receive signal from S/C orbiting Jupiter. The investigated techniques for GS enhancement are focused to offer improved Allan deviation and higher SNR to ESA GS, improving the accuracy of radio science signal and enabling an increased number of GS for radio science mission.

2 ALMASat-EO TT&C communication subsystem

As a vital subsystem of the microsatellite platform ALMASat-EO, the TT&C architecture has been designed paying particular attention to the reliability of the whole subsystem, together with the stringent requirements in terms of power, mass and volume typical of microsatellite platform. The communication system includes a main and a backup electronic board, in cold redundancy, in order to avoid mission failure due to problems on the TT&C electronic hardware. Moreover, as a critical subsystem in ALMASat-EO architecture, a dedicated emergency power line and current limiter is introduced, for the main and backup boards both, in order to guarantee the proper functionality even in case of serious failure.

The board is based on 32-bit Cortex microcontroller [18], which manages the interfaces with other electronic equipments, performs the telemetry data and command protocol and manages the RF transceivers. The RF signal is generated and received through two integrated low power and narrowband transceivers Chipcon CC1020 [19], which directly mo/demodulates data using Gaussian Frequency Shift Keying (GFSK) modulation at both 4.8 and 9.6 Kbps at UHF band. Two transceivers have been used in order to separate the uplink signal from the downlink one and obtain a faster communication system.

The same antenna system, consisting of 4 half-wavelength dipoles in a Vase Turnstile configuration, is used for both uplink and downlink. A circulator is introduced in order to separate the high power signal (downlink) to the low power signal (uplink). Furthermore, a 6-port hybrid coupler (2 input and 4 output ports) realized in microstrip and wireline cable technology, is added for connecting both TT&C boards at the same antenna system.

The electronic board is able to receive telemetry data from the On-Board Data Handling (OBDH) subsystem through a serial interface RS232, performs the TM Space Data Link Protocol and introduces the Reed-Solomon (255,223) channel coding, as specified by the Consultative Committee for Space Data Systems (CCSDS) in [20] and [21], and generate a downlink signal at UHF band. The board RF output power is 10 dBm and an external PA is necessary in order to reach the output power value necessary for a reliable RF link between the S/C and the GS. Moreover, the uplink command signal is received, demodulated, checked for consistency and if the packet is not corrupted the data field is extracted and sent to the OBDH board through serial interface.

Figure 3 shows the placement of the whole TT&C subsystem device inside the dedicated tray of the S/C structure, which is the closer to the antenna system, on the top of the S/C architecture (refer to

Figure 1 at page 11). The two green rectangular boards are the redundant TT&C electronic boards, while UHF power amplifier will be placed between them. Moreover, a signal splitter and an hybrid coupler complete the front-end of the communication system allowing to connect both boards to the same antenna system at the same time. Coaxial cables for RF signal connection are not shown in this figure.
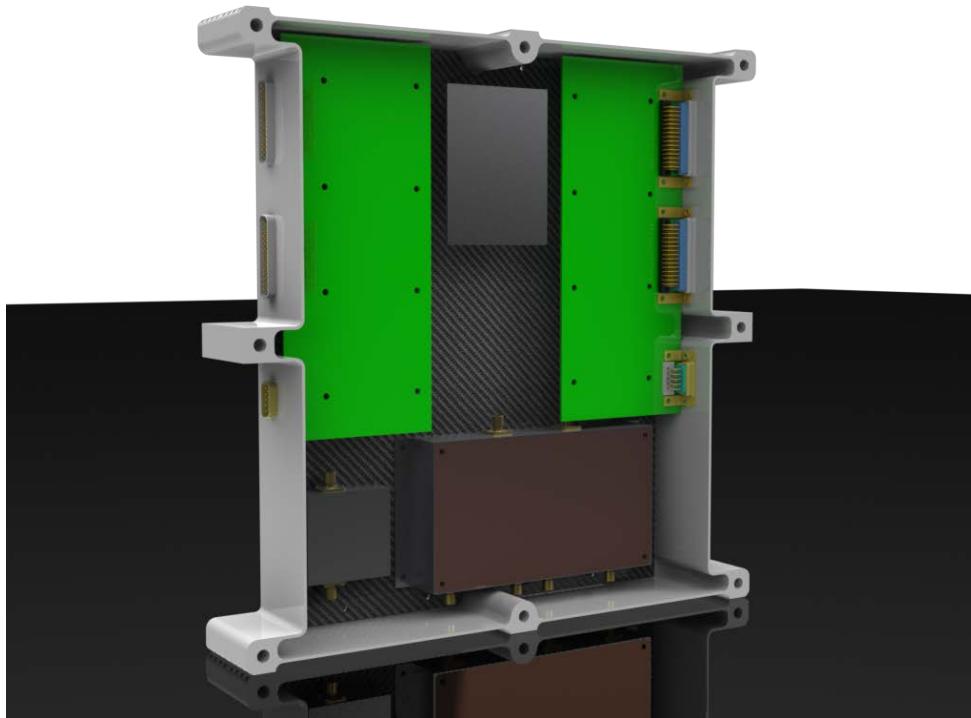
Figure 3: ALMASat-EO tray dedicated to the TT&C system

2.1 Requirements

The more stringent requirements for designing the whole TT&C system were represented by the limitations in terms of dimension and power consumption. As shown in Figure 3, the available space inside the tray is clearly limited by the redundancy of the system and the demand of electromagnetic isolation among different subsystem components: each RF device (i.e. PA, coupler, splitter) needs a specific box in order to avoid signal reflection and propagation inside the tray. As a consequence of the necessity for electromagnetic isolation, the overall volume of the entire subsystem increases: the maximum dimension allowed for the electronic board were 190x90 mm. Furthermore, the board should be as light as possible but at the same time resistant to vibration and acceleration to whom the S/C is subjected during a space launch. To satisfy the aforementioned

requirements, the whole board has been designed using integrated and low power circuits in Surface Mount Technology (SMT).

Concerning the total available power, the mission power budget assigns to the TT&C subsystem not more than 9 W. It must be noticed that for TT&C system the PA represents the greater contribution to the overall consumed electrical power and the RF output power needed to establish a reliable link is derived by the link budget, shown in section 2.2. Fortunately, thanks to the low distance of the satellite orbit and the three axis stabilization that allows for a good pointing and the use of a quite directive antenna system, the link budget is satisfied with a maximum RF output power of 2 W, that means a total consumption of 8W for the entire subsystem during downlink communication.

Obviously, the link budget also considers data rate requirement. Typically, TT&C communication system does not need for high data rate communication. Considering the time interval dedicated to telemetry communication during an orbit and the total amount of data to be transmitted, taking also into account the information overhead introduced by the communication protocol, a minimum data rate of 4.8 Kbps can satisfy the requirement in terms of amount of transmitted data and power needed.

2.2 UHF downlink path link budget

This paragraph shows the link budget of downlink path only, usually more critical than the uplink one, owing to the high RF power available at the GS. The link budget shown in Table 3 is divided in three different sections:

- The spacecraft
- The media
- The Ground Station

The S/C section takes into account a vase turnstile antenna configuration that is thoroughly described in section 2.6 and offering a gain equal to 4.1 dB in direction of maximum gain. In the media section attenuations introduced by atmosphere, ionosphere and the distance between S/C and GS are introduced, together with losses derived from non-perfect S/C antenna pointing or polarization mismatch. Atmospheric and ionospheric effects were taken into account. In fact, although radio waves at frequencies greater than 100MHz can normally pass through the ionosphere, they can be modified by the presence of free electrons and the Earth's magnetic field. At UHF and above the absorption at a frequency f on an oblique path with angle of incidence I is in general proportional to:

Eq. (1) $$\sec(i)/f^2$$

At middle latitude, the absorption for a one-way traverse of the ionosphere at 20 degrees of elevation angle is about 0.3 dB. Greater absorption can occur for low elevation angle.

Atmospheric absorption phenomena can occur caused by the presence of gases, especially at low elevation angle. The total amount of loss is directly proportional to the frequency of the link: a conservative value of 0.5dB has been considered in Table 3. Rain loss has been neglected due to the low frequency of the link (rain attenuation can be neglected at frequencies below about 5 GHz [2]). Moreover, polarization loss consists of imperfection in manufacturing of both S/C and GS antennas and depolarization effects such as the presence of crosspolar components of the electric field.

At last, the GS section takes into account attenuations derived from GS antenna non idealities and receiver noise added to the signal due to the temperature of the receiver device. Finally, a data rate of 4.8 Kbps, and a relative channel bandwidth of 25 KHz, is considered together with a high Bit Error Rate (BER) margin of 10^{-7}.

The result of such a link configuration is a high safety margin of 16.6 dB in average condition and 6.7 dB for the most critical case, considering the higher data rate of 9.6 Kbps. The high margin is necessary to offer always a reliable link even in case of degradation of the PA or impossibility to obtain a perfect antenna pointing. Furthermore, the high margin allows for downlink communication during the initial tumbling motion of the S/C: the margin can compensate the lack of the S/C antenna gain and the higher polarization mismatch.

It must be noticed that during this first phase of the in-orbit motion the satellite is not controlled and so the antenna pointing is not guaranteed. Typically, it is not a mission requirement, to communicate with the satellite during the de-tumbling phase, but the opportunity to receive a signal to track the satellite could be useful.

Spacecraft	Average case	Worst case	Unit
Spacecraft Transmitter Power Output:	2,0	2,0	Watt
In dBW:	3,0	3,0	dBW
Spacecraft Transmission Line Losses:	-1,0	-1,0	dB
S/C Connector, Filter or In-Line Switch Losses:	-1,0	-1,0	dB
Spacecraft Antenna Gain:	4,1	4,1	dBiC
Spacecraft EIRP:	5,1	5,1	dBW
Downlink Path			
Spacecraft Antenna Pointing Loss:	-2,0	-4,0	dB
Antenna Polarization Loss:	-2,0	-4,0	dB
Path Loss:	-145,0	-145,0	dB
Atmospheric Loss:	-0,5	-1,0	dB
Ionospheric Loss:	-0,3	-0,8	dB
Rain Loss:	0,0	0,0	dB
Isotropic Signal Level at Ground Station:	-144,7	-149,7	dBW
Ground Station			
Ground Station Antenna Pointing Loss:	-2,0	-3,0	dB
Ground Station Antenna Gain:	16,2	16,2	dBiC
Ground Station Transmission Line Losses:	-2	-3,0	dB
Ground Station LNA Noise Temperature:	300	300	K
Ground Station Transmission Line Temp.:	300	300	K
G.S. Transmission Line Coefficient:	0,6310	0,5012	
Ground Station Effective Noise Temperature:	695	675	K
Ground Station Figure of Merrit (G/T):	-14,2	-15,1	dB/K
G.S. Signal-to-Noise Power Density (S/No):	67,7	60,8	dBHz
System Desired Data Rate:	4800	9600	bps
In dBHz:	36,8	39,8	dBHz
Telemetry System Eb/No:	30,9	21,0	dB
Telemetry System Required BER:	1,00E-07	1,00E-07	
Telemetry System Required Eb/No:	14,3	14,3	dB
Link Margin	**16,6**	**6,7**	**dB**

Table 3: UHF downlink budget

2.3 Design of the TT&C electronic board

After the calculation of the link budget and the definition of the trade-off between link parameters (i.e. data-rate and channel bandwidth versus available power supply, antenna directivity versus satellite pointing capability), the second step in the design of the TT&C electronic board is the definition of the main sections of the board itself. In particular, four areas were defined:

- Microcontroller (μC): it is the core of the board which manages all the board components. The STM32F107 family of the ARM Cortex microcontroller was chosen, because of the high operative frequency (up to 72 MHz), the high internal memory (64 to 256 Kbytes of Flash memory and up to 64 Kbytes of general-purpose SRAM), the high number of general purpose pin and dedicated interfaces and the relative low power consumption;

- RF transceiver: a great number of Commercial Off The Shelf (COTS) integrated components perform the function of RF wireless transceiver. Considering the link parameters defined in the link budget (low data rate and channel bandwidth, low available power), the Chipcon CC1020 transceiver was chosen as best solution taking into account also the versatility of the circuit;

- Interfaces: the TT&C board must exchange data directly with other subsystems of the satellite and at the same time should have connections to the internal CAN BUS of the S/C. Moreover, specific interfaces toward backup subsystems are necessary in critical situation: the TT&C board is the only subsystem that could wake-up backup devices in case of failure of the main ones;

- Power supply: as a common architecture for the whole S/C, each subsystem receives a 28 V voltage signal from which derives the stabilized internal voltage for the proper functioning of the whole board.

2.3.1 Microcontroller

The microcontroller is the core of the TT&C electronic board. It manages the overall activities of the communication subsystem. The STM32F107 family of the ARM Cortex microcontroller was chosen, taking into account the trade-off between performances and power consumption. The chosen Cortex μC is a powerful device for a microsatellite: the high number of operations required by the communication system and the large number of peripheries to be used have highlighted the necessity to use powerful μC for ALMASat-EO electronic boards. Figure 4 shows the electronic

schematic for µC operation. An external quartz clock is added to give a 24 MHz reference signal which is internally multiplied to obtain the 72 MHz operational clock. Tantalium capacitors have been chosen for the internal power supply section. An external battery is added for real-time clock synchronization. Interfaces between TT&C board and the rest of ALMASat-EO electronic subsystem are shown in Figure 7 in paragraph 2.3.3.
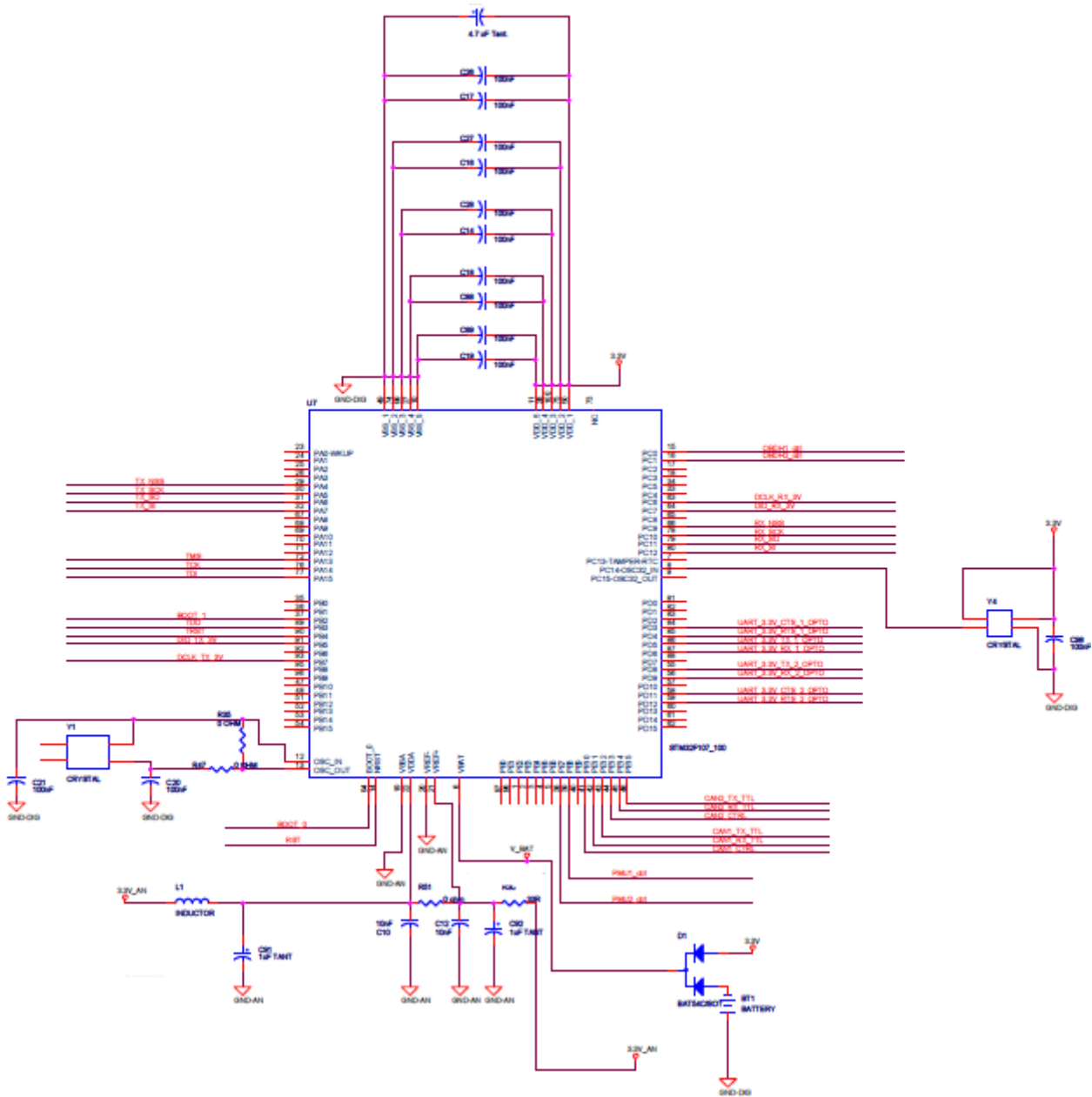
Figure 4: Cortex microcontroller schematic

During downlink transmission of telemetry data, the Cortex receives informations of the overall S/C status through dedicated Universal Asynchronous Receiver-Transmitter (UART) interfaces or the CAN BUS, directly collected collected by the OBDH board. Then, the bit stream is processed

performing the TM Space Data Link Protocol and the Reed-Solomon channel coding, as specified by the Consultative Committee for Space Data Systems (CCSDS) in [20] and [21]. Finally, digital data are sent to the RF transceiver CC1020, that generates the RF signal frequency modulated.

On the other hand, concerning uplink command, the RF signal is demodulated and decoded by the RF transceiver. Then, the bit stream is sent to the Cortex for the opposed elaboration of the CCSDS protocol and channel decoding. Finally, once the information bits are extracted, the command is sent to the OBDH board through UART interface or CAN BUS for the processing of the required information. Furthermore, the µC manages Serial Peripheral Interface (SPI) interfaces for CC1020 internal registers setting

2.3.2 RF transceiver

The RF section consists of two CC1020 RF transceivers. A separate integrated circuit was used for transmission and reception in order to obtain a faster communication system at the expense of a little increase of the circuit complexity that can be undertaken by the Cortex µC.

The CC1020 integrated circuit is a complete transceiver in UHF band. It supports FSK modulation and coherent Gaussian FSK modulation (GFSK). It is programmable with a microcontroller through SPI for a communication up to 153.6 Kbps with a channel beamwidth of 500 KHz and a maximum output power of 10 dBm.

The inter-frequency section of the transceiver is able to perform:

- Demodulation of the incoming signal;
- Filtering and amplification of the received signal through two integrated LNA and an automatic gain control sequence;
- Generation of Received Signal Strength Indicator (RSSI) which can be used for internal check of the link condition;
- Signal modulation from the incoming bit stream from the µC;
- Synthesis of the transmitted frequency and power amplification.

The CC1020 circuit is connected to the Cortex µC through a SPI for the internal register setting and an UART interface for the bidirectional transmission of data received or to be transmitted. Figure 5 shows the digital net required by the CC1020 transceiver. Particular attention was kept to the definition of the layout of the Printable Circuit Board (PCB) for the RF section:

- A band-pass filter was introduced in order to cut-off all the spurious frequencies located outside the channel bandwidth;

- A matching network was inserted between the CC1020 and the coaxial connector in order to match the circuit output impedance with the 50 Ohm impedance of connectors and cables.

Figure 6 shows the adopted solutions for RF filters and matching networks designed for the engineering model of the TT&C electronic board described in paragraph 2.4.
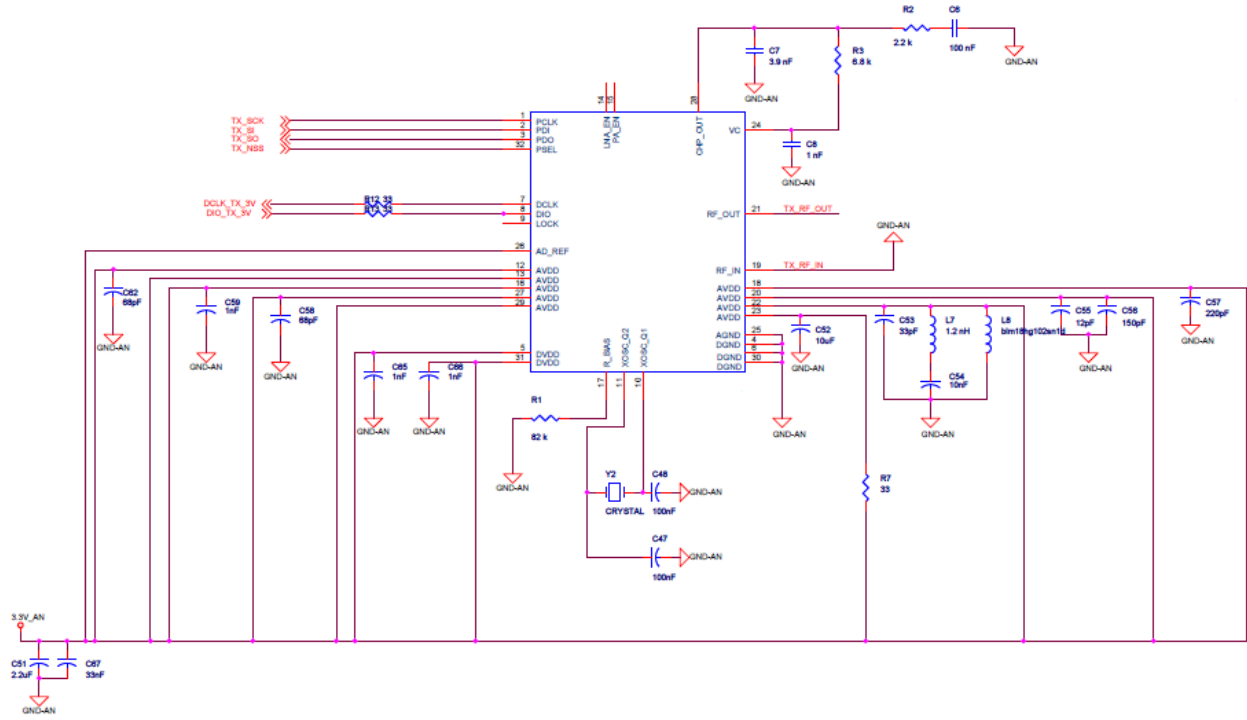
Figure 5: CC1020 schematic
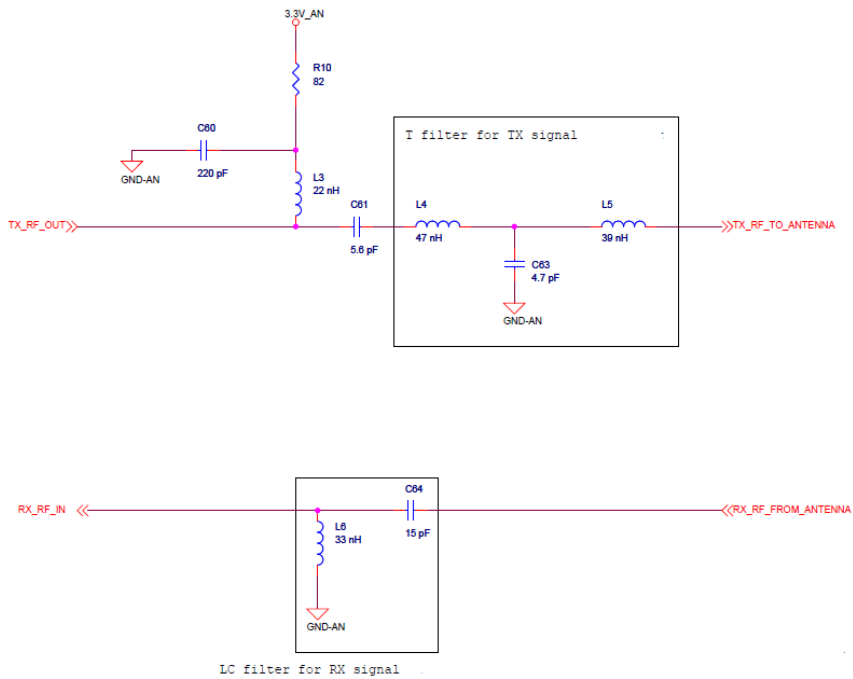
Figure 6: Filter and matching network schematics

2.3.3 Interfaces

The TT&C board has to exchange data mostly with the OBDH subsystem. In fact, each information received is demodulated and checked for consistency internally the TT&C, then sent to the OBDH board that will proceed to the decoding of the command. In the same manner, each telemetry information is collected by the OBDH and sent to the TT&C board that will provide to transmit data to the GS.

The bidirectional communication between TT&C and OBDH boards is performed through serial interface RS232. As a consequence of the redundancy of the last subsystem, each TT&C board contains two serial interfaces, one for each OBDH board. As shown in Figure 8, optocouplers were added to each signal path in order to physically interrupt the electrical continuity between the microcontroller of the TT&C board and the OBDH board not in use and avoid the leakage current. Furthermore, a CAN BUS interface is present on the board in order to directly receive data from the sensors on-board the satellite and as a backup of the serial communication interface.

Despite the decoding of general commands is performed by the OBDH, some particularly critical commands are decoded directly by the TT&C board: for instance, in case of failure on the main OBDH itself, the TT&C system is able to decode the command of activation of the backup board providing a power-up signal for the aforementioned board; the same service is also defined for the Power Management Unit (PMU): in case of failure of the main board, which manages the power supply of the entire satellite, the TT&C board is able to switch-on to the backup board. In light of this, a dedicated power supply line is connected directly to the electronic board, which receives a 28 V signal and internally generates the 5 V and 3 V needed for the proper functioning of the board. A complete block diagram of the electronic board interfaces with the other spacecraft subsystems is shown in Figure 7.
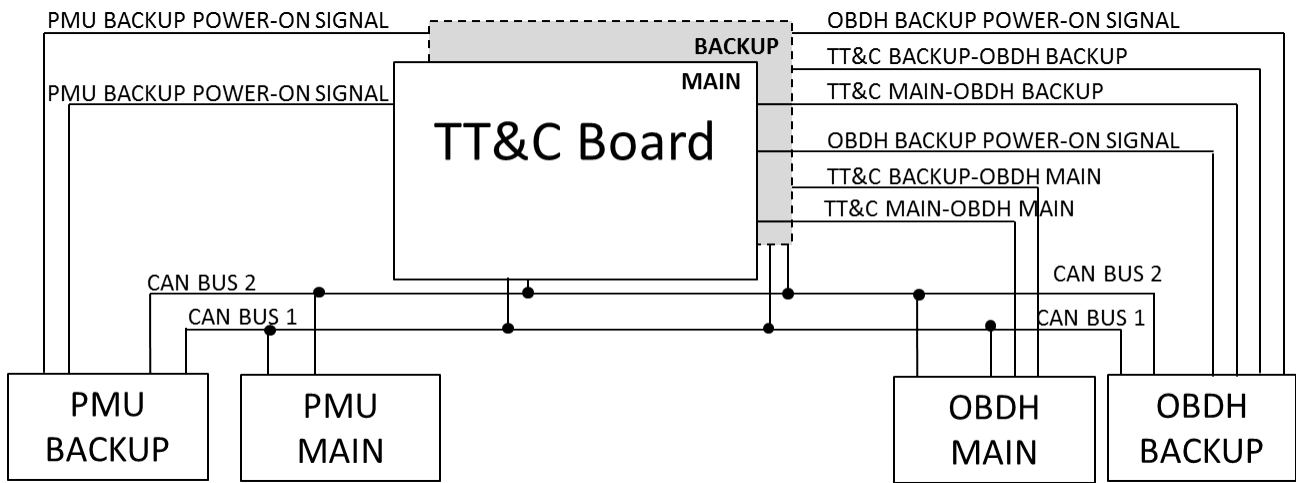
Figure 7: Block Diagram of the TT&C electronic board interfaces
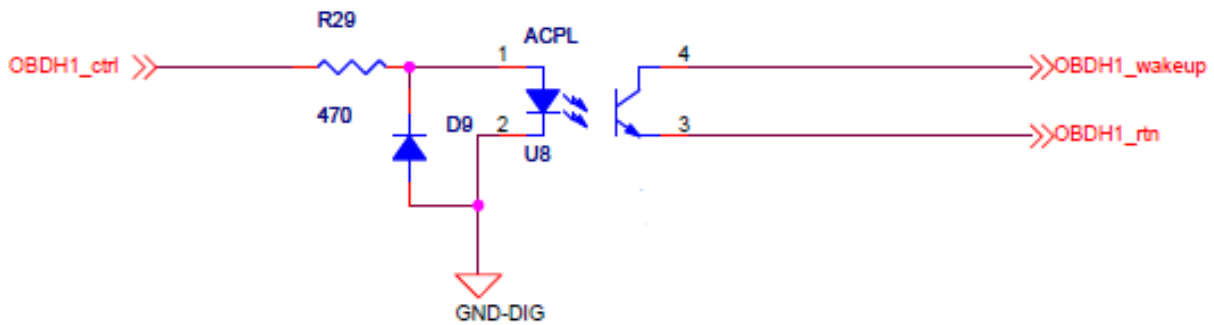
Figure 8: Schematic of the optocoupler

2.3.4 Power supply

The whole satellite power bus consists of a 28 V signal connected to all the internal subsystem. Then, each subsystem is able to regulate the internal voltage, and the proper value of current, for the proper functioning of the internal circuit. Despite the little increasing of mass and volume of each electronic board, this architecture allows a dedicated regulation of the power supply and a simpler design of the power board.

The power section of the TT&C board receives a 28 V signal through a connector located on the power bus of the satellite. A first DC/DC converter is used to obtain a stabilized voltage at 5 V for the power supply of the Cortex μC, RS-232 and CAN BUS integrated circuit and optocouplers. Moreover, a second step of DC/DC converter is introduced to obtain a dedicated 3 V stabilized voltage for the power supply of the RF section.

2.4   Electronic board engineering model

Figure 9 shows the first prototype of the TT&C electrical board. The right part of the board contains the power section: two DC/DC converters are used to obtain the regulated operational voltages of 5 V and 3 V. On the top centre of Figure 9 a dedicated CAN connector allows to directly connect the board to the satellite CAN BUS while the upper-left connector is dedicated to the serial interfaces and direct links with the OBDH and PMU boards. Finally, the RF section is shown on the left-bottom side of Figure 9: the RF path was designed as short as possible in order to minimize interferences and losses on the RF signal, while coaxial SMA connectors allow to connect the transceivers to the antenna system.

The board has a total mass of 160 g and an overall size of 185x80 mm. The power consumption is about 0.85 W in receive-mode only, while 7.5 W is the peak power consumption during downlink transmission (for 2 W RF output power).
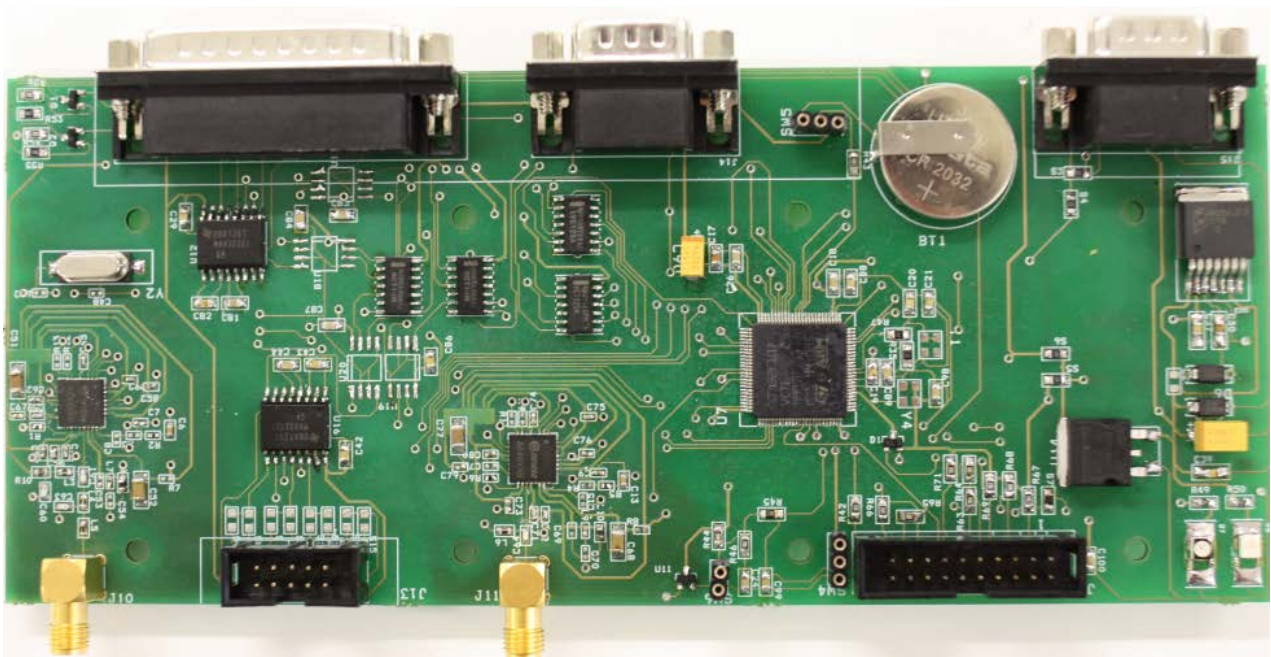
Figure 9: TT&C subsystem electronic board Engineering Model

2.5 Development of the embedded software

2.5.1 Operative microcontroller software
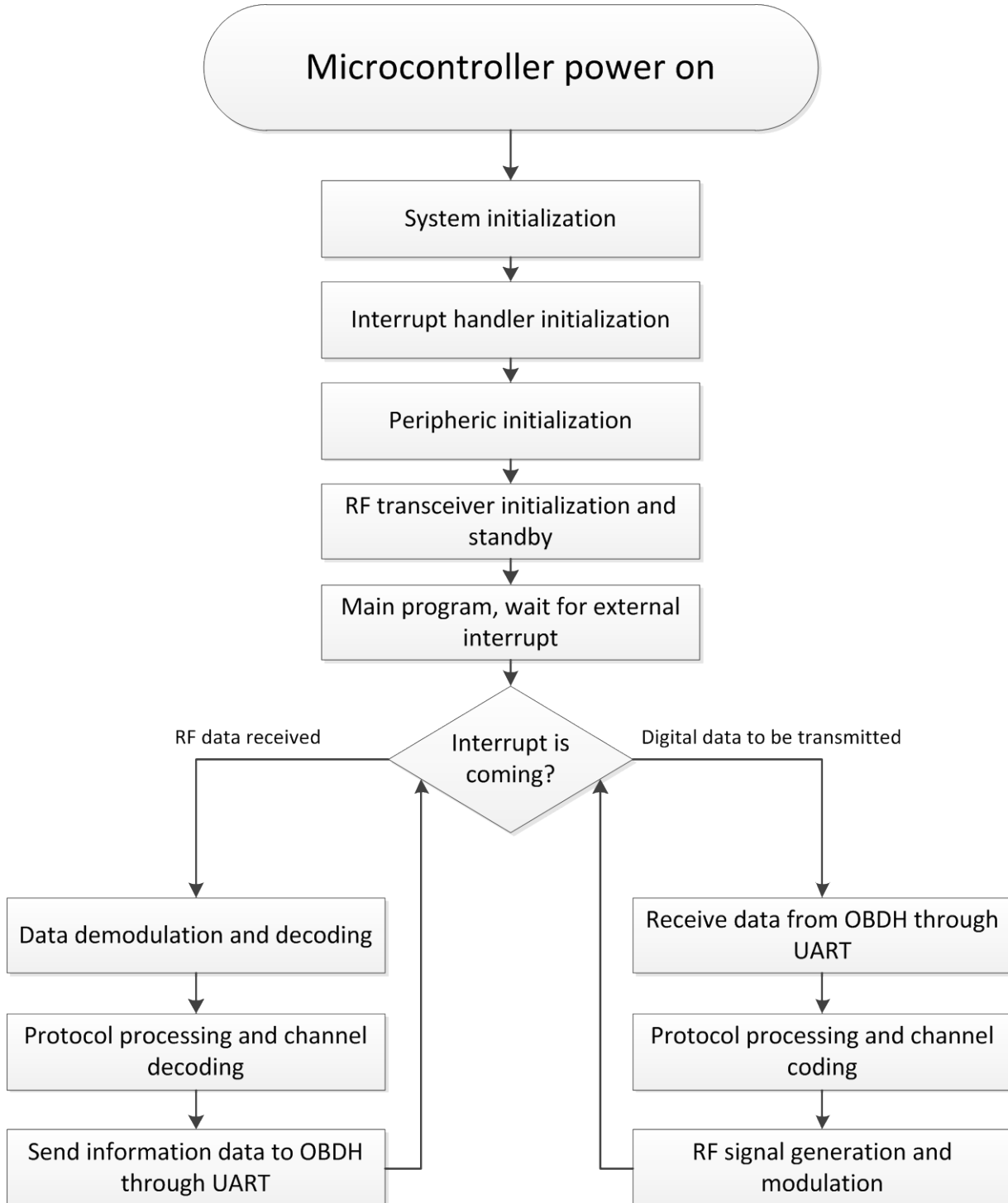
Figure 10: Functional diagram of the microcontroller embedded software

Figure 10 shows the functional diagram of the embedded software in C language that was developed for programming the Cortex µC operational behavior. The main requirement in such a software is the response rapidity to external stimulus. In fact, after a first phase of system and interfaces setup, the microcontroller waits for external input signals. During this phase RF transceiver for transmission is set in powerdown mode in order to minimize the total power consumption.

Then, if a RF signal is received from the GS, the µC is ready to receive the decoded bit stream and start the operation for extract information bits. After that, commands are at once sent to the OBDH board. Similarly, if telemetry data are received from the OBDH board, the µC should be ready to process them, applying the CCSDS protocol and channel coding and send the output bit stream to the RF transceiver in order to generate the downlink signal as soon as possible.

External stimulus to the Cortex are processed using interrupt hierarchy: for instance, reception of commands represents the highest priority action, being vital for the S/C to receive each command sent from the GS, while the transmission of the beacon, that is the periodic downlink signal containing main telemetry data, is characterized by the lowest priority, because to postpone the transmission of the beacon of several seconds does not imply critical consequences on the S/C mission.

2.5.2 CC1020 configuration

The CC1020 configuration can be defined writing a set of internal register through a 3-wire SPI interface. Particular attention must be kept to the RF transceiver configuration. In particular, the rapidity of the power-up sequence could affect the sensitivity of the analog receiver chain and a good trade-off must be chosen. Considering the high reliability that the TT&C communication system should offer the receiver sensitivity has been considered the main requirement for the transceiver.

Main transceiver setting are summarized hereafter:

- LNA: the current in the internal LNA is set to the maximum allowed value to improve sensitivity at the expense of power consumption;
- Phase Locked Loop (PLL) waiting time: the waiting time from PLL lock until RX power-up is set to the minimum available value of 26 µs;
- Automatic Frequency Control (AFC): the digital data slicer uses an average value of the minimum and maximum frequency deviation detected as the comparison level. Once a shift

in the received frequency larger than the expected deviation is detected, a bit transition is recorded and the average value to be used by the data slicer is calculated. For better data decision accuracy the number of bits used for the averaging is set to the maximum allowed;

- Calibration: to compensate for supply voltage, temperature and process variations, the VCO and PLL must be calibrated. The calibration is performed automatically and sets the maximum VCO tuning range and optimum charge pump current for PLL stability. The calibration time is set to the maximum allowed value to obtain a best accuracy during calibration of PLL loop filter bandwidth.

2.6 Antenna system

A unique UHF frequency band is used for uplink and downlink paths on–board ALMASat-EO, giving the possibility to use the same antenna system for both transmission and reception. Two major issues have characterized the front-end design: the use of an RF transceiver for TX or RX only and the redundancy of the TT&C board, with a main and a backup ones that have to be connected at the same antenna system at the same time.

These requirements are satisfied using two circulators, in order to separate the high power transmitted signal path to the low noise received one, as shown in Figure 11 where the green blocks are the common device while the red ones represents the specific downlink or uplink components. The two circulators are directly connected to the hybrid coupler input ports. Being a passive components, the hybrid coupler and the antenna system are used for both downlink and uplink paths. Bidirectional arrows in Figure 11 underline this technical aspect. The hybrid coupler used in ALMASat-EO is a passive six-ports beam forming network, realized using an hybrid technique that make use of microstrip lines and wireline cables. An RF signal connected to one of the two input ports generates four 90 degrees phase shifted signal at the same frequency at the four output ports. Phase shifted signal are connected to a vase turnstile antenna in order to generate circular polarization [22]. The vase turnstile antenna configuration was selected in order to guarantee a circular polarization and a moderate gain of 4.1 dBi together with a large beamwidth of 30 degrees that can reduce problems related to a non-perfect antenna pointing. It consists of four dipoles assembled with a 42-degrees angle with respect to the S/C structure placed on the top of the satellite structure, in order to obtain the radiation pattern main beam pointing toward the Earth.

Antenna radiation characteristic are shown in Figure 12 (both diagrams are normalized with respect to the maximum gain of 4.1 dB for the $\varphi=90°$ plane and 0 dB of gain for the $\theta=90°$ plane): it can be

noted from the diagram on the left that the main lobe of the antenna is centered at θ=180° (i.e. directed towards the GS); from the diagram on the right, showing the gain for θ=90°, it can be noted that the gain is almost constant offering the possibility of a reliable link during the de-tumblimg initial phase. Reflection coefficient and Voltage Standing Wave Ratio (VSWR) are shown in Figure 13: an S11 coefficient less than -45 dB and a VSWR of about 1.2 for the whole channel bandwidth allow for minimum power dissipation.
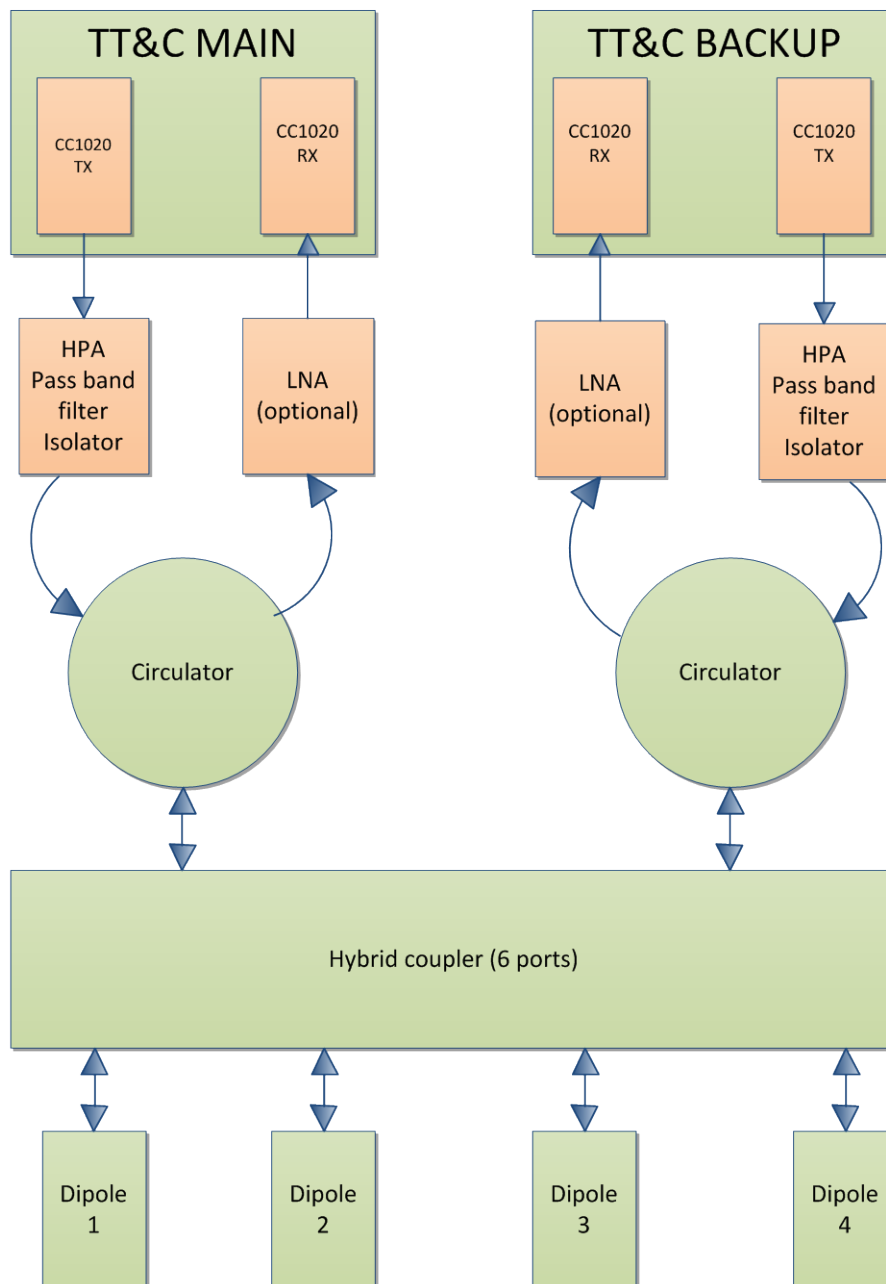
Figure 11: ALMASat-EO TT&C antenna system
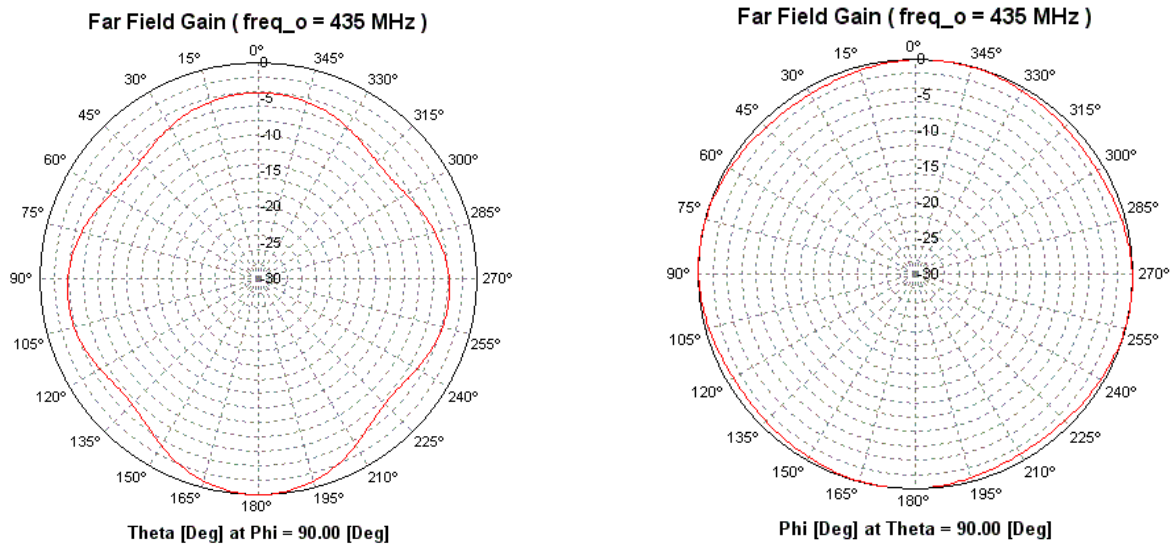
Figure 12: UHF antenna system 2D radiation patterns
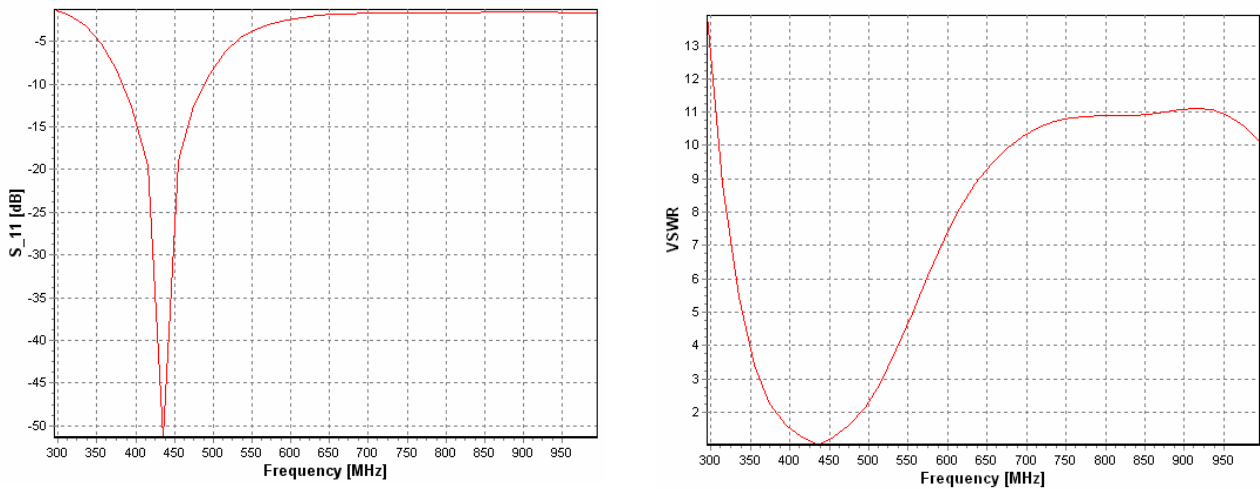
Figure 13: UHF antenna system S11 and VSWR parameters

2.7 Communication tests

A test campaign was performed at the University of Bologna microsatellite laboratory. The purpose of the test is an evaluation of the RF signal characteristics (i.e. signal spectrum, occupied bandwidth), the performance of the board during RF operations (sensitivity, power consumption and time necessary for power on sequence) and the BER of the link reproducing the nominal conditions derived from the link budget. Two engineering model boards, as the one shown in Figure

9, were assembled and used for the test. Because of the lack of an anechoic room for RF test at Forlì campus facilities, far field measurements were performed in an open space where the presence of some obstacle could create unwanted propagation effects as reflection and multipath.

2.7.1 RF signal

Figure 14 shows the spectrum of the GFSK modulated signal centered at 433.5 MHz, setting the transceiver with a data rate of 4.8 Kbps. A pseudorandom sequence defined by the polynomial $x^9 + x^5 + 1$ has been used in order to generate a balanced spectrum. The frequency deviation is set to 2.475 KHz from the carrier deriving a theoretical channel bandwidth of 25 KHz. Figure 14 was obtained setting the TT&C board in periodical transmission of a packet of 1024 bytes generated using the aforementioned polynomial at the maximum output power of 10 dBm and a simple dipole antenna for UHF frequency band. The spectrum analyzer, an Agilent N9320A, was connected to a general purpose dipole antenna. The TT&C board and the spectrum analyzer were placed at a distance of about 5 meters in order to recreate far field condition. The total deviation of 4.950 KHz between the two symbol of the modulation scheme used is confirmed together with the whole channel spacing.
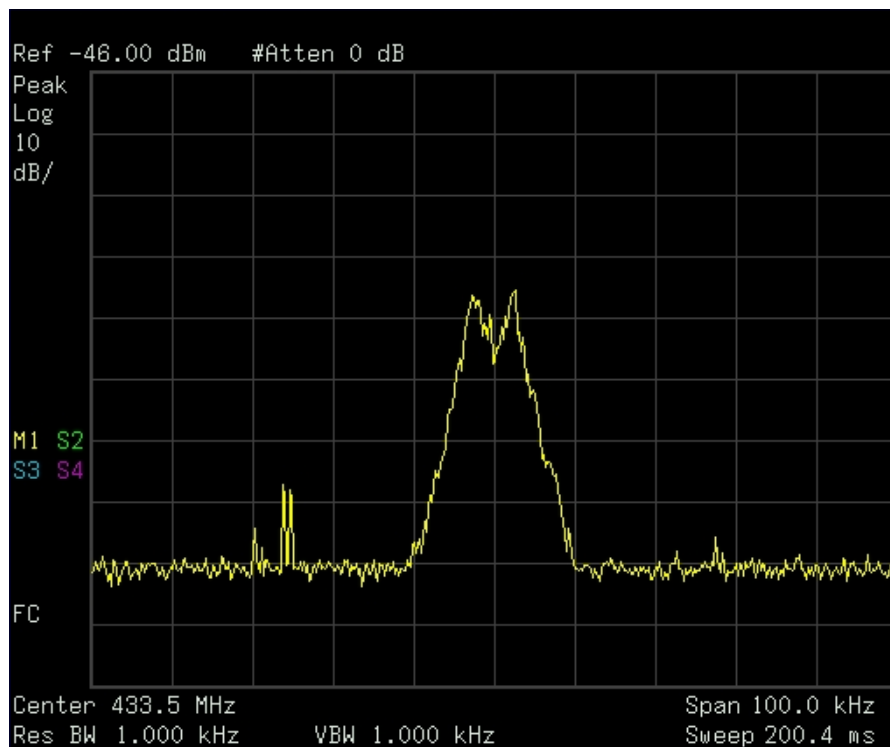
Figure 14: GFSK modulated signal spectrum
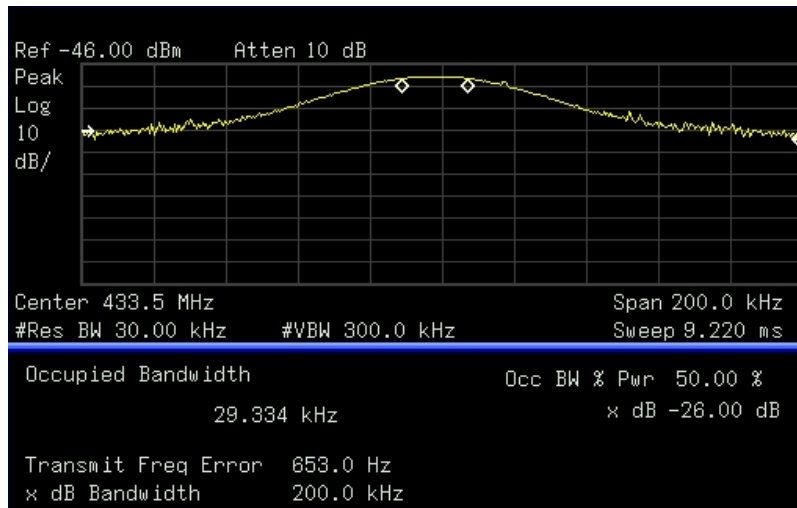
Figure 15: Occupied bandwidth for 50% of channel power
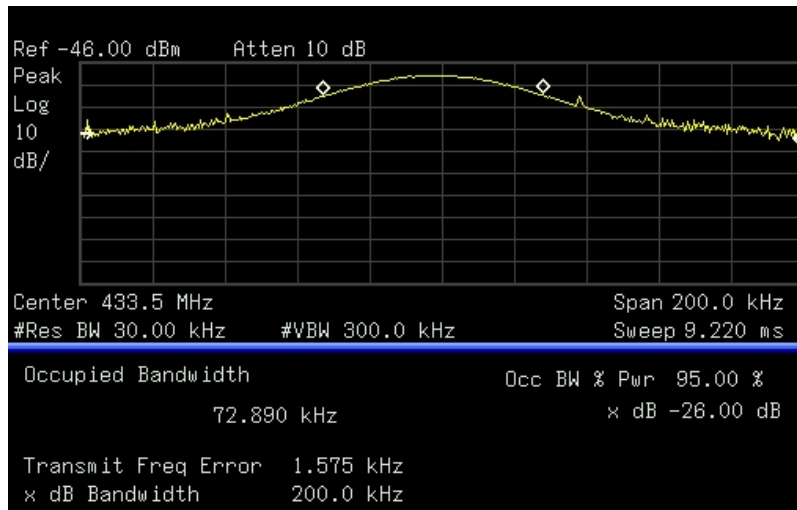
Figure 16: Occupied bandwidth for 95% of channel power
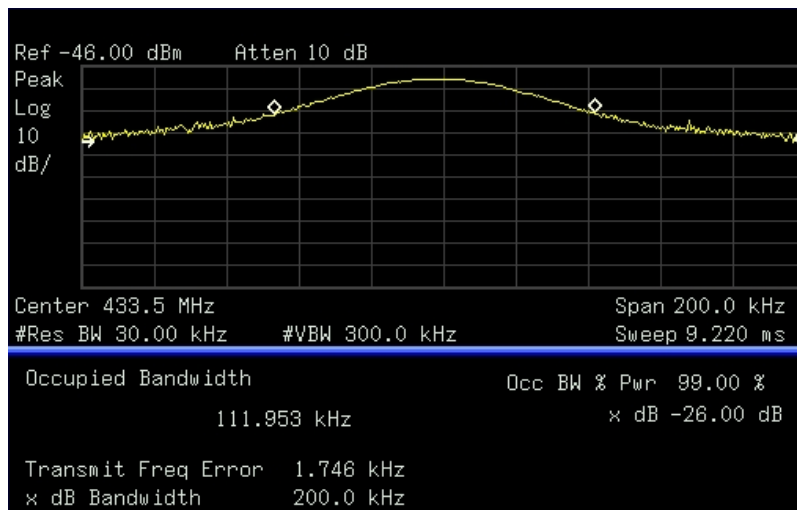
Figure 17: Occupied bandwidth for 99% of channel power

Occupied bandwidth for different percentage of signal power is shown from Figure 15 to Figure 17, obtained with the same measurement setup of Figure 14. A bandwidth of 29.334 KHz has been measured containing the 50% of the channel power, while the total channel spacing is larger for higher percentage of power: 72.890 KHz for 95% and 111.953 KHz for 99% of the whole transmitted power.

2.7.2 TT&C board performance

As one of the more stringent requirement for the design of a microsatellite subsystem, the power consumption has been carefully monitored. During nominal operation, the TT&C board is waiting for incoming digital signal from the OBDH board or RF signal from the GS. So, the only circuit to be powered on are the microcontroller, the board interfaces and the transceiver used for receive the RF signal. With the power supply net described in paragraph 2.3.4, the current consumption is about 30 mA for a total power consumption of about 0.85 W. During RF transmission the output power should be at least 33 dBm, according to the link budget. In order to reach this value an external UHF power amplifier is added, as the CC1020 allows for 10 dBm. During this operation, the whole power consumption of TT&C board plus the PA reaches the value of about 7.5 W.

Moreover, even if the uplink path is not critical from the point of view of the link budget, the receiver sensitivity was checked for more precise information about the uplink condition. The CC1020 datasheet reports a value of -112 dBm as circuit sensitivity for a BER of 10^{-3}. This value is clearly incompatible with the required BER of the uplink path, that is fixed at 10^{-7}. During the test campaign, a value of -105 dBm was measured as transceiver sensitivity for the required BER.

Finally, the transmitter power on sequence time, a critical parameter of the TT&C board architecture, was carefully checked. In fact, due to the short interval time available for communication during an orbit, the transmitter power-on sequence should be as quick as possible. The CC1020 allows for a preliminary transceiver internal register setting and the possibility to switch off the transmitter chain without delete the circuit configuration. So, when the µC receives data to be transmitted, it has to wake up the transmitter circuit and start the downlink communication. Using two different transceiver for transmission and reception, the power-on sequence of the transmitter is significantly faster: the register setting is done with the SPI at the maximum frequency of 115.2 KHz, the RF chain (crystal oscillator core and bias generator) need a total interval time of few ms for power up, so the total transmitter power-on sequence is performed in less than a second.

2.7.3 Bit Error Rate

Figure 18 shows the setup of the measurement chain for the BER test. Two TT&C engineering model boards are used, the first one as a transmitter and the second one as a receiver. As antenna system, a single dipole UHF antenna is used instead of the Vase Turnstile configuration described in paragraph 2.6. Far field condition is recreate in open space environment, as far as possible to obstacles that could affect the signal propagation as buildings or trees, but unwanted propagation effects as reflection and multipath cannot be completely avoided. The received signal is split using a directional bridge, in order to connect both the spectrum analyzer and the TT&C board. 1.5 dB of attenuation is inserted on the RF signal connected to the electrical board while 16 dB is the attenuation to the spectrum analyzer: both attenuations were added to the measured power values. The received power is also monitored through an internal RSSI of the CC1020. Coaxial cables are used for all the RF signal connections. After demodulation and decoding, the bit stream is sent to a PC through UART interface, and stored for post-processing. A bit stream of all "zeros" is generated and applied to the $x^9 + x^5 + 1$ polynomial, then the BER is calculated counting the number of received "ones", taking into account that one bit error will generate 3 received ones and that the first 9 received bits should be discarded. A software in C language has been developed for the storage of the received bit stream while the post processing of BER calculation has been performed in Matlab environment.
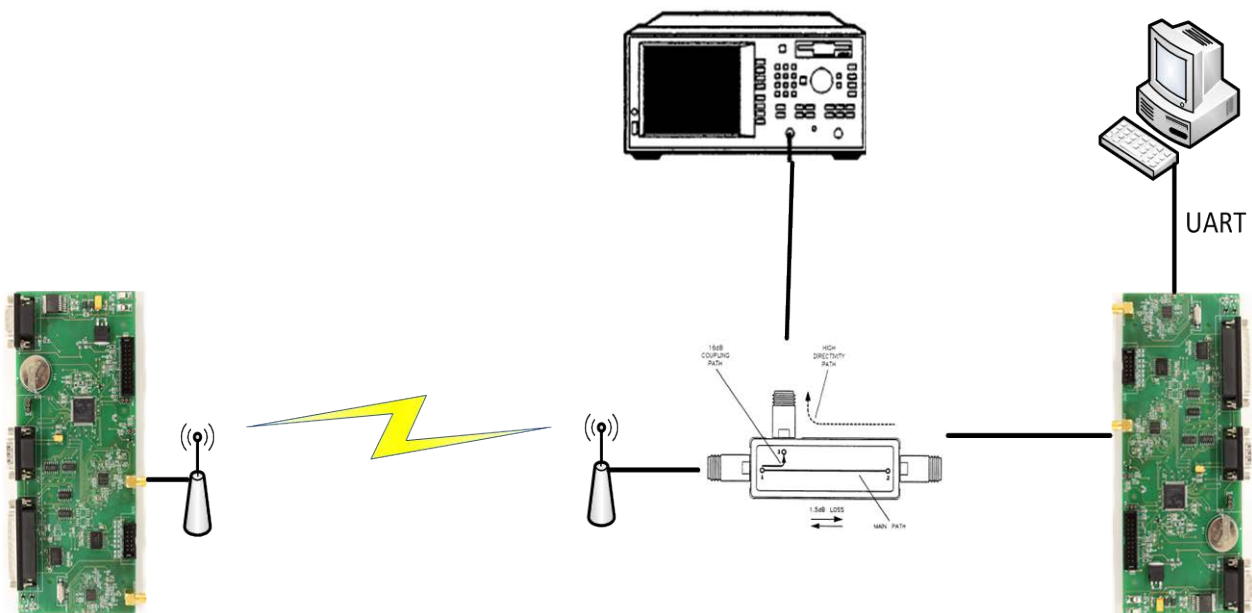
Figure 18: Setup of the BER chain measurement

Figure 19 shows the BER for the downlink path. The received power is set in order to recreate the link budget average condition, adjusting the RF transceiver output power (from the minimum allowed of-20 dBm to the maximum value of 10 dBm) and introducing calibrated attenuators before the directional bridge on the receiving side. No external PA have been added. For a complete investigation, the measurement campaign was repeated switching the TT&C boards with the same results. Measurement result shows that the RF transceiver offers demodulation and decoding capability very close to the theoretical BER for coherent GFSK. The slight degradation of performance of 0.15 dB at BER 10^{-7} shown in Figure 19 is probably due to the not ideal environment used for far field propagation test, due to the lack of an anechoic room. Anyway, the link budget offers a considerable margin so this degradation could be accepted.

Coding gain is not considered in this test campaign because, while the implementation of coding algorithm is already developed and inserted in the µC embedded software, the decoding algorithm is still under development and so it was impossible during the test campaign to introduce this feature.
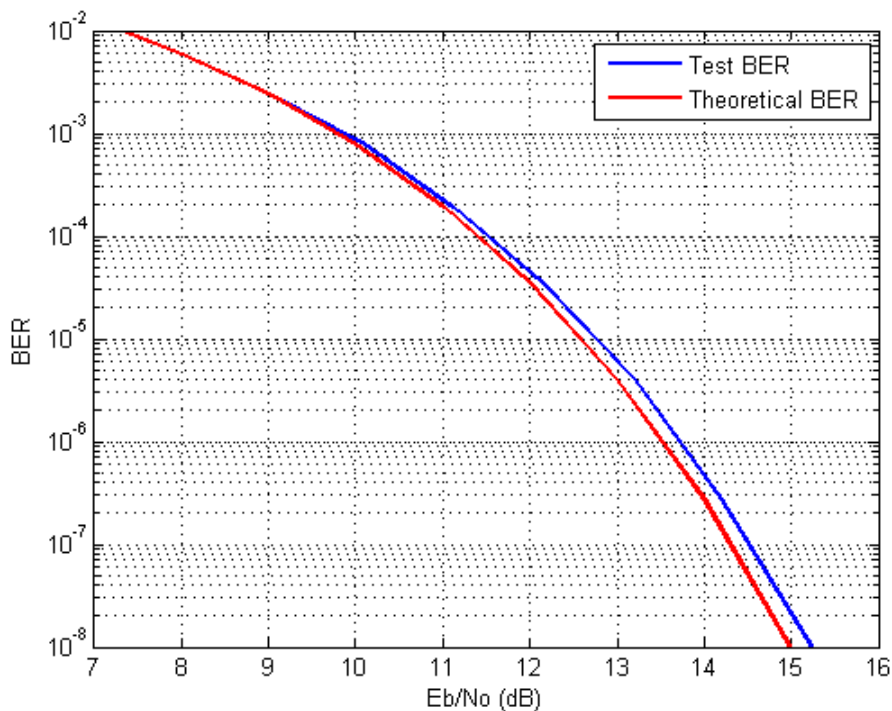
Figure 19: BER of the downlink path

3   ALMASat-EO high-speed transmitter subsystem

The ALMASat-EO mission goal is the test of a compact, innovative multispectral camera for Earth observation. An S-band high data rate transmitter, named HSTX, was designed and developed as an integrated part of the ALMASat-EO optical payload, as shown in Figure 20, allowing the establishment of the downlink connection for sending Earth images to the GS.

Considering the huge amount of data collected by the multispectral camera and the relative short time interval available for the whole downlink of Earth images, the resultant requirement in term of available data rate has highlighted the necessity for a dedicated downlink subsystem. As a matter of fact, the TT&C system performance is inadequate and a faster and more powerful transmitter is necessary.

The HSTX was designed to meet basic requirements of small satellite platforms in LEO orbit: low mass, low power consumption and low cost. In particular, the total power consumption of a radio link can be reduce minimizing the amount of retransmission due to demodulation and decoding errors in the receive chain that affects the total throughput. In light of this, in order to maximize the final throughput of a LEO orbit link, generally limited by geometry and short duration of the contact passes, a Software Defined Radio (SDR) architecture was developed, allowing reconfigurability of main link parameters (i.e. channel coding, modulation, pulse shaping and final data rate) with the key advantage of adapting the link to the current channel condition, [23] [24] [25]. The HSTX reconfigurability is obtained using a reprogrammable FPGA platform as the subsystem core.

The overall architecture consists of two different boards: a Digital Processing Unit (DPU), based on the FPGA platform, performing the digital signal processing, and a Transmitter Back-End (TXBE), an analog board which performs frequency up-conversion and filtering, designed for 2.4 GHz free license frequency band. It must be noted that the aforementioned architecture allows the possibility to easily re-use the DPU at higher frequencies (X- and Ka-band) together with an appropriate analog module. The key advantage of such an architecture is the possibility to re-use the DPU board in future missions that could foresee the use of higher frequency bands. As a matter of fact, the DPU output consists of an analog inter-frequency signal, centered at 10 MHz, that could be up-converted, filtered and amplified using a suitable TXBE to a final frequency band of 8400-8500 MHz (X-band downlink) or 31800-32300 MHz (Ka-band). Furthermore, designing two separate board instead of a bigger one easily allows to meet requirement in terms of occupied volume, that

could be critical in a limited platform as a microsatellite. Furthermore, considering the limited dimension of the separate TXBE board it is easier to include the electronic device in an RF enclosure in order to avoid RF interference and guarantee complete RF shield. Disadvantages derived from this electrical board separation consist of a slight increase of the total weight due to the introduction of RF connectors and duplication of common electronic circuit. For instance, the regulated power net is replicate in both the DPU and the TXBE. Moreover, the coaxial cable for the DPU output RF signal introduces a small of degradation in signal integrity and power.
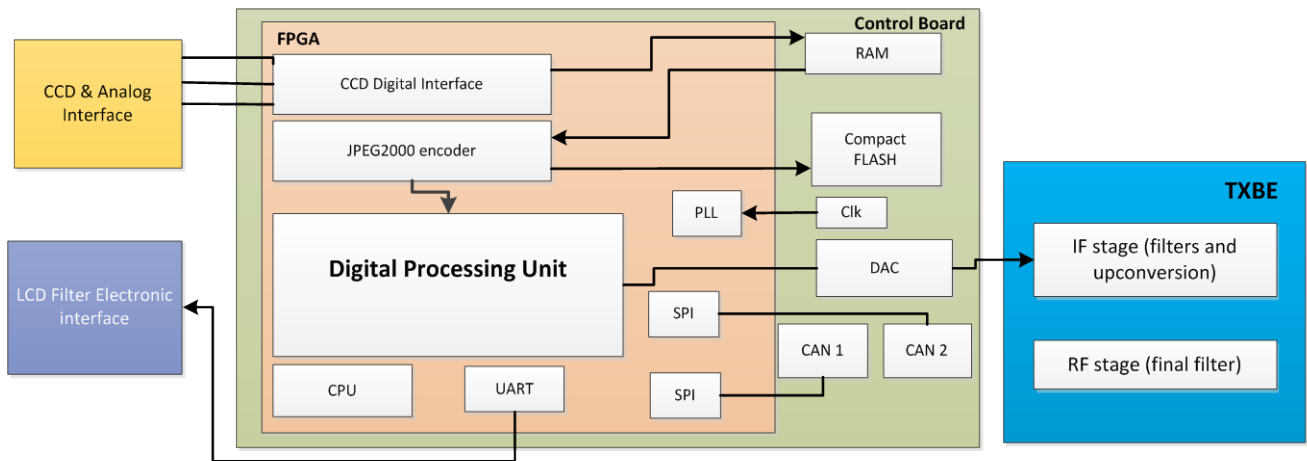
Figure 20: block diagram of the ALMASat-EO optical payload electronic

3.1 Requirements

The HSTX design was driven by the main requirement of available final data rate, which has to allow the downlink of the overall amount of data collected by the multispectral camera.
During an ALMASat-EO orbit the optical payload collects Earth images of 2048x2048 pixel of resolution. Each pixel is coded using 14 bit, for a total amount of

Eq. (2)
$$image_{no\_compress} = 2048 * 2048 * 14 = 58720256 \; bit$$

As shown in Figure 20, a JPEG2000 encoder is introduced in order to minimize the amount of data to be transmitted. Although a lossy encoder allows a compression factor of about 100, a standard lossless encoder allows for a compression factor of 4, for a total amount of bit of:

Eq. (3)
$$image_{lossless} = 58720256/4 = 14680064 \; bit$$

In order to cover an area of 65x80 Km, 6 images are collected, each of them covering an area of 65x80 Km and with a huge overlapping area. As a consequence, a band of 6 images consists of:

Eq. (4)
$$band = 14680064 * 6 = 88080384 \ bit$$

Thanks to the wide overlapping area among the 6 images, a second compression algorithm, named multilayer algorithm, can be used offering again a compression factor of about 4. It must be noted that higher compression factor can be reached using more powerful multilayer algorithm but the computation required is incompatible with the FPGA device chosen for ALMASat-EO optical payload. Therefore, a single band take up:

Eq. (5)
$$band_{lossless} = 88080384/4 = 22020096 \ bit$$

The goal of ALMASat-EO mission is to acquire Earth image of an area of 1000x80 km each passage, so about 16 bands are necessary; so it is possible to derive the total amount of data to be transmitted as following:

Eq. (6)
$$area_{lossless} = 22020096 * 16 = 352321536 \ bit$$

resulting in about 352 Mbit. Furthermore, it should be taken into account the overhead of data to be transmitted due to the transmission protocol and channel coding techniques. The total overhead could be estimated as the 15% of the information bit, so a final value of 400 Mbit can be considered as the total amount of information collected by the multispectral camera for each passage. The available time for downlink depends on the orbit parameter: it can be assumed that an average good orbit with 20 degree of elevation allows for 10 minutes of reliable link between ALMASat-EO and the GS at the University of Forlì facility. However, only half of the available time could be used for the downlink of collected images, as telemetry data eventually commands have to be transmitted and received during the same orbit. Therefore, 300 seconds can be considered as available downlink time. Having chosen a QPSK modulation, as explained in paragraph 3.4.3, each symbol of the modulation constellation consists of 2 bit. So the final data rate should be:

Eq. (7)
$$data\ rate = \left(\frac{400}{2}\right)/300 = 0,66\ Msps$$

Finally, it should be considered that only a partial number of orbits can be used for Earth images downlink. Furthermore, the contemporary acquisition and downlink of Earth images could be problematic in terms of available time and supplied power for both operations. Moreover, other activities such as attitude and orbital manoeuvres could be actuated, reducing the available time for images transmission. As a consequence, the possibility to save images data of multiple passages has been introduced, at the expense of the required final data rate in a single passage of the S/C. It can be supposed that data collected during three passages have to be transmitted during a single orbit, so the final required data rate is:

Eq. (8)
$$final\ data\ rate = 0,66 * 3 = 1,98\ Msps$$

This is the basic requirement for the HSTX operation. Then, some restrictions derived from the chosen strategy of polyphase decomposition for the interfrequency signal generation have fixed the final data rate to 2.5 Msps.

3.2   Link budget

The link budget shown in Table 4 was carried out taking into account the same contributes on the RF signal of the UHF link budget shown in Table 3 at page 18. The S/C section takes into account a patch array antenna configuration that is thoroughly described in section 3.5 and that offers a gain higher than to 9 dB in direction of maximum gain. As in the UHF link budget, attenuations introduced by atmosphere, ionosphere and the distance between S/C and GS are considered, together with losses derived from non-perfect S/C antenna pointing or polarization mismatch.

As for the UHF band, the S-band is not critical from the point of view of atmospheric and ionospheric absorption. Moreover, the resulting wavelength of about 12 cm avoids precipitation interaction and rain absorption is neglected. At middle latitude, the ionospheric absorption for a one-way traverse of the ionosphere at 20 degrees of elevation angle is about 0.2 dB. Greater absorption can occur for low elevation angle.

Atmospheric absorption phenomena can occur caused by the presence of gases, especially at low elevation angle. The total amount of loss is directly proportional to the frequency of the link: a

conservative value of 0.3dB has been considered in Table 4. Moreover, polarization loss consists of imperfection in manufacturing of both S/C and GS antennas and depolarization effects such as the presence of crosspolar components of the electric field.

The high data rate e of 2.5Mbps, and the relative large channel bandwidth, introduces high level of noise in the receiver. Considered a BER margin of 10^{-6} the result of such a link configuration is a safety margin of 7.2 dB in average condition and 3.7 dB during worst condition. The gain obtained thanks to the implementation of channel coding techniques is not shown in the link budget. In fact, the amount of produced overhead could be critical from the point of view of data to be transmitted. The use of such a technique will be evaluated after the definitive assignation of ALMASat-EO orbit and the calculation of the total time interval available for the downlink.

Spacecraft	Average case	Worst case	Unit
Spacecraft Transmitter Power Output:	5,0	5,0	W
In dBW:	7,0	7,0	dBW
In dBm:	37,0	37,0	dBm
Spacecraft Transmission Line Losses:	-0,5	-0,5	dB
S/C Connector, Filter or Switch Losses:	-1,0	-1,0	dB
Spacecraft Antenna Gain:	9,0	9,0	dBiC
Spacecraft EIRP:	14,5	15,5	dBW
Downlink Path			
Spacecraft Antenna Pointing Loss:	-1,0	-2,0	dB
Antenna Polarization Loss:	-3	-4	dB
Path Loss:	-158,0	-158,0	dB
Atmospheric Loss:	-0,3	-0,5	dB
Ionospheric Loss:	-0,2	-0,5	dB
Rain Loss:	0,0	0,0	dB
Isotropic Signal Level at Ground Station:	-148,0	-150,5	dBW
Ground Station			
Ground Station Antenna Pointing Loss:	-2,0	-3,0	dB
Ground Station Antenna Gain:	34	34	dBiC

Ground Station Transmission Line Losses:	-1	-2	dB
Ground Station LNA Noise Temperature:	300	125	K
Ground Station Transmission Line Temp.:	300	290	K
Ground Station Sky Temperature:	450	450	K
G.S. Transmission Line Coefficient:	0,7943	0,7943	
GS Effective Noise Temperature:	719	542	K
Ground Station Figure of Merrit (G/T):	3,43	5,66	dB/K
GS Signal-to-Noise Power Density (S/No):	83,02	85,75	dBHz
System Symbol Rate:	2500000	2500000	sps
In dBHz: (assuming α=0.35)	65,28	65,28	dBHz
System Eb/No:	17,7	20,5	dB
System Required BER:	1,00E-06	1,00E-06	
System Required Eb/No:	10,53	10,53	dB
Link Margin	**7,2**	**3,7**	**dB**

Table 4: S-band downlink link budget

3.3 Design of the electronic boards

3.3.1 Digital Processing Unit

The DPU performs the digital signal processing realizing a programmable multi-rate system. Figure 21 shows the block diagram of the developed board and the demoboard used for the development of the software. First of all, digital information is processed by applying channel coding: though both Reed-Solomon and convolutional coding techniques were implemented the SDR architecture allows to adapt the channel coding to the link condition. Therefore, both encoder could be used in a concatenated structure with the consequent huge overhead or, alternatively, a single coding technique can be selected. Moreover, the overhead of the single coding technique can be chosen through puncturation technique.

The second step consists of pulse shaping and data rate selection. A multi-rate system was designed exploiting the polyphase decomposition concept [26]: instead of a unique digital FIR filter a set of shorter FIR filter has been used in parallel minimizing the total delay and allowing the possibility to vary the transmitter final data rate, changing the number of used filter. Afterwards, the phase modulation is performed exploiting the simplification deriving from assuming validity of:

Eq. (9). $$F_{clk} = 4 * F_{IF}$$

where F_{clk} is the internal frequency clock of the FPGA whereas F_{if} is the desired output frequency. With this condition, the key advantage is that sine and cosine function are sampled in correspondence of $\pi/2$, π, $3/2\,\pi$ and 2π values and multiple, that is equal to multiply for one of the three value (-1, 0, +1) with a remarkable computational advantage performing the Quadrature Phase Shift Keying (QPSK) modulation. At last, Digital to Analog Conversion (DAC) is performed in order to obtain an RF modulated signal at the inter-frequency of 10 MHz.

Channel coding, pulse shaping and modulation follow CCSDS and ECSS recommendations in order to be compatible with worldwide standard. As a consequence, commercial Ground Stations equipment can be used for receive and decoding the downlink signal.
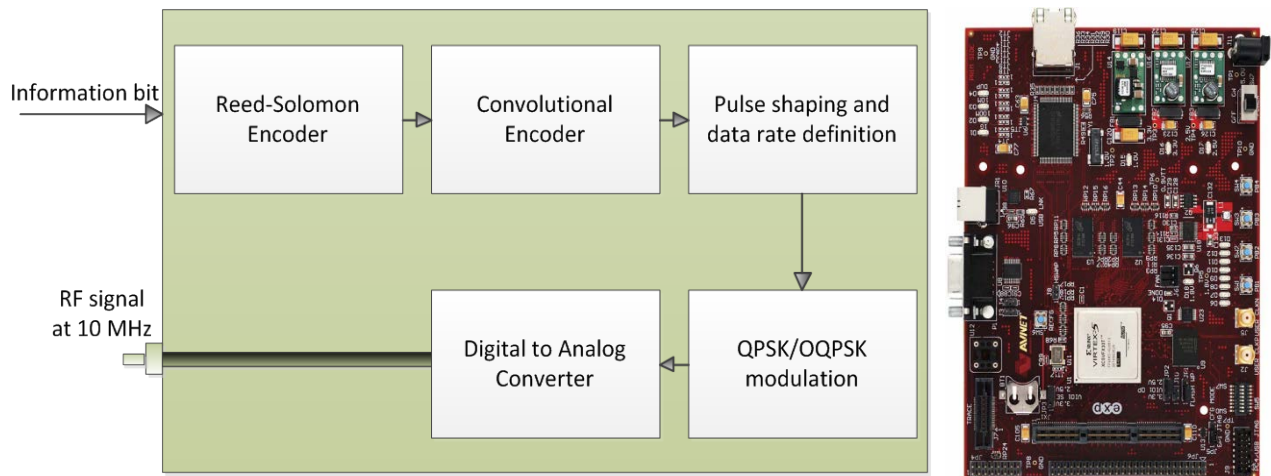
Figure 21: architectural block scheme and FPGA development board

3.3.1.1 FPGA device

The selected FPGA is a Xilinx fx30t Virtex 5 device [27]. It was chosen as an optimum trade-off between the power consumption, the device characteristic and the cost. Furthermore, despite the engineering model of the DPU has been realized using a terrestrial FPGA, a radiation hardened version is available, allowing the possibility to choose the device for space application without change the board layout.

Main characteristic of the Xilinx fx30t Virtex 5 are summarized in Table 5:

Characteristic	Value	Unit
Configurable logic blocks	89088	
Distributed SRAM	1392	Kbits
I/O blocks	960	
Maximum system frequency	400	MHz
Embedded power PC	1	

Table 5:FPGA device features

3.3.1.2 Interfaces

Figure 22 shows the interfaces of the DPU control board. Concerning the power supply, as for the TT&C board, stabilized signal at 5 V and 3.3 V are derived from ALMASat-EO power bus consisting of a 28 V signal connected to all the internal subsystem. The board can be managed by the OBDH board directly connected by mean of UART and CAN BUS. Moreover, SPI interface is present allowing the connection of external temperature sensors. The three communication protocols are managed by the FPGA device, through a dedicated I/O blocks. Acquired images are received by mean of a dedicated CCD digital interface implemented directly in the FPGA device. After the digital processing necessary for the downlink transmission, a DAC is introduced for the generation of the interfrequency signal directly connected to the TXBE board. Finally a JTAG connector is present on the board for the configuration of the FPGA device.
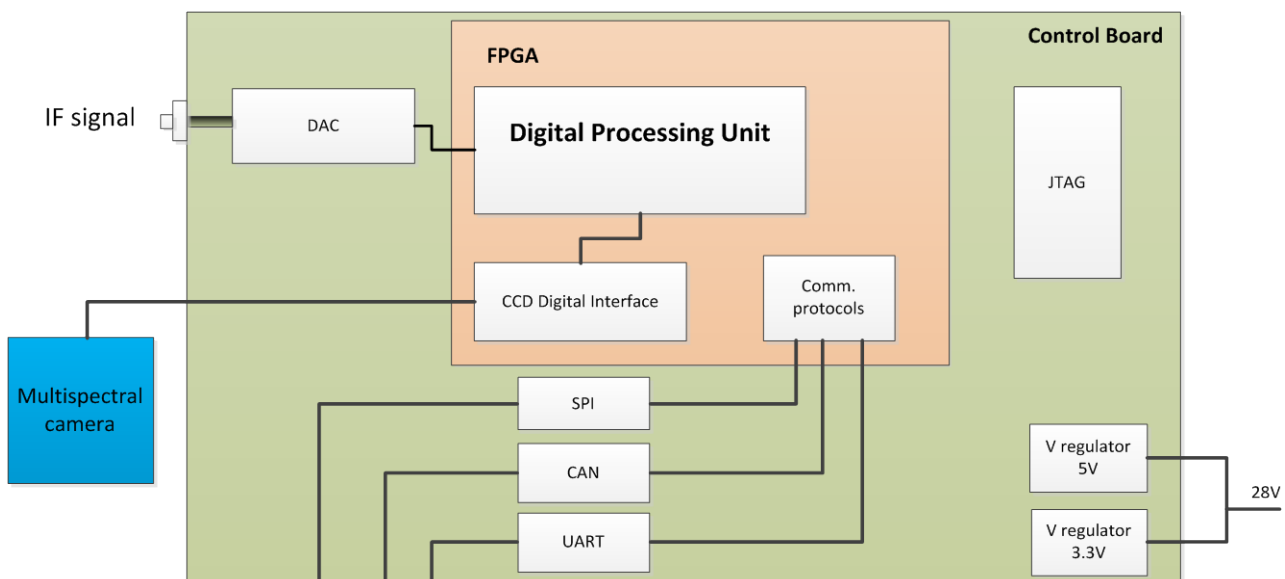
Figure 22: interfaces architectural block scheme

3.3.2 Analog back-end

As shown in Figure 23, main operations of the TXBE consist of frequency up-conversion, performed through two consecutive stages of programmable Voltage Controlled Oscillator (VCO), and filtering. The board is controlled by a microcontroller that switches on the two up-converters only when the RF incoming signal is received from the DPU in order to minimize the power consumption. Three different analog filters are inserted on the RF signal path to avoid spurious emission.
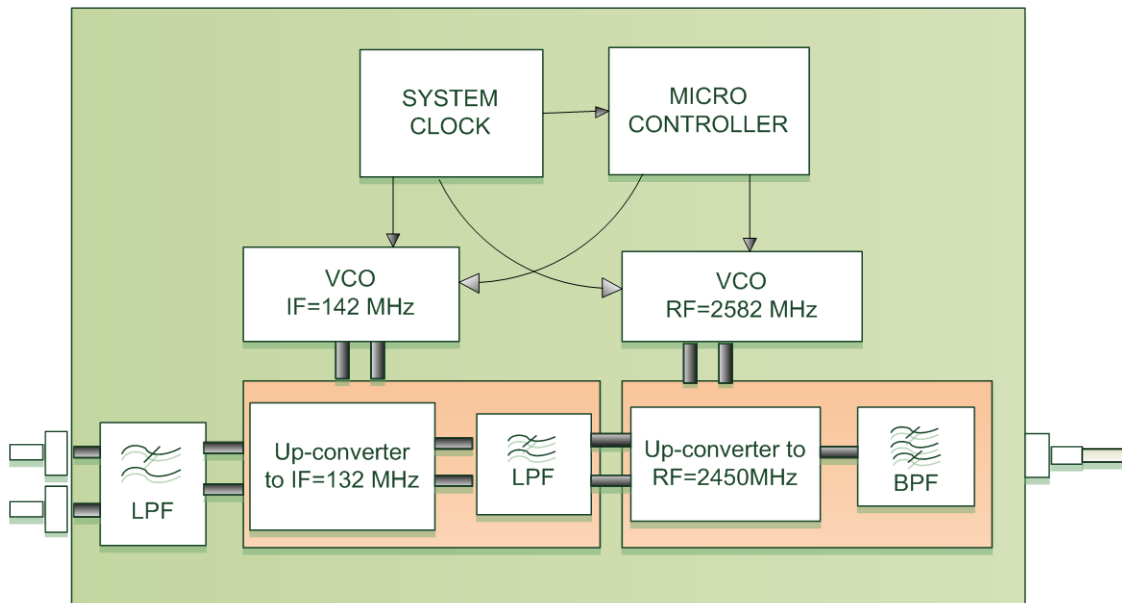
Figure 23: Transmitter Back-End block scheme

3.3.2.1 Microcontroller

The microcontroller of the TXBE board is in charge to manage the two VCOs and up-converters, setting the internal registers of the aforementioned devices. Due to the absence of communication interfaces as UART or CAN BUS, a simple and low-cost ATMEGA162 microcontroller was chosen, with advantages in terms of power consumption and with respect to the more complicated CORTEX microcontroller used in the TT&C board (see section 2.3.1). The integrated circuits register setting is performed through SPI interfaces. The system clock is 14.7456 MHz.

3.3.2.2 Up-conversion and filters section

The up-conversion section receives in input the differential 10 MHz signal generated by the DAC of the DPU. With reference to Figure 23, the IF signal is at first lowpass filtered through a simple RC

filter to suppress spurious emission of the DAC. Then it is subjected to a first up-conversion to an intermediate frequency of 132MHz. After that, a second lowpass filter is inserted after the first up-conversion to reject the image centered at 152 MHz. Due to the stringent requirements in terms of rejection of the signal image generated by the up-converter, a 3 stages LC filter has been designed, shown in Figure 24. The 132MHz signal is then up-converted to the final frequency 2.45 GHz. Figure 25 shows a detail of the RF and IF sections of the TXBE engineering model. Impedance matching networks, frequency up-conversion and filtering sections can be noted.
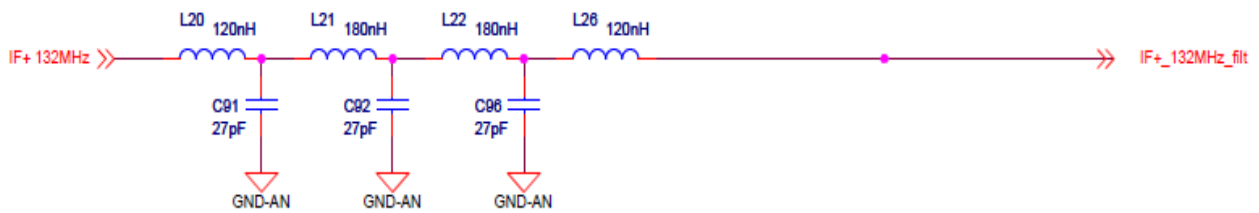
Figure 24: 132 MHz low pass filter schematic
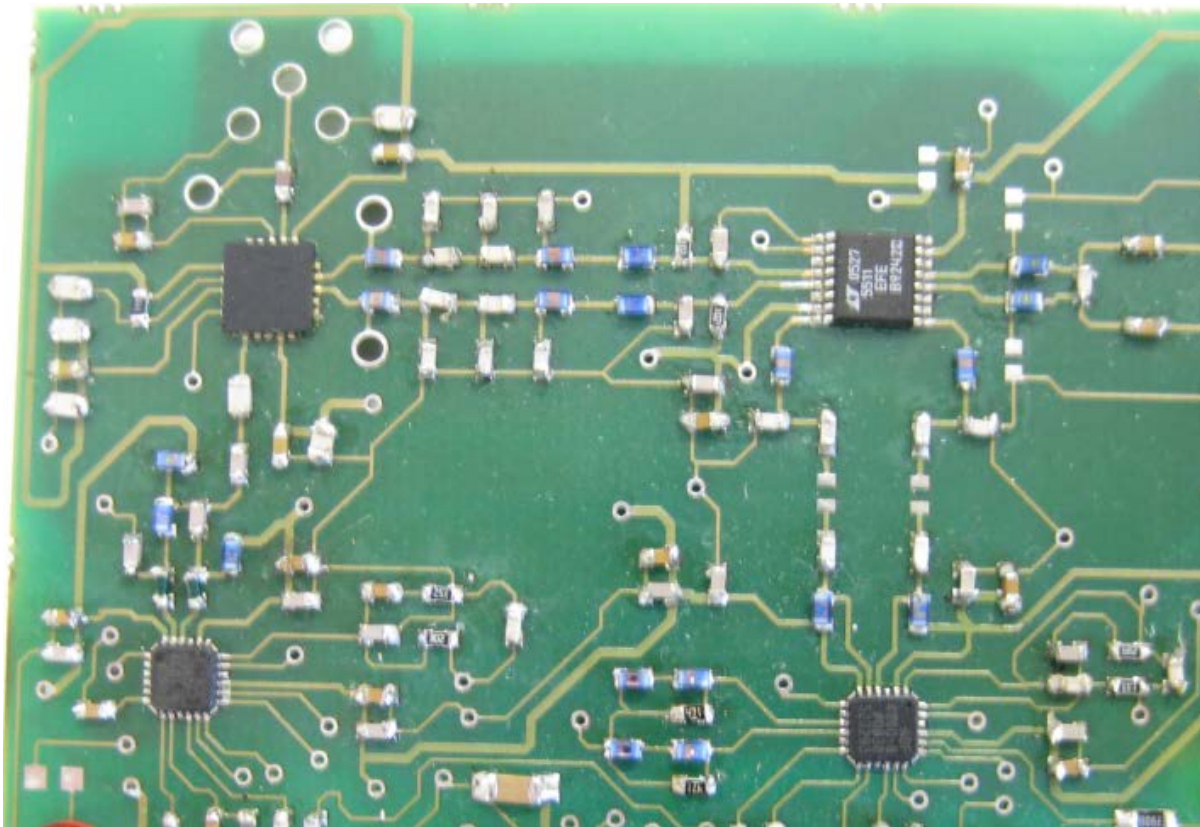
Figure 25: Up-conversion circuit on the engineering model

Finally, the 2.45 GHz signal is subjected to a bandpass filtering. The S-band Band Pass Filter (BPF) is the most critical analog circuit of the TXBE board, because of the higher frequency and the small bandwidth required. In order to meet the requirements of channel interference and spectral confinement a Hairpin microstrip filter has been chosen, offering a good trade-off between RF filter capability and total volume occupied.

Figure 26 shows the layout of the Hairpin microstrip filter and the prototype manufacture. Five hairpins were necessary to meet the requirement of attenuation for the image signal, at the expense of larger dimension and higher insertion loss with respect to three hairpins solution. The filter prototype has been designed using AWR Microwave Office, considering as main requirements the image signal attenuation and the insertion loss. Main characteristics of the microstrip filter are summarized hereafter:

Characteristic	Value	Unit
Carrier frequency	2.45	GHz
Pass band	50	MHz
Insertion loss	0.7	dB
Image rejection	20	dB
Signal attenuation (200 MHz from the carrier)	200	MHz

Table 6: Hairpin filter characteristics

Figure 27 shows the hairpin filter prototype spectrum characteristic, fed with a continuous wave spanning from 2 GHz to 3 GHz with an RF power of 10 dBm.
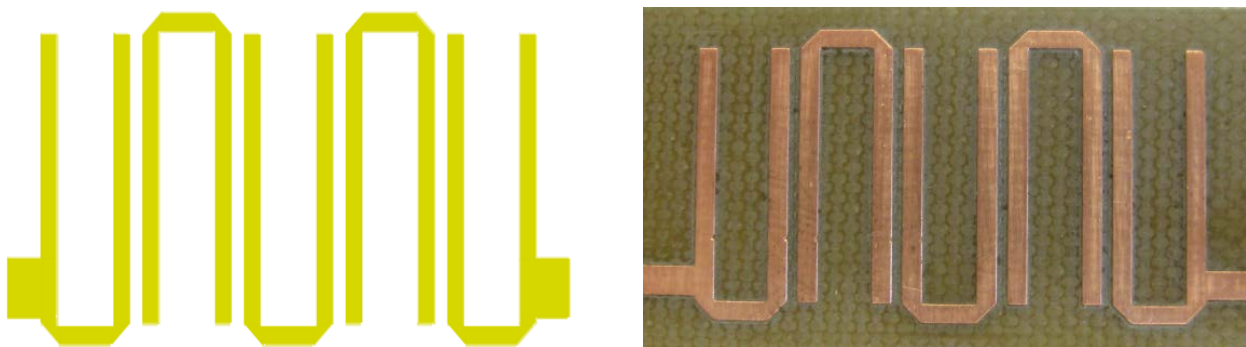
Figure 26: a)Microstrip hairpin filter layout; b) prototype manufacture
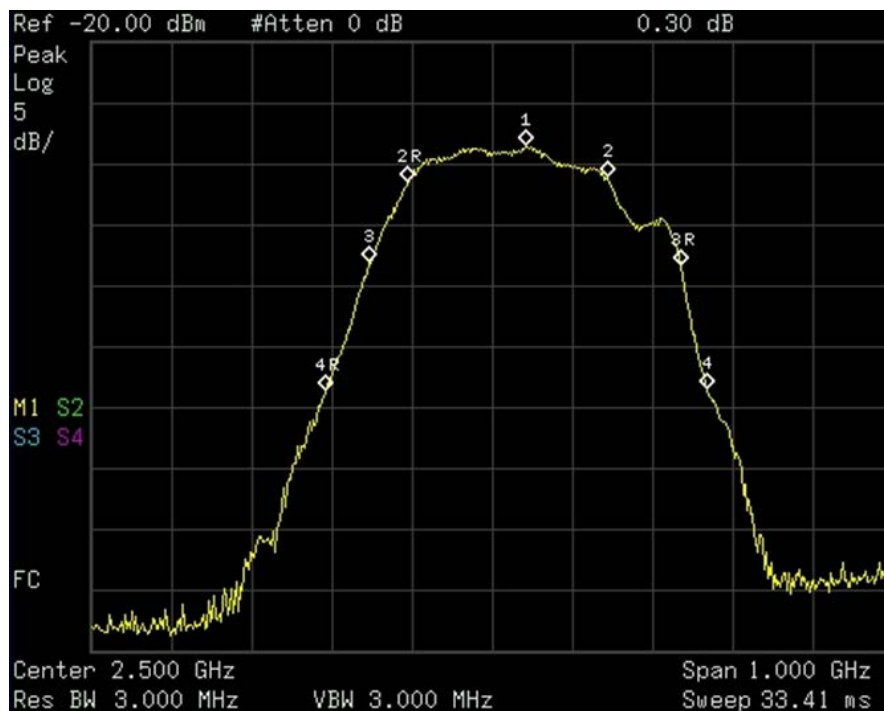
Figure 27: Hairpin filter characteristic

3.4   Development of the VHDL software

The whole code for digital signal processing by mean of the FPGA device was realized in VHDL language. Having selected the Xilinx Virtex 5 FPGA device, Xilinx Integrated Software Environment 11.3 was selected as platform for the development of the code, offering integrated tools and dedicated libraries for the Xilinx FPGA devices. Performance of the developed software as the pulse shaping or the digital modulation have been evaluated importing the VHDL code output in Matlab environment. An engineering model of the FPGA board is still under realization at the moment this thesis is written.

3.4.1 Channel coding

A concatenated configuration has been implemented for channel coding, in compliance with ECSS and CCSDS recommendation for easy interoperability with GS demodulators: outer Reed-Solomon (R-S) code, [28] [29] [30], with error correction capability of 8 or 16 R-S symbols for burst-noise channel; interleaver matrix with depth up to 5; inner convolutional code with variable coding rate from 1/2 to 7/8 for random channel errors, compatible with the Viterbi decoder [31] [32].

Any combination of Reed-Solomon correction capability, interleaver depth and convolutional code coding rate is selectable. In particular, the puncturation technique has been implemented for

convolutional coding in order to reach coding rate up to 7/8. Obviously, the two concatenated codes involve an increase of the total amount of data to be transmitted. Depending on channel condition and available bandwidth it is possible to vary the amount of overhead bits. The output of VHDL code has been used as input for a simulator implemented in Matlab environment: the channel effect was considered together with demodulation and channel decoding at the receiver side. A set of simulation was performed in order to evaluate the efficiency of the implemented channel coding techniques and the actual coding gain in different link condition and link parameters.

In order to investigate the actual coding gain, an analysis of the BER at different Signal to Noise Ratio (SNR) was carried out together with an analysis of final throughput at different data-rate and channel coding overhead. Figure 28 shows the theoretical advantage deriving from the use of different channel coding solutions, as reported in [33] for a BPSK signal, while the gain obtained through the channel coding implemented in the FPGA device is shown in Figure 29. The only R-S (255,223) offers about 3.5 dB of gain at BER 10^{-6}, with a degradation with respect to the theoretical gain of less than 0.3 dB. A concatenated solution is also shown, consisting in convolutional code at rate 1/2 and the aforementioned R-S code. Results are slightly worse than the theory, with a degradation of about 0.6 dB at BER 10^{-6} probably due to the not ideal interleaver. The last solution presents a total gain of more than 7 dB but the generated overhead is too high and incompatible with the high amount of data to be transmitted.
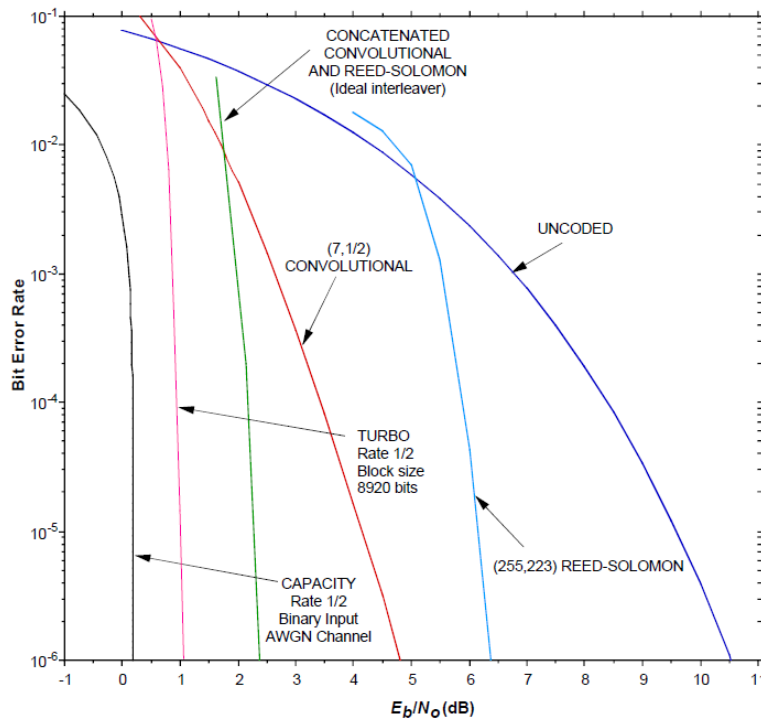
Figure 28:Theoretical advantage from channel coding
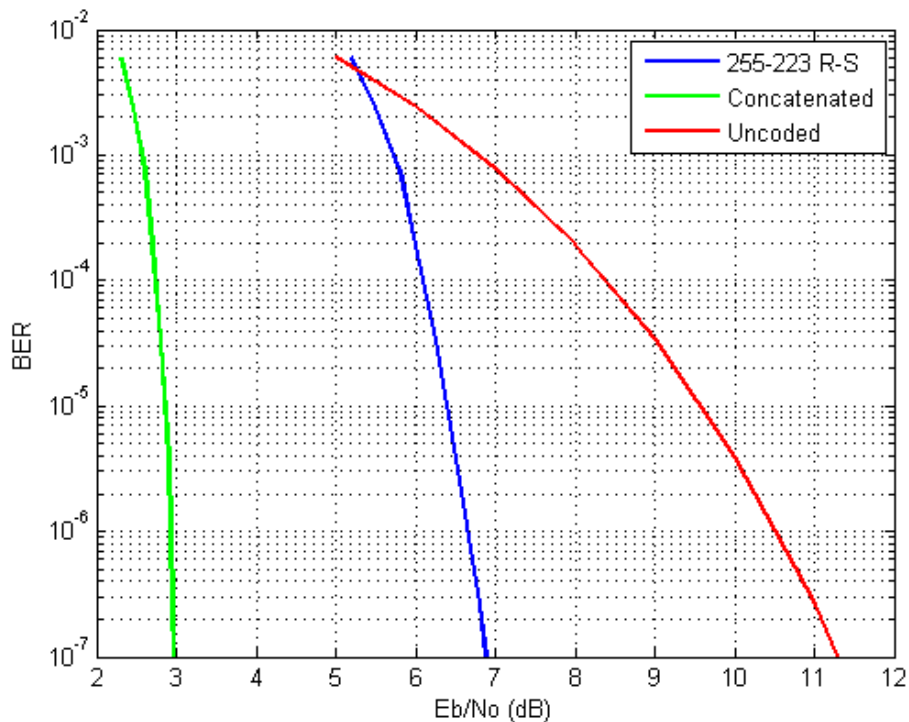
Figure 29: Channel coding obtained through VHDL code

3.4.2 Pulse shaping

Pulse shaping is performed exploiting the polyphase decomposition [34] [35] [36]. The filter design follows the frequency response sample method, considering (N-1)/2 samples and deriving the other half for symmetry and applying the Inverse Discrete Fourier Transform (IDFT), obtaining in this way the N samples of the Square Root Raise Cosine (SRRC) impulsive response. Furthermore, changing the interpolation factor introduced by the polyphase filter it is possible to change the final data rate from the minimum value of 1.25 Msps to the maximum value of 13.3 Msps. These values of data rate are the consequence of the selected frequency of 40 MHz of the master clock reference of the FPGA. In addition, also the roll-off factor (default value $\alpha=0.35$) is selectable and reconfigurable. Figure 30a shows the baseband spectrum of the SRRC transfer function for a data rate of 2.5 Msps. The figure is obtained in Matlab environment importing the samples of the SRRC function generated through the VHDL code implemented in the FPGA device. As can be noted, the main lobe has a bandwidth of about 1.7 MHz, conforming with a 0.35 roll-off factor. The secondary lobe is 40 dB suppressed with respect the main one. inter-channel interference is further improved using analog filters in the TXBE board. Furthermore, Figure 30b shows the impulse response in the time domain of the same SRRC pulse shaping function.
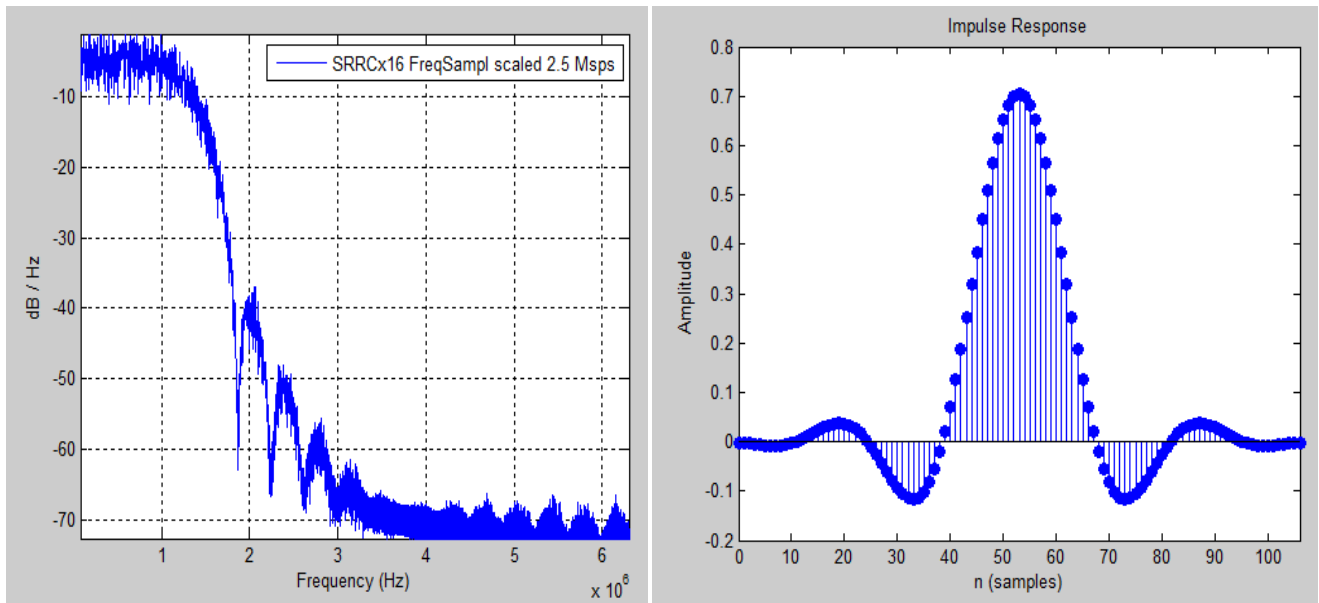
Figure 30: a)SRRC transfer function, SRRC impulse response

3.4.3 Modulation

QPSK modulation has been selected for the high data rate link as it allows a good trade-off in terms of occupied bandwidth and demodulator complexity, on equal final data rate. Moreover, it is largely used for space communications and compatible with a large variety of commercial GS equipment. Using Eq. (1), the QPSK modulation is obtained changing the sign of the polyphase filter samples, keeping the same value or simply setting a value of 0. In fact the key advantage is that sine and cosine function are sampled in correspondence of $\pi/2$, π, $3/2\ \pi$ and 2π values and multiple, that is equal to multiply for one of the three value (-1, 0, +1) with a remarkable computational advantage performing the Quadrature Phase Shift Keying (QPSK) modulation, [37] [38]. In addition, the OQPSK modulation, that is a QPSK modulation with the in-phase and quadrature components of the signal with a $\pi/4$ phase different, is implemented and can be selected for the downlink transmission.

Phase modulation has also been chosen thanks to the advantage due to constant amplitude envelope. As a matter of fact, the constant envelope allows the use of a great efficiency RF power amplifier (PA), working also in saturation region, without loss of information. In this way the total efficiency of the communication system is improved, meeting one of the main microsatellite requirements.

Figure 31 shows the output modulated signal of the DPU board imported in Matlab environment. The signal is centered at the frequency of 10 MHz. As can be noted, different bandwidth is due to

different final data rate. In particular, Figure 31a shows the spectrum for 2.5 Msps data rate 2.5 with a total occupied bandwidth of 3.4 MHz while Figure 31b shows the spectrum for 5 Msps data rate that occupies about 7 MHz of bandwidth.
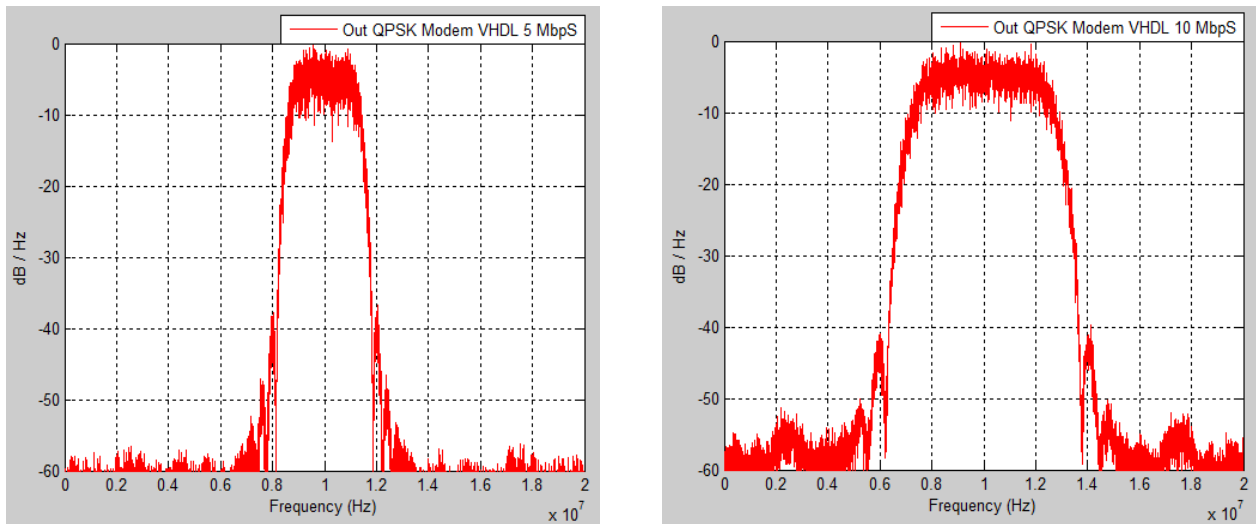
Figure 31: Spectrum of the modulated signal (QPSK) with a) 5Mbps and b) 10 Mbps

3.5   S-band antenna system

The S-band downlink communication system is characterized by the high data rate and the relative high value of power required for establishing a reliable link. Being the available power a strict limitation for a microsatellite platform, a medium-high gain antenna is required. Table 4 takes into account a gain of 9 dB for the onboard antenna: this value was adopted as a consequence of the following considerations. First of all, the S-band should be placed at the bottom face of the satellite, the one turn towards the Earth in order to avoid RF interferences with the TT&C antenna system placed of the ALMASat-EO top plate. In addition, during launch operation, the bottom of the S/C is anchored to the launcher through a separation system and the total available space is limited. Furthermore, wire antennas as quadrifilar helix antenna are very sensitive to mechanical vibrations the S/C is subject to. The best solution in terms of occupied volume and total weight is represented by a patch antenna, [39] [40] [41] [42]. Furthermore, requirements as the large beamwidth (at least 45 degrees) and the impedance matching are easily obtainable. At S-band the wavelength l of the signal in air is about 12 cm so the dimension of a single patch antenna should be approximately less than $l/2 = 6\ cm$, considering that the electrical wavelength on the substrate is shorter than the one in air. The available dimension on the bottom plate of the S/C is square of 15x15 cm, so an array of

four radiating elements has been chosen as optimum choice, easily offering a gain of about 9 dB required for the stability of the link.

Antenna requirements are sketched in Table 7:

Requirement	Value	Unit
Carrier frequency	2.45	GHz
Minimum frequency bandwidth	4	MHz
Polarization	Circular	
Maximum axial ratio	4	dB
Minimum beamwidth	30	Degrees
Minimum gain	9	dB
Maximum dimension	15x15	cm

Table 7:S-band antenna requirements

The material chosen for the antenna manufacture is the RO3730 of Rogers Corporation, which offers good performance in the temperature range the S/C is subjected to. RO7330 characteristics are summarized in Table 8.

Parameter	Value	Unit
Dielectric constant	3	
Dissipation factor	0.0013	
Substrate thickness	1.524	mm
Copper thickness	70	µm
Coefficient of thermal expansion	12	ppm/°C

Table 8: Substrate characteristics

Considering a dielectric constant of 3 the electrical half-wavelength is about 5 cm.

The design of the array patch antenna started with the definition of the single element and then building the final array structure. Different solutions have been investigated and are described in the next paragraph.

3.5.1 Single antenna

The first solution to be investigated is a circular patch, as the one shown on the left of Figure 32, while the right part of the same figure shows the 3D radiation pattern, with a maximum gain in the direction perpendicular to the antenna plane of 4.2 dB, a 1-dB beamwidth of 30 degrees and 3-dB beamwidth of 45 degrees. The particular shape, with three incision directly on the conductive surface, is a method for improve the circular polarization for the downlink signal. Circular polarization is a tough requirement for patch antenna but at the same time is largely used for satellite radio communication in order to minimize the polarization loss during such a distant link. Despite good results in terms of impedance matching and average gain in the required beamwidth, the final polarization is too elliptical, with an axial ratio of about 7 dB. As a consequence a different solution has been designed.
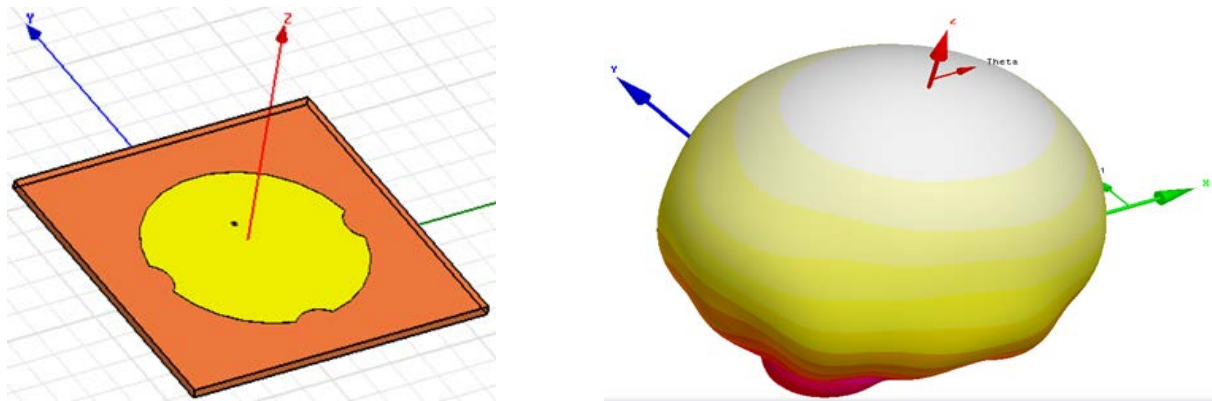
Figure 32: Circular single patch antenna and relative 3D radiation pattern

The second solution is represented by a simple square patch antenna, as shown in Figure 33. The blue triangles represent two incision to be applied directly on the conductive surface in order to improve the axial ratio. Though for a single patch the area of these two triangles is well defined to obtain the best performance in terms of polarization and gain, in an array structure the area can varies on each square element because of capacitance effect due to the proximity of array elements to each other and to the signal supply network. Figure 34 shows the maximum gain with respect to the input frequency. At the desired frequency of 2.45 GHz the maximum gain is about 4.3 dB, that is constant for a wide bandwidth of 200 MHz. As can be noted in Figure 35, the reflection coefficient is optimized for the 2.45 MHz, with a minimum value of -28 dB at the center of the bandwidth and with an average value of -15 dB for the whole channel. The axial ratio of the single square patch element is about 4 dB, with a good enhancement with respect to the circular patch, so the square solution has been adopted for the array structure.
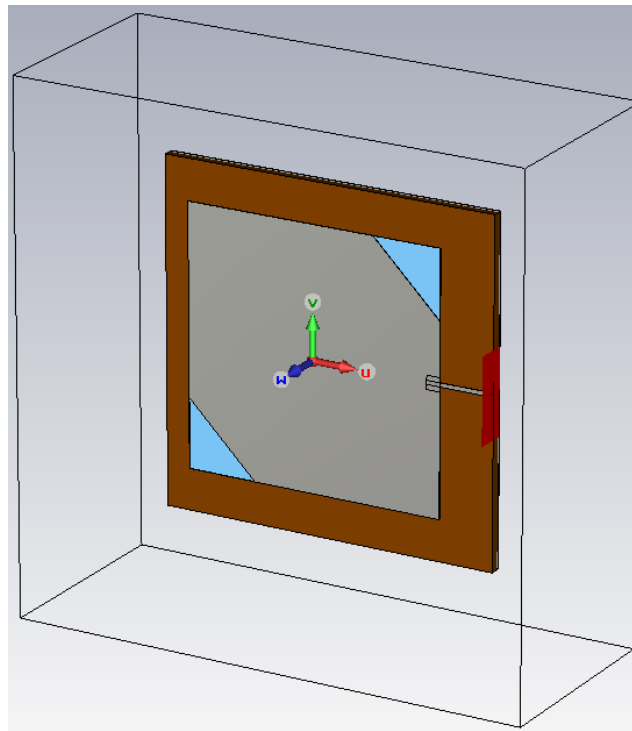
Figure 33: Layout of the square patch antenna
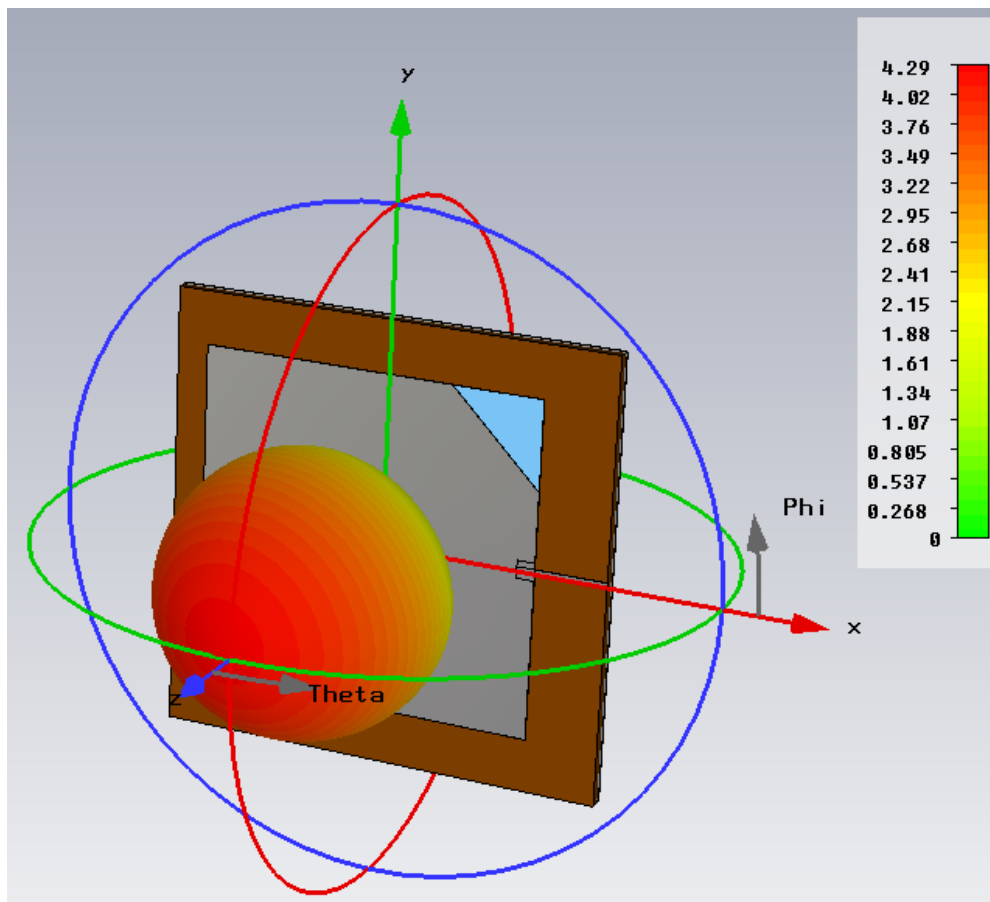
Figure 34: Gain of the square antenna
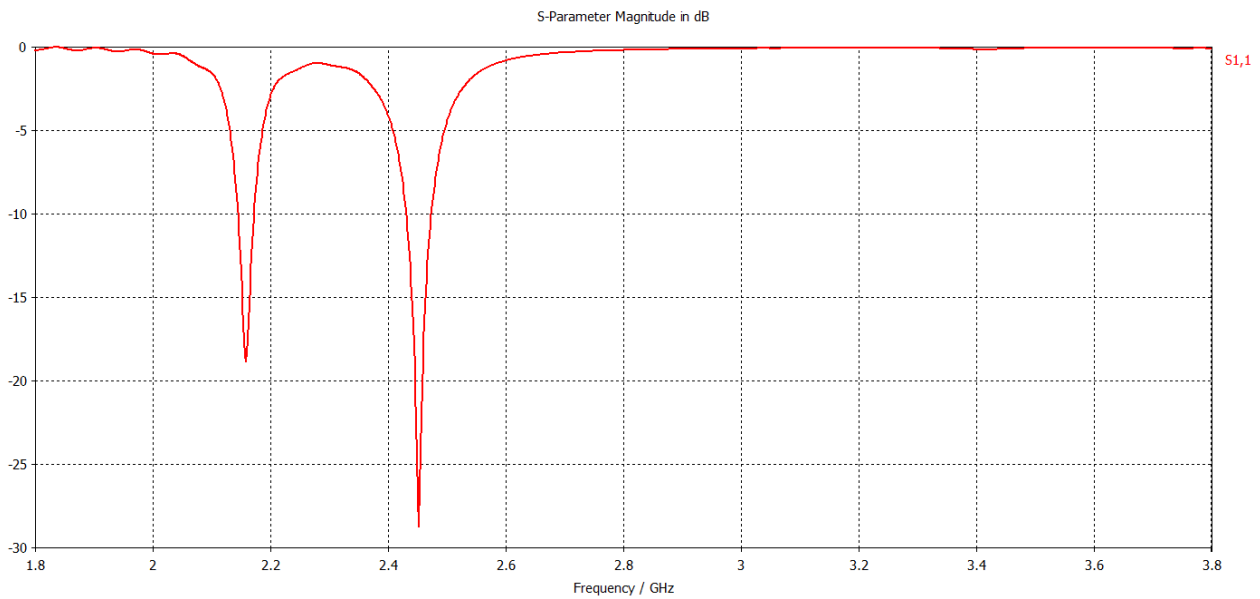
Figure 35: Reflection coefficient of the square antenna

3.5.2 Four elements array antenna

The array structure has been carried out putting four square elements at a distance of 2 cm each other. Figure 36 shows the layout of the array patch antenna. Theoretically, a 4 elements array antenna should offer an improvement of about 6 dB with respect to the gain offered by a single antenna with the same characteristic. The 3D pattern radiation of the array antenna is shown in Figure 37. A maximum gain of 9.65 dB is reached in the direction perpendicular to the antenna plane, with 5.5 dB more than the single gain. The 1-dB beamwidth is 31 degrees, so the initial requirement is satisfied. In addition, a very good impedance matching has been reached in the desired bandwidth at each of the four antenna ports. Figure 41 shows the reflection coefficient S11, that is less than -14 dB in a bandwidth of about 10 MHz centered at the carrier frequency of 2.45 GHz. Same results have been obtained for the other antenna elements, here omitted for simplicity. The most problematic requirement to be accomplished is the antenna polarization. From Figure 38 to Figure 40 the axial ratio of the antenna is shown for values of the φ angle equal to 0°, 30° and -30°. A value of 6.4 dB is constant for the whole beamwidth, exceeding the maximum allowed ellipticity of 2.4 dB. Circular polarization is hardly obtainable for patch antenna: each element should be fed with signal at different phase introducing λ/4 transformer but this solution hardly fit in the available dimension. Different solution consisting in a fed line on the bottom of the substrate is under investigation.
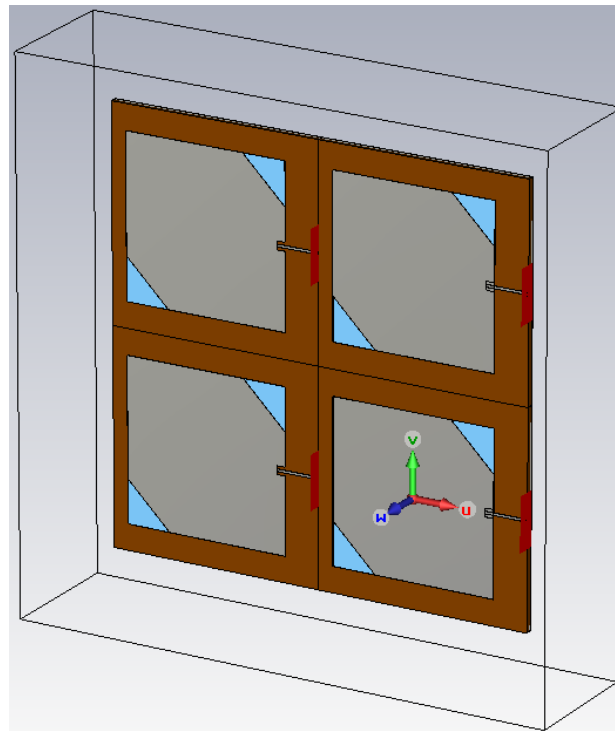
Figure 36: Layout of the array antenna
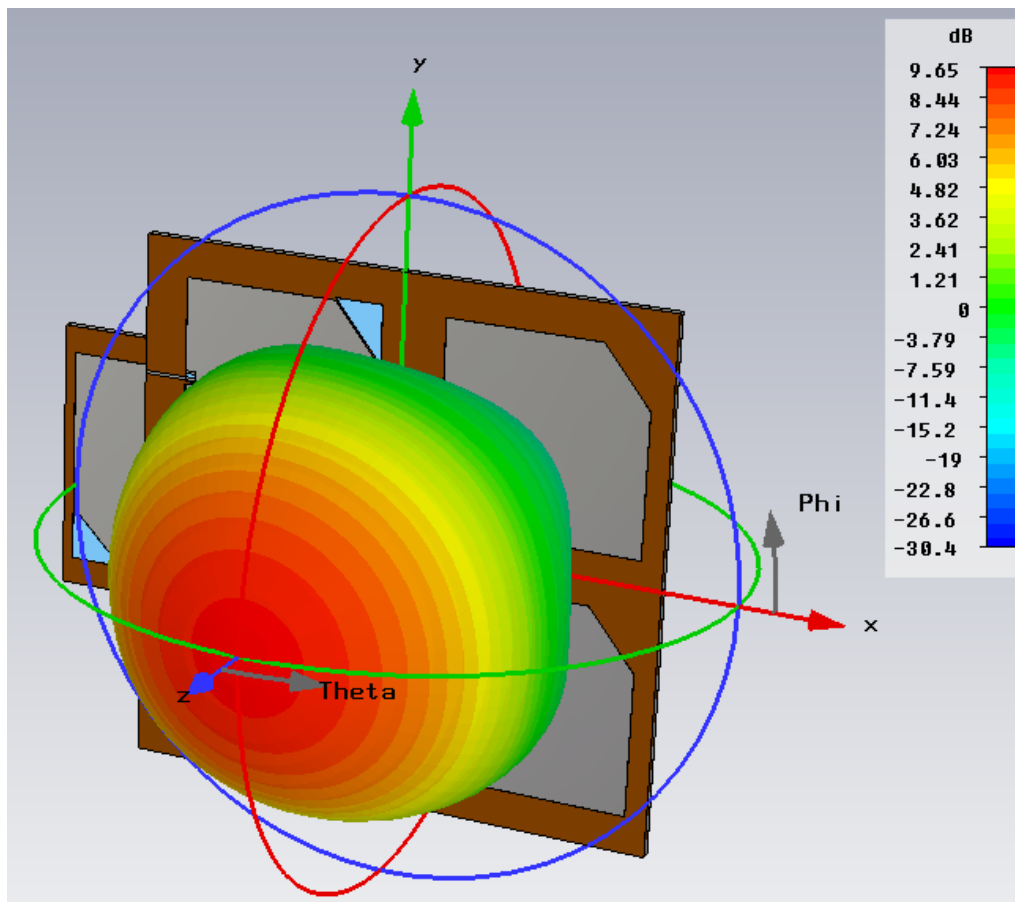
Figure 37: 3D radiation pattern of the array antenna
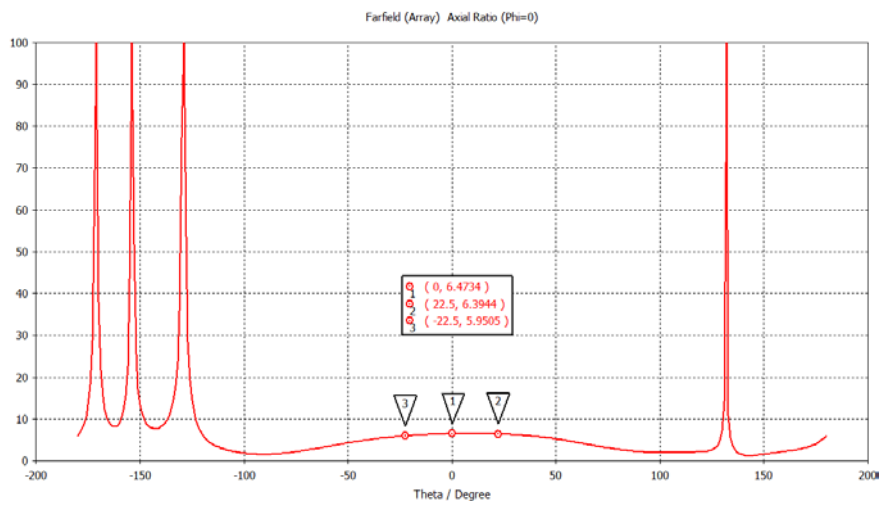
Figure 38: Antenna axial ratio for φ=0°
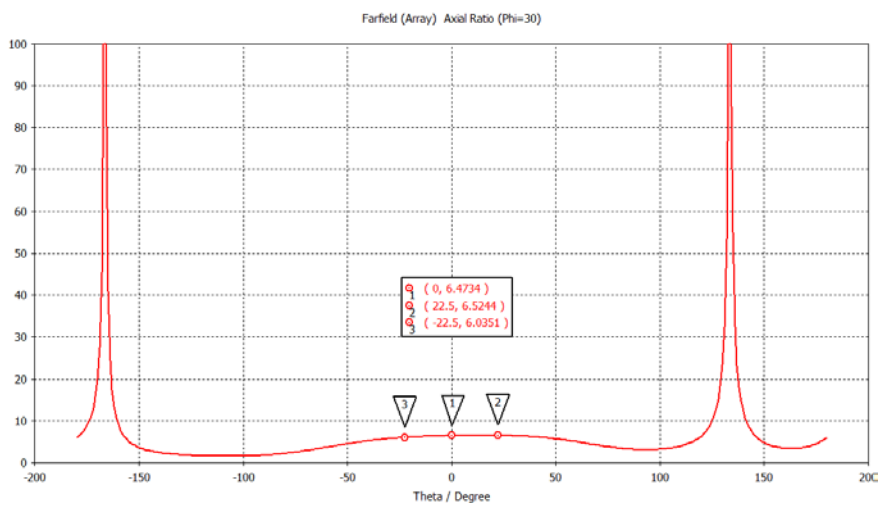
Figure 39: Antenna axial ratio for φ=30°
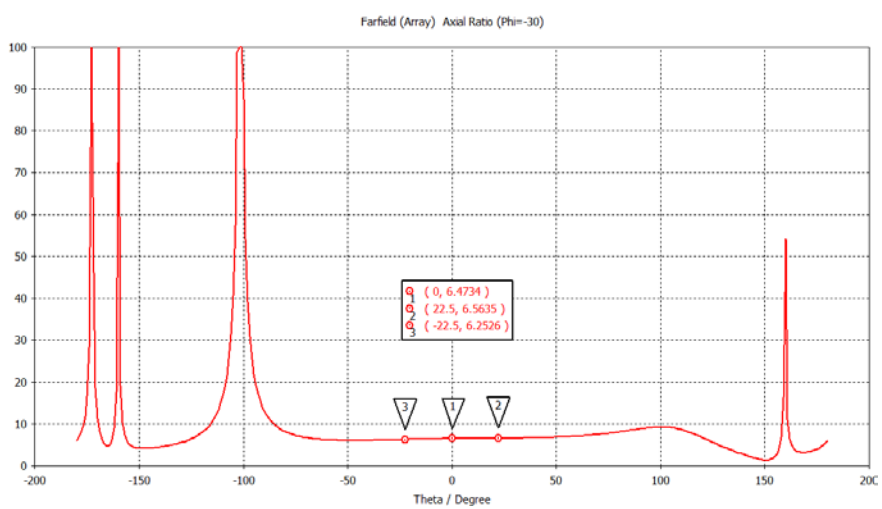
Figure 40: Antenna axial ratio for φ=-30°
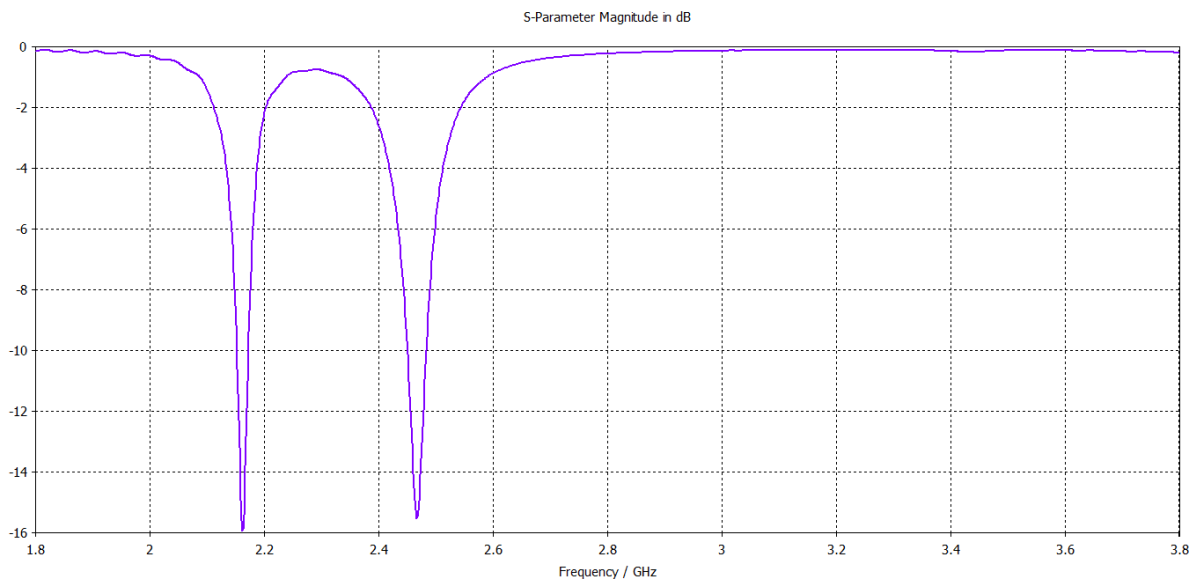
Figure 41: Reflection coefficient of the square antenna

4   Inter-satellite space communications

SFF enables the collective use of multiple spacecraft to perform the function of a single, large, virtual instrument. Formation Flying missions involve the tracking and maintenance of spacecraft in a desired geometric configuration, requiring to the distributed spacecraft to exert collaborative control of their mutual positions and orientations. The mutual nearness of spacecraft in controlled formation requires inter-satellite communication to exchange position and orientation information and to pass thruster actuation commands. In particular, attitude and orbital manoeuvre algorithms must ensure the minimum delay in performing the control of the formation geometry. As a consequence, one of the main challenge in such a mission is to design the appropriate communication protocol that accommodates a great communication reliability together with the minimum delay in a simplified hardware. A proposed solution based on adaptation of IEEE 802.11 terrestrial protocol is described in this section, together with a simulation of the resulting communication delay and the effect on SFF attitude and determination control.

Furthermore, advantages arising from SSL can also concern radio science missions. The satellite to satellite configuration is particularly interesting if we consider the possibility to receive radio signal on-board a S/C instead of at GS, as in the classical downlink configuration. Considerations on this aspect are described in section 6, as an application field of the proposed solution of GS enhancement.

4.1   Overview of satellite formation flying
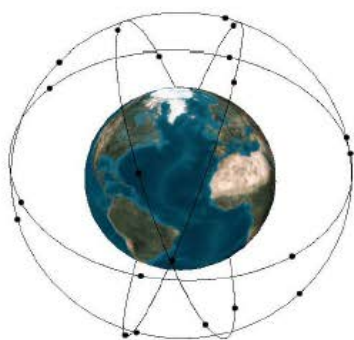
| Constellation with regularly spaced satellites with separation on a global scale | Satellites operating interdependently and cooperatively | Satellites with a hierarchy of authority |
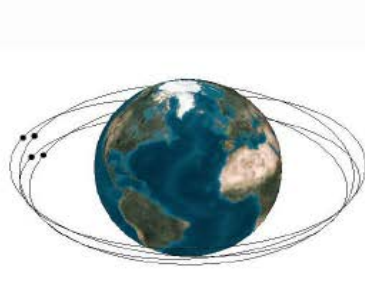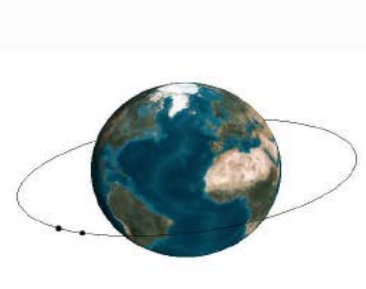
Table 9: Satellites formation types [44]

According to Shaw et al. a "distributed satellite system" refers to the coordinated operation of many satellites to perform a particular function. In general to be formation flying, several spacecraft must either maintain constant or time varying configurations, and formation flying in this context implies that there is at least a minimal level of collective autonomy [43]. Spacecraft formations are summarized in Table 9.

Constellation is, at present, one of the most used formation flying method for Earth observation purposes because of the resulting benefits in terms of coverage capabilities. TanDEM-X and TerraSar-X are an example of hierarchy of authority being TanDEM-X the "add-on" to the already in-orbit TerraSar-X; the two satellites are able to maintain a very short relative distance (250 to 500 m) enabling the first configurable SAR interferometer in space [45].

Although many of the main drivers for satellite formation flying arise from the numerous potential benefits of replacing future large satellites with a number of smaller, less massive satellites, clusters and constellations can actually refer to satellites of any size. By flying in a formation, and spreading functionality across a cooperating and communicating cluster, significantly improved functionality beyond that of a much larger single spacecraft can be achieved. The cluster may be reconfigured on-orbit to perform alternative tasks in a mission, or even redeployed onto different missions. The addition of one or two members to the cluster may quickly and simply enhance the collective performance and multi-mission capability of the formation While each satellite requires a complete set of fundamental subsystems, for example, power generation, structure, communication system and a control system, the payloads can be distributed, reducing the design and development work that would have been required to ensure that the individual payload requirements on a larger spacecraft were not conflicting. For science missions in particular, a constellation or cluster of spacecraft could be beneficial for improved sampling rates using more sensors. Production costs could be reduced through the development of multiple similar spacecraft on a production line, compared to the production of a single complex satellite. The associated costs of design and development of this process would be reduced further once the initial investment had been made. A major advantage of using multiple satellites is launch flexibility which can significantly benefit cost control measures, ultimately reducing overall mission cost as satellites can be launched when the market demands [44][46].

In the following table some of the main advantages/disadvantages proposed in [46] are reported.

Advantages	Disadvantages
• Multi-mission capability and design flexibility • Adaptability guaranteed by the potential increment or upgrade of the spacecraft number • Reduced design and development because of the use of standardized components (referred to the specific mission constellation) • Distributed redundancy • Subsystem distribution may allow a reduction in size (costs) • Capability of setup a large number of mission secondary objectives	• Each cluster requires its own core system (with respect of a single spacecraft this may increase complexity of formation members) • Initialization and maintenance of the formation • Sensors misalignments may introduce additional errors • Ground system complexity • Increased quantity of space debris (if not equipped with de-orbiting subsystem)

Table 10: Potential advantages and disadvantages of Formation Flying [46]

In Table 11 is presented a list of present and future formation flying missions.

	Constellation	Cluster	Leader/Follower
Science	POES(1988-2015), 2	Cluster (2000), 4	Earth Orbiter-1 (2000) / Landsat 7 (1999), 2
	GOES (1995-2014),2	Magnetospheric Multiscale Mission (2010), 4	GRACE (2002), 2
	The A-Train Constellation (2002-2005), 6	SMART-3 (2010), 3	Xeus (2014),2
	Space Technology-5 (ST-5) (2005), 3	Constellation-X (2011), 4	TerraSAR-X (2008)/TanDEM-X (2010)
	Twins (2005), 2-3	GEC (2011), 4	
	GPM and EGPM Constellation (2007-2012), 5	LISA (2012),3	
	COSMO Skymed (2007-2010), 4	Darwin (2015), 4	
	RapidEYE (2010), 5	Generation-X(2020+), 6	

		Life Finder (2020+)	
		Planet Imager (2020+)	
Military	GPS (1978-1994), 24	Techsat21 Flight Experiment (2003), 3	
	GLONASS (1982-1998), 24		
	Galielo (2008-2020), 30		
	NPOESS (2008), 5		
Communications	Iridium/Globalstar/Teledesic Skynet/Odyssey		

Table 11: Present and Future formation flying missions

4.2   Reuse of terrestrial technologies

Recently, low layer communication protocols for SFF were abundantly investigated [47], including consideration about X.25, ATM, IEEE 802.11, CCSDS Proximity-1 and CCSDS AOS. In particular, the use of protocols born for terrestrial application has been taken into account, considering the possibility to scale up the physical layer (power and range requirements above all). The most important benefit arising from the reuse of terrestrial COTS consists of a significant reduction of the overall cost of the communication subsystem. As a key point, the implementation of IEEE 802.11 protocol was acknowledged as a possibility for formation flying mission in [48], [49] and [50], providing a viable solution in spite of the large inter-node distance that will arise in space applications. Furthermore, an analysis of the adaptation needed of 802.11 protocol for inter-satellite links (ISL) was included in [51], taking into account inter-frame timing and dynamic contention window adaptation.

This section focuses at first on the development, analysis and simulation of a proposed low layer protocol, based on IEEE 802.11, adapted in order to guarantee the minimum delay for orbital manoeuvres. The Medium Access Control (MAC) layer, based on the Carrier Sensing Multiple Access Collision Avoidance (CSMA/CA) technique, has been considered for the medium sharing, minimizing retransmission and increase the final throughput. A simulation platform for the proposed solution has been developed and results compared with different protocol typologies used for SFF, such as the deterministic Token Ring Protocol (TRP). Moreover, constellation formed by 3 to 8 S/C have been considered.

A statistical analysis of the delay introduced by the low level protocol has been performed. Key parameters, such as the duration of the Backoff Time period (BOT), the length of the Contention

Window (CW) and the maximum allowed retransmissions have been optimized, with the purpose of minimize the total delay and the probability of manoeuvre unsuccessful. The second purpose of the work is the analysis of the degradation introduced by the communication protocol delay during orbital and attitude manoeuvres in SFF, including the proposed protocol simulation platform in a manoeuvre simulator. Being vital the satellite maintenance of a desired geometry configuration, orbital manoeuvres are a crucial operation for formation flying mission. Unfortunately, this operation is inevitably affected by the latency introduced by communication protocol. The proposed simulation platform allows for an evaluation of attitude and orbital determination algorithms performance degradation, taking into account all the consequences introduced by lower layer communication protocol.

4.3   Proposed communication protocol

The proposed protocol is based on the assumption of a star network topology and the presence of a network coordinator, acting as a Master, while all the other S/C are referred as Slaves. The overall algorithm is based on standard 802.11, with the same temporal slot time division, and Binary Exponential Back-Off (BEB) algorithm.

It must be noted that the information for maintaining the mutual positions and orientations are collected directly by the Master, independently with respect to the GS. Informations about the attitude and mutual position are sent by Slaves after an expiration time or in reply of a Master request. Also for this radio communication, the CSMA/CA protocol is applied in order to resolve medium access collision. Furthermore, in case of failure of the S/C initially designed as a Master, any Slave can replace this role: in fact a common communication subsystem can be used on-board all satellites belonging to a SFF, enabling the change of the S/C acting as a Master without an hardware increase in terms of mass, size and cost. The monitoring of the Master proper functioning can be monitored directly from the GS with a periodic communication; in case of failure the substitute can be selected automatically after an expiration time in a predefined sequence or from the GS with a dedicated message to the new Master. Omnidirectional antennas and common front-end equipment are assumed in this analysis.

4.3.1 IEEE 802.11 DCF based architecture

As abundantly investigated in [52], applicability of DCF protocol in terrestrial outdoor networks is clearly demonstrated. In order to adapt this protocol for SFF some considerations have to be introduced. Arrival delay for the ACK messages must be extended taking into account the maximum range of the constellation. Arrival delay consists of one way signal propagation and processing time. For 10 µs propagation delay the maximum range is about 3 Km. A delay of 20 µs allows for a 6 Km range and so on. Processing time can be evaluated in 10 µs. As a consequence, the ACK_timeout_period must be extended to a value much larger than the SIFS (10 µs) suggested by the protocol standard.

The proposed communication protocol concerns the following steps:

- The coordinator sends a broadcast manoeuvre command. Different addresses in the data message allow different Slaves to identify the proper command

- After receiving and decoding the message, each Slave S/C starts the CSMA/CA contention protocol for sending back an acknowledge message (ACK_1). As expected in a contention based protocol, during this phase some satellite cannot transmit back the ACK_1 because of medium contention or the impossibility to find a free time slot to transmit

- At the end of the first CW, after receiving the ACK_1 from Slaves, the three-way handshake protocol is performed by the Master, sending a second acknowledge message (ACK_2). Slaves who don't have sent back the ACK_1 for any reason are not in the addressee list of ACK_2. In this way each satellite can know if it have to repeat the CSMA/CA algorithm for sending the ACK_1 in the next CW

- Point *b* and *c* is repeated for each CW, which duration will be investigated in section 3

- When all the Slaves ended the protocol, the manoeuvre is performed. In case one or more Slaves does not accomplish the ACK sequence, an abort message is sent from the Master in order to stop the desired manoeuvre.

The CW length is not increasing, in order to minimize the total communication latency. This change is compatible with the proposed solution because, generally speaking, the number of Slaves trying to send back the ACK message to the Master is decreasing in greater in the first CW than in the other.

4.3.2 IEEE 802.11 PCF based architecture

With respect to the aforementioned protocol, a modified version is also proposed, involving a PCF procedure occurring when only two Slaves are remaining to send back the ACK_1. With reference to the protocol previously described, point *a, b* and *c* are not subject to change. In order to minimize the total delay the Master starts a PCF session for the last two Slaves.

4.3.3 Simulation

As a first step, a statistical analysis of the proposed low layer protocol has been performed. Three CW have been considered at maximum in order to reduce the total latency. The length of the three CW is directly affected the total latency. Using long CW allows for a very low percentage of transmission unsuccessful but, on the other hand, the total delay could become incompatible compared with manoeuvre precision and accuracy.

For comparing protocol performance with different CW length, two reference requirements have been considered: the transmission successful probability of the entire manoeuvre communication and the delay introduced at 99.5 % of successful probability. Moreover, the cumulative function distribution of the probability that an ACK message coming from whatever S/C is transmitted in the channel within a time slot is also investigated.

Figure 42, Figure 43 and Figure 44 show the aforementioned transmission successful probability and cumulative function distribution of the transmission of an ACK message within a slot time in the cases CW=16-16-16, CW=24-24-24 and CW=24-16-8 respectively. For each figure, the 6 lines are referred to case studies from 3 to 8 Slave satellite. Statistical results are based on 10000 simulation for each case studies.

In Table 12 the percentage of transmission unsuccessful are shown. It can be noted that, especially for a Slaves number greater than 5, only with CW equal to 24 we obtain an acceptable number of failure. Rows 1 and 3 of Table 12 show two case studies with an equal total amount of time slot, but with a different distribution. A lower unsuccessful probability is obtained considering a greater CW as first one, and decreasing the other.

Table 13 shows the average delay. It can be noted that a delay of 2 ms is derived because of the communication latency. Obviously, the larger delay is obtained with CW equal to 24 time slot, but this configuration allow for a lower failure percentage.
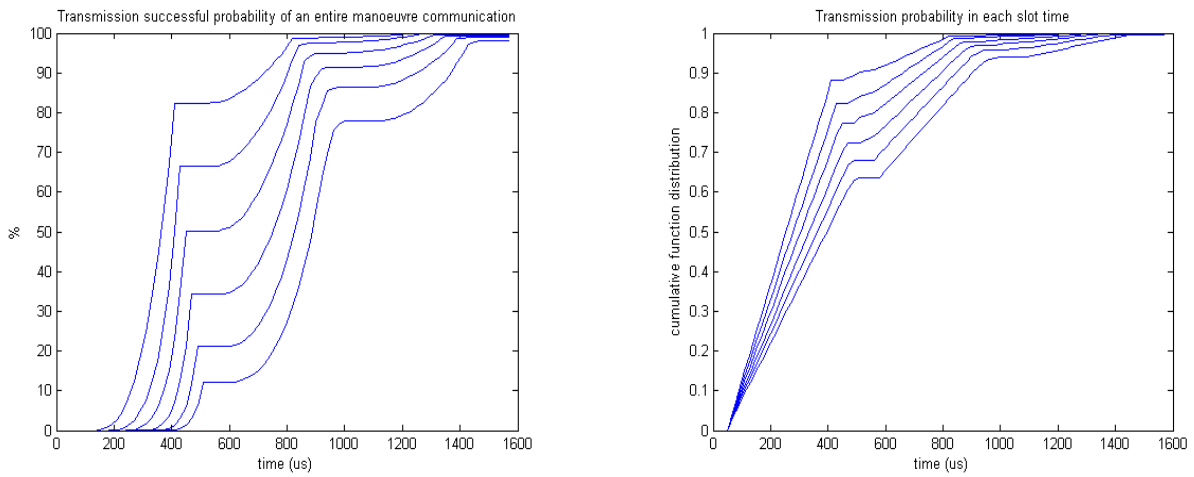
Figure 42: Transmission successful probability (left) and cumulative function distribution (right)
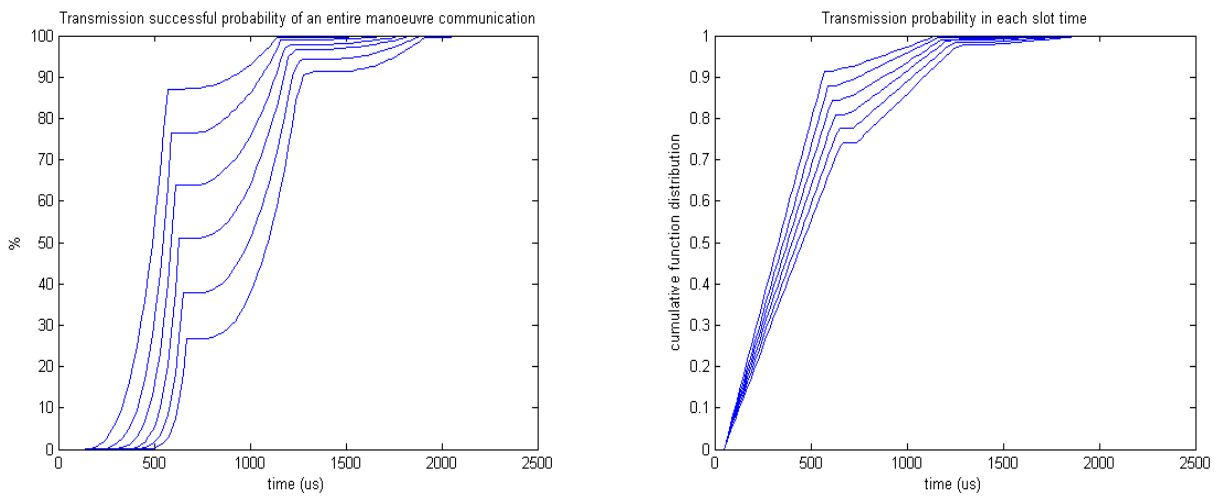
Figure 43: Transmission successful probability (left) and cumulative function distribution (right)
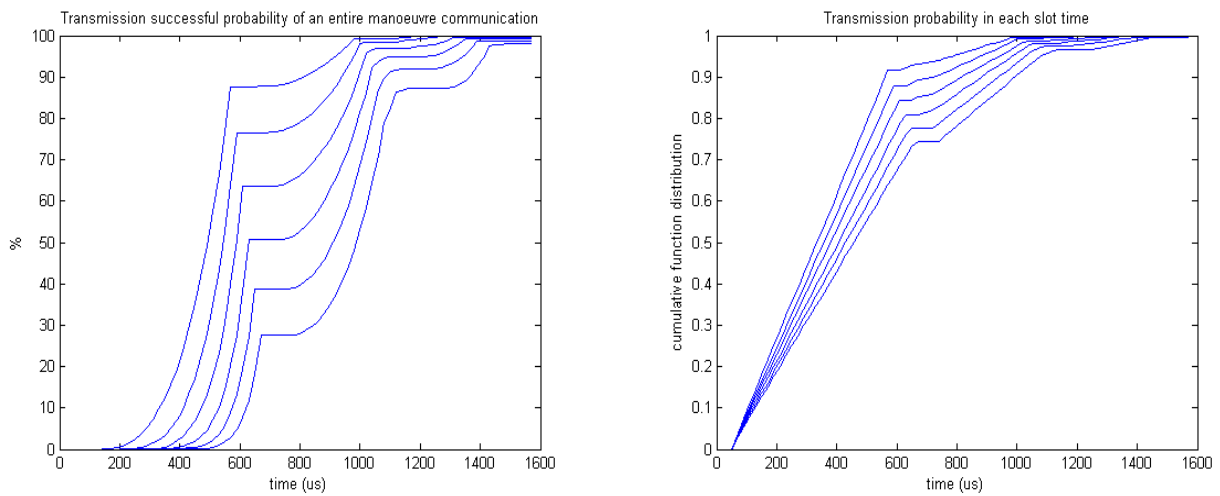
Figure 44: Transmission successful probability (left) and cumulative function distribution (right)

N° S/C Slave	3	4	5	6	7	8
CW length=16-16-16	0.08	0.13	0.47	0.57	1.31	2
CW length=24-24-24	0.03	0.05	0.08	0.17	0.29	0.41
CW length=24-16-8	0.1	0.18	0.48	0.69	1.36	2.04

Table 12: percentage of transmission unsuccessful

N° S/C Slave	3	4	5	6	7	8
CW length=16-16-16	1160	1230	1290	1550	1550	1550
CW length=24-24-24	1140	1610	1750	1810	1870	1930
CW length=24-16-8	1190	1250	1310	1570	1570	1570

Table 13: average delay at 99.5 % of successful probability (in μs)

Table 14 and Table 15 show the same data of Table 12 and Table 13 considering the PCF modified version. As investigated in [52], the standard PCF 802.11 protocol must be changed because the 10 μs SIFS does not allow for greater range in the SFF. Furthermore, the Master is involved in a more complex computational analysis of the SFF. Anyway, considering an increase up to 30 μs the PCF version begin feasible. As it can be noted comparing values of Table 12 and Table 14, the unsuccessful probability is drastically reduced, especially when using shorter CW. Despite the average delays shown in Table 15 are similar to those shown in Table 13, the important reduction of transmission failures points out the advantages in using this modified version.

N° Sat Slave	3	4	5	6	7	8
CW length=16-16-16	0	0	0.03	0.13	0.39	0.70
CW length=24-24-24	0	0	0.1	0.1	0.07	0.11
CW length=24-16-8	0	0	0.03	0.14	0.27	0.66

Table 14: percentage of transmission unsuccessful

N° Sat Slave	3	4	5	6	7	8
CW length=16-16-16	660	880	1170	1210	1410	1570
CW length=24-24-24	820	1160	1490	1530	1570	1610
CW length=24-16-8	820	1000	1330	1370	1410	1570

Table 15: average delay at 99.5 % of successful probability (in μs)

4.4 Effect of communication error/delay on SFF attitude determination and control

Attitude determination and control are major tasks in the spacecraft formation flight missions, necessary to keep the relative distances of satellites in accordance with the mission guidelines.

In order to describe mathematically the satellite formation orbital dynamics, many different representations have been used in literature [53]. The classical representation is provided by Euler-Hill equations also known as Clohessy-Wiltshire (HCW) used in early 1960s to analyze the spacecraft rendez-vous [54].

The importance of keeping the satellite formation at a fixed relative distance between each other, require the modeling and implementation of the orbital disturbances. Vaddi, Vadali, and Alfriend [55] used the HCW equation in order to include the J_2 perturbation while Sabatini and Palmerini [56] have included also the drag perturbation needful in low orbit formations.

A large number of controllers have been studied in the past as in [56], [57] and [58]. SSF dynamic representation in synergy with the orbital control laws allow the fulfillment of the mission purposes and can be implemented in a simulation environment, to study the evolution of the concerned system.

This paragraph is intended to describe the result of a software developed in Matlab environment for the simulation of the effect of communication delay on SFF attitude determination and control. The output of the previous simulator have been used as input value for the delay generated by the communication protocol.

4.4.1 Simulator layout

The reference frame considered for the chief-deputy relative motion is the classical Hill coordinate frame, where x is aligned whit the orbital radius, z is aligned to the orbital angular momentum and y completes the right handed coordinate system.

The unperturbed system for a chief-deputy formation, provided by HCW representation, is presented hereafter:

Eq. (10)
$$\begin{bmatrix} 0 & 0 & 0 & 1 & 0 & 0 \\ 0 & 0 & 0 & 0 & 1 & 0 \\ 0 & 0 & 0 & 0 & 0 & 1 \\ 3n^2 & 0 & 0 & 0 & 2n & 0 \\ 0 & 0 & 0 & -2n & 0 & 0 \\ 0 & 0 & -n^2 & 0 & 0 & 0 \end{bmatrix}$$

where the state vector is represented by $[x \quad y \quad z \quad \dot{x} \quad \dot{y} \quad \dot{z}]^T$ and n is the chief mean motion.

The J_2-only perturbed systems is:

Eq. (11)

$$\begin{bmatrix} 0 & 0 & 0 & 1 & 0 & 0 \\ 0 & 0 & 0 & 0 & 1 & 0 \\ 0 & 0 & 0 & 0 & 0 & 1 \\ a41 & a42 & a43 & 0 & 2\omega_z & 0 \\ a51 & a52 & a53 & -2\omega_z & 0 & 2\omega_z \\ a61 & a62 & a63 & 0 & 2\omega_z & 0 \end{bmatrix}$$

and the J_2+drag system is:

Eq. (12)

$$\begin{bmatrix} 0 & 0 & 0 & 1 & 0 & 0 & 0 \\ 0 & 0 & 0 & 0 & 1 & 0 & 0 \\ 0 & 0 & 0 & 0 & 0 & 1 & 0 \\ b41 & b42 & b43 & b44 & 0 & 0 & b47 \\ b51 & b52 & b53 & b54 & b55 & b56 & b57 \\ b61 & b62 & b63 & 0 & b65 & b66 & 0 \\ 0 & 0 & 0 & 0 & 0 & 0 & b77 \end{bmatrix}$$

All the components presented in the systems are fully described in [56]. In the last equation a seventh component has been introduced for the drag contribution.

By making use of Matlab/Simulink development environment, a dynamical simulator has been implemented. The unperturbed, J_2 and J_2+drag systems have been included in the simulator tool in order to evaluate the deputy position errors which represent the parameter to be controlled. A classical LQR controller has been included in the simulation tool.

The simulation scheme is presented in Figure 45. A control delay block has been included to take into account the communication latency provided by the protocol. The unperturbed orbit and the J_2-only perturbed orbit are presented in Figure 46.
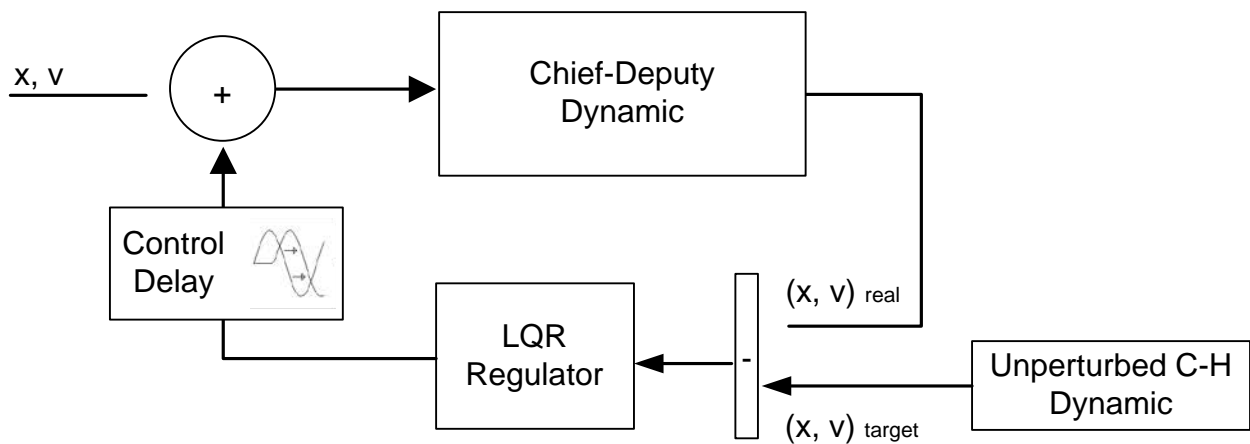
Figure 45: Matlab/Simulink simulation layout
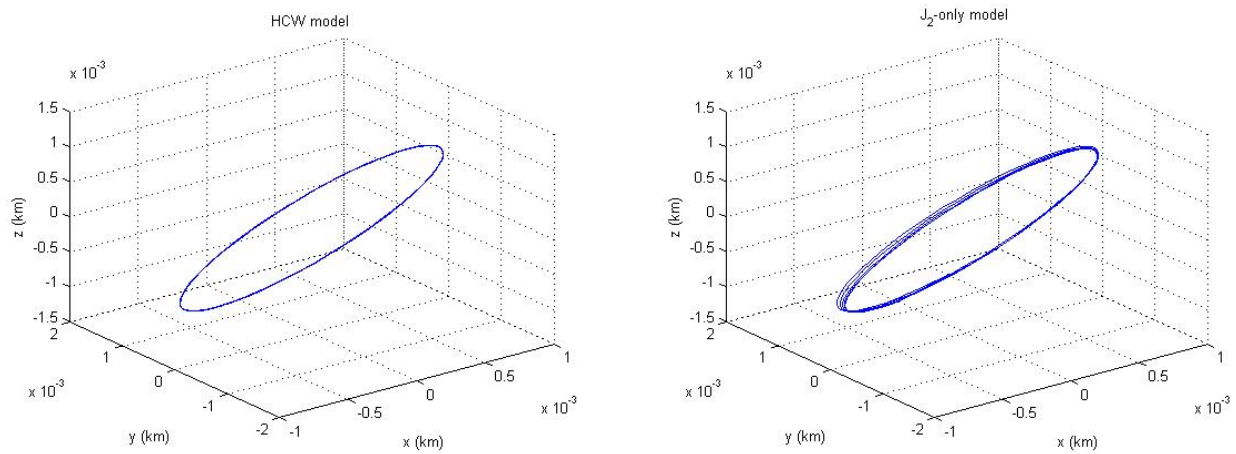
Figure 46: HCW model (right) and -only perturbed (left) deputy orbit

The target trajectory is a closed solution of the HCW equation where the initial state vector is computed as:

Eq. (13)
$$\begin{bmatrix} A_0 cos(n) \\ -2A_0 sin(nt) \\ 2A_0 cos(nt) \\ -A_0 n \, sin(nt) \\ -2A_0 n \, cos(nt) \\ -2A_0 n \, sin(nt) \end{bmatrix}$$

where orbital parameters are $[a \quad e \quad i \quad \omega \quad \Omega \quad \theta_0] = [7000km \quad 0 \quad 97.87° \quad 0 \quad 0 \quad 0]$ and with $A_0 = 0.5$. In order to lead to zero the position error, the controller output computes the required dv and applies it to the simulator. The thruster dynamic is not simulated.

4.4.2 Simulator results

Some different simulations have been performed to evaluate how the control signal delay affect the deputy position with respect the chief. Two main purposes have been achieved: a stability analysis point out the amount of delay could be critical in the control system, whilst a performance analysis consider the dV increment due to the delay.

The stability analysis output is the error between the controlled deputy trajectory and the target one.

Table 16 summarizes the error obtained with simulations. System instability has been found during the analysis at 1.5 seconds of delay, but the shorter maximum delay provided by the communication protocol does not destabilize the system. The maximum positioning error showed in

Table 16 must be taken into account if any further delays are encountered, in order to satisfy the positioning requirements.

The performance analysis returned a positive trend needed in the control dV. Accordingly with the maximum error given from the stability analysis, the dV trend increases accordingly to the delay increment. The not optimized control action and the consequent increment of the required dV due to the delay, render mandatory a carefully evaluation of the needed propellant in order to fully satisfy the mission purposes especially if a delay is present in the control signals.

Delay [sec]	0.1	0.5	1	1.5
Max Error [m]	4.2E-4	2.2E-3	0.3191	Inf.

Table 16: Stability analysis errors
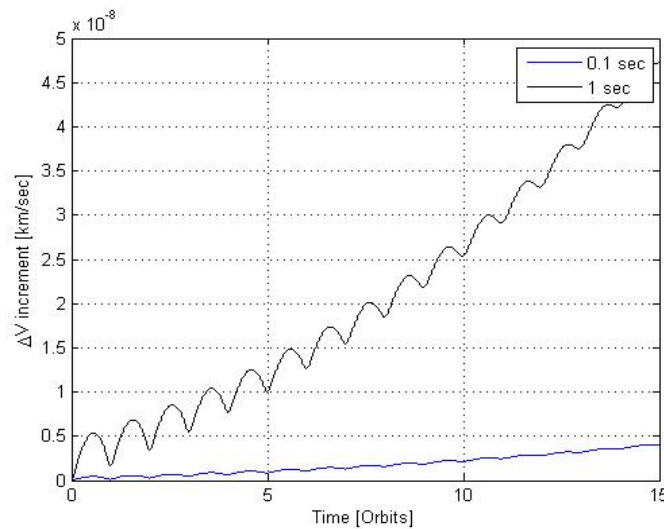
Figure 47: delayed control dV increment

5   ESA Ground Segment

As mentioned in the first section, a considerable part of the work presented in this thesis is related to the enhancement of Ground Segment capability, particularly related to radio science missions applications: enhancements of HPA phase stability and array tracking configurations have been implemented and tested. Since the research activities described in sections 6 and 7 have been carried out at ESOC facility working directly on equipments and structures actually used in ESA GS, the whole discussion is related to the ESTRACK facilities.

In order to exhaustively introduce the subject of the research activity, a brief description of ESA GS and their capability is reported in this section together with functional block schemes and future development trends [59] [60] [61].

5.1   ESTRACK facilities
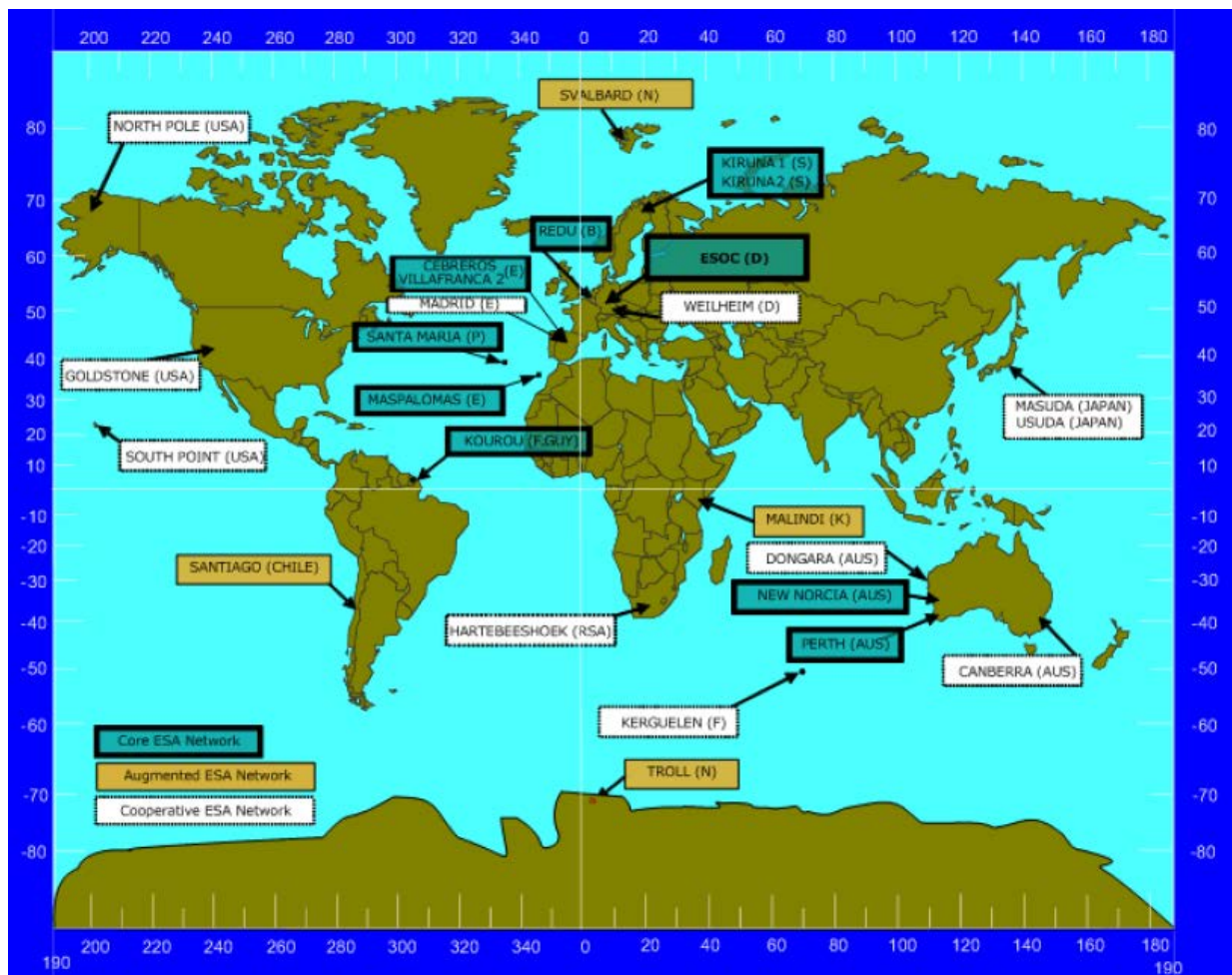
Figure 48: ESTRACK network

At the moment, ESTRACK represents ESA's capability to provide links between in orbit spacecrafts and the Operations Control Centre at ESOC. The core of ESTRACK network includes nine stations in six different countries:

- Kourou (French Guyana);

- Maspalomas, Villafranca and Cebreros (Spain);

- Redu (Belgium);

- Santa Maria (Portugal);

- Kiruna (Sweden);

- Perth and New Norcia (Australia).

Furthermore, two groups of GS's, named *Augmented ESA network* and *Cooperative ESA Network,* extend the ESTRACK coverage capability, as shown in Figure 48.

The ESTRACK stations are designed in accordance with the European Cooperation for Space Standardization (ECSS) standards and are compatible in the majority of cases with the international CCSDS recommendations in order to ensure

interoperability between space agencies. The complex is designed to provide global space link connectivity coverage for a wide range of space missions:

- Deep Space missions;

- Near-Earth missions, (e.g. Geostationary Transfer Orbits, Medium Earth Orbits, Geostationary Orbits, Highly Eccentric Orbits, Lunar Orbits, Lagrangian Orbits;

- LEO missions.

The technology development both in Space and Ground segments has recently resulted in the migration to higher frequency bands (from S- to X-, Ku- and Ka-bands), to more sophisticated modulation and coding schemes and to very high data transfer rates.

5.1.1 Deep Space Antenna stations

Being designed for Deep Space missions, Deep Space Antenna (DSA) stations host 35 metre parabolic antenna and state-of-the-art HPA, offering very high maximum EIRP at both S- and X-bands and high reception capability at S-, X- and Ka-bands.

Currently, DSA complex consists of:

- DSA-1, located at New Norcia and built in 2002;

- DSA-2, located at Cebreros and built in 2005;

- DSA-3, located at Malargue, Argentina, under construction,

As shown in Figure 49, Beam Wave Guide (BWG) feed system has been chosen, together with cryogenically cooled to 15 K degrees LNA, 20 KW HPA and auxiliary subsystems such as ranging calibration, frequency reference and power distribution.

DSA stations are also equipped with Delta Differential One-Way Ranging, a new technology enabling highly precise spacecraft location and tracking.

At the moment, DSA-1 is providing support to Mars Express, Rosetta and Venus Express missions, while DSA-2 supports Venus Express for routine operations and is available for back-up of Mars Express. Moreover, DSA GS will be employed for future ESA missions like BepiColombo.
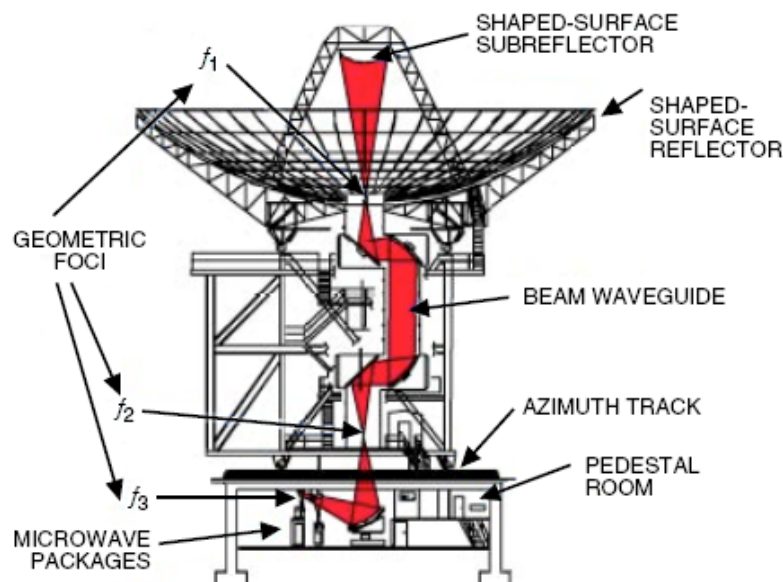
Figure 49: Schematic of a 35-m BWG antenna

On both stations, the frequency reference generation is based on a Hydrogen Maser with very high long term frequency stability. Moreover, the Telemetry and Telecommand System (TMTCS) receives SLE conformant Telecommand data via OPSNET from the Spacecraft Control Systems. It provides telecommand data and clock to the Intermediate Frequency Modem System (IFMS) Uplink Modulator (ULM), which provides the Phase Shift Key (PSK) modulation of the telecommand bit stream onto a sub-carrier, successively used to phase modulate the uplink carrier at 230 MHz. The telecommand chains are redundant and the various switches allow flexible signal routing.

5.1.1.1 New Norcia (DSA-1)

Specifically, S- and X-bands were selected for both uplink and downlink on DSA-1. Both the S- and X-band uplink paths consist of a primary chain and a backup one, the former including a 20 KW HPA while the latter a 2 KW HPA. For each frequency band, two up-converters are used and further equipment provides for redundancy switching, thus allowing either Left Hand Circular Polarization (LHCP) or Right Hand Circular Polarization (RHCP) transmission in a given band. Moreover, a dichroic mirror included in the BWG structure enables the transmission of a 20 KW signal in S- and X-band simultaneously.

- TX maximum EIRP: S-band 127 dBm (SHPA) or 117 dBm (SLPA);
    X-band 137 dBm (XHPA or 127 dBm (XLPA);
- RX G/T: S-band: 37.5 dB/K
    X-band: 50.1 dB/K

5.1.1.2 Cebreros (DSA-2)

DSA-2 does not include S-band. The antenna provides X-band transmission, as well as X- and Ka-band receive capability (X/XKa). The uplink path consist of a primary chain and a backup one, the former including a 20 KW HPA while the latter a 2 KW LPA. The possibility of adding a Ka-band transmitter is contemplated but not easy to be realized. Two up-converters are used and further equipment provides for redundancy switching, thus allowing either LHCP or RHCP.

- TX maximum EIRP: 138 dBm (XHPA), 128 dBm (XLPA), 118 dBm (XSSPA),
- RX G/T: X-band: 50.8 dB/K (at 10 deg of elevation)
    Ka-band: 55.8 dB/K (at 10 deg of el.)

5.1.1.3 Malargue (DSA-3)

A third deep-space antenna (DSA-3) is under construction at Malargue, desert of Mendoza, Argentina. The ESA project guidelines for DSA-3 focus on the already existing antenna structure DSA-2, in order to minimize the changes, downtime and cost. Hence, DSA-3 station will be able to operate at X- and Ka-band. While Ka-band is, at present, an option like in Cebreros, Ka-band downlink capabilities are likely to be implemented soon, contrarily to Ka-band uplink. The DSA-3 project also gives the opportunity to exploit the use of a new receiving band, namely the K-band, ranging from 25.5 to 27 GHz. The K-band will strongly enhance the communication bit rate, thanks

to the huge available bandwidth, which is three times larger than that used at Ka-band. This upgrade is driving the study and development of K-band dichroic mirror and antenna feed that could be reused also for transmitting chain.

5.1.2 Kiruna (KIR) station

KIR consists of two terminals, KIR-1 and KIR-2, both providing S-band transmit and S- and X-band receive capability (S/SX). These terminals provide tracking, telemetry, telecommand and radiometric (such as ranging, Doppler and meteo) measurements services.

KIR-1 station characteristics are as follows:

- Antenna diameter: 15 metre;
- TX maximum EIRP: 101 dBm;
- RX G/T: S-band: 27.7 dB/K (at 5 deg of el.)

        X-band: 36.9 dB/K (at 5 deg of el.)
- Polarization: LHCP or RHCP;

5.1.3 Kourou (KRU) station

KRU-1 terminal provides S- and X-band transmit, as well as S- and X-band receive capability (SX/SX). This station provides tracking, telemetry, telecommand and radiometric measurements, System Validation Test and Listen-In-Test services.

Station characteristics are as follows:

- Antenna diameter: 15 metre;
- TX maximum EIRP: S-band 111.2 dBm (S-band HPA) or 104.7 (using S-band LPA)

          X-band 112.8 dBm;
- RX G/T: S-band: 29.1 dB/K

        X-band: 41 dB/K
- TX polarization: LHCP or RHCP at both frequency bands;

5.1.4 Maspalomas (MSP) station

MSP station consists of MSP-1 antenna which provides S- and X-band transmit, as well as S- and X-band receive capability (SX/SX) and tracking, telemetry, telecommand and radiometric measurements services.

Station characteristics are as follows:

- Antenna diameter: 15 metre;
- TX maximum EIRP: S-band 102.1 dBm (using S-band LPA)

    X-band 112.8 dBm;

- RX G/T: S-band: 29.2 dB/K

    X-band: 37.5 dB/K

- TX polarization: LHCP or RHCP at both frequency bands;

5.1.5 Perth (PER) station

PER-1 terminal provides S- and X-band transmit, as well as S- and X-band receive capability (SX/SX). This station provides tracking, telemetry, telecommand and radiometric measurements services.

Station characteristics are as follows:

- Antenna diameter: 15 metre;
- TX maximum EIRP: S-band 108 dBm (S-band HPA) or 102 (using S-band SSA)

    X-band 112.8 dBm;

- RX G/T: S-band: 27.5 dB/K

    X-band: 37.5 dB/K

- TX polarization: LHCP or RHCP at both frequency bands;

5.1.6 Redu (RED) station

RED station consists of two deep space terminals, RED-1, RED-2 plus a smaller antenna named RED-3. RED-1 antenna provides S-band transmit and S-band receive capability (S/S) and tracking, telemetry, telecommand and radiometric measurements services.

RED-1 station characteristics are as follows:

- Antenna diameter: 15 metre;
- TX maximum EIRP: 102.5 dBm;
- RX G/T: S-band: 29.6 dB/K
- TX polarization: LHCP or RHCP;

RED-2 terminal provides Ka-band transmit and Ka-band receive capability (Ka/Ka), allowing four simultaneous data relay return feeder link channels at 20 GHz, data relay test loop and reception of the satellite pilot and connection to the ESA Earth Terminal (EET).

RED-2 station characteristics are as follows:

- Antenna diameter: 13.5 metre;

- TX maximum EIRP: 114.5 dBm;

- RX G/T: S-band: 42.5 dB/K

- TX polarization: linear;

5.1.7 Villafranca (VIL) station

VIL consists of two terminals, VIL-1 and VIL-2, both providing S-band transmit and S-band receive capability (S/S). These terminals provide tracking, telemetry, telecommand and radiometric measurements services.

Station characteristics are as follows:

- Antenna diameter: 15 metre both antennas;

- TX maximum EIRP: 102.9 dBm VIL-1 (S-SSA);

  101 dBm VIL-2 (S-SSA), 109 dBm (SHPA) ;

- RX G/T: S-band: 28.9 dB/K VIL-1;

  28.23 dB/K VIL-2;

- TX polarization: LHCP or RHCP both antennas.

5.2 Downlink telemetry chain

Figure 50 shows the typical downlink chain of ESTRACK stations. Apart from the aperture of the parabolic dish antenna and the frequency bands that each stations is able to receive, the reported architecture is common to each ESTRACK facility. With reference to Figure 50, from left to right the received signal is processed as follows:

- The signals is received by the antenna;

- The mode coupler polarizer separates the components for the received right and left hand circular polarisation signals;

- The two polarizations are routed via waveguide to the diplexers, which separate the uplink and downlink signals (waveguide switches allow the selection of the signal chains);

- The signal is amplified by solid state low noise amplifiers;

- Down-converters convert the received signals to the first intermediate frequency of 420MHz to 520MHz in the L-Band. The output of the down-converters is defined by the programmed frequency of the local oscillator synthesizers

- A switching unit, incorporating hybrid couplers, splits the IF signal into two equal parts for telemetry reception and tracking purposes

- The signals are now routed via cross site cables (optical or coax) from the antenna equipment room (Figure 50) to the antenna downlink switch in the MER (Figure 51);

- From the antenna downlink switch, the L-Band left hand circular and right hand circular polarization signals are routed to the second down-converter

- The Output of the down-converter is always a 70MHz phase modulated signal and therefore the local oscillator synthesizers are programmed to provide the correct mixing frequency
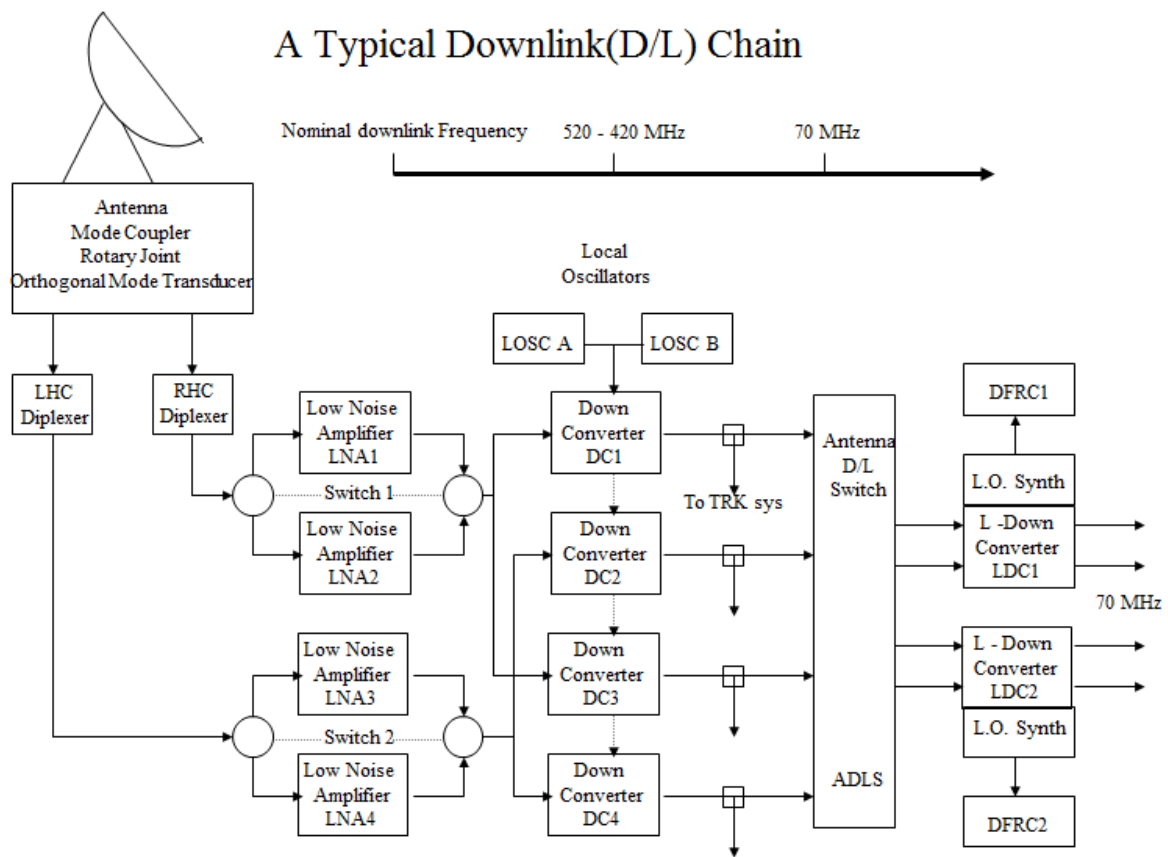
Figure 50: GS downlink chain

The MER includes all devices for intermediate frequency and baseband signal processing. With reference to Figure 51, that shows the ESTRACK station telemetry chain, the 70 MHz signal from the L-Band down converters is routed to the IFMS inputs via the 70 MHz switch (SMSW) (the switch could also provide a test signal to lock the base-band in a 70MHz test loop). The MER can contains more than one IFMS. The IFMS common front end (CFE) converts the analogue signal to a digital representation. Then, the DCE estimates the phase and gain differences between the two channels and provides these estimates to the other modules. Finally, the remnant carrier demodulator demodulates the downlink signal after locking onto the sub-carrier and the ranging demodulator demodulates the ranging tones.
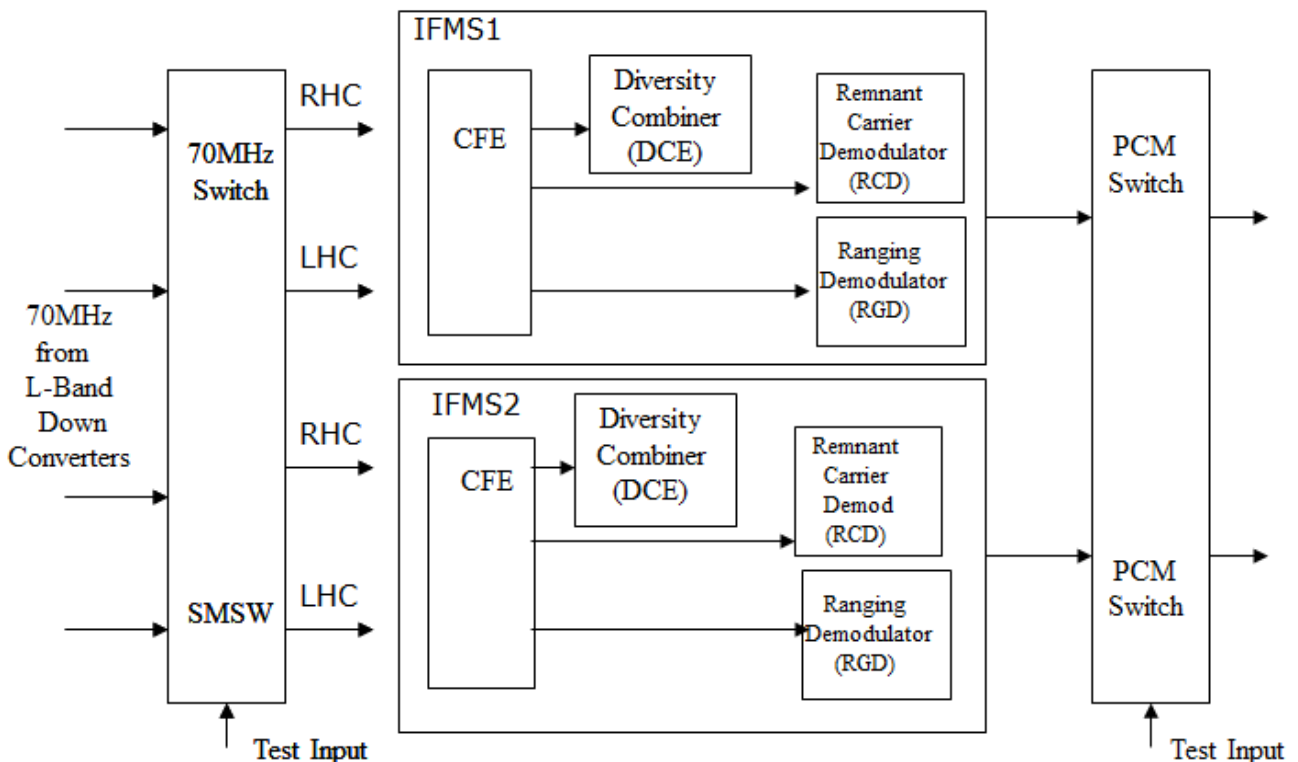
Figure 51: Telemetry chain

5.3 Uplink command chain

Figure 52 shows the typical downlink chain of ESTRACK stations common to each ESTRACK facility. With reference to Figure 52, from right to left the received signal is processed as follows:

- The Telecommand and Ranging video signals are modulated onto a 230 MHz carrier which is fed into the Antenna U/L Switch. Each Station is equipped with Two Telecommand

Encoder Subsystems and one Ranging System. Telecommanding always has priority over Ranging;

- The 230 MHz signal from the Antenna Uplink Switch is fed across site from the Main Equipment Room to the Antenna Equipment Room;

- The signal is then split and fed to into two up-converters which convert the 230 MHz signal to the required Uplink frequency of the spacecraft (for reference S-band in Figure 52). The actual output frequency of the up-converter is defined by the programmable frequency of the Local Oscillator Synthesizer;

- The Uplink signal is now ready to be amplified before transmission to the spacecraft. The amplification infrastructure varies from site to site (KPA, SSPA, TWT, Low Power Amplifiers). Both amplifiers have complete redundancy;

- The Uplink signal is routed to the selected RHC or LHC Diplexer and the Orthogonal Mode Transducer and thus to the Antenna.
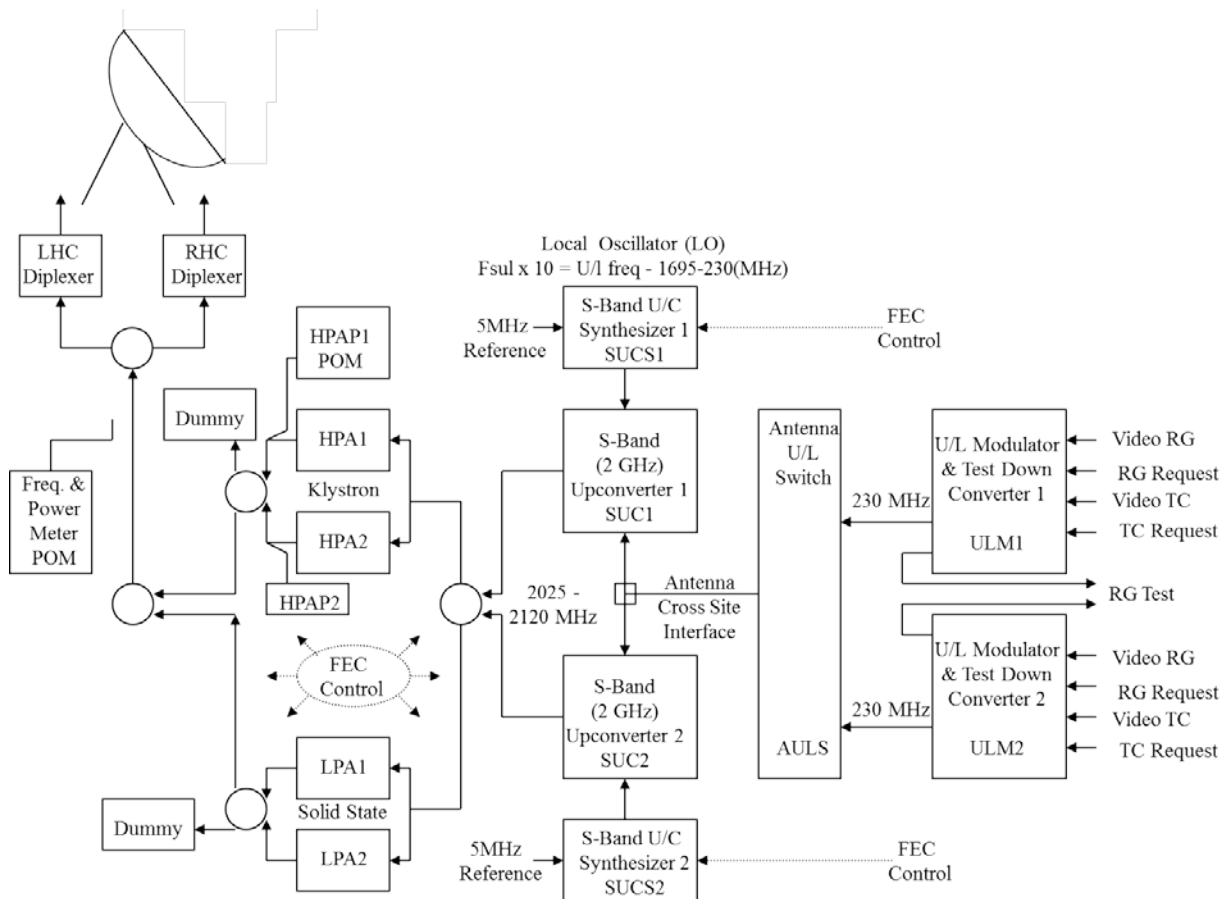
Figure 52: Command chain

6   Allan deviation enhancement technique

This section presents a method for improving the phase stability of HPA by mean of voltage controlled phase shifter. A different approach to improve the phase stability with respect to the classical methods used is proposed. Instead of introducing a tight control of the temperature of the water (±0.1 °C in present 20 KW HPA), the new idea is to compensate the phase variation of the HPA (water or air cooled) by mean of a phase shifting of the input signal in the opposite direction.

A complete test campaign has been performed on a 2 KW air cooled X-band KPA in order to demonstrate the validity of the method.

This work follows a preliminary and simulation study [62] carried out at ESOC, which focused on KPA used in ESA Deep Space Antenna as a consequence of the high levels of power demanded by new ESA missions.

6.1   Motivation and objective

In the last ten years, the number of ESA and NASA radio science missions is largely increased. Initially conceived as an exploratory tool, radio science techniques have provided considerable knowledge of the atmosphere and gravity of planets, some of which was originally unanticipated. One of the main observable during different type of radio science experiments (such as radio occultation, solar corona and solar wind tests and so on) is the phase of the received radio signal. As explained in the next paragraph, the communication system affects the signal introducing phase variation. The phase instability of the communication system will be noise for the Radio Science experiments.

The total phase instability could be divided in three main causes:

- the Ground segment;
- the Space segment;
- the media.

Concerning the RF part of the Ground segment, in an uplink configuration, the HPA represents the main contribution to the phase noise (discounting the contribution of the Frequency Reference multiplied by the Frequency Converter): the better performances of the HPA in terms of phase stability the more precise the ranging accuracy during radio science experiments.

The end-to-end accuracy in a S/C Doppler link is usually represented by the Allan Deviation (ADEV) at typical integration times of 1000 sec, where the link between the Allan Deviation and the relative velocity error along the line of sight is given by the equation

Eq. (14) $\delta_y = 2\Delta v/c$

where σ_y is the Allan Deviation, Δv is the relative velocity error and c is the speed of light.

Deep space missions link budget often require to use a KPA at the GS because of the power level demanded with low ADEV level. As a reference case, we consider the BepiColombo ESA mission, demanding a maximum value of ADEV of 10^{-15} @ 1000 sec for the entire Ground segment.

Unfortunately, the KPA suffers for temperature variation of the body, acting like a filter (see appendix 8.2A.1for an overall explanation of the phenomena).

The state-of-the-art technique for temperature stability is based on de-ionized liquid cooling system. Even though this technique offers an excellent reduction of the ADEV, it is very expensive and implies a large amount of maintenance. On the other hand, air cooling system is simpler and cheaper, but best performances allow for a temperature stability error of $\pm 3°C$. Figure 53 shows the water cooling systems for current 20 KW KPA and Figure 54 shows the air cooling system for 2 KW KPA.

As a consequence, using air cooling system a different phase stability technique is necessary in order to achieve a comparable level of ADEV. The difference of KPA ADEV using the two mentioned cooling systems can be noticed comparing the ADEV values shown in

Figure 55 and Figure 56, referred to water and air cooling system respectively.

The main objective of this study is to get stability performance on simpler air cooled amplifier similar to the one of more complex water cooled. This is a critical aspects of new ESA missions demanding more accurate radio link in terms of ADEV together with an increase of the HPA output power.

In order to achieve better performances of ADEV using air cooling system, a different technique is presented in this document. This technique is based on the measurement of the long-term phase perturbations introduced by the HPA and a compensation of the noise by phase-shifting the input signal in the opposite direction.

Furthermore, the proposed technique is valid for whatever frequency band and for any HPA output power and even for any subsystem (waveguides, diplexer, narrowband filter). All the results

presented in this document are referred to X-band, where availability of devices was complete (HPA, phase shifters and mixer). All the system can be used at different frequency bands (e.g. Ka-band) simply replacing the devices with something working at the proper frequency. This is an important aspect, allowing at the system the possibility to be used for any HPA in a future. In particular, at the moment there are not HPA at Ka-band with liquid cooling system, so it could be a good field of application for the proposed system.

Figure 53: water cooling system

Figure 54: air cooling system
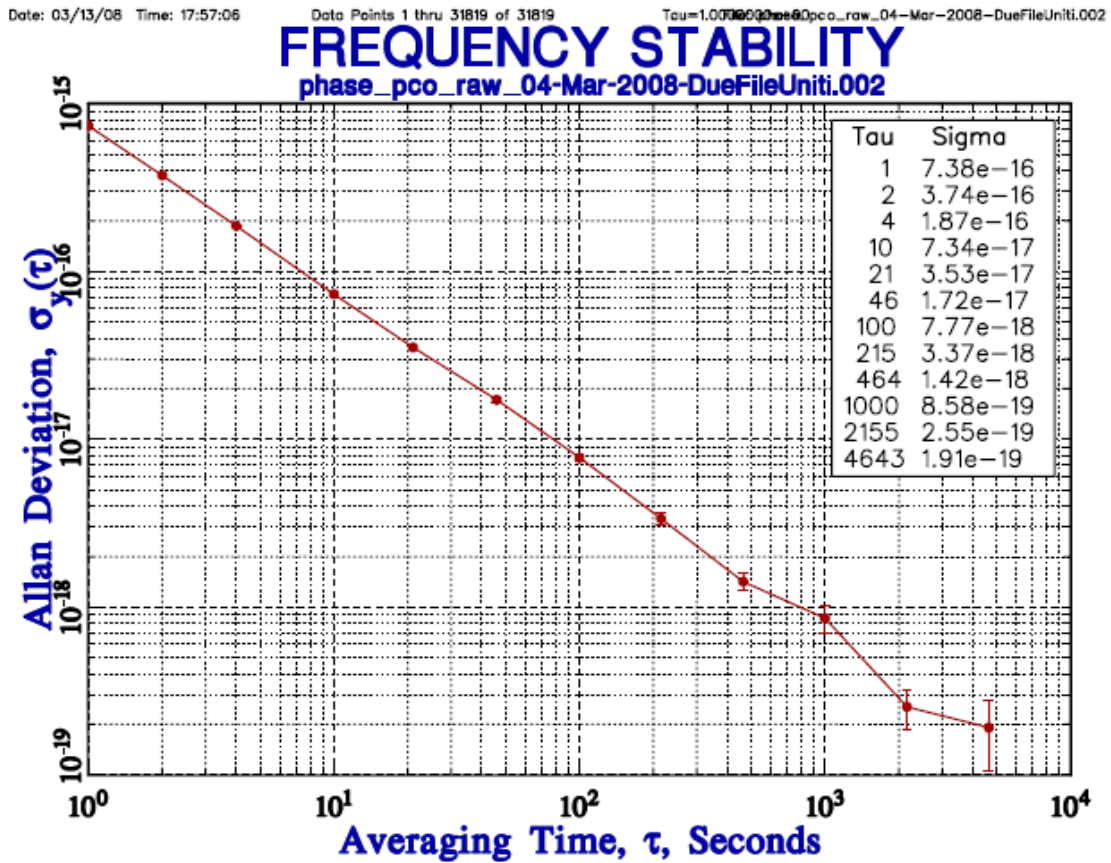
Figure 55: ADEV of 20KW X-KPA with water cooling system
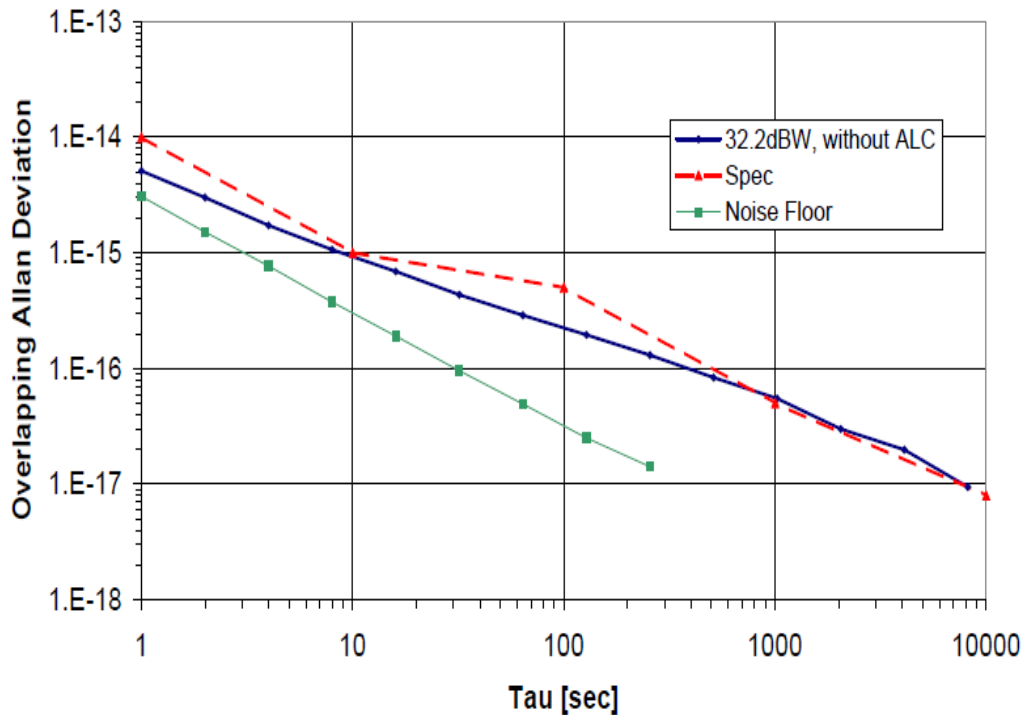
Figure 56: ADEV of air cooled 2KW XKPA

6.2 Theory

6.2.1 Origin of phase instabilities

Phase instabilities are analyzed in a different way depending on their frequency of variation rate. Quick phase variations (roughly over 1 Hz) are treated as phase noise and the analysis shall consider the filtering effects of phase locked loops. Slow phase variations (below 1 Hz) are measured normally in terms of period (seconds) and are treated as Allan Deviation. Due to the very low frequency of these phase instabilities, there is generally no filtering effect coming from phase locked loops. The origin of the instabilities can be split into three uncorrelated effects:

- Thermal phase variations
- ADEV at constant temperature.
- No linearities impact

Thermal phase variations are produced by the variation of the thermal environment combined with the phase stability over temperature of the different units of the system. The ADEV characterization of the system (or unit) at a constant temperature allows us to measure other variations not related with the temperature (flicker noise, PLL components noise and so on). Finally the non-linear response of some elements can generate phase instabilities like the AM/PM combined with amplitude variations.

6.2.1.1 Temperature related

Most phase instabilities come from the sensitivity of the output phase to the environmental temperature. This dependence can be tested in the laboratory by measuring the phase variation with temperature, normally in electrical degrees per temperature degree (°/°C). In this note the phases for ADEV are computed in cycles, then it is necessary to divide by 360 to pass from degrees to cycles. Additionally the temperature profile over time of ground station equipment rooms (AER or MER) can be registered providing the additional data required in the simulation of the phase variations introduced by the equipment.

This phase stability, combined with the thermal variation of the environment shall be converted in a similar behaviour than the ADEV.

6.2.1.2 Instabilities at fixed temperature

Additionally there are some phenomena that generate noise at very low offset from the carrier (flicker noise, random walk frequency noise, …) and introduce additional phase variations in the low frequency offset region. This effect can be characterised by measuring the ADEV of the equipment at fixed temperature. Except some particular cases like the frequency references of the GS, this contribution is smaller than the temperature related contribution.

The theoretical knowledge about the sources of these contributions is not complete and there is no way to simulate them. The only data would come from the empirical characterisation for the ADEV of the equipment.

6.2.1.3 Non linearities

Some non linearities can also introduce phase variations. The main element will be the AM/PM conversion of the amplifiers added to the presence of AM noise or amplitude fluctuations produced by slow variation of the input signal power (like the presence of solar corona fluctuations that will cause slow rate attenuation variations). This effect can be analysed separately for the elements presenting non linearities, with the knowledge of the AM/PM characteristics and the amplitude variations with time.

6.2.2 Definition of ADEV

The Allan deviation was introduced to characterise the stability of clocks or frequency references (one port devices). Since the ideal clock does not exist, normally one clock has to be characterised against another similar or better. The formulation of the Allan deviation allowed to define the quality of a clock and is widely accepted.

The instantaneous output voltage of a precision oscillator can be expressed as:

Eq. (15) $$V(t) = (V_0 + \varepsilon(t))\sin(2\pi v_0 t + \theta(t))$$

where V_0 is the nominal peak voltage amplitude, $\varepsilon(t)$ is the deviation from the nominal amplitude, v_0 is the nominal frequency, $\theta(t)$ is the phase deviation from the nominal phase $2\pi v_0 t$ and is the cause of phase instability.

Frequency stability of a precision oscillator is defined in terms of the instantaneous, normalized frequency deviation, y(t), as follows:

$$y(t) \equiv \frac{v(t) - v_0}{v_0} = \frac{1}{2\pi} \frac{d\phi}{dt}$$

Eq. (16)

where $v(t)$ is the instantaneous frequency (defined as the time derivate of the phase divided by 2π). Phase instability, defined in terms of the instantaneous phase deviation can also be expressed in units of time (time deviation), as:

$$x(t) = \frac{\phi(t)}{2\pi v_0}$$

Eq. (17)

Derived from Eq. 2 and Eq. 3, the instantaneous, normalized frequency deviation is:

$$y(t) = \frac{dx(t)}{dt}$$

Eq. (18)

So the phase instability could be indicated with the following expression:

- $\phi(t)$ = Instantaneous phase deviation
- $y(t)$ = Instantaneous fractional frequency deviation
- $x(t)$ = Instantaneous time deviation

The ADEV is the representation of the instability in the time domain. It is defined as:

$$\sigma_y^{Allan}(\tau) = \sqrt{\left\langle \frac{(\overline{y}(t,\tau) - \overline{y}(t-\tau,\tau))^2}{2} \right\rangle}$$

Eq. (19)

where $< \dots >$ means the mathematical expectance. As we can consider the processes ergodic, the statistical expectance can be replaced by their computation over the time. Moreover:

$$\overline{y}(t,\tau) = \frac{1}{\tau} \int_{t-\tau}^{t} y(s)ds = \frac{x(t) - x(t-\tau)}{\tau} = \frac{\Delta_\tau x(t)}{\tau}$$

Eq. (20)

is called the average fractional frequency deviation over the time interval (t-τ , t). We call τ the averaging time. The Allan variance can also be written like this:

$$\sigma_y^{Allan}(\tau) = \sqrt{\left\langle \frac{(x(t) - 2x(t-\tau) + x(t-2\tau))^2}{2\tau^2} \right\rangle}$$

Eq. (21)

Replacing the mathematical expectance by their equivalent over the time (it is allowed if the process is ergodic), we obtain:

Eq. (22)
$$\sigma_y^{Allan}(\tau) = \sqrt{\frac{1}{2T}\lim_{T\to\infty}\int_{-T}^{T}\frac{(x(t)-2x(t-\tau)+x(t-2\tau))^2}{2\tau^2}dt}$$

converging for every τ and for every noise process present in oscillators.

During measurement, we have time deviation samples $x(0),x(\tau)\dots x(m\tau)$ over the time $T=m\tau$. The discrete variation of Eq. 8 is:

Eq. (23)
$$\sigma_y^{Allan}(\tau) = \sqrt{\lim_{m\to\infty}\frac{1}{m-1}\sum_{j=2}^{m}\frac{[x(j\tau)-2x((j-1)\tau)+x((j-2)\tau)]^2}{2\tau^2}}$$

A typical estimator of the ADEV is given by:

Eq. (24)
$$S_y^{Allan}(\tau,m) = \sqrt{\frac{1}{m-1}\sum_{j=2}^{m}\frac{[x(j\tau)-2x((j-1)\tau)+x((j-2)\tau)]^2}{2\tau^2}}$$

6.2.3 ADEV of a HPA

The phase of the amplifier is the phase of the S parameter S21. The transmission lines of the amplifier and the transistor characteristics affect this phase. Additionally the amplifier can be wide band (acting more like a transmission line, case of the Low Noise Amplifier (LNAs), Solid State Power Amplifier (SSPAs) and buffers) or narrowband (acting more like a filter, case of the klystrons). In particular, the KPA suffers for a variation of the dimension of internal copper tube introducing a variations of the group delay generating phase instability.

The impact of the temperature over the phase stability of a broadband amplifier can be approached in a first attempt by the group delay (see the filter description in appendix 8.2A.1) or the thermal characteristics of the substrate considering the device as a transmission line. For narrowband amplifiers we can consider the device like a filter with the thermal characteristics of the material of the Klystron cavities. In any case an experimental characterization is recommended to assess the behaviour of the possible non-linear responses of the active devices. This characterization is extremely important for high power devices (like SSPA and Klystrons) whose thermal design is very critical.

The proposed architecture for compensating the phase variation introduced by the HPA is based on a real-time measurement of the phase fluctuation and a compensation of the noise through a controlled phase shift of the input signal. The basic idea is to force the output of the phase detector, measuring the phase difference between the input and the output of the HPA, to be zero in order to

eliminate the instability introduced by the device. A phase shifter is used to change the phase of the input signal according to the phase difference measured between the input and the output.

6.2.4 ADEV compensation circuit

The simpler solution for performing such a control consists of a closed loop, as the one shown in Figure 57, in which a mixer is used as phase detector for measuring the phase difference between HPA input and output signals, while a Voltage Controlled Phase Shifter (VCPS) is used as an actuator in order to perform the compensation of the noise of the input signal. A low pass filter (LPF) is necessary for filter the high frequency components of the mixer output while an integrator is introduced for the stability of the loop.

The loop is similar to a first order PLL circuit, even if the output value of the control loop is a phase value instead of a frequency value.
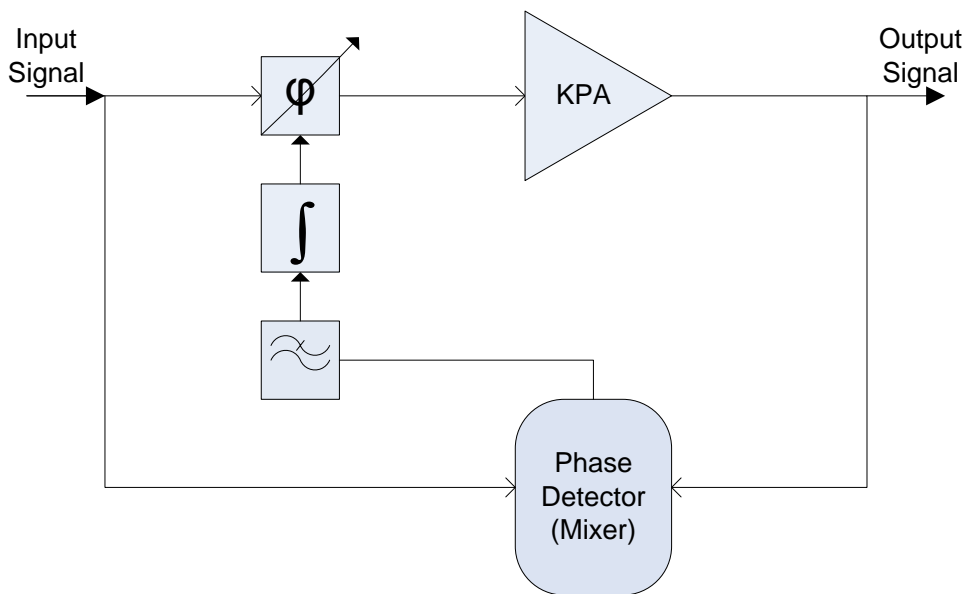
Figure 57: Phase compensation architecture

Considering two sinusoidal signal as input and output of the HPA, the output of the mixer used as phase detector, could be written in the following way:

Eq. (25)

$$v_1(t) = V_1 \sin(\omega t + \varphi_1(t))$$
$$v_2(t) = V_2 \sin(\omega t + \varphi_2(t))$$

and directly from Eq. (25):

Eq. (26)
$$v_O(t) = K\,v_1(t)\,v_2(t) = \frac{K V_1 V_2}{2}\left[\cos(\varphi_1(t) - \varphi_2(t)) - \cos(2\omega t + \varphi_1(t) + \varphi_2(t))\right]$$

where ω is the signal pulsation (that is not affected by the HPA) while φ_1 and φ_2 are the phases of the input and output signals respectively. The high frequency components is filtered, so it is possible to measure the continuous component, which is proportional to the phase difference between the inputs:

Eq. (27)
$$v_O(t) = K_d \cos(\Delta\varphi(t))$$
where

Eq. (28)
$$\Delta\varphi(t) = \varphi_1(t) - \varphi_2(t)$$

A calibration procedure is necessary in order to compensate an offset eventually introduced by the asymmetries of the mixer, so it could be written:

Eq. (29)
$$V_p = \frac{V_{max} - V_{min}}{2}$$
$$V_0 = V_{max} - V_p$$

and from Eq. (27)

Eq. (30)
$$v_O(t) = V_0 + V_p \cos(\Delta\varphi(t))$$

The $\Delta\varphi(t)$ value is recorded at a sample rate of 1 Ks/s. A mean value is calculated each 100 samples in order to reduce the noise introduced by the measurement chain.

6.2.5 Control voltage calculation

The control voltage loop architecture needs to calculate the correct phase shifter input voltage for each correction of the phase noise. The input voltage is calculated multiplying the integral output by the loop gain. The loop gain depends on the behaviour of the VCPS and is calculated as:

Eq. (31)

$$loop\_gain = \frac{\Delta V_M}{\Delta V_{PS}}$$

where ΔVM is the voltage difference on the mixer output (that is the difference between the maximum and minimum voltage on the mixer output) while ΔVPS is the relative voltage range needed at the VCPS input to obtain ΔVM. During the calibration procedure the loop gain value is calculated and stored.

6.3   Implementation

6.3.1 Test setup

A block scheme of the test setup is shown in Figure 58. Through a power splitter the output of the signal generator is equally divided in order to have a reference value at one mixer output and feed the KPA at the same time. Two phase shifters are inserted before the signal is connected to the KPA: the first one is the VCPS used for the phase compensation, the second one is a manual phase shifter used during the calibration of the mixer. In particular, the manual phase shifter is used for improving the system sensitivity. The VCPS used is the Hittite-HMC-C010 which allows phase shift range of 800º at X-band with control voltage range of 0-5 V.

The KPA output signal is attenuated in order to obtain the same power value at the second mixer input port during noise floor measurement and KPA ADEV measurement. This is an important aspect of the measurement campaign because the measurement result of the noise floor depends on inputs power level: the higher the power level, the lower the ADEV value. The output of the mixer is lowpass filtered and sampled at a selectable sampling rate.

The acquisition board is controlled by a Labview software, which also calculates in real-time the voltage signal for controlling the VCPS in order to compensate the phase instability. In particular, for eliminating the noise introduced by the measurement chain, a mean voltage value is calculated each 100 samples, then this value is used as input for the integral function. The voltage output is obtained multiplying the integral output by the loop gain.

In order to verify the compensation actuated by the system, a set of measurement of the KPA ADEV without control was performed. With respect to the test bench shown in Figure 58, a very similar setup has been used during this test campaign, shown in Figure 59. Obviously, the

retroaction performing the control was disabled, keeping the acquisition board and software only to save samples for the post-processing ADEV calculation.

A similar setup configuration has been used also for the noise floor measurement, excluding the KPA and the attenuator from the measurement chain, shown in Figure 60.

In particular, the flowing devices have been used during operational tests:

- Signal Generator: HP 8673B

- Mixer: ANAREN 73230

- Splitter: ANAREN 41130

- Analog voltage controlled phase shifter: HITTITE MHC-C010

- Manual phase shifter: NARDA 3753B

- Acquisition board: National Instruments BNC2110
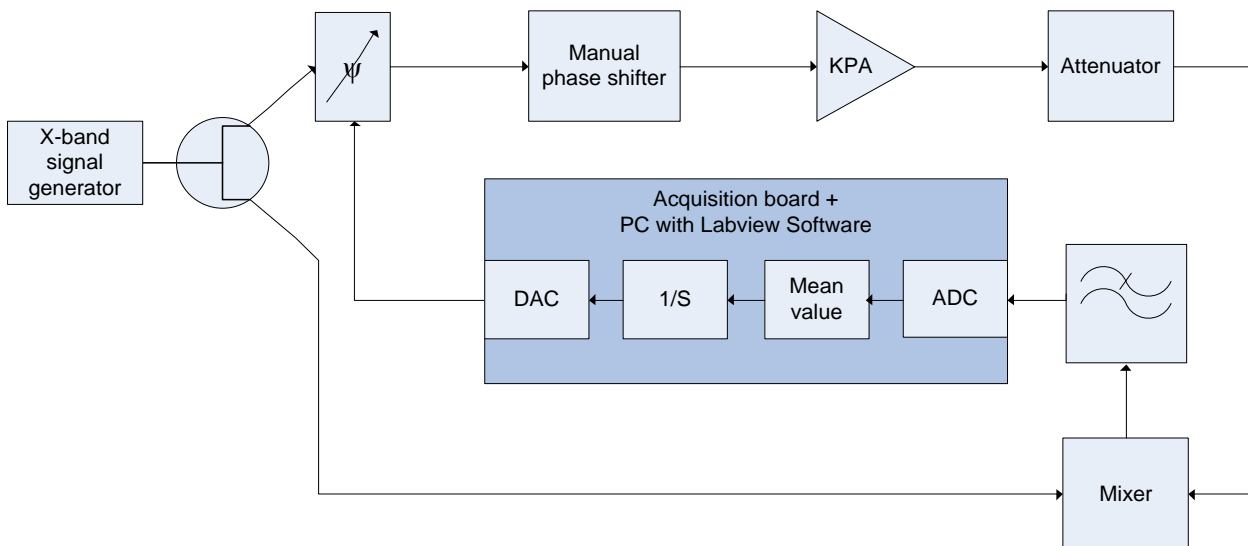
Figure 58: Block scheme of the setup during KPA ADEV measurement
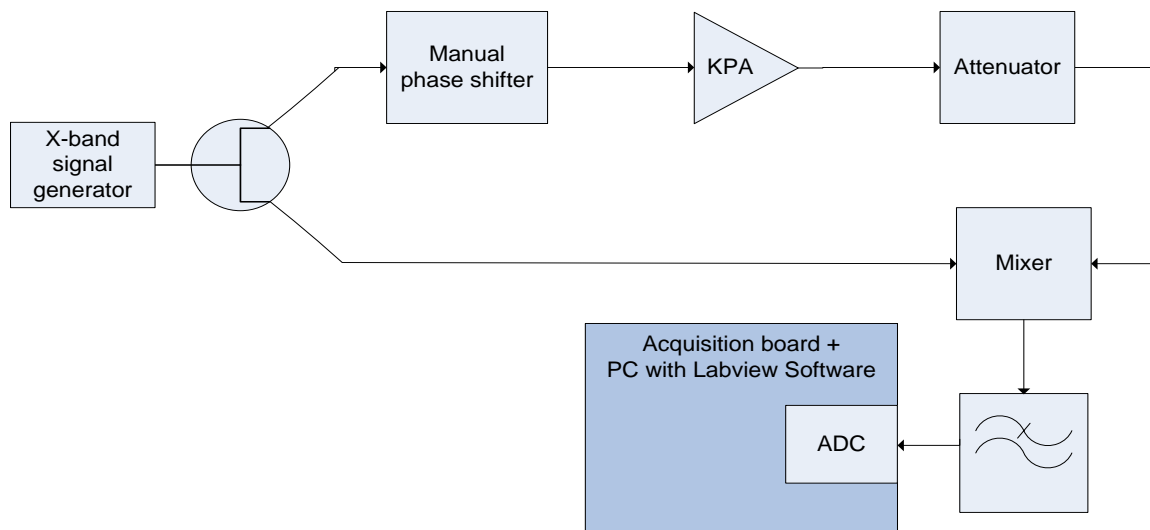
Figure 59: Block scheme of the setup during KPA ADEV measurement without control
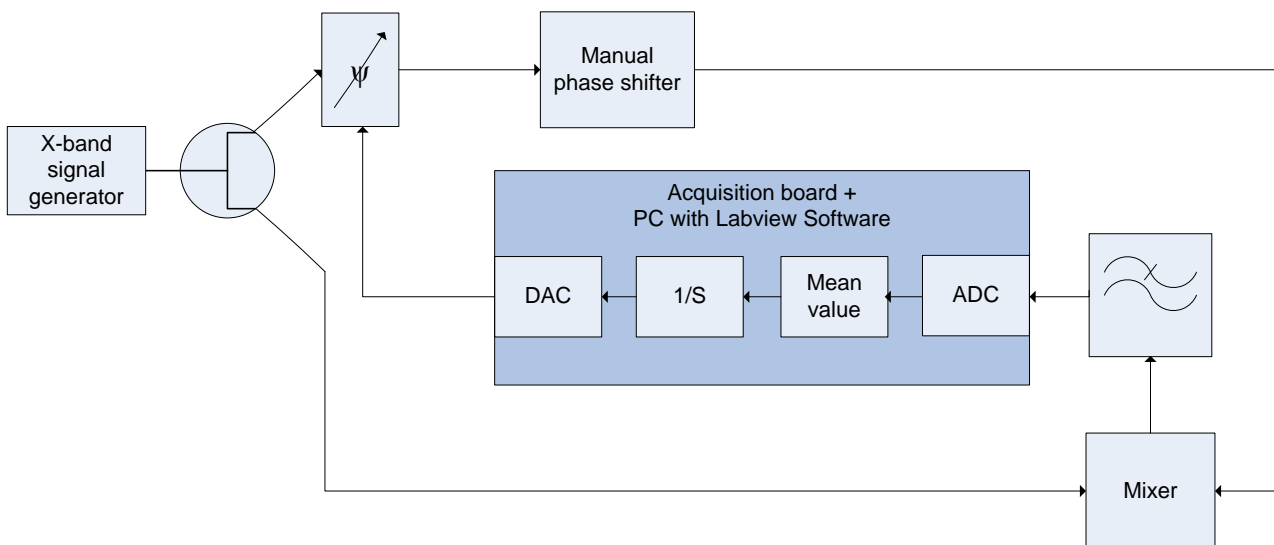
Figure 60: Block scheme of the setup during noise floor measurement

6.3.2 Measurement

6.3.2.1 Sensitivity

Measuring the system sensitivity, particular attention must be paid to the initial phase difference between the mixer inputs. In particular it has been observed that the minimum ADEV occurs when the phase difference is 90º. Figure 61 shows ADEV for different phase shift, obtained setting properly the manual phase shifter, with a synthesizer output power of 0 dBm. It can be noted a lower value of ADEV (of about a factor of 5) in correspondence of a phase difference of 90 º. For a better understanding of the problem, an exact calculation of the ADEV of a mixer has been added in appendix 8.2A.3.

This result can be explained with reference to [62]. Figure 62 shows the mixer output curve with a phase shift from 0º to 180º. The sensitivity is largest at 90º due to the higher slop of the curve: smaller errors in voltage correspond to smaller error in the phase difference. As the phase deviates from 90º the slope is lower and errors are bigger. As a consequence, particular attention must be paid to set the manual phase shifter in order to have a 90º phase shift between mixer inputs at the beginning of the measurement.
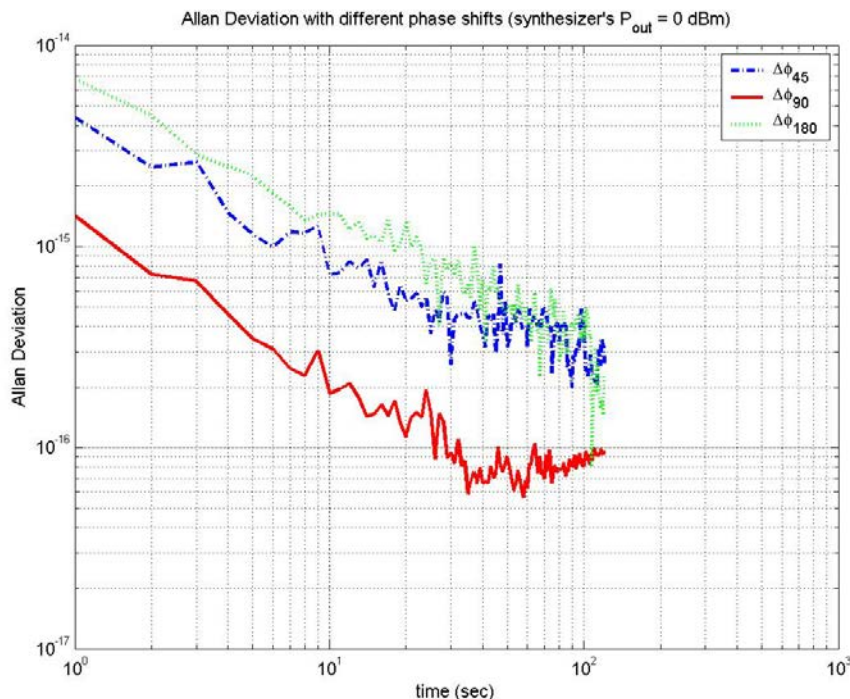
Figure 61: System sensitivity depending on mixer input phase difference
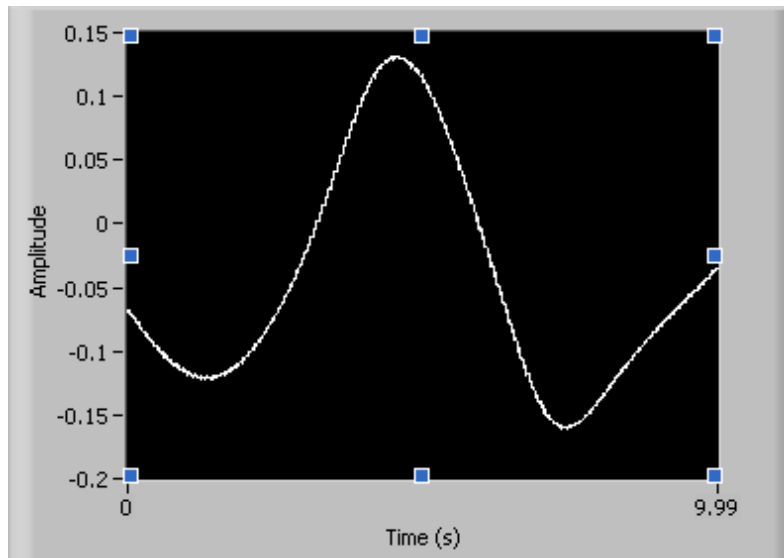
Figure 62: Mixer output

6.3.2.2 Calibration

During a measurement, the first operation to be done is the mixer calibration. The calibration is performed varying the phase shift from 0º to 180º of the input signal and saving the maximum and minimum voltage of the curve (shown in Figure 62). These values are then used to calculate the $\Delta\varphi$. In order to improve the measurement, the phase can be shifted in a short range around 90º: in this way the curve obtained is a line and errors between the actual and the calculated control voltage is largely reduced. Figure 63 shows the improved calibration curve.

A calibration equal to the initial one is performed at the end of the measurement, in order to be sure that the mixer behaviour is not changed during the test.
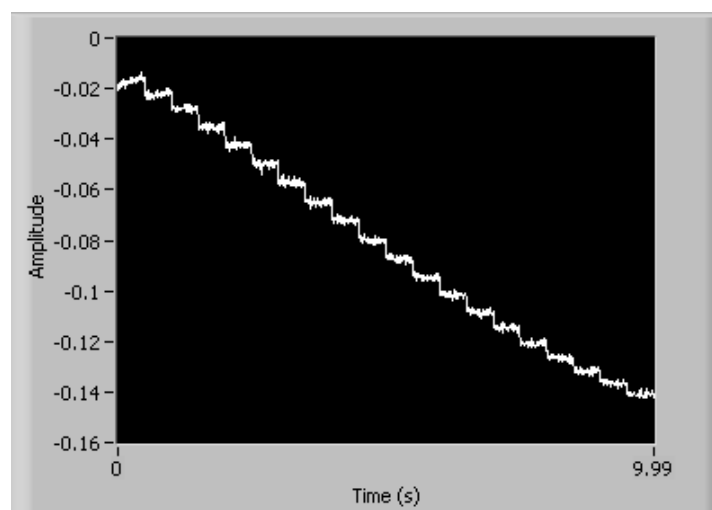
Figure 63: mixer output around 90°

6.3.2.3 Estimation of the slope

As can be seen in Figure 62, quadrature points, in which the system has an increase of the sensitivity, can belong on part of the curve with positive or negative slope. The estimation of the slope is particularly important because can determine the stability or instability of the loop. In fact, it affects the way the control calculates the output voltage. There are two possibilities: when the slope is positive, if the phase difference increases, the voltage increases; on the other hand if the slope is negative, when the phase difference increases, the voltage decreases. In other words, if we know which the slope is, then we can know the sign of the phase stability.

The Labview software estimates automatically the slope during the calibration procedure, in order to guarantee the stability of the loop and correct phase compensation.

6.3.2.4 Acquisition and phase control

After the mixer calibration, the second step of the test is the storing of the mixer output voltage samples and the control of the phase instability. The first working point will be a quadrature point, that is a voltage for which the output mixer voltage is close to 0 V. This point is chosen with reference to the calibration curve.

A time label indicates the duration of the test. This information is used during the post-processing to know exactly the number of samples stored each second.

Even if the maximum sampling rate of the acquisition board is 200 Ks/S, the latency introduced by the loop, explained in Section 6.3.4.1, affects the speed of the test, so a sampling rate of 1 Ks/S has been used as a good trade-off between the sampling rate and the total amount of data to be recorded. The phase instability is compensated multiplying the integrator output by the loop gain The calculated value is then added or subtracted to the previous loop voltage output, depending on the slope (see Section 6.3.2.3). Final controls are added to avoid the loop output voltage to exceed the VCPS input voltage range. At the end of the measurement, three different files are created for the post-processing operation: one containing the Vp and Vo values; the second one containing the duration of the test (in second) and the last one with all the voltage samples.

6.3.2.5 ADEV post processing

Stored voltage values are saved in a .txt file, then the ADEV computation is performed in post-processing. A routine has been developed in Matlab environment: it performs the import of the data, the calculation of $\Delta\varphi$ values from voltage ones and the ADEV computation.

6.3.3 Problems

6.3.3.1 Measurement depending on input power

The system sensitivity is depending, other than on the phase difference between mixer inputs, on the mixer inputs power. Allan Deviation as a function of power levels of the synthesizer is shown in Figure 64. As expected, the bigger the power, the better the noise floor.

This is a critical aspect because the mixer has a maximum input power of 4 dBm on one input and 12 dBm on the other one that limits the synthesizer maximum output power. On the other hand, with reference to Figure 58, it can be noted that during noise floor measurement the attenuation introduced in one mixer input is higher than in the other because of the phase shifters on the link.

Using the setup shown in Figure 58, during noise floor measurement we have a power level on the mixer input connected to the phase shifter of about -4 dBm. As a consequence, during KPA ADEV measurement a variable attenuator is introduced in order to obtain the same power level and can compare the results with a noise floor obtained in the same condition.
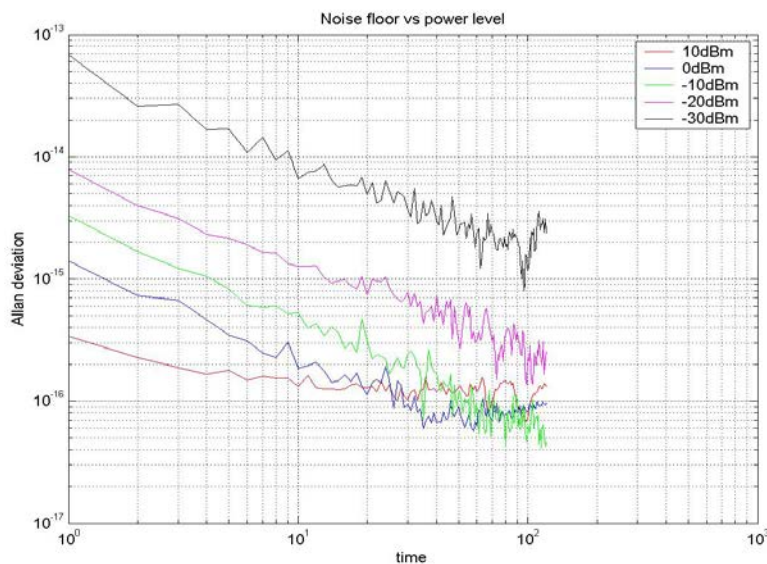
Figure 64: Noise floor depending on input power

As a conclusion, we can deduce that the best conditions for the measurements with respect to floor noise are:

- Input signals to the mixer in quadrature (phase difference of 90º);

- High input power (with a maximum value of 4 dBm at the mixer input).

6.3.3.2 Calibration on a shorter voltage range

As described in Section 6.3.2.2, in order to improve the measurement, the phase can be shifted in a short range around 90º during the calibration.

Considering the VCPS characteristic, usually a first calibration was performed varying the control voltage of the phase shifter from 1 to 3 V, allowing a phase change of about 320º. Then, using the manual phase shifter, the quadrature point has been moved in correspondence of the intermediate voltage of 2 V. After setting the manual phase shifter, a new calibration was performed varying the control voltage of the phase shifter from 1.8 to 2.2 V, obtaining the curve shown in Figure 63 and a reduction of the measurement error.

6.3.4 Limitations

6.3.4.1 Latency of the loop

One important limitation affecting the sensitivity of the system is the speed of the control. In order to suppress the noise introduced by the system, the control voltage is computed using a mean value over 100 samples. This means that the real-time control works at a rate 100 times lower than the sampling rate. Moreover, the rate of the control is affected by the latency of the loop: each time a control of the phase shift has to be performed, the control voltage has to be computed. These operations, plus some control necessary for ensuring the right behaviour of the control, add latency on the loop, slowing down the control rate. A possible solution to this problem could be represented by the use of more powerful PC and acquisition board.

6.3.4.2 Temperature instability and mechanical vibration

As it is well known, the environment temperature affects the ADEV of the measured device: the higher the temperature instability, the higher the ADEV. In previous work, devices under test were put in regulated temperature environment, as an oven, to maintain a constant temperature during

measurement or to relate the temperature with ADEV results. Unfortunately, because of the dimension of the KPA under test, it was impossible to use a similar setup.

Additionally, at the same time of the test campaign, the ESOC GSRF was under complete restructuration and the mechanical vibration of the works impact the test results.

6.4 Test campaign

6.4.1 Measurement environment

First of all, some considerations about the environment of the measurement chain are necessary. The KPA used for the tests is assembled in a crowded rack and without temperature control; furthermore phase measurements are very sensitive and depending on the external temperature; moreover cables phase is very sensitive to variations and touching them or other devices of the measurement chain during tests can add noise to the measure. As a consequence measurements can be affected by the environment. In order to minimize this unwanted contribute of noise, all the measures were performed during night, without people working in the same laboratory.

6.4.2 Power level setup

As explained in previous Section, the power level at each point of the measurement chain has influence on the system sensitivity. Moreover, devices have input power limitation to be respected.

During the noise floor test (see Figure 60 as reference for the setup) the following power level has been used:

- Signal generator: +10 dBm (maximum value allowed);
- Mixer LO input= -3 dBm.13 dB of attenuation are introduced by the splitter (3 dB), phase shifters (8 dB), cables and connector (2 dB);
- Mixer RF input: -3 dBm. With respect to Figure 60 an attenuation of 10 dB has been introduced in order to have the same power level at both mixer input port.

In order to obtain the same power level at the mixer input ports and to compare the results of the KPA ADEV with the noise floor the same power condition has been recreated during KPA ADEV measurement (see Figure 58 for reference):

- Signal generator: 0 dBm;
- KPA input: -13 dBm;

- Mixer LO input= -3 dBm. An attenuation of 10 dB between the KPA output and the mixer port was inserted, as shown in Figure 58 in order to obtain the same power level. During test the KPA was working very close to the saturation region (60.5 dBm of output power) and the coupling output port (coupling factor of 50 dB) was used for the KPA output signal. About 3 dB of attenuation was introduced by cables and connectors.
- Mixer RF input: -3 dBm.

Higher values of KPA input and output power have been used in order to verify if the ADEV is affected by operational condition of the amplifier near to the saturation. In this document only tests that have highlighted different ADEV values are reported.

6.4.3 Numerical results

As mentioned in Section 6.1, the objective of the study is the medium term phase stability. In particular we want to calculate ADEV for a maximum time of 10000 seconds.

For each test, the KPA has been switched on at least half an hour before starting the voltage measurement, in order to allow the KPA to stabilize the output signal, in terms of power level and phase stability.

As mentioned in Section 6.3.1, three different ADEV measurements have been performed: the noise floor of the chain, the KPA ADEV without control and the KPA ADEV with control.

Figure 65 shows the comparison of the results of the different tests (vertical red lines are inserted as reference for different integration time). First of all, it can be noticed the great difference between the KPA ADEV with and without control: controlling the phase instability with the technique we propose the ADEV is more than one magnitude order less during the integration period of 10000 seconds.

ADEV values at different time and for different tests are shown in Table 17 sketched hereafter.

At 1000 seconds of integration time we have a value of ADEV of 4.81E-18 that easily allows for an ADEV value of 1E-15 for the overall GS.

As can be seen from Figure 65, the noise floor and the controlled KPA ADEV, represented with the green and red line respectively, are very close. It suggests the possibility that, improving the system sensitivity and the noise floor as well (acting on the limitations explained in Section 6.3.4.1 and 6.3.4.2), an improvement in the KPA ADEV measurement precision could be obtained.
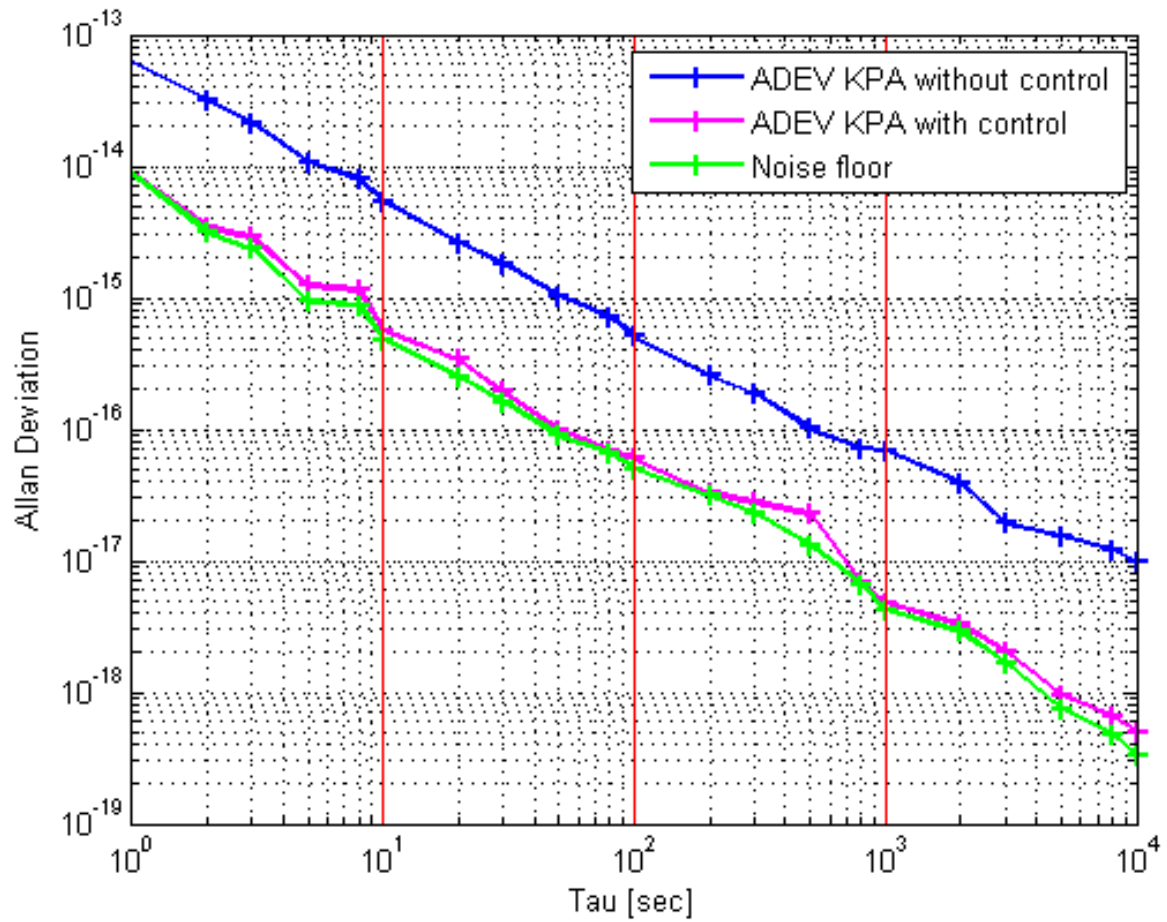
Figure 65: measured ADEV

Time	ADEV Noise floor	ADEV KPA controlled	ADEV KPA without control
10	4.77E-16	5.59E-16	5.44E-15
50	8.99E-17	9.93E-17	1.04E-15
100	5.00E-17	5.99E-17	5.10E-16
500	1.31E-17	2.27E-17	1.01E-16
1000	4.22E-18	4.81E-18	6.91E-17
5000	7.43E-19	9.45E-19	1.54E-17
10000	3.29E-19	4.98E-19	9.80E-18

Table 17: ADEV values at different integration time

Figure 66 shows the comparison between the measured KPA ADEV with phase compensation and previous measurement of the ADEV of the same device without phase instability control. It can be noticed that for medium-high integration time the enhancement introduced by the phase compensation is significant. The improvement consists of about a factor of 6 at 100 sec, more than a magnitude order factor at 1000 sec and a factor of 15 at 10000 seconds. For low integration time the enhancement is not so relevant.
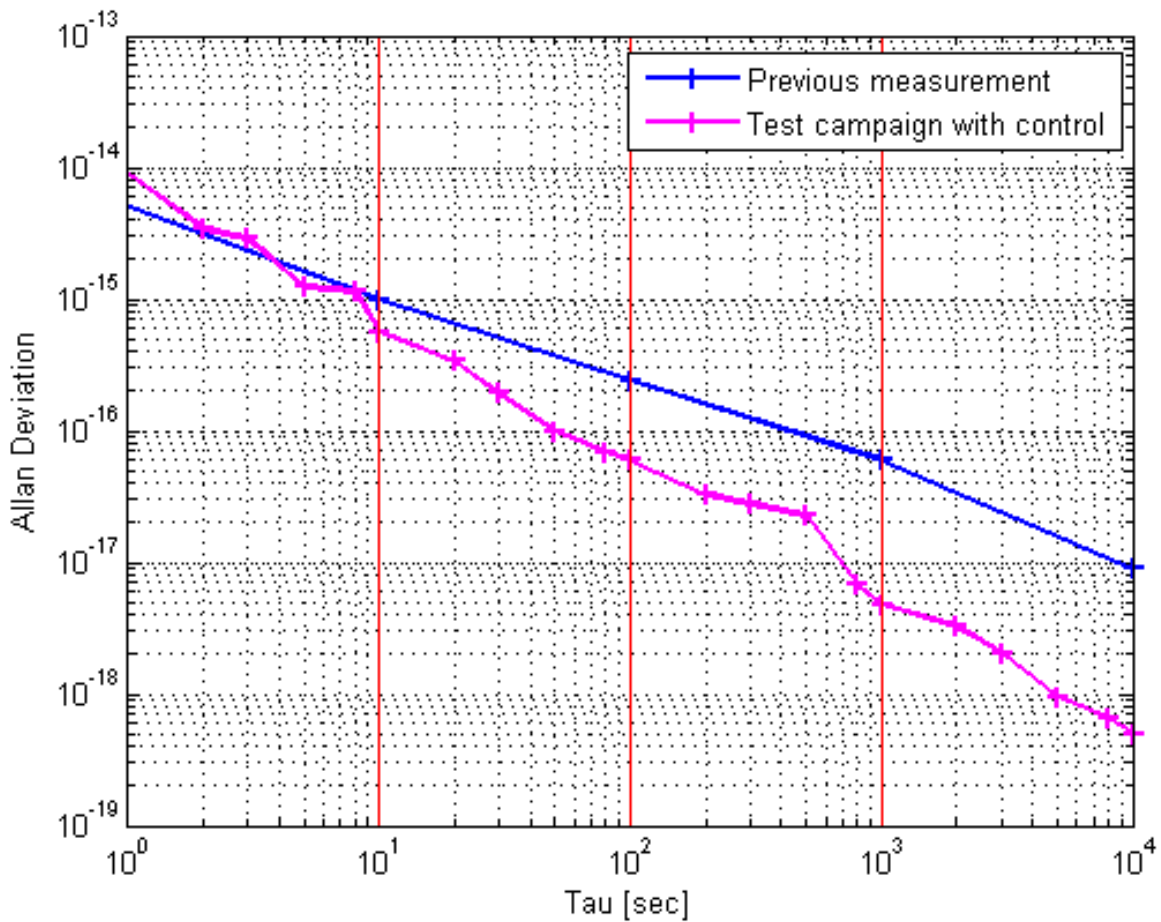
Figure 66: measured ADEV and ADEV of DNK7703 prototype

Moreover, Figure 67 shows a comparison between the measured KPA ADEV and the ADEV of the state-of-the-art X-band 20 KW KPA with liquid cooling system, tested on March 2008.

The very low ADEV obtained with liquid cooling system, that allow for a temperature variation in the body of about ±0.1°C, is still unreachable with the proposed system, but the difference is largely reduced. A factor of 10 is the ADEV difference at 10 and 100 seconds of integration time, while at 1000 seconds the air cooled KPA ADEV is higher than the liquid cooled by only a factor of 6. ADEV values at different time and for different tests are shown in Table 18.

Time	2 KW KPA, air cooling, phase compensation	20 KW KPA, liquid cooling
10	5.59E-16	7.34E-17
100	5.99E-17	7.77E-18
1000	4.81E-18	8.58E-19

Table 18: ADEV values at different integration time
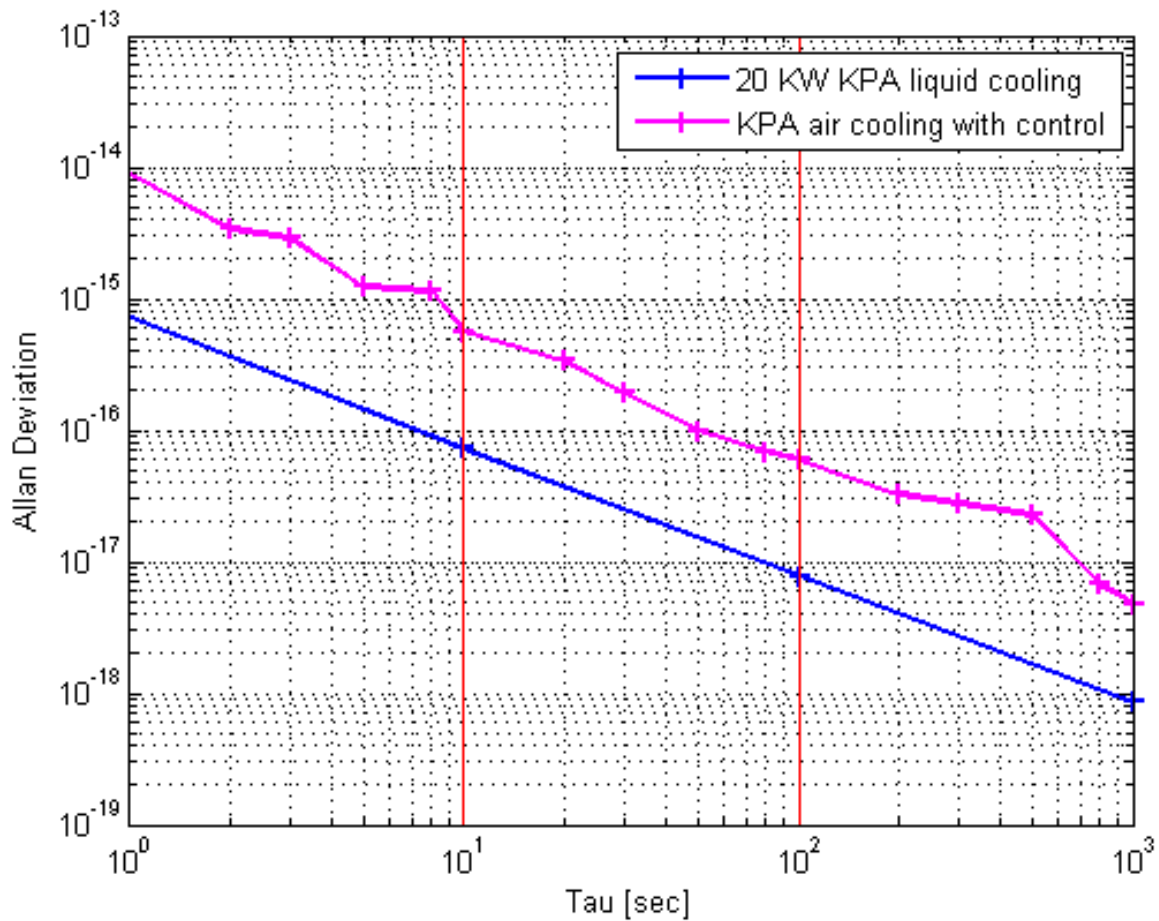
Figure 67: measured ADEV and 20 KW liquid cooling ADEV

Finally, Figure 68 shows the analysis of the KPA ADEV with respect to the amplifier input power. Four different input power values has been considered in the KPA input power range (from -18dBm to -10 dBm). As can be noticed a slight difference of a factor of 2 among the ADEV tests has been measured but there is not a linear trend between the input power and the relative ADEV. The minimum value of ADEV is related to an intermediate power level of -13 dBm, while the level of Allan Deviation for the minimum and the maximum input power is basically the same. Anyway, a difference of a factor of 2 can be easily introduced by the environmental noise: as already explain

the measurement chain is very sensitive to external mechanical vibration and this phenomena could slightly affects the final measurement.
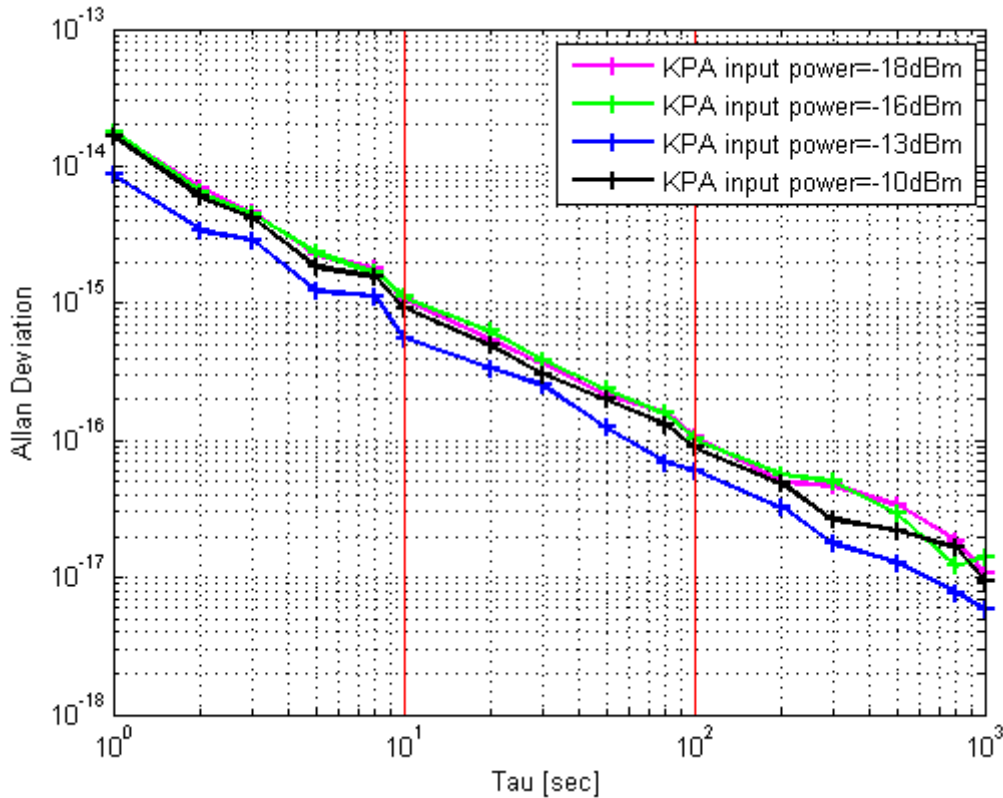
Figure 68: KPA ADEV for different amplifier input level

6.5   Future application

The proposed phase compensation circuit has been designed and tested with reference to a 2 KW S-band KPA. Anyway, the theory of phase noise reduction through real-time phase shifting and compensation can be easily applied to a variety of different devices that introduce phase noise on a RF signal (i.e.: waveguide sections; narrowband filter, antenna beam waveguide).

Considering the small volume and mass occupied by the whole compensation chain the implemented circuit can also be easily mounted both on on-board and on-ground segment. As shown in Figure 69, the overall hardware consists of a signal splitter, a mixer, a voltage controlled phase shifter and some coaxial cables. Furthermore, an electronic board must be used for analog to digital conversion of the input signal, the calculation of the voltage control and the analog to digital conversion of the output signal.

Moreover, the proposed method can be quickly adopted at any frequency band (S-, X-, Ka-bands and so on). In fact, it needs only to change the operative frequency range of the signal splitter and the mixer, while all the others signal are direct current (DC). A deep explanation of the motivation and advantages of higher frequency migration is reported in appendix 8.2C.

In sections 6.5.1, 6.5.2 and 6.5.3 all the possible future application and their advantages are deeply explained.
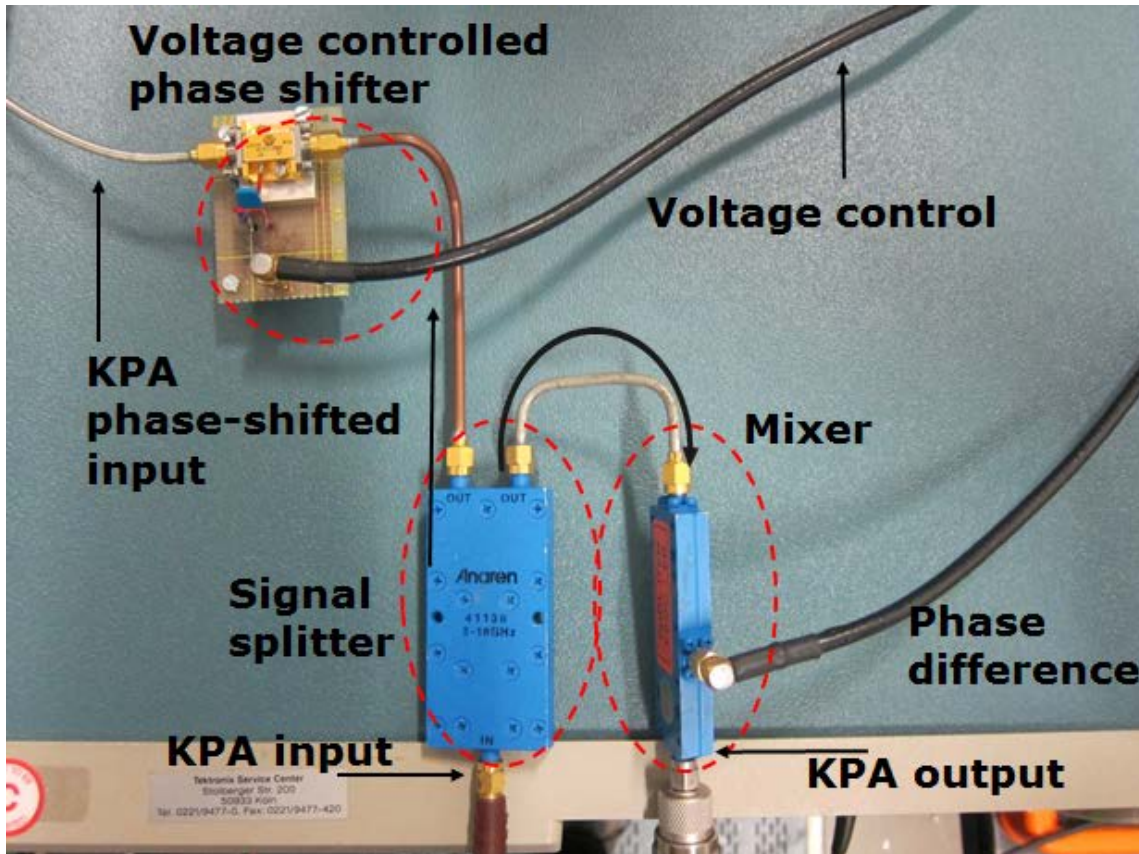
Figure 69: hardware of the ADEV compensation circuit

6.5.1 Ground segment application

The primary application of the proposed phase compensation method is related to an enhancement of the total ADEV introduced by a KPA. The ideal objective would be to make the ADEV of an air cooled KPA equal to the one of liquid cooled KPA. This results will allow a deep reduction of complexity and cost of KPA cooling system, as shown in Figure 70. Analyzing the values of Table 18, it can be noticed that a difference of a factor of 5 or 6, depending on the integration time of interest, still remains between the ADEV of KPA using air and liquid cooling system; nevertheless,

with the introduction of the compensation circuit the two values are quite comparable and the use of air cooled KPA could be taken into account also for high stringent ADEV requirement mission.

Moreover, the circuit can also be applied to other devices of the GS introducing phase noise, such as narrowband filters or waveguide sections reducing in this way the overall amount of phase noise in the GS chain. A detailed analysis of the phase variation introduced by waveguide sections is inserted in appendix 8.2A.3.

Finally, in order to reach a very high value of phase stability in a satellite link, the same circuit can be mounted directly on the antenna beam waveguide, reducing in this way the phase noise introduced by the antenna feed. In fact, the small volume occupied by the proposed architecture allows for an easy installation of the device also in critical environment such as the antenna beam waveguide.

Figure 70: air cooling and liquid cooling system in ESA GS

6.5.2 On-board satellite application

Traditionally, one-way radio science experiments (atmospheric and ring occultations and bistatic radar observations) were carried out using a downlink mode where a radio signal emitted from the spacecraft was received by a GS on Earth.

As a matter of fact, although uplink radio science was identified since the very beginning as the optimal configuration for completing these types of measurements, the easier-to-implement downlink architecture was selected due to the high development costs needed for the assembly of the onboard instrumentation (a proper RF receiver).

Recent study committed by ESA [16] have pointed out a viable architecture for performing radio science experiments exploiting an uplink configuration. The so-called OBRAS (On-Board Radio Science experiments) architecture addresses the concept of executing radio science experiments in uplink mode. In this configuration, the ground station represents the emitter while the S/C can receive single- or dual-frequency signals at UHF, S, X or Ka-band, as shown in Figure 71.
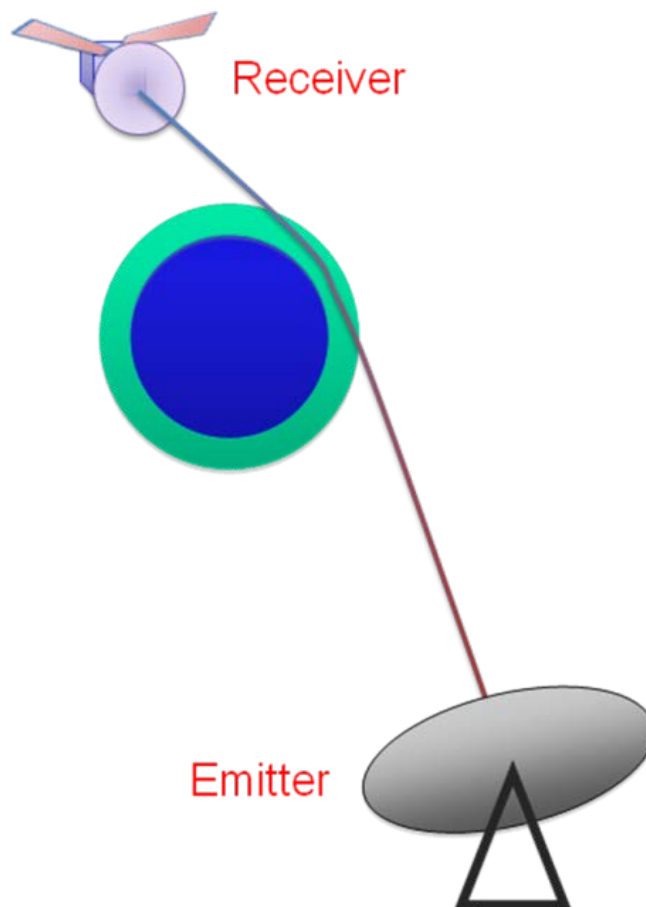

Figure 71: Uplink configuration

The main advantage offered by the uplink configuration is the improvement of the signal-to-noise ratio (SNR), due to the much larger power availability when transmitting from the Earth. In comparison with the classical downlink configuration, the change in the receiver noise (much higher on-board the S/C, if compared to the cryogenic LNAs at the G/S) plays in the opposite direction, but is pretty much compensated by the higher transmitted power which significantly increases the link margin, a key factor when considering outer planet missions. A higher SNR entails shorter integration times, higher vertical resolution and larger vertical range of measured densities during neutral atmospheric occultation experiments, and allows a more precise disentanglement of atmospheric effects, noise and scintillation due to dispersive media.

For instance, the technique of carrying out range rate measurements in a one-way uplink configuration is particularly attractive, especially for the possibility to track from the ground several different S/C simultaneously, travelling in a volume of space included in the ground antenna beamwidth. This could greatly simplify mission operations as, at present, each S/C must be tracked by a different ground antenna at the time, with an obvious increase of mission operations costs (when several ground antennas are available at the same deep space complex, e.g NASA DSN) or severe visibility constraints (when a single ground antenna is available per deep space complex, e.g. ESA ESTRACK).

The conclusions which can be drawn from Table 19 are quite obvious. The error budget, in terms of ADEV, is dominated by the space segment, in particular because of the phase instability introduced by the Ultra Stable Oscillator (USO), that generates the frequency reference on-board. In the absence of a significant improvement in the performance of the on-board frequency systems, one-way systems are not competitive with an analogous two-way system, based on the same assumptions in terms of the ground and space segments technologies. It is worth mentioning that the new oscillator and atomic clock technologies described in [64] that, when combined, could create a master oscillator for use in deep-space navigation, are unfortunately far from being easily available in the next few years.

In light of this, the introduction of a real-time phase compensation system can highly increase the stability of the phase of the on-board frequency reference and reduce the overall error budget for a one-way uplink range-rate link. Considering an enhancement up to 2 order of magnitude, so that the value of the error budget for the USO would be 1,00E-15, the same enhancement would be introduced also in the end-to-end uplink error budget (all other noise sources are fewer than 1,00E-15 @ 1000 seconds of integration time), allowing in this way the range rate uplink configuration.

Furthermore, the low mass and low volume occupied by the compensation circuit allow to introduce the device without a huge increase of the total weight of the spacecraft.

RANGE-RATE ERROR BUDGET	
Type (1-sigma @ 1000 sec, one-way)	Value
SPACE SEGMENT	1,00E-13
S/C electronics (RX Chain)	3,00E-17
Frequency Standard (using USO)	1,00E-13
HGA assembly	4,07E-15
S/C structure	5,00E-16
GROUND SEGMENT	3,06E-15
Frequency Standard (using LITS)	6,00E-16
G/S electronics (TX chain)	1,50E-15
Ground Antenna	2,50E-15
Station Location	6,00E-16
EOP	3,00E-16
Earth Solid Tides	2,50E-16
MEDIA	5,10E-15
Residual plasma (at 90° of SEP)	1,00E-15
Residual troposphere (using MWRs)	5,00E-15
END-TO-END UPLINK OBRAS	1,00E-13

Table 19: Error budget for a one-way uplink range-rate link

6.5.3 Satellite to satellite

Analog considerations can be made concerning radioscience experiments through SSL, also analyzed in OBRAS proposal. In this configuration, two S/C in orbit around the same planet can be used as transmitter and receiver of single- or dual-frequency signal, as shown in Figure 72.

SSL radioscience offers a new perspective on atmospheric measurements which considerably extends the scientific merits of radio occultation experiments with respect to those carried out from the ground. The radio signal emitted by one spacecraft as it disappears behind the planet and its atmosphere is recorded by the other spacecraft, which samples Doppler frequency shift, phase,

polarisation, propagation time and amplitude and allows inferring neutral and ionospheric gas densities as well as neutral pressures and temperatures.

As for uplink configuration, the real-time phase compensation system onboard both S/C could bring to a low final range-rate error budget. With respect to Table 19, the high error introduced by the USO can be largely improved. Moreover, with respect to the classical downlink architecture error budget, this unexplored technique would allow to cancel out completely the error contributions due to the to the media propagation (residual plasma and troposphere). Distinct advantages of SSL radio occultation, for instance the Jupiter atmosphere occultation shown in in Figure 73, measurements include (a) the ability to measure local time sectors normally not sampled from Earth; (b) the ability to measure latitude sectors normally not sampled from Earth; (c) an improved SNR due to the close proximity of emitter and receiver, which allows more accurate density measurements especially far from Earth in the outer solar system and (d) the ability to use radio frequencies that cannot be used for radio occultations measured from Earth due to their attenuation in the Earth's atmosphere.
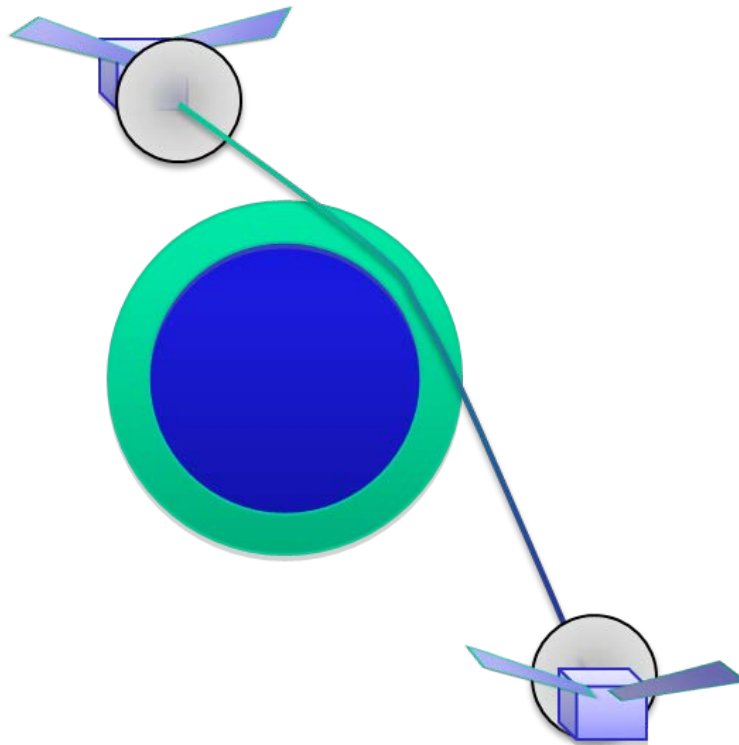
Figure 72: Satellite to satellite link configuration
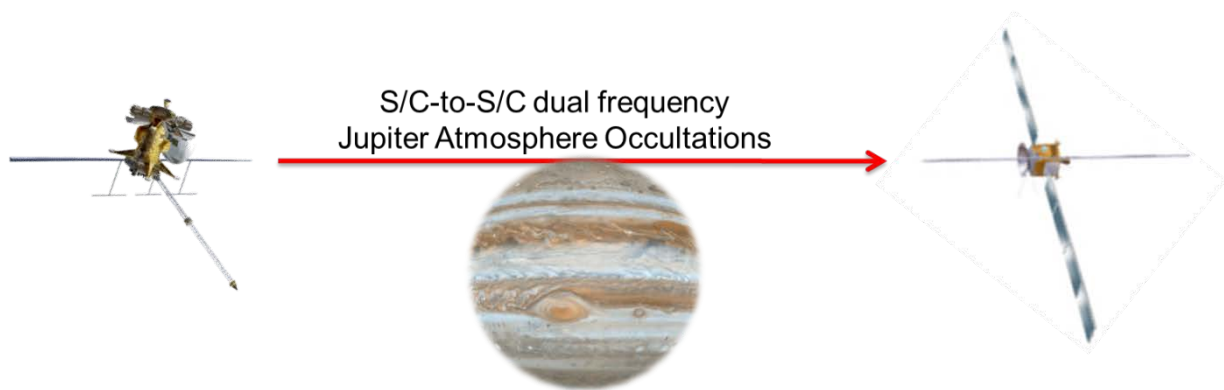
Figure 73: satellite to satellite link for radio science mission

6.5.4 Different frequency bands

Even if the proposed method has been designed and verified at X-band, it can be quickly adjusted for any frequency band (S-, X-, Ka-bands and so on). The only required operation is the change of the operative frequency range of the signal splitter and the mixer, while all the others signal are direct current (DC).

This aspect is particularly interesting related to the Ka frequency band. In the recent years, the trend of both NASA and ESA GS is a transition to higher frequency link with the advantages of wider available bandwidth and higher antenna gain (see appendix 8.2C). Newest ESA DS GS like DSA-2, located in Cebreros-Spain, and the under construction DSA-3, located in Malargue-Argentina, include Ka-band signal chain. Despite of this, in ESA GS at present, there are not liquid cooled 20 KW KA-band HPA. In other words, there are not state of the art HPA with liquid cooling system. In light of this, the application of the proposed solution could bring to obtain lower ADEV value that cannot be obtain in other way.

7 Two antennas arraying tracking with IFMS

This section presents an idea for performing two antennas arraying tracking using ESA tracking stations (ESTRACK) facilities.

The main purpose of this study is to verify the possibility to exploit the Diversity Combiner Equipment (DCE) capability in an array tracking configuration: in the proposed system the two signals fed to the DCE will be the same signal, with the same polarization, received by two different Ground Station (GS) instead of the standard approach where the DCE receives as input the left and right circular polarization of a signal received by a single antenna. So, this method is applicable only for two antennas arraying.

Using two different antennas in an array configuration, in case of antennas with the same aperture size, it would theoretically guarantee an increase of 3 dB of the Signal to Noise Ratio (SNR) with respect to the single dish technique, A simulator has been developed in order to check the behavior of the DCE in the new configuration together with the predicted amount of losses from the theoretical gain of 3 dB. A test campaign has also been performed in ESOC GSRF to demonstrate the possibility to implement this technique in ESA GS.

7.1 Motivation and objective

New ESA deep space missions are always demanding higher stable links, with greater value of SNR allowing higher data rate and better precision in measurement, as shown in . A New Deep Space Antenna (DSA) is going to be built in Malargue (Argentina), after the one in New Norcia (Australia) and Cebreros (Spain), in order to increase the number of GS able to track deep space mission spacecrafts (S/C). GS are equipped with state-of-the-art 35-m parabolic dish antenna and 20 KW High Power Amplifier (HPA). A future increase of the antenna dimension or the HPA output power for an enhancement of the GS Equivalent Isotropic Radiated Power (EIRP) is not without drawbacks: on one side, 70–m parabolic antenna is affected by additive losses due to mechanical errors or deformation of the structure; on the other side, 20 KW Klystron HPA (KPA) demands very expensive cooling system, implying a large amount of maintenance, to eliminate the considerable amount of phase instability that is generated because of the high temperature the device reaches during operation.
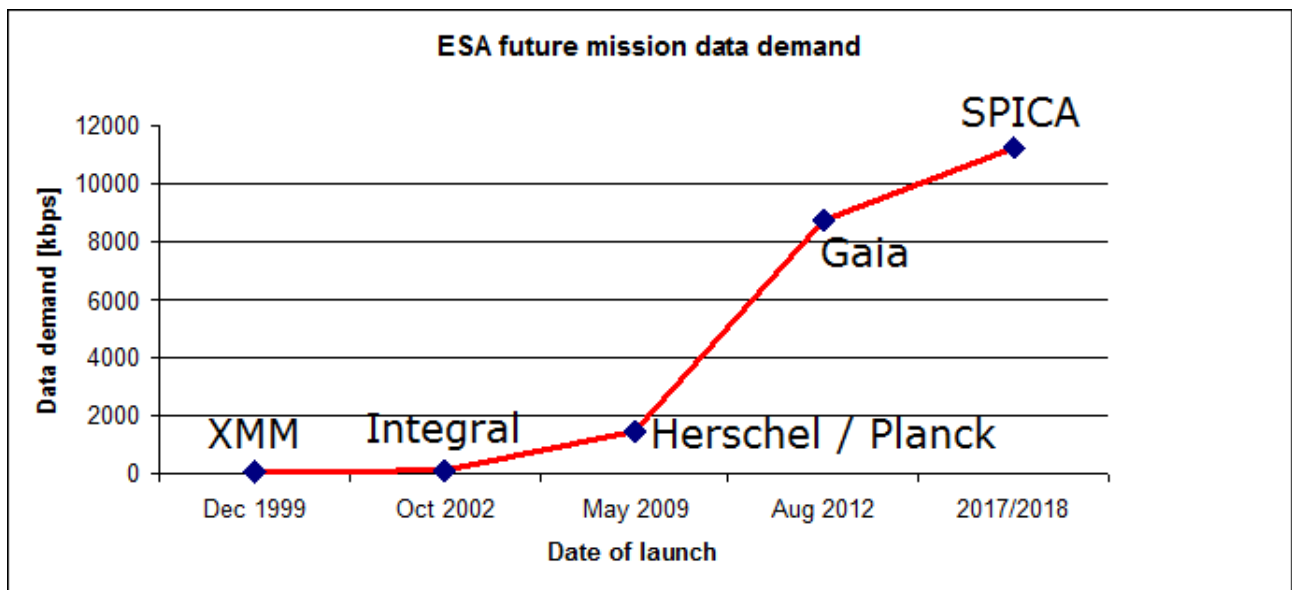
Table 20: ESA future mission data demand
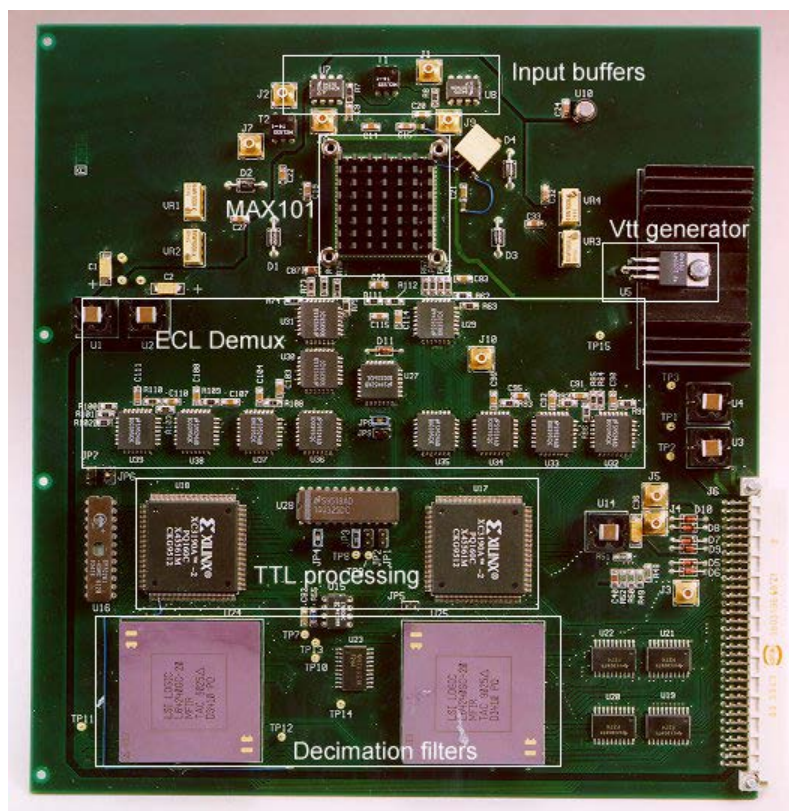
Figure 74: DCE electronic board

Figure 75: IFMS equipment

The proposed solution for an increase of the final SNR of the downlink is the realization of a tracking array configuration: a viable solution could be represented by using at the same time two antennas of the same site. This configuration allows to take advantage of the short baseline between the antennas, the common Main Equipment Room (MER) and Intermediate Frequency and Modem System (IFMS) (shown in Figure 74) containing the DCE that can be used for combining the two received signals (shown in Figure 75).

The main objective of this study is to verify the possibility to take advantage of the DCE capability for performing array tracking with two antennas. The DCE is currently part of the GS IFMS, allowing the combination of the right and left circular polarization of a signal received by an antenna. The same device can be used for the combination of two different signals representing the same wave received with two different antennas, and with the same circular polarization.
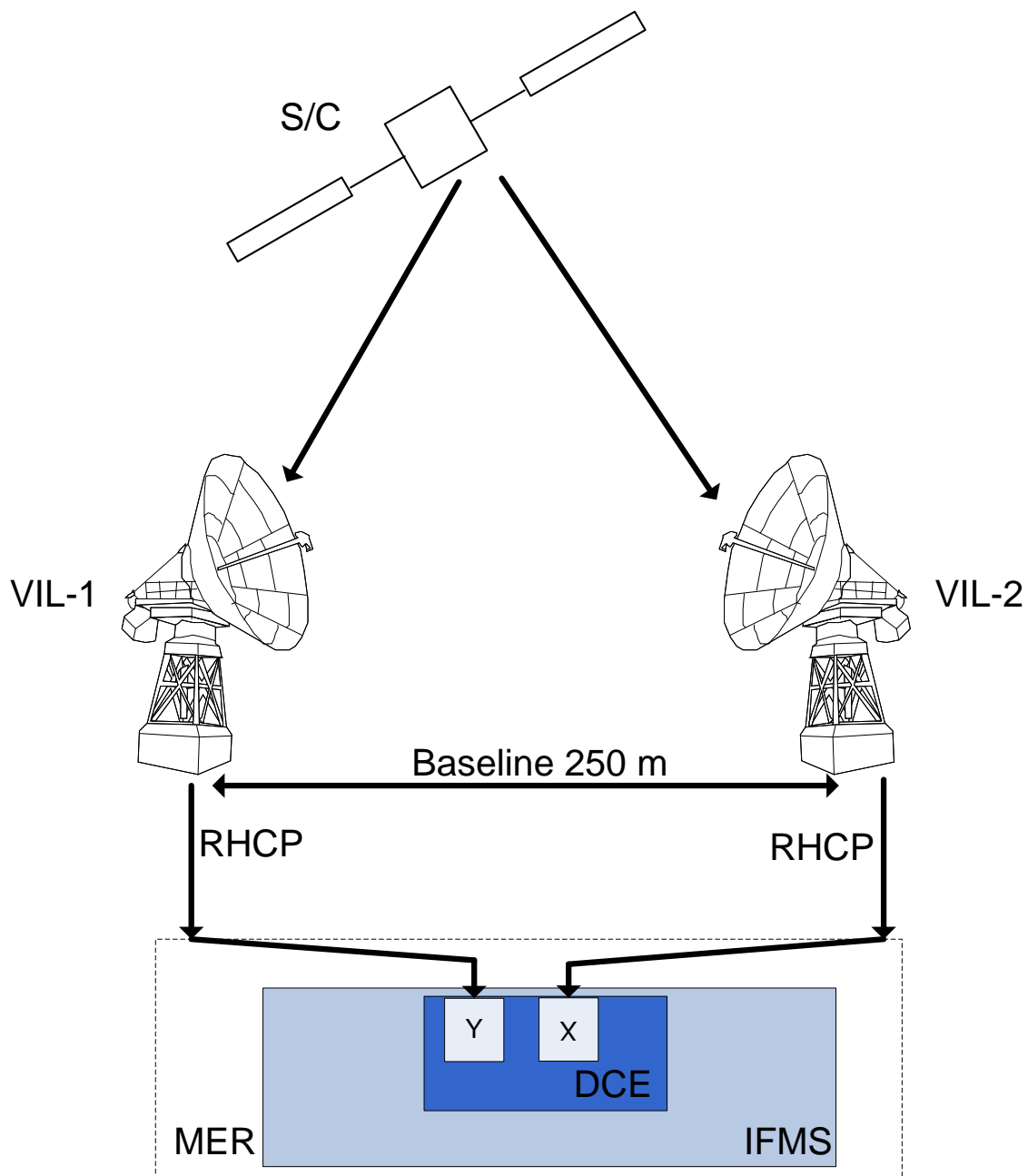
Figure 76: Array tracking technique using VIL-1 and VIL-2

The case study is represented by a possible array tracking architecture using VIL-1 and VIL-2, two of the three antennas built at the ESA Villafranca (Spain) facility. This is a perfect example of ESA facility that can be used in an array downlink configuration. Figure 76 shows the array configuration taken into account: the main polarization (RHCP in the figure) received by two antennas pointing the same S/C are connected to the DCE input channels. Moreover, in this configuration the short baseline between the two antennas and the possibility to use the same IFMS and DCE are important advantages.

In order to verify the feasibility of the aforementioned architecture, two steps have been performed: first of all, a simulator of the DCE has been developed, in order to understand the limitation and the actual behavior of the device; then a test campaign have been performed in ESOC GSRF, using an IFMS and DCE and simulating S/C downlink signal received by different antennas.

Future steps of the study consist of more detailed test campaigns considering ranging test for the delay calibration of the two channels and differential Doppler effect between the two antennas that can affect the final result of the antenna arraying.

7.2   Theory

This Section is intended to explain basic DCE concept and capability. For a more complete understanding of the ESA GS architecture, an overview of the IFMS architecture and functionality is added in appendix 8.2B.

7.2.1 Scenario

When a S/C establishes a downlink using circular polarization, in an ideal scenario all of the transmitted power would be confined to the nominal polarization. Actually, a number of different factors (e. g. partial failure of the S/C attitude control of the antenna) determines a radiation of some part of the power in the orthogonal polarization. A diversity combiner id required to optimize the received SNR by combining the two polarization channels before demodulation is performed. In this way depolarization losses are minimized.

Combiner requirements are as follows:

- Estimation of the phase difference between LHCP and RHCP carriers in order to aligned the signals before combination technique;
- Estimation of the relative signal levels so that it can set the combiner tap gains to achieve maximal ratio combination.

Although the signal combination can be done at any step of the receive chain, the most practical solution is determined by the need to correlate signals and in particular the remnant carrier. In remnant carrier configuration the final configuration leads to an arrangement where the diversity combiner function is put together with the remnant carrier extraction before the demodulator.

7.2.2 Signal combining

The ESTRACK IFMS system implements a receive chain for both the right and left-hand circular polarization antenna ports. Whilst S/C radiate nominally in one polarization it is possible that power is distributed between the two orthogonal polarizations as seen by the ground station antenna. A combiner is required for combining the two orthogonal channels in order to maximize the signal-to-noise ratio at its output.

In general, the signals available at the output of the LHCP and RHCP circularly polarized channels of the DCE may be written as L(t) and R(t), thus:

Eq. (32)
$$L(t) = A \times \cos\psi \times m(t) + n_L(t)$$

Eq. (33)
$$R(t) = A \times \sin\psi \times m(t) \times G \times e^{j\vartheta} + n_R(t)$$

where m(t) is the (complex) signal modulation waveform, $n_L(t)$ and $n_R(t)$ are the (complex) noise waveforms, A is the signal amplitude, ψ is the polarization angle, θ the phases difference between LHCP and RH signals, G is the gain of the RHCP receiver chain relative to the LHCP receiver chain.

The output of the combiner, C(t), is given by:

$$C(t) = \cos\tilde{\psi} \times L(t) + \frac{\sin\tilde{\psi}}{\tilde{G}} \times e^{-j\tilde{\vartheta}} \times R(t)$$

Eq. (34)

where $\tilde{\psi}$, $\tilde{G}$ and $\tilde{\vartheta}$ are estimate values of ψ, G and θ respectively, available in the receiver.

If the estimated parameters are known exactly the DCE output is:

Eq. (35)
$$C(t) = A \times m(t) + \cos\psi \times n_L(t) + \sin\psi \times e^{-j\vartheta} \times n_R(t)$$

allowing for the perfect reconstruction of the modulated signal SNR without polarization losses.

As mentioned in the previous Section, this device could be useful for the implementation of an array tracking technique: instead of combining both circular polarizations of a signal received by a

single antenna, we can receive the same signal with two different GS and combine the two received signal, with a theoretical gain of +3 dB with respect to the single antenna reception.

The proposed idea is represented in Figure 76. The received signals from VIL-1 and VIL-2 antennas are fed to the MER, and used as input of the DCE of the IFMS. In this scenario, the main polarization, that is the polarization with the greater amount of power, received from each antenna is connected to the DCE input channels (for instance RHCP in Figure 76).

An important consequence when performing antenna array tracking tests is that DCE input signals L(t) and R(t) may be written as:

Eq. (36)
$$L(t) = A \times \cos\psi \times m(t) + n_L(t)$$

Eq. (37)
$$R(t) = A \times \cos\psi \times m(t) \times G \times e^{j\vartheta} + n_R(t)$$

In other words, the trigonometric function depending on the polarization angle does not determine a difference in the two signals amplitude.

7.2.3 Combiner architecture

In order to combine the two input channels, the combiner must estimates the polarization angle, the relative carrier phase and the channel gains.

The carrier in each polarization channel is individually phase-locked to a common reference and a coherent carrier level estimate is used to set the gain weights. This technique could also be used for suppressed carrier signals but it would require two completely separate demodulator chains for the two polarizations followed by soft combining of the resultant outputs.

To track $\tilde{\psi}$ and $\tilde{\vartheta}$ the basic requirement is for the best possible estimates of the signals in *L(t)* and *R(t)*. If data is available for a time T which is large compared with the symbol duration then *L(t)* and *R(t)* contain many independent samples. For the ESTRACK system the performance of a maximal ratio combiner is required. To optimize the SNR the samples should be combined with a weight proportional to the rms signal and inversely proportional to the noise power. We initially assume that the noise powers in *L(t)* and *R(t)* have been equalized. We also assume that the receivers provide a matched filter for the signal. Then the optimum SNR is given by the complex quantities:

Eq. (38)

$$AL = \int_0^T L(t) \times \tilde{m}*(t)dt$$

Eq. (39)

$$AR = \int_0^T R(t) \times \tilde{m}*(t)dt$$

The quantity $\tilde{m}(t)$ is the demodulator output, which is assumed to be substantially correct. The demodulator will also complete the carrier tracking process, and it is assumed that any carrier offset in $L(t)$ and $R(t)$ is removed by $\tilde{m}*(t)$. However, there may be a constant phase offset between $\tilde{m}(t)$ and $\tilde{m}*(t)$ due to phase ambiguities in the demodulation process. It may also be noted that the quantities AL and AR are so-called *sufficient statistics* for the presence of a signal $\tilde{m}(t)$ in $L(t)$ and $R(t)$. A sufficient statistic contains all the information in the data samples about the parameter being estimated, in this case the amplitude and phase of $\tilde{m}(t)$. The expected values of AL and AR are:

Eq. (40)

$$< AL >= A \times \cos\psi \times < m(t) \times \hat{m}(t) > + n_{AL}$$

Eq. (41)

$$< AR >= A \times \sin\psi \times G \times e^{j\vartheta\times} < m(t) \times \hat{m}(t) > + n_{AR}$$

The noise voltages n_{AL} and n_{AR} will have variances $2\sigma^2{}_{AL}$ and $2\sigma^2{}_{AR}$ which are much less than $2\sigma^2$ due to the averaging process. However, this noise should be taken into account when estimating the signals. Thus it can be written:

Eq. (42)

$$| \overline{AL} |^2 = | A |^2 \times \cos^2\psi \times (\overline{m^2})^2 + 2\sigma^2{}_{AL}$$

and as a consequence:

$$| A | \times \cos\psi \times \overline{m}^2 = \sqrt{| AL |^2 - 2\sigma^2{}_{AL}}$$

Eq. (43)

$$| A | \times \sin\psi \times G \times \overline{m}^2 = \sqrt{| AR |^2 - 2\sigma^2{}_{AR}}$$

Eq. (44)

The estimate of ψ and ϑ derived from AR and AR are:

Eq. (45)
$$\psi_{est} = \tan^{-1}\left\{ \frac{\sqrt{|AR|^2 - 2\sigma^2_{AR}}}{\tilde{G}\sqrt{|AL|^2 - 2\sigma^2_{AL}}} \right\}$$

Eq. (46)
$$\vartheta_{est} = \arg(AR) - \arg(AL)$$

Finally, the value of $\tilde{\psi}$ and $\tilde{\vartheta}$ will be given by an averaging process such as:

Eq. (47)
$$\tilde{\psi}_{new} = (1-\lambda)\times\tilde{\psi}_{old} + \lambda\times\psi_{est}$$

Eq. (48)
$$\tilde{\vartheta}_{new} = (1-\lambda)\times\tilde{\vartheta}_{old} + \lambda\times\vartheta_{est}$$

The combiner has two complex input streams clocked at the decimator output rate. The block diagram can be divided into two sections, as shown in Figure 77: the high-speed signal path and the lower speed estimator path.

The high speed processing consists of the phase-correction complex multiply and gain weighting followed by an addition. The combined output stream is clocked out at the input rate for further processing by the selected demodulator.

The estimator path consists of a programmable digital delay which can be implemented using fast static RAM. This delay is required in order to align the demodulator signal estimates with the incoming samples. The complex multipliers which remove the modulation from the sample stream are followed by an accumulator which integrates the results over a programmable time period. The sample rate at the output of this integrator is sufficiently low that subsequent processing can be performed using a DSP. The estimator update rates can be programmed to give fast update rates for near-earth missions and slow rates for deep-space missions.

Whilst the combiner itself is relatively straightforward it requires that each demodulator in the system is capable of regenerating an estimate of the original modulation waveform. The fidelity of this estimate must affect the accuracy of the combiner parameter estimates and thus the overall performance of the combiner.

There is not enough information in *AL* and *AR* to update the estimate of $\tilde{G}$. One possibility is that *G* is found by measuring out-of-band noise in each of the two channels. Assuming that the noise in each channel is white it would be possible to measure the noise power and a narrow band away from any signal components and then adjust the gains accordingly. An alternative would be to use a

calibration signal prior to the pass. This signal would be introduced at the front-end and could be used to calibrate both the relative gain and the relative phase of the two channels.
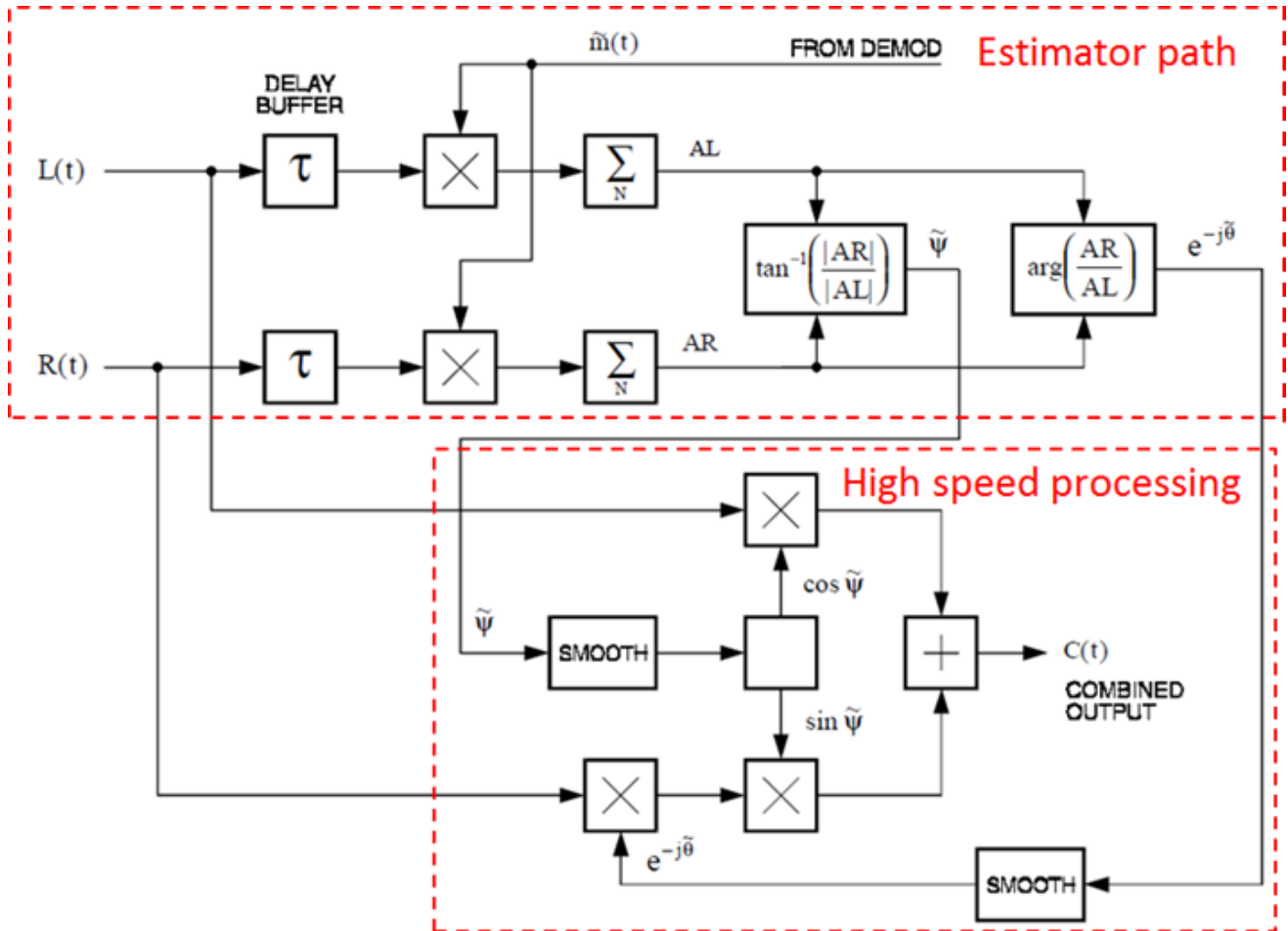

Figure 77: Combiner structure

7.3   Simulation

A simulation model of the DCE has been developed in Matlab/Simulink environment, with the purpose of simulate the DCE behaviour when used for array tracking operation, bypassing the lack of previous data to compare our test results. This software can be used to simulate two different DCE behaviours: the DCE standard approach, with two orthogonal circular polarization of the same signal as input; or the proposed approach, in an array configuration.

In the first configuration the output consists of the SNR attenuation introduced by the non-perfect estimation of the signal parameters, with respect to the maximum available SNR defined by the sum of the two orthogonal signal. This analysis has been largely performed and described in [65] and has been use as reference for determine the simulator correct behaviour.

The second configuration of the simulator, the most important from the point of view of this study, calculates the gain that DCE can provide in array tracking configuration, with respect to the single signal SNR. In other words, considering that in theory the DCE should be provide a gain of 3 dB, the simulator determine the amount of gain that is lost because of estimation errors of the signal parameters.

The first step in the software development was to consider a simple carrier as input signal. This is the simplest case and is also the first test that has been performed in ESOC GSRF.

Then, a modulated signal has been taken into account. Cluster mission has been considered as case study, and in particular a telemetry signal with the same characteristic of the one generated by this S/C was generated as simulator input (see [68] for reference).

7.3.1   Architecture

The Simulink block scheme of the simulator is shown in Figure 78. The *DCE input signal* block generates directly 70 MHz signals, because down conversion from the downlink frequency to the IFMS input 70 MHz are not considered. Output signals are the VIL-1 and VIL-2 received signal (see Eq. (32) and (33) for reference), with uncorrelated noise because of the different receiver equipment. Moreover, the m(t) signal represents the modulation waveform $\widetilde{m}(t)$, a demodulator output which is assumed to be substantially correct.

The three generated signals are then used by the estimator path, as indicated in Figure 77: the Sufficient statistics block calculates the quantities AR and AL, as explained in Eq. (40) and (41) (the remaining two output of the block are just a replica of the waveform generated by the first

block); after that, the *Estimator* block uses the sufficient statistics in order to estimate the value of $\tilde{\psi}$ and $\tilde{\vartheta}$ (see Eq. (45) and (46) for reference) whilst the *Smooth filter Theta* and *Smooth filter Psi* are added in order to avoid errors in case of a phase jump of π radians that can affect the estimated quantities.

The high speed processing path (see Figure 77 for reference) is represented by the *Combiner* block performing phase correction, gain weighting and addition of the signals. The output of this block represents the combined signal and a comparison between the input and output SNR give us the final simulator output data, as described in the previous Section.

Figure 78: simulator block scheme

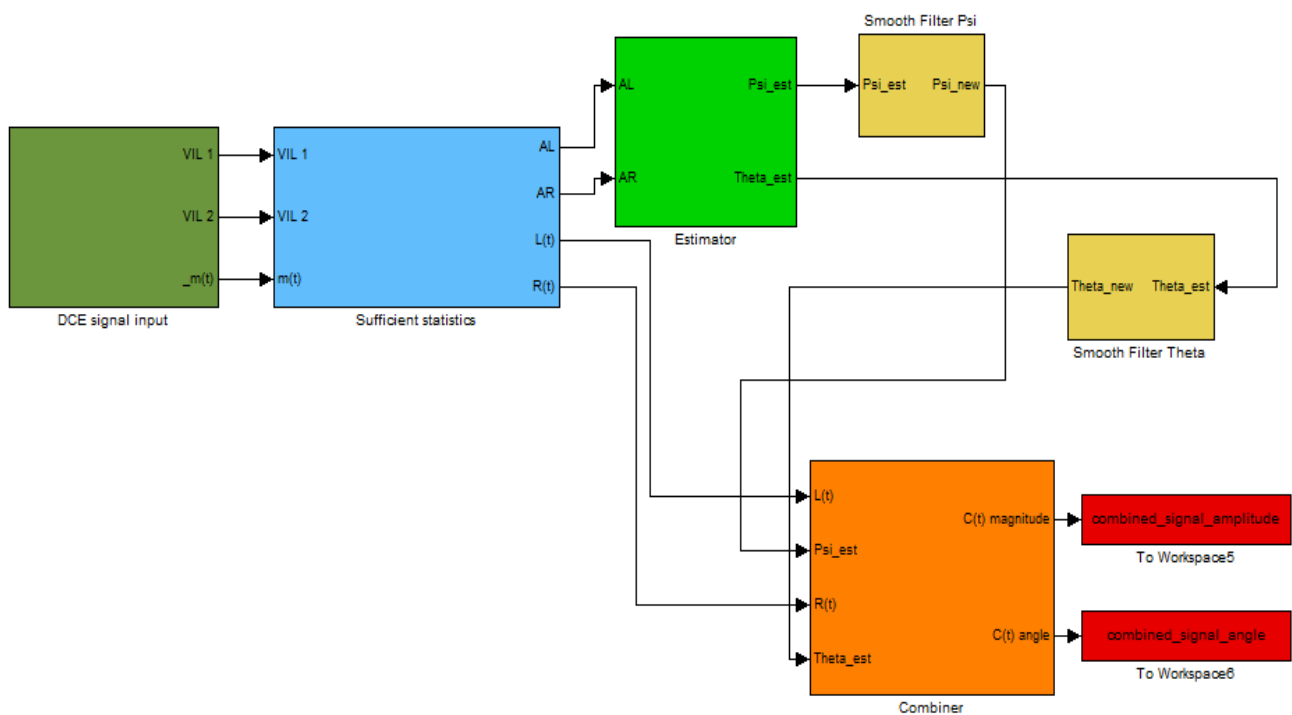A list of different parameters can be chosen by the user, in order to simulate different operational situation:

- The value of the depolarization angle φ;
- The value of the phase difference between the two signals;
- The value of the smooth filter parameter, as described in Eq. (47) and (48);
- The SNR value of the input signal;
- The operational mode (standard DCE or array tracking).

124

The two simulators for carrier-only and modulated signal have a very similar architecture: in fact, the only block changing its behaviour is the *DCE input signal*, that will generate a phase modulated waveform instead of a carrier.

7.3.2 User interface

Two different versions of the simulator have been developed, considering different input signals:

- Carrier-only: this simplified version of the simulator generates two sinusoidal carriers to simulate the antennas received signals. It represents the first approach to the array tracking study;

- Telemetry signal: this more realistic version of the two antennas array tracking generates telemetry signals. As reference, the Cluster mission downlink modulation has been taken into account, where an SP-L coded data directly modulates the carrier.

With respect to the overall architecture, between the two versions of the simulator only the first block generating the DCE input signal is different. The DCE architecture remains unaltered. The parameters the user can set are listed in Table 21 sketched hereafter:

PARAMETER	UNIT	DESCRIPTION
Configuration		This parameter lets the user select between the two DCE configurations. Indicating 1 the user chooses the usual configuration with the orthogonal polarization as inputs; setting 2 the user chooses the array configuration. Default value = 1
Carrier Frequency	MHz	Frequency of the carrier. It should be set to 70 MHz in order to simulate the frequency at the DCE input channel. Default value = 70
Depolarization angle	deg	Angle that indicates the part of the total power of the received signal that is split on the main and on the orthogonal polarization (see Eq. 18 and Eq. 19 for reference). During simulation of the array configuration this value does not influence the final results and is always estimated as an angle of 45° by the DCE. Default value = 0
Phase difference	deg	Angle that indicates the static phase difference between the two DCE input signals. Default value = 20
Equalization	dB	This value gives the user the possibility to insert a difference on the

impairment		power of the two DCE input signals. The left channel is always considered with the maximum available power, while the right channel has a power equal to the difference between the left channel power (in dB) and this parameter. Default value = 0
Smooth filter gain		This value indicates the gain of the smooth filter introduced in order to avoid higher variation of estimated parameters. It should be in the range [0:1]. The default value is 0.99 and should not be changed by the user. Default value = 0.99
SNR min value	dBm	This is the minimum value of the SNR that is taken into account during simulation. Default value = 10
SNR max value	dBm	This is the maximum value of the SNR that is taken into account during simulation. Default value = 80

Table 21: User parameters

7.3.3 Simulator output

The meaning of the output of the simulator is related to the configuration in which the simulator itself is set.

When the user sets the configuration parameters to '1', that is he sets the simulator in the usual configuration with the two orthogonal polarization of the signal connected to the DCE input channels, the final output of the simulator is the difference between the sum of the power of the two input signals (the two orthogonal polarization) and the power of the DCE output combined signal. So, a value of 0 dB means that the DCE output has a power equal to the sum of the power of the inputs and that the DCE has perfectly combined the two signals. A negative value indicates the amount of loss in the combining process.

On the other hand, when the user sets the configuration parameters to '2', that is he sets the simulator in the array configuration, the final output of the simulator is the SNR gain that the DCE gives at the output, combining the main polarization of the two signals received with the two different antennas. In this case, a value of 3 dB means that the maximum theoretical SNR gain is reached, while a value lower than 3 dB indicates that the DCE is not able to perfectly combine the two input signals.

The output is calculated for each integer value of the SNR between the input parameters SNR min value and SNR max value and saved in the variable gain that the user can find in the workspace.

Moreover, a plot of the variable gain varying the SNR of the input channels is also produced. Figure 79 and Figure 80 show the output graph for the usual and the array configuration of the DCE respectively.
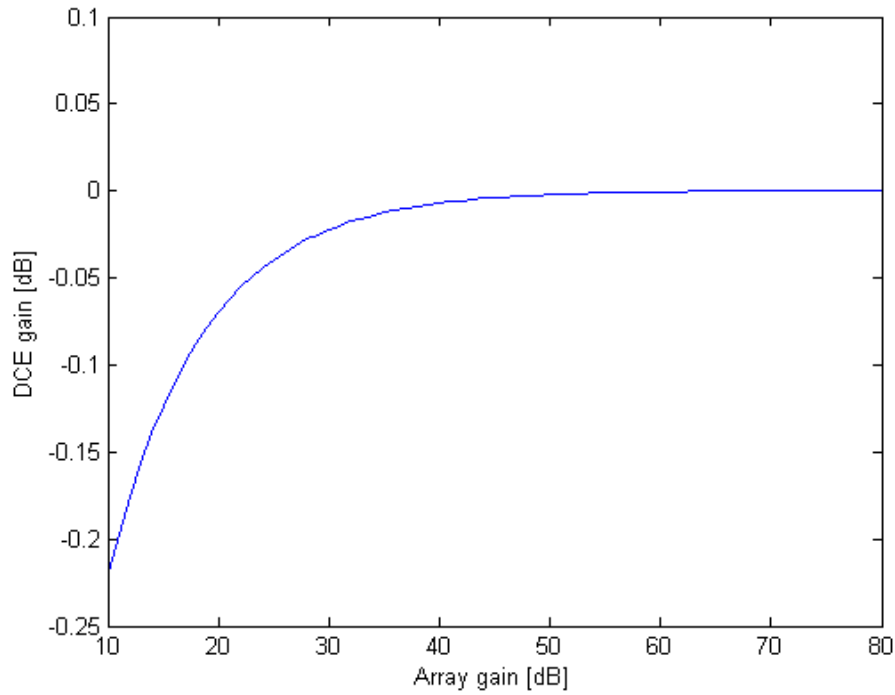

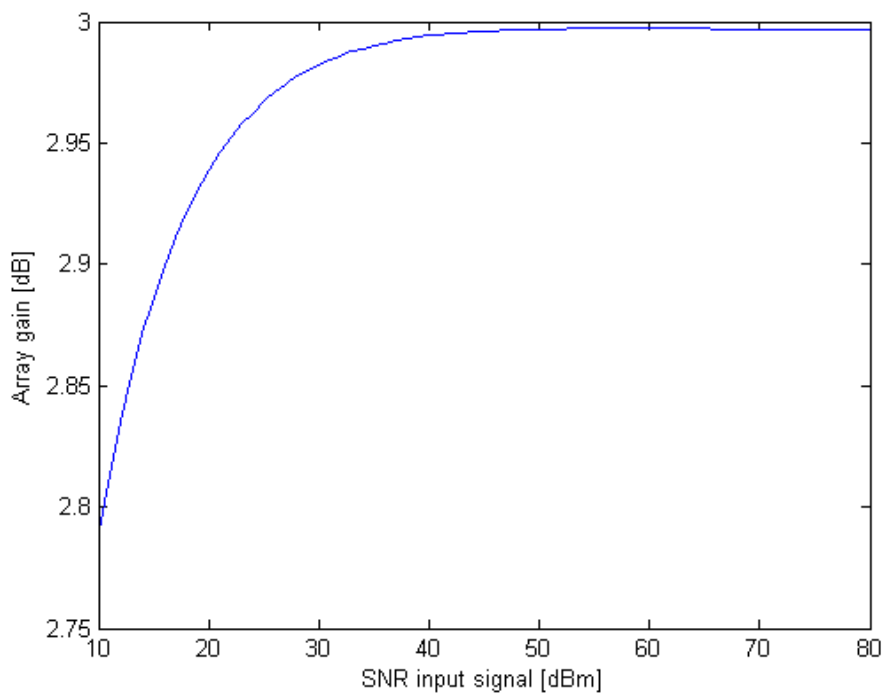**Figure 79: orthogonal polarization configuration SNR output gain**

Figure 80: array configuration SNR output gain

7.3.4 Simulation results

In this Section the results of the simulated array tracking using the DCE are presented. The simulator is able to generate as input signal a sinusoidal carrier or a telemetry signal. However, from an analysis of the results, it can be noticed that the telemetry modulation does not introduce higher amount of gain loss with respect to the carrier-only input, so the results of this Section are referred to the telemetry simulation only.

Particular attention has been paid on two fundamental aspects of the array tracking configuration: the different phase delay, that can be inserted on the signal by the GS baseline and cables, and a non-perfect equalization of the input signals power.

Figure 81 shows the array tracking gain considering different phase delay between the two input signals, i.e. the angle θ of Eq.23. For perfectly aligned signal a gain very close to the theoretical gain was generated. Different values of phase difference, and in particular also the case of input signal in quadrature, do not introduce relevant loss of the final DCE gain.

Figure 82 shows the gain obtained considering different values of power for the two DCE inputs. Four cases has been considered, with a step of 0.5 dB of power difference. AS can be noticed, the higher the difference on input power the higher the loss of the total gain. With respect to the perfect equalized situation, a difference of 0.5 dB introduces a loss of about 0.2 dB, a difference of 1 dB introduces a loss of 0.5 dB, a loss of about 0.6 dB is obtained with a power difference of 1.5 dB while for the worst case taken into account of 2 dB of difference a maximum gain of 2.1 dB has been obtained, with a total loss of 0.9 dB.

All these operational situations were simulated during the test campaign performed in ESOC GSRF and the results have been used as reference values for measurement.
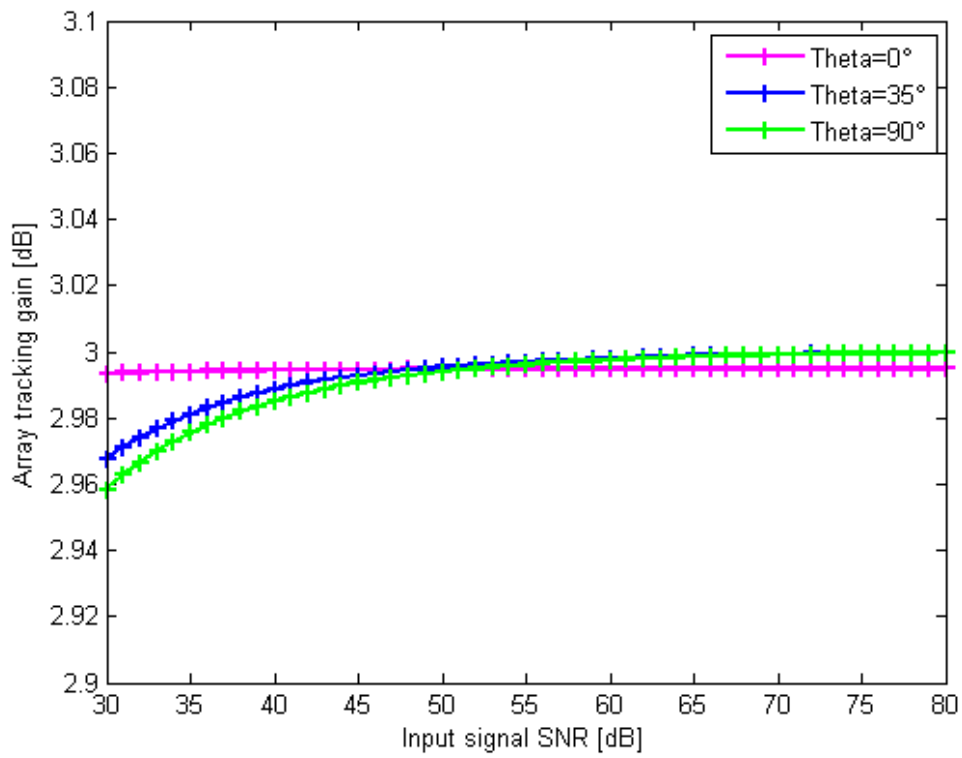
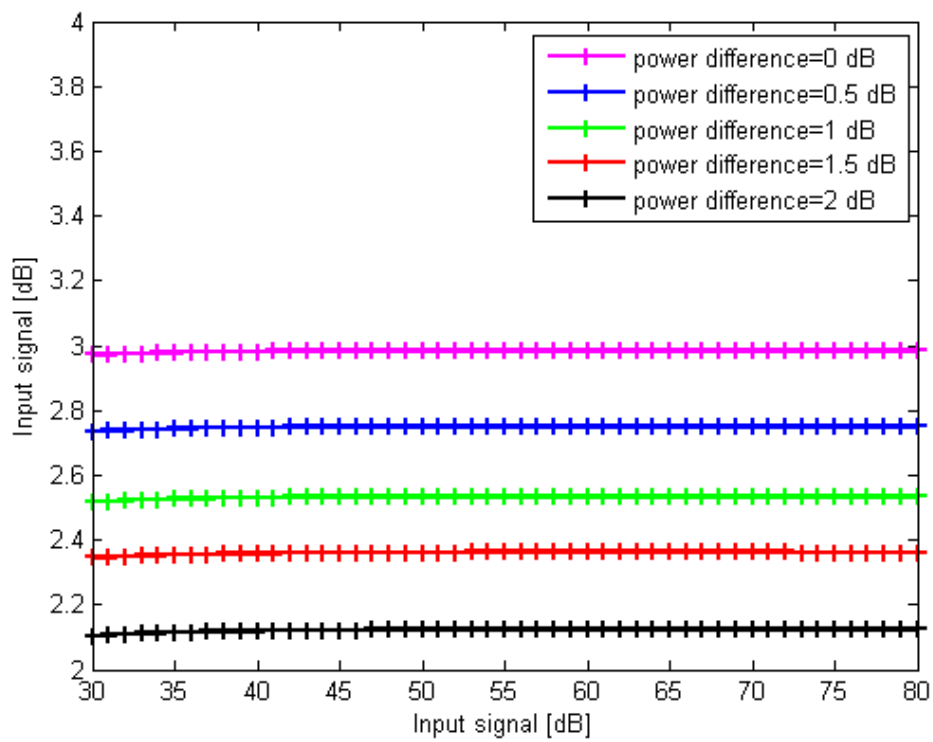**Figure 81: Simulated array tracking gain for different phase delay**

Figure 82: Simulated array tracking gain for different input power difference

7.3.5 Criticalities

Analysing simulation result, some problems in the array tracking configuration by mean of the DCE were pointed out and taken into account for the subsequent test in GSRF.

As a matter of fact, as a consequence of the requirement the DCE was designed for, this device expected at the input two signals representing the two orthogonal circular polarization of the received signal, in which the transmitted power is split following the trigonometric rules explained in Eq. 18 and Eq. 19. Then, the algorithm used for the estimation of the polarization angle works on the assumption that we have such input signals. Actually, during array tracking tests we have input signal as in Eq. 22 and Eq. 23. This aspect is analysed in Section 7.3.5.1.

Moreover, a phase change of one of the input is necessary in order to simulate the phase change due to the baseline between VIL-1 and VIL-2. We can assume that one signal has phase equal to 0° whilst the other one is phase shifted of θ°. This aspect is analysed in Section 7.3.5.2.

7.3.5.1 Signal power

Expecting input signals as in Eq.(32) and (33), the DCE implements an algorithm assuming that the total power of the transmitted signal is split on the two polarizations following a trigonometric distribution. Therefore, at first it calculates the so-called sufficient statistic *AL* and *AR*, containing information on the sine and the cosine of the depolarization angle ψ, and then it applies the trigonometric function **Errore. Il segnalibro non è definito.**$\tan^{-1}$ in order to detect an estimated value of the angle.

If we consider Eq. (36) and (37) it is easy to understand that whatever depolarization angle we have, the DCE estimate value of the angle will always be $\pi/4$. However, the estimate of the polarization angle is used by the DCE just to assign a coefficient of importance to the signals: the higher the power, the more important the signal information.

Simulation results have pointed out that in order to have the maximum gain from the combined signal is important to have two input signals with an equalized power. A difference in signals power affects the total gain. This is confirmed by the test campaign results described in Section 7.4.2.

7.3.5.2 Signal phase shift

In an array tracking operation with VIL-1 and VIL-2 in the ESTRACK facility of Villafranca, signals will be received with a phase delay due to different distance between the S/C and each

antenna and cables of different length between each antenna and the MER (see Figure 76 for reference). So the two input signal of the DCE can be written as:

Eq. (49)
$$L(t) = A \times \cos\psi \times m(t) \times e^{j\alpha} + n_L(t)$$

Eq. (50)
$$R(t) = A \times \sin\psi \times m(t) \times G \times e^{j\beta} + n_R(t)$$

where α and β represents the phases of LHCP and RHCP signals. As the phase of the signal is not a deterministic value but is always related to the another signal, we can replace the two phases α and β with phase difference θ and obtain the expression of Eq. (32) and (33).

After these consideration, it is clear that for testing the array tracking technique it is necessary to shift the phase of one DCE input signal of a value of θ degrees in order to reproduce the phase shift introduced by the aforementioned array architecture.

7.4   Test campaign

The test campaign performed in ESOC GSRF has been divided in three different steps, in order to achieve a complete behavioural description of the DCE. The main output parameters obtained during tests are:

- DCE gain measurement using a sinusoidal carrier as input;
- DCE gain measurement using S/C downlink telemetry signal as input ;
- BER improvements using S/C telemetry signal as input.

DCE gain measurement using a sinusoidal carrier: this is the simpler case that has been considered. The actual improvement of SNR at the output of the DCE has been measured, using a sinusoidal carrier as IFMS input signals.

DCE gain measurement using a S/C downlink telemetry signal: the actual improvement of SNR at the output of the DCE has been measured, using a S/C downlink telemetry signal as input. VEX1 has been chosen as reference S/C set with an external Telemetry clock of 262144 Hz and an asynchronous symbol rate of 5.

BER improvements using S/C telemetry signal: the improvement in terms of BER of a telemetry signal thanks to the gain added by the combiner has been measured. The same telemetry signal of the previous measurement set was used.

The theoretical gain that is expected at the DCE output is +3 dB. This value represents the maximum gain that is achievable using an array of two antennas without error in the estimate process. An error in the determination of parameters shown in Eq. (34), will lead to a reduction of the total gain. Moreover, the higher the SNR of the input signal of the DCE, the lower the error on the determination of the parameters and, as a consequence, the lower the gain reduction.

7.4.1 Setup

All the measurements have been performed at ESOC GSRF. Figure 83 shows the measurement setup block scheme. An 8.4 GHz signal generator has been used for simulating the two received signals, by mean of a splitter. On one channel a phase shifter has been inserted, to simulate the signal phase delay introduced by the antenna baseline and the different signal path on the antennas of the array. Then, the two signals are connected to a common X-band to L-band down-converter with two independent channels, followed by a second L-band down-converter in order to obtain 70 MHz input signals for the IFMS. At this intermediate frequency two independent noise sources are added for reproducing the uncorrelated receiver noise. At last, the two signals are directly connected to the X and Y input of the IFMS.

Signal parameters such as the carrier level, the polarization angle and the phase difference have been observed through dedicated IFMS interface software, recorded during 300 seconds measurements and elaborated in post-processing in Matlab environment.

An important phase of the test setup has been represented by the power calibration. The purpose of this procedure is to equalize the two signals connected to the IFMS inputs in order to have the same power level at both ports. Being fixed the signal generator output power, with reference to the setup of Figure 83 it is possible to use the independent noise generators and the pin diode to equalize the signals.

A limitation of the chain measurement has been represented by the phase shifter. This device has been inserted for simulate the phase delay introduce by the antennas. Unfortunately, different phase shifts introduce different attenuation values on the signal. With respect to the nominal attenuation introduced with a phase shift of 0°, the measured attenuation range of values is ± 0.5 dB. The power variation has been compensated with the step attenuator, which allows for step of 1 dB.

At last, the differential Doppler effect that can be created because of the relative motion between the S/C and each antenna has been neglected during this first test campaign.
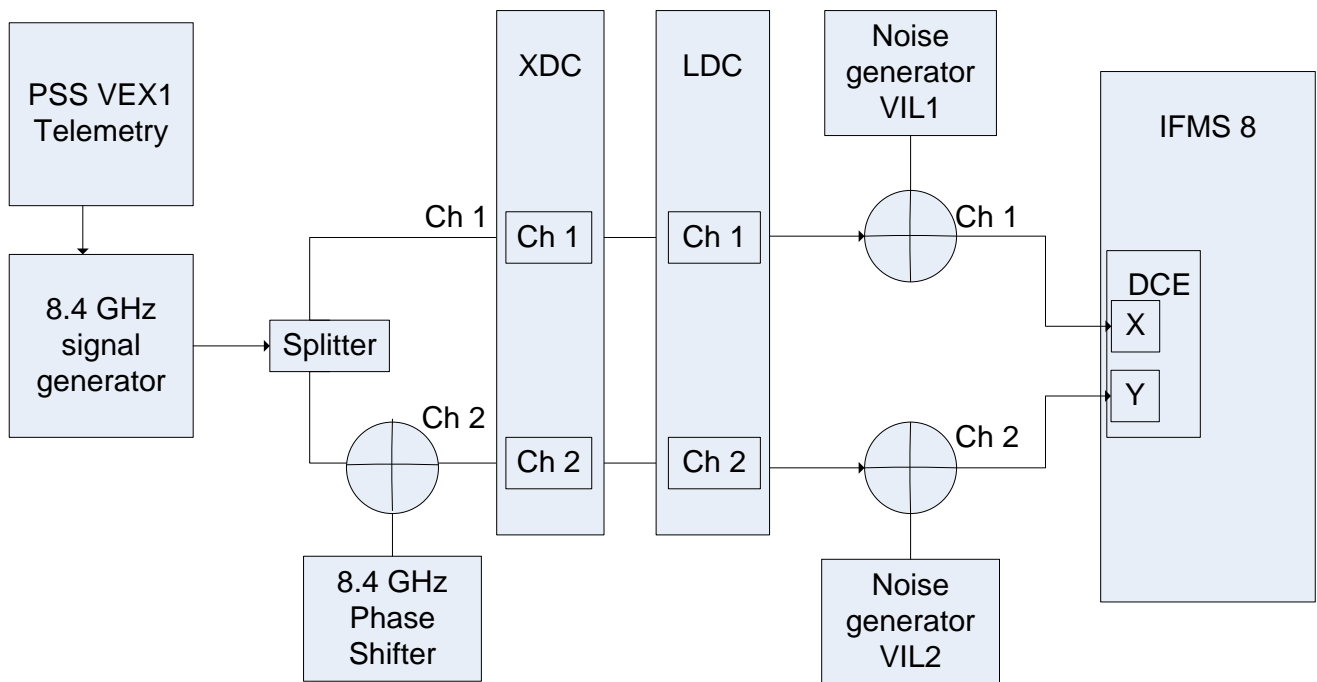
Figure 83: Measurements setup block scheme

7.4.2 Results

Two different cases of power level were simulated during the test campaign. The first measurement set has been performed with an SNR level of the DCE input channels equal to 75 dBm; a second measurement set has been performed considering a worst case with a final SNR level at the DCE input channels equal to 55 dBm.

In detail, the level plan of the measurement setup shown in Figure 83 is here reported:

- Signal generator: the signal generator output power was set at -50 dBm during the first set of measurement (best case) and -70 dBm during the second set of measurement (worst case).

- DCE input channels: the main signal is split in two different channels in order to simulate the two different antennas. Each path introduces a different attenuation on the signal. The objective of the initial calibration was to have an equal at the two DCE input port. In particular, for the best case a power of 45 dBm was set for the carrier while for the worst case a power of 65 dBm was set. In order to compensate all the attenuations introduced by cables, splitter and phase shifter a step attenuator, with a step of 1 dB, has been used on each channel. Moreover, a fine calibration has been performed acting on the down-converter gain.

- Level noise: a different noise generator was introduced on each channel in order to simulate uncorrelated signal on the two path. A level of 120 dBHz has been introduced on each channel in order to obtain the final SNR input level of 75 dBm (best case) and 55 dBm (worst case).

The equalization impairment has been simulated using the step attenuator on one channel. The same device has been used also to compensate the different attenuation introduced by the phase shifter, that was not static but changed with the phase shifting.

During the SER measurement the same chain with the same level plan has been used. The step attenuator was used on both channel in order to obtain different value of Es/No at the DCE input channel. Test results can be compared with the simulated results shown in Figure 81 and Figure 82 for the same value of SNR.

7.4.2.1 Carrier only

Different tests have been performed considering a large number of operational situation. First of all, the combiner gain for different phase shift has been measured. Then, the same data has been collected introducing a power difference between the two IFMS inputs. At last, a series of measurement have been performed changing basic DCE parameters, such as the correlation bandwidth and the estimation mode.

At a preliminary analysis, the most important criticality for performing array tracking with IFMS consists of the phase delay of the two input signals. In order to combine signals an accurately time-align prior combination is necessary. According to [66] and [67], the IFMS provides an input signal delay adjustment of ±25 ns on each input channel. So, the first step of the test campaign was focused on the analysis of the gain in different phase delay (θ) situation. Figure 84 shows the measured power for θ=35° (external phase shifter=0°). In this condition the DCE offers a gain of 2.95 dB. The DCE does not introduce an appreciable gain loss because of the phase delay. Figure 85 shows the measurement result when the incoming signal is in quadrature, that is with a phase delay of about π/4. Not even in this operational condition the DCE gain is far from the theoretical maximum gain, with a gain of 2.9 dB. Finally, Figure 86 shows the results of the worst case considered, with a phase delay of 213.5°. An average gain of 2.8 dB during the test has been measured, with a loss of about 0.2 dB. After this analysis we can conclude that even with large delay between IFMS input signals the DCE works properly and allow for tracking array techniques.
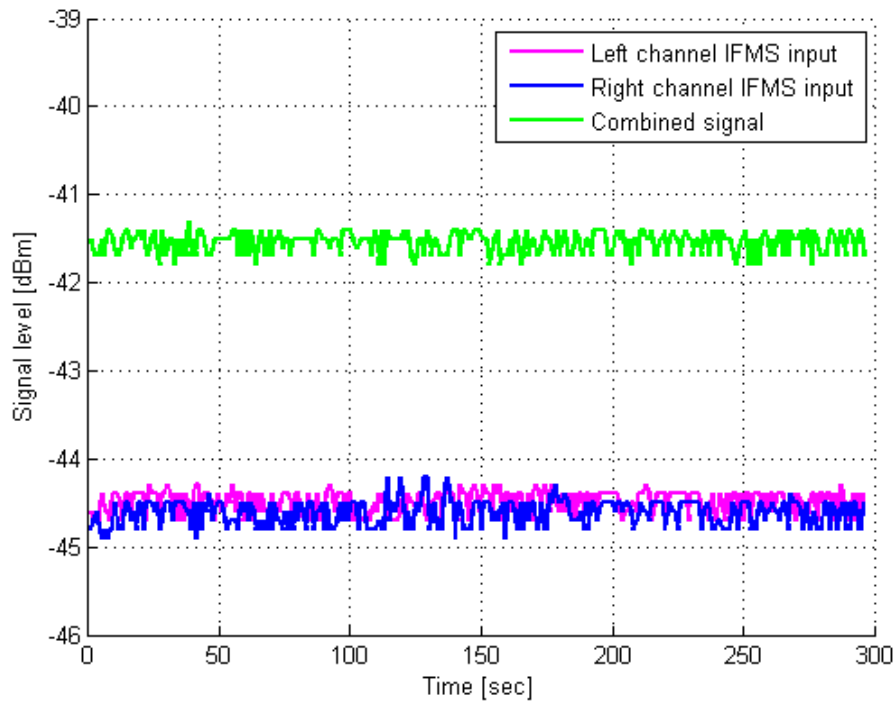
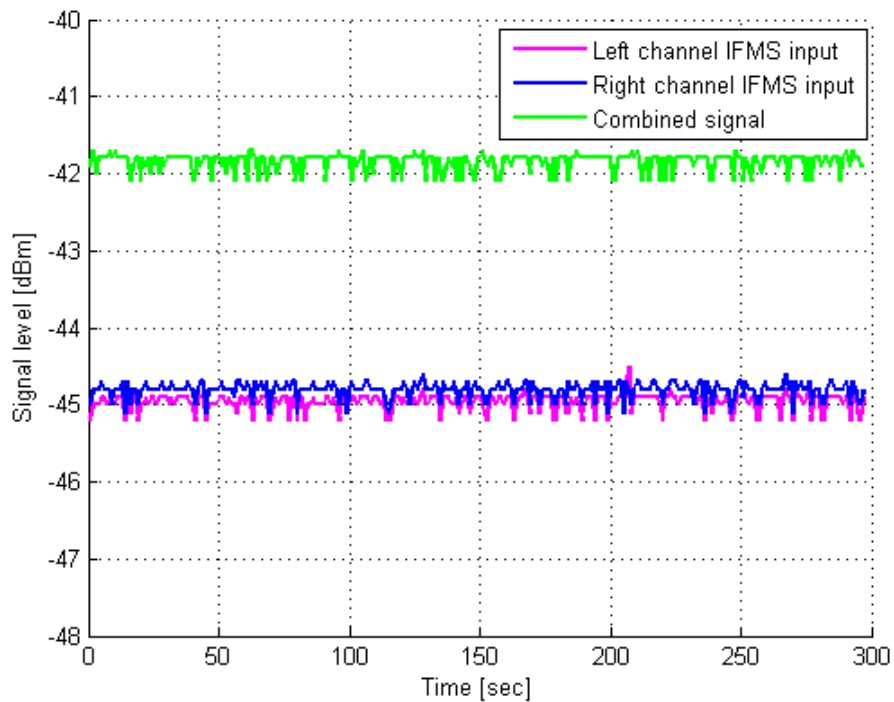**Figure 84: array gain considering a phase shift of 35°**

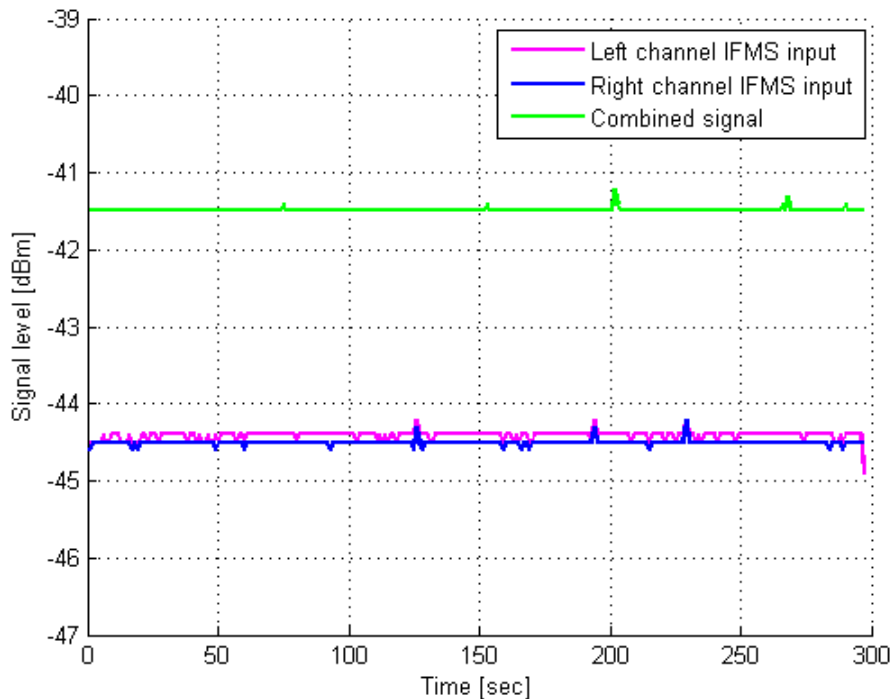**Figure 85: array gain considering a phase shift of 92°**

Figure 86: array gain considering a phase shift of 213.5°

As a second step, an input power difference has been introduced in order to investigate how a non-perfect equalization of the IFMS power inputs affects the total DCE gain. From Figure 87 to Figure 90 measurement results are shown. The general trend that has been measured is that the higher the power difference the higher the loss of gain with respect to the maximum theoretical one.

In detail, Figure 87 shows the gain with a 0.5 dB of power difference. It can be noticed that with respect to the channel with the higher power the total gain is 2.7 dB, with a loss of 0.3 dB from the maximum available gain.

Furthermore, Figure 88 represents the case of 1 dB of power difference, In this case the maximum gain is 2.5 dB. In Figure 89, 1.5 dB of power difference has been inserted, with a 2.3 maximum gain. At last, Figure 90 shows the results of the combination process with 2 dB of power difference between the two signals. A value of 2.1 dB is the maximum gain reachable in such a configuration, with a loss of 0.9 dB.
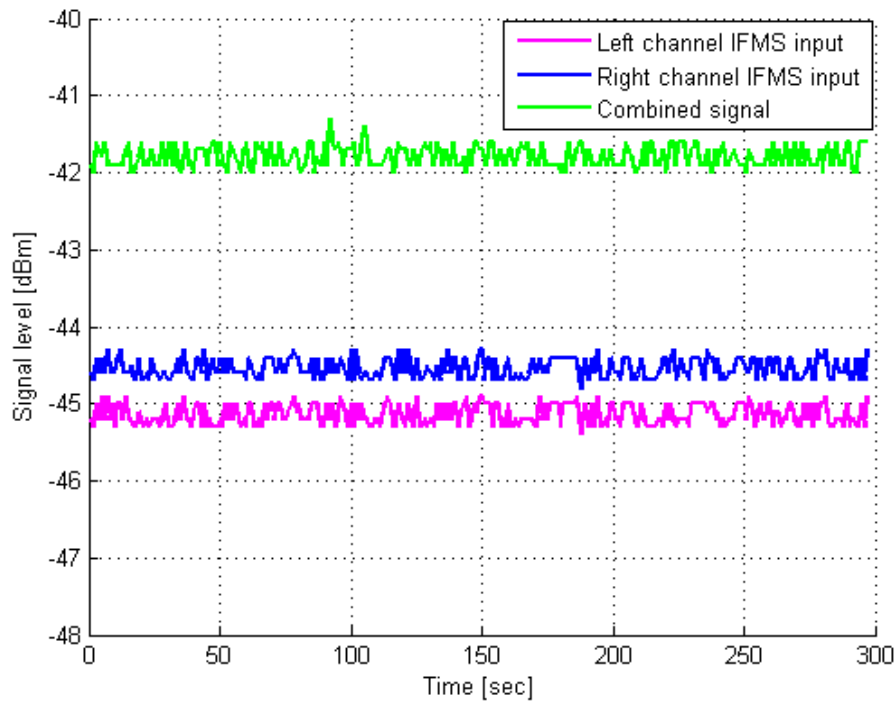
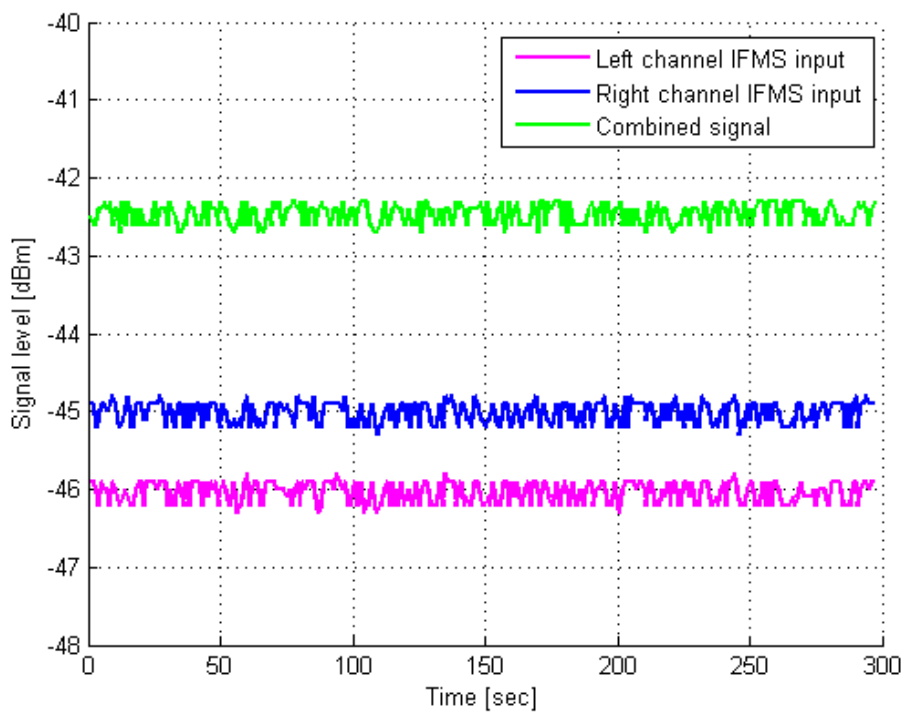**Figure 87: array gain with 0.5 dB of power difference**

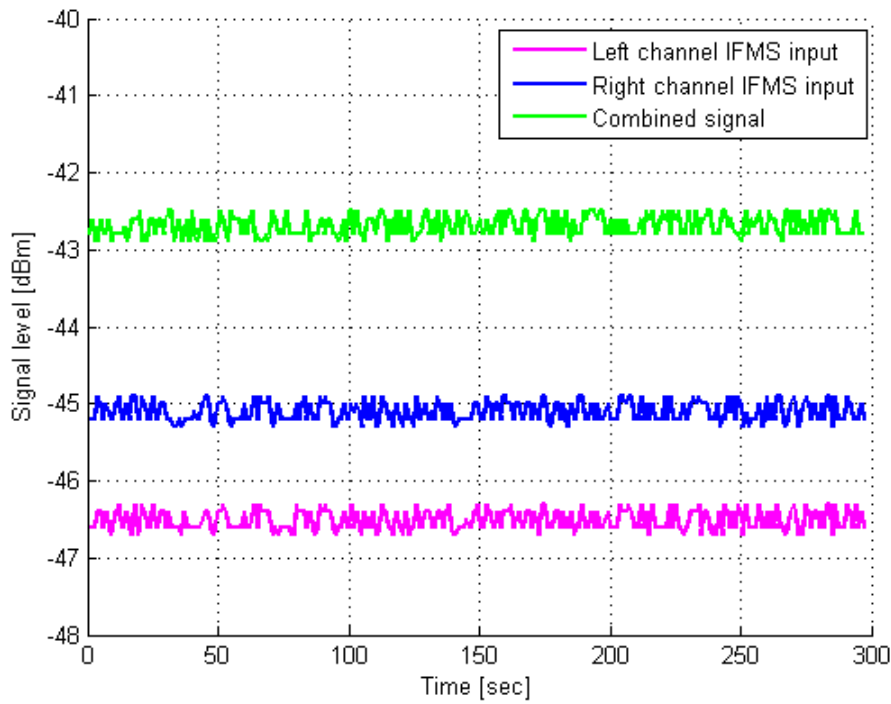**Figure 88: array gain with 1 dB of power difference**

Figure 89: array gain with 1.5 dB of power difference
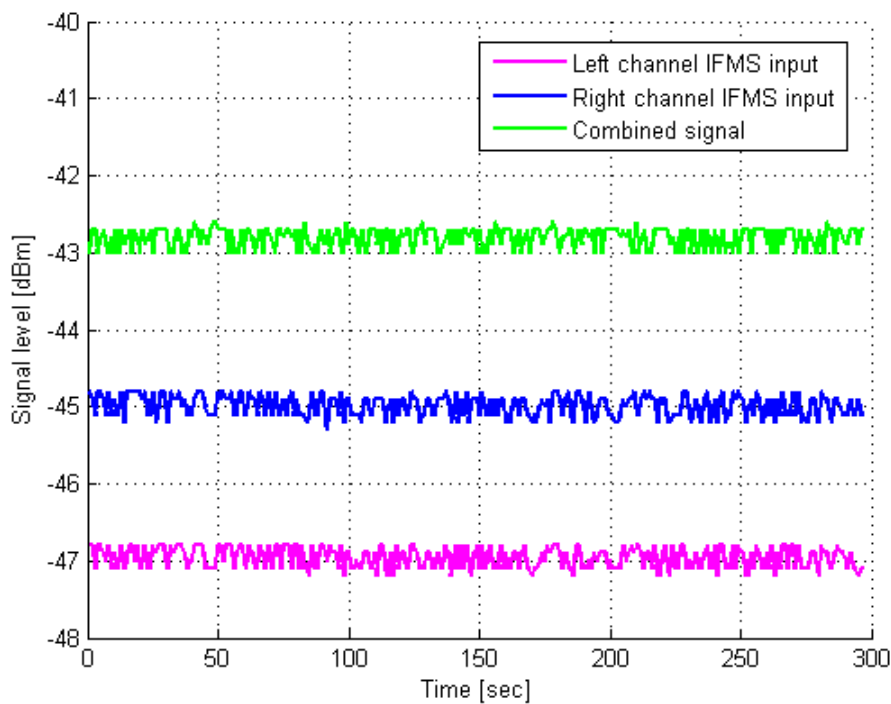
Figure 90: array gain with 2 dB of power difference

During previous test the following parameters have been used:

- correlation bandwidth: 1 KHz;
- estimator mode: NORMAL.

The same tests have been performed using different combination of these parameters: in particular a correlation bandwidth of 500 Hz and 300 Hz and the other two estimator mode (BIAS CORRECTED and INDIPENDENT LOOP) have been considered.

Relevant change in the total DCE gain has not been measured. During all tests the DCE has generated a combined signal with a gain very close to 3 dB.

For instance, two measures of signal power are shown in Figure 91 and Figure 92, for a correlation bandwidth of 300 Hz and the estimator mode independent loop. A gain of about 2.9 dB has been measured in both cases.

Figure 91: array gain considering correlation bandwidth=300Hz

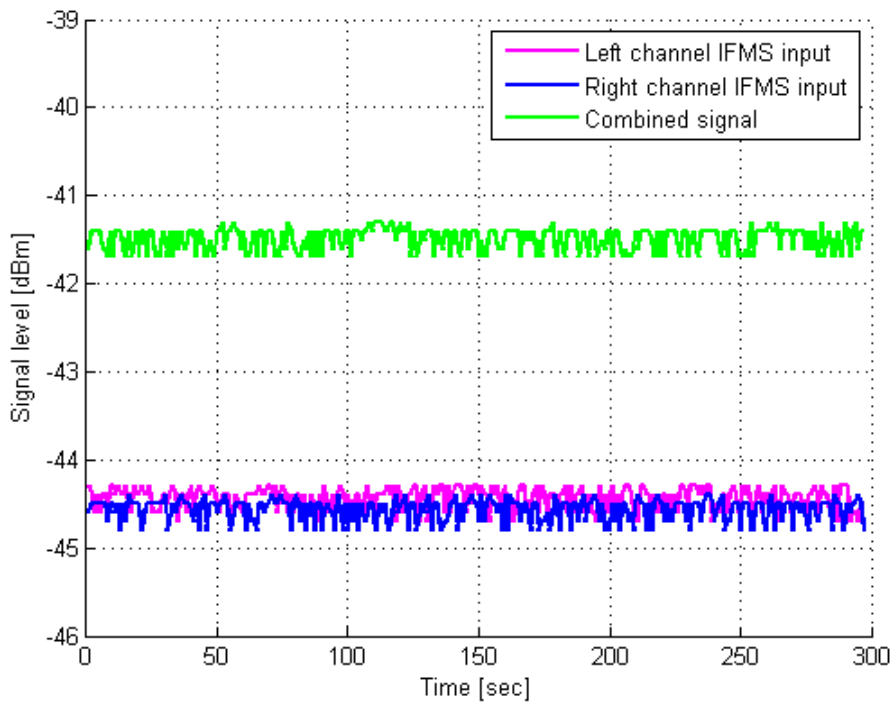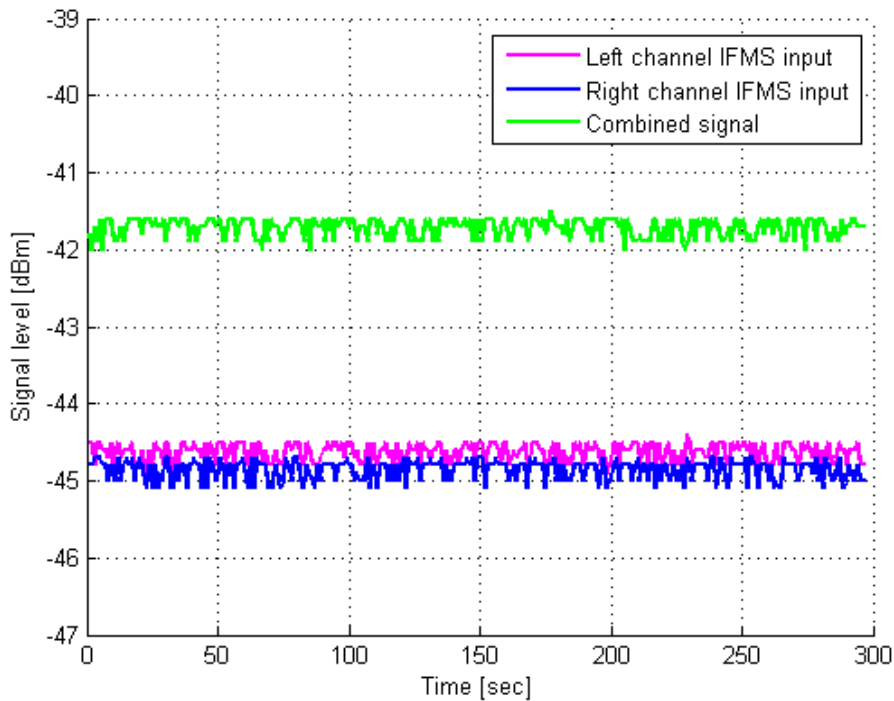**Figure 92: array gain considering correlation mode= independent loop**

7.4.2.2 Telemetry signal

The second step of the test campaign was focused on the same test described on Section 7.4.2.1 but using a S/C telemetry signal in order to simulate a more realistic scenario. VEX1 telemetry has been chosen as reference S/C.

As for the previous tests, the DCE had not shown a loss of the combining gain greater than 0.2 dB for different phase delay, as shown in the two figures sketched hereafter.

Figure 93 shows the gain of the combined telemetry signal with phase delay equal to 33°. An average gain of 2.92 dB is the result of 300 seconds of test. Moreover, Figure 94 shows the gain for θ=87.6°. 2.8 is the average gain that has been measured during the test.

Figure 95 and Figure 96 shows the test results for the same phase delay using a carrier level of -65 dBm, that is an SNR value of 55 dBm. Also for this lower value of SNR the DCE is able to combine the received signal, introducing an average loss of 0.2 dB for a theta angle of 33° and 0.25 dB for a phase delay of 87.6°.

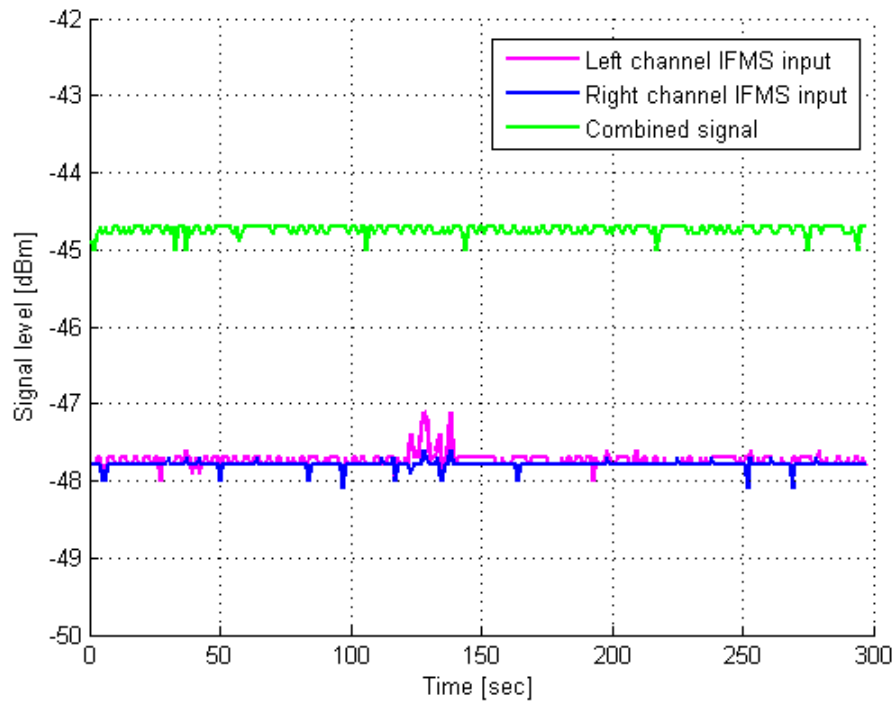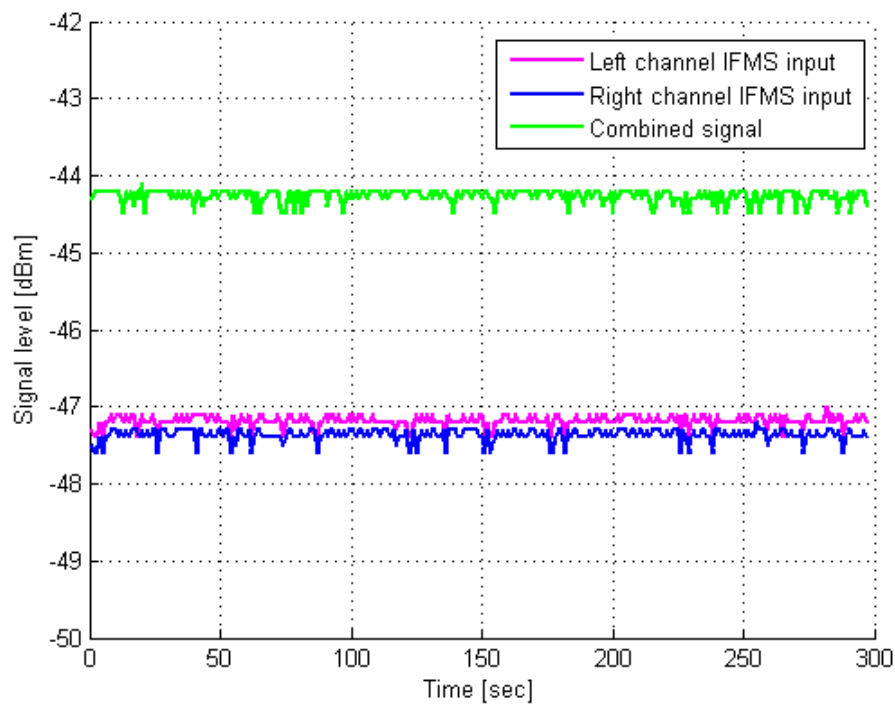**Figure 93: array gain considering a phase shift of 33°**

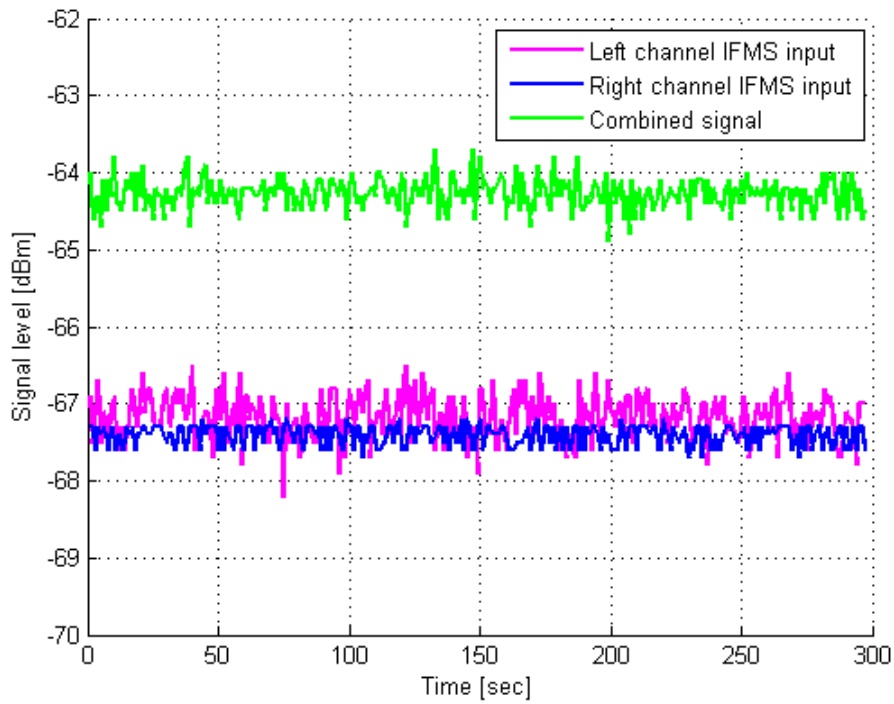**Figure 94: array gain considering a phase shift of 87.6°**

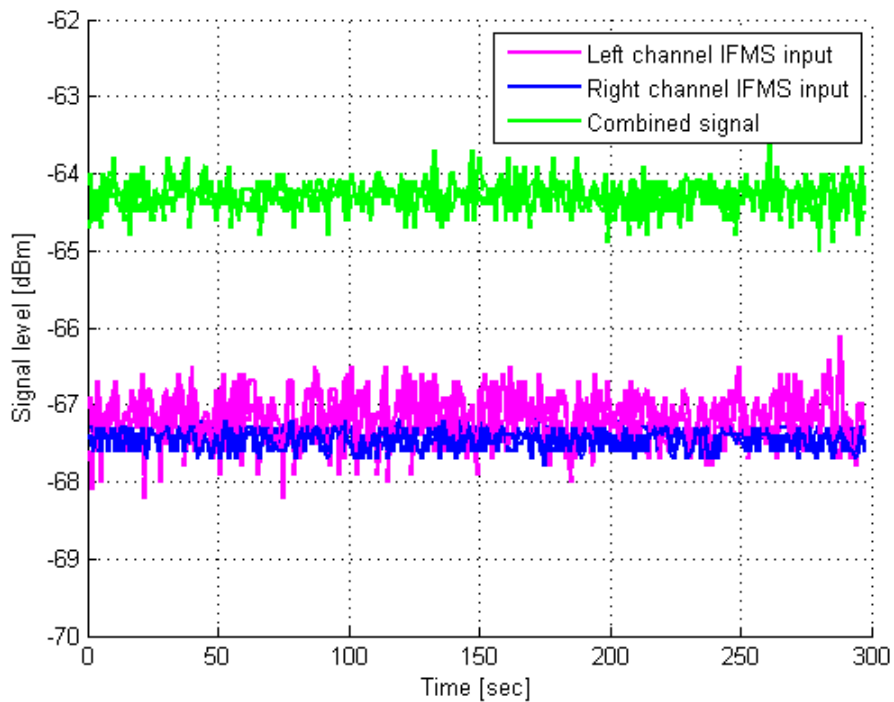**Figure 95: array gain considering a phase shift of 33°**

Figure 96: array gain considering a phase shift of 87.6°

Input power equalization tests have been performed using telemetry signal. A difference of 0.5 dB, 1 dB, 1.5 dB and 2 dB has been introduced. As for the phase shift test there are not relevant differences between carrier and telemetry input signal tests. A loss of about 0.3 dB, 0.5 dB, 0.7 dB and 0.9 dB has been measured respectively.

Moreover, DCE parameters have been changed in order to check if different configuration of the combiner can allow for a higher total gain. As in the previous case, no relevant differences have been measured changing the correlation bandwidth and the estimator mode.

7.4.2.3 Bit Error Rate

BER tests have been performed using the measurement chain shown Figure 83, adding a PSS generating telemetry signal directly connected to the signal generator in order to generate a modulated signal, and a PC with a Labview software for real-time calculation of the BER. The IFMS input power has been varied in a range of 10 dB and different phase shift between the two input signals have been introduced through the phase shifter. BER has been calculated in the following way: a constant frame of 255 octets was generated by the PSS, using the Reed-Solomon code and the randomizer. Than the demodulated frames received by the IFMS were compared with the original one in order to calculate the error probability. From the error rate than the Es/No of the subcarrier has been calculated.

Figure 97 shows the gain of the array combining technique for different subcarrier Es/No and for different phase shift. This gain has been calculated as the difference between the Es/No values of the single channel and the combined signal . It can be noticed that for values greater than 0 dB the total gain is between 2.8 and 3 dB. For low value of the subcarrier Es/No the gain reaches the lower value of 2.6 dB. Each line of the picture represents the gain for a different phase delay between the two inputs. In all cases the total gain is very close to the theoretical one of 3 dB, without a significant difference due to the total delay introduced on one IFMS input.

From Figure 98 to Figure 101 a comparison between the Symbol Error Rate (SER) of the single channel and the combined signal for different phase delay is shown. The lower value of the SER for the combined signal is the expected consequence of the measured gain. It is important to highlight that the subcarrier Es/N0 values are referred to the single channel. It means that both the SER of the single channel and the combined signal were calculated with reference to such a value of the subcarrier Es/No for the single channel. The Es/No of the combined channel would be the same value plus the gain shown in Figure 97.

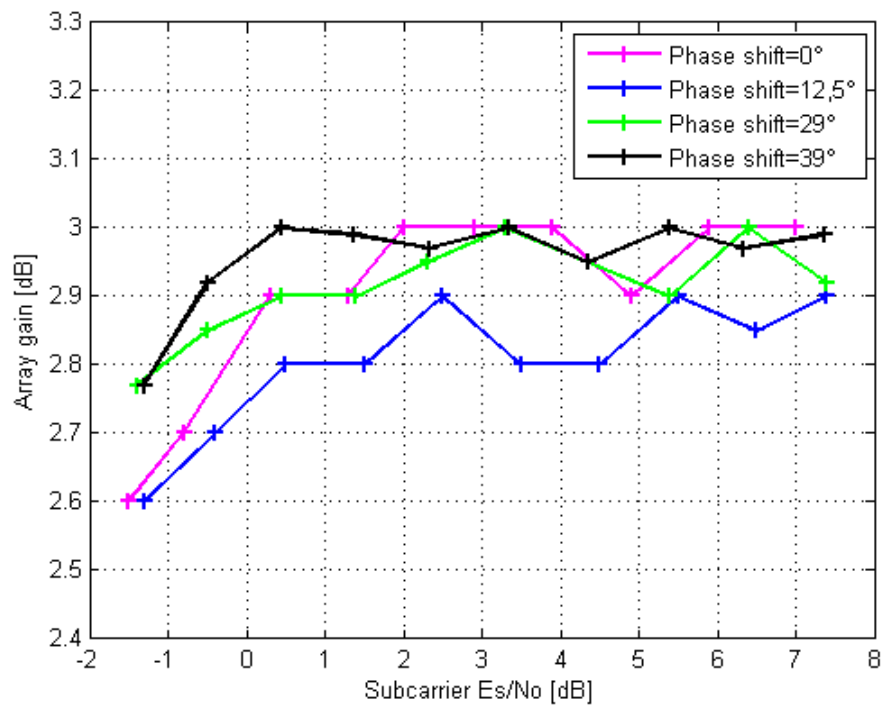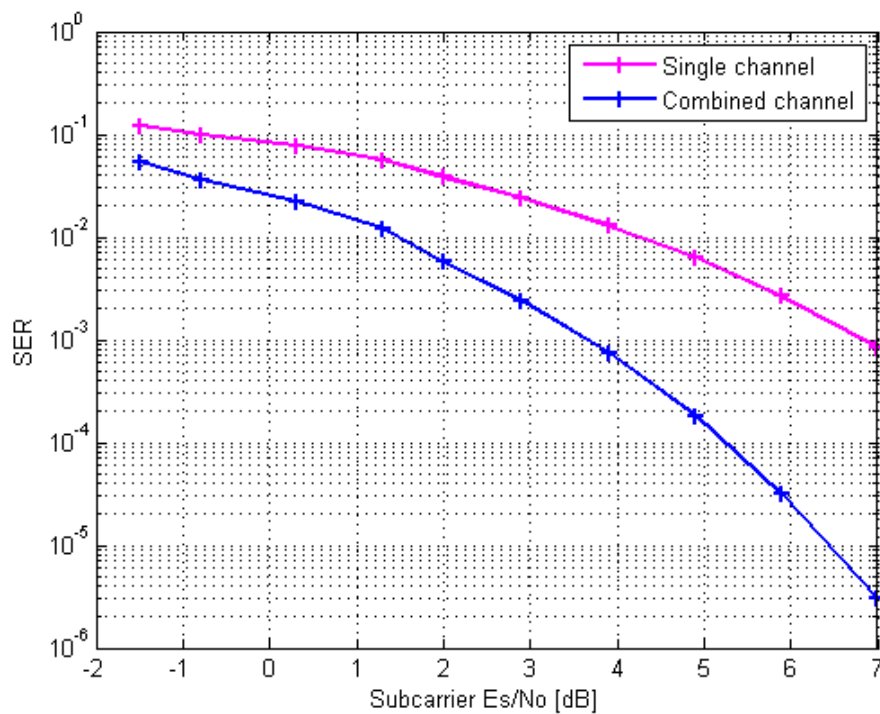**Figure 97: array gain for different phase delay**
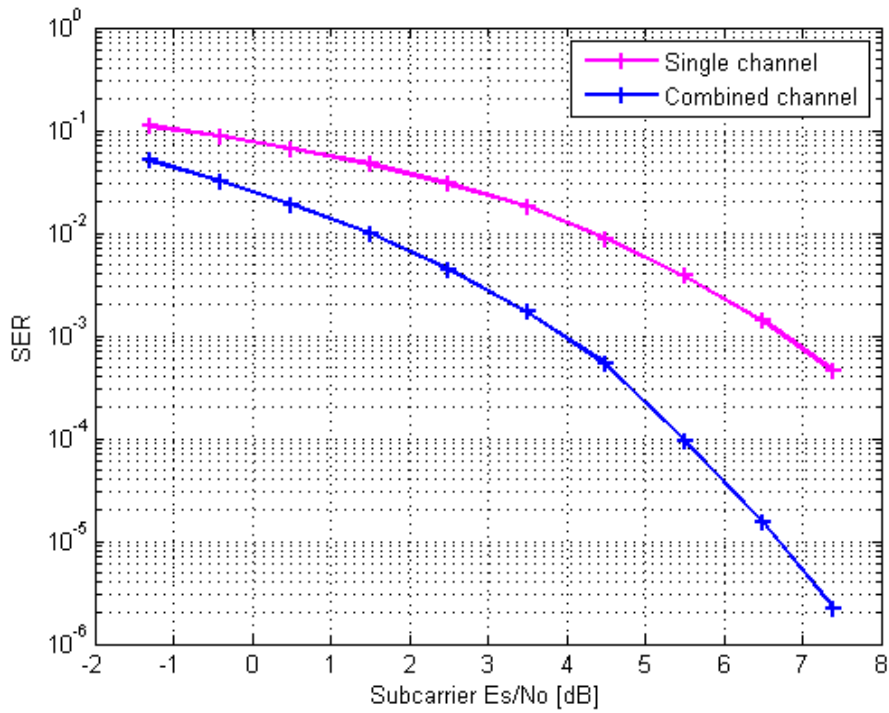

Figure 98: SER for phase delay=0°
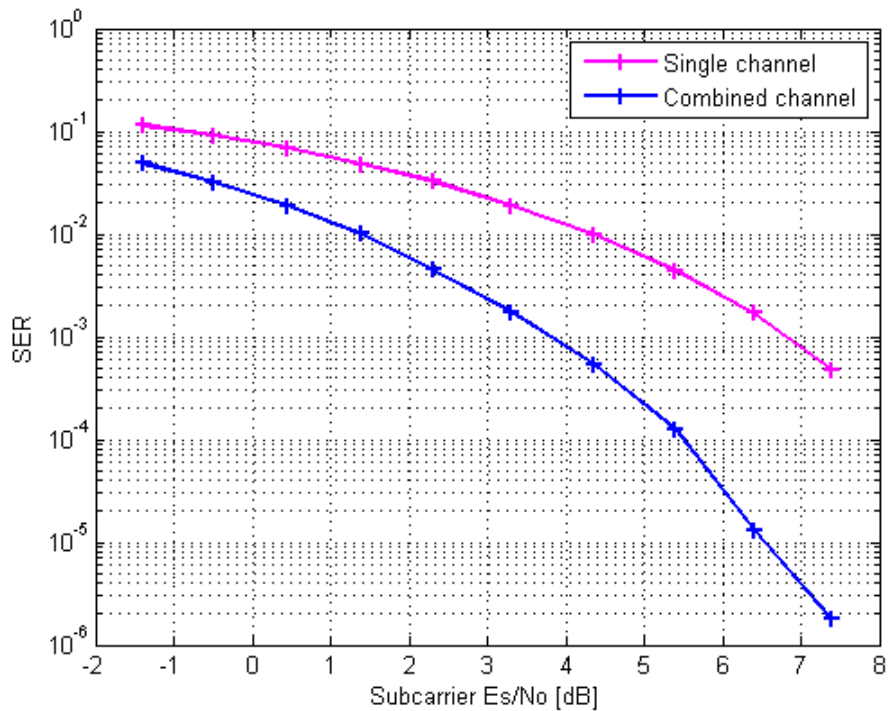
Figure 99: SER for phase delay=35°

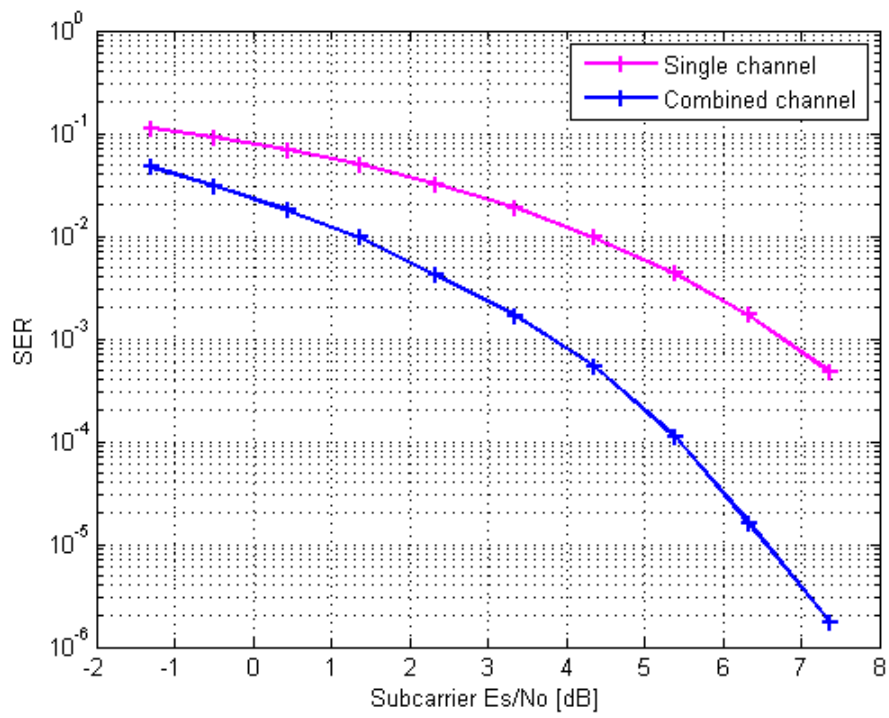**Figure 100: SER for phase delay=92°**

Figure 101: SER for phase delay=213.5°

8   Conclusions

8.1   On-board space communications

The work described in this thesis was carried out at the University of Bologna, in the Microsatellite laboratory of the engineering aerospace faculty. The design and development of on-board communication system is related to a space program started in 2004 that led to the completion of the microsatellite ALMASat-1 that has been successfully launched on-board the VEGA maiden flight, and the development of a second microsatellite, called ALMASat-EO, a three-axis stabilized microsatellite, operating in LEO orbits and able to capture images of the Earth surface.

Two communications systems were realized: the TT&C bidirectional link for command and telemetry at UHF band and an S-band high data rate transmitter integrated in the optical payload for downlink of the Earth images.

For both communication systems a complete study was carried out: at first the definition of the link budget was performed, considering the restriction in terms of available power on-board the satellite, the GS performance and required service. Then, a viable architecture was chosen and the electrical boards have been designed, realized and tested at University of Bologna facility. Furthermore, the antenna system for each subsystem was designed and implemented.

The TT&C subsystem consists of a unique electronic board, in cold redundancy, based on Cortex microcontroller and Chipcon CC1020 RF transceiver, directly connected to the satellite OBDH subsystem. It is able to establish a bidirectional link at UHF band at 4.8 or 9.6 Kbps, for the uplink of command and downlink of telemetry data. The whole electrical board together with the developed embedded software is thoroughly described. Moreover, the result of communication test campaign is presented. The link allows for a high reliable communication with a BER equal to 10^{-7}.

The S-band transmitter consists of two different boards, a digital one based on Xilinx Virtex 5 FPGA for the baseband processing of the signal: channel coding, pulse shaping and modulation are digitally performed. A second analog board has been developed for the up-conversion and filtering of the RF signal. The whole system allows for a fast connection up to 5 Mbps: the high data rate is due to the necessity of transmit to the GS a huge amount of data collected during multiple orbit from the multispectral camera on-board the ALMASat-EO spacecraft.

A second study on microsatellite application, considering the increasing interest in the development of constellations of microsatellite, in particular those flying in close formations has brought to the analysis of communication protocol for Satellite Formation Flying. SFF is the concept that multiple

satellites can work together in a group to accomplish the objective of one larger, usually more expensive, satellite. Coordinating smaller satellites has many benefits over single satellites including simpler designs, faster build times and so on. The study has the objective to understand how delay and communication errors affect the attitude determination and control of the SFF and the implementation of a more efficient solution based on the terrestrial IEEE 802.11 protocol. A simulator of the protocol delay and the attitude control has been developed in Matlab environment. The proposed solution is more efficient than the 802.11 standard especially for SFF up to 8 S/C. For a large number of satellite the total delay remain unaltered.

8.2   Ground segment

A six months training period at ESOC, Darmstadt, has given the possibility to directly work on device and equipment actually in use on ESA GS. Two GS enhancement techniques were designed, implemented and tested at ESOC facility.

The first solution is aimed to the implementation of a real-time phase compensation system initially designed for KPA but with the possibility to be applied at any RF equipment and at any frequency band. This solution is different from the standard ADEV control technique based on the temperature stability, which requires expensive and complicated liquid cooling system. The design, the implementation and the test campaign is thoroughly described in this thesis. The real-time compensation is performed at first acquiring through a Labview application the phase variation between the input and output signal of the RF device and then applying an equal and contrary phase variation to the input signal in order to follow the long term phase shift. The test campaign performed on a 2KW X-band KPA has highlighted an enhancement of the overall ADEV of the device with respect to the phase instability that the KPA introduces with a simple air cooling system, despite some limitations encountered during tests, such as the environmental noise. The measured ADEV of the KPA obtained with the proposed phase control is about one order of magnitude lower than the ADEV of the same device without the phase instability compensation. As a consequence the performance in terms of ADEV of the air cooled KPA with real-time phase compensation become closer to the performance of the water cooling system temperature control technique, which is more problematic regarding cost and maintenance.

Future test campaign should take into account the possibility of a carrier frequency shift during the compensation that could affect the final result. Moreover, it has to be considered the possibility to use the device not only for a carrier signal but also for a Telecommand signal, especially at X-band.

At Ka-band this problem is not relevant because this frequency band is not use for Telecommand transmission. Future activities shall include the development of the phase stabilisation system as a stand-alone equipment for Ka-band and the integration with the future Ka-band HPA. The development of the system for X-band as a stand-alone equipment will allow the use of air cooled HPAs (namely simpler and cheaper) for applications now reserved to more stable water cooled HPAs.

The second work carried out at ESOC has the objective of simulating and implementing a technique to perform two antennas array tracking using existing GS architecture and the IFMS device in particular. The Villafranca complex, with the two 15-m antennas VIL-1 and VIL-2, was chosen as reference structure for the study. Motivations and objective of the study are presented, as well as the theory of the IFMS and the DCE, the setup used during the test campaign and the obtained results. A DCE simulator was implemented in Matlab/Simulink environment and validated against data available in the design report of the IFMS, for simulate the current and proposed configuration of input channels. Then a test campaign was performed in ESOC GSRF. The Vex1 telemetry signal has been used as signal source at X-band. Two separated down-converter chain were used in order to simulate VIL-1 and VIL-2 antennas. Finally an IFMS and the DCE inside the device were used to combine the two received signal, while a Labview application was used for the calculation of the BER in order to derive the effective gain introduced by the array tracking system.

The results obtained through the test campaign have highlighted that the overall SNR gain at the output of the DCE used in array configuration is very close to the maximum theoretical gain of 3 dB, considering input channel power equalization and for static phase difference between the two input channels of the DCE. Moreover, basic requirements to obtain the maximum available SNR gain were identified, as the input channel equalization. In conclusion, two antennas array tracking by mean of existing GS equipment looks as a solution for increasing the received signal power and allows for mission data demand without additional costs.

Next steps will be focused on more detailed test campaign in GSRF simulating differential Doppler effect. In fact, the motion of the tracked S/C makes the relative distance with respect to the two antennas variable with time. So, a differential Doppler effect can affect the signal phase of the two received signals. As a consequence, during tracking operation the phase difference between the two input signals can be variable with time. This aspect can affect the maximum available SNR gain at the DCE output. The dynamic phase difference can be simulated through a voltage controlled phase shifter inserted on one channel in order to reproduce the actual effect according to relative S/C

dynamics. An upgrade of the simulator related to the same aspect is also needed. The last step of the study will be related to perform on-site test in Villafranca station using VIL-1 and VIL-2 antennas to track a real S/C. During this test campaign particular attention should be paid to the use of down-converter with the same characteristic in order to avoid difference in the frequency between the two DCE input channels. In addition, ranging test should be performed for a delay calibration on the two channels.

References

[1]   G. Maral, M. Bousquet, "Satellite communications systems", Wiley, 2002

[2]   B. G. Evans, "*Satellite communication systems 3rd edition*", The Institution of Electrical Engineers, 2000, London, United Kingdom

[3]   A. C. Clarke, "*Extra-terrestrial relays*", Wireless World, 1945, pp. 305-308

[4]   ESA ESTRACK

[5]   M. M. Sweeting, "*UoSAT-an investigation into cost-effective spacecraft engineering*", Institution of Electrical Radio Engineers, 1982, pp. 363-378

[6]   M. M. Sweeting, "*UoSAT microsatellite mission*", Electronics & Communication Engineering Journal, IEE, June 1992

[7]   M. Fouquet and M. N. Sweeting, "UoSAT-12 minisatellite for high performance Earth observation at low cost", proceedings of IAF, 1996

[8]   M. Fouquet and M. N. Sweeting, "*Earth Observation using Low Cost SSTL Microsatellites*", Symposium on Earth Observation Sensors & Technology, 47th IAF Congress, 7-11 October 1996, Beijing China

[9]   P. Tortora, E. Troiani, "The Microsatellite research program at Università di Bologna", 54° International Astronautical Congress, 29/09-03/10 2003, Bremen, Germany

[10]   P. Tortora et al, "ALMASat-1 launch onboard the Vega maiden flight", XX AIDAA congress, 29/06-03/07 2009, Milano, Italy

[11]   N. Melega, P. Tortora et al, "Multispectral Earth observation using the enhanced ALMASat microsatellite bus", IAA Conference on University Satellites, January 2011, Rome

[12]   http://www.eurolaunch.org/?id=16291

[13]   http://www.dlr.de/hr/desktopdefault.aspx/tabid-2317/3669_read-5488/

[14]   http://www.csr.utexas.edu/grace/

[15]   http://themis.ssl.berkeley.edu/index.shtml

[16]   D. Cinarelli, A. Di Domenico, A. Palli, S. Martì, N. Salerno, L. Simone, P. Tortora, I. Müller-Wodarg, "*On-Board Radio-Science: Science Requirements, System and Architectural Trade-offs and Preliminary Performance Analysis*", 5th ESA TT&C Workshop, European Space Technology Centre (ESTEC), Noordwijk, 21-23 September 2010

[17]   M. K. Dougherty et al, "JUICE (Jupiter Icy moon Explorer): a European-led mission to the Jupiter system", EPSC-DPS meeting 2011.

[18]   http://www.st.com/internet/mcu/class/1734.jsp

[19]   http://www.ti.com/product/cc1020

[20]   Consultative Committee for Space Data System, "TM Space Data Link Protocol", CCSDS 132.0-B-1, Blue Book, September 2003

[21]   Consultative Committee for Space Data System, "TM Synchronization and channel coding", CCSDS 132.0-B-2, Blue Book, August 2011

[22]   D.M. Pozar, "A Relation Between the Active Input Impedance and the Active Element Pattern of a Phased Array", IEEE Transactions on Antennas and Propagation, vol.51, no.9, September 2003.

[23]   C. Dick "The platform FPGA: enabling the software radio", 2002

[24]   P. Nikitin, E. Normark, C. Wakayama, R. Shi, "VHDL-AMS modeling and simulation of BPSK transceiver system", http://www.ee.washington.edu/faculty/nikitin_pavel/papers/ ICCSC_2004.pdf, ICCSC 2004

[25]   J. Delahaye, G. Gogniat, C. Roland, P. Bomel, "Software radio and dynamic reconfiguration on a DSP/FPGA platform", 3rd Workshop an software radios, proc. pp. 143-151, Karlsruhe, Germany March 2004

[26]   F. J. Harris, C. Dick, M. Rice, *Digital Receivers and Transmitters Using Polyphase Filter Banks for Wireless Communications,* IEEE transactions on microwave theory and techniques, Vol. 51, April 2003

[27]   http://www.xilinx.com/support/documentation/data_sheets/ds100.pdf

[28]   M. Perlman, J. Lee, "Reed-Solomon encoders: conventional vs Berlekamp's architecture", JPL publication 82-71, NASA, December 1982

[29]   G. Almeida et al, "A Reed-Solomon algorithm for FPGA area optimization in space application", Second NASA/ESA conference on adaptive hardware and systems, 2007

[30]   K. Way, S. Yang, "Field programmable gate array implementation of Reed-Solomon code, RS (255,239)", http://www.ce.rit.edu/~sjyeec/papers/nyworkshop-rs-codec.pdf, October 2005

[31]   U. Tuntoolavest, R. Intharasakul, "Nonbinary Convolutional Encoder for Vector Symbol Decoding on FPGA board", International conference on Communicaqtion technology, ICCT 2006

[32]   S. Hema, V. Suresh, P. Ramesh, "FPGA implementation of Viterbi Decoder", Proceedings of the 6th WSEAS Int. Conf. on Electronics, Hardware, Wireless and Optical Communications, Corfu Island, Greece, February 2007

[33] Consultative Committee for Space Data System, "TM Synchronization and channel coding-summary of concept and rationale", CCSDS 130.1-G-1, Green Book, June 2006

[34] M. A. Eshtwie, M. Othman, "FPGA Implementation of an Optimized Coefficients Pulse Shaping FIR Filters",ICSE2006, Kuala Lumpur, Malaysia, 2006

[35] J. Harris, C. Dick, M. Rice, "Digital receivers and transmitters using polyphase filter banks for wireless communications", IEEE transactions on microwave theory and techniques, vol. 51, no. 4, April 2003

[36] J. Langlois, D. Al-Khalili, R. Inkol, "Polyphase filter approach for high performance FPGA-based quadrature demodulation", Journal of VLSI Signal Processing 32, 237–254, 2002

[37] J. Frigo, T. Braun, J. Arrowood, M. Gokhal. "*Comparison of High Level FPGA Design Tools for A BPSK Signal Detection Application*" Software Defined Radio Technical Conference and Product Exposition (SDR), November 2003

[38] M. Kovac, "BPSK, QPSK, modulator simulation model", http://www.feec.vutbr.cz/ EEICT/2007/ sbornik/03-doktorske_projekty/02-zpracovani_signalu/04-mifokovac.pdf

[39] D. M. Pozar, "Microstrip antennas", Proceeding of the IEEE, vol. 80, 1992

[40] T. A. Milligan, "Modern antenna design", J. Wiley & sons, New York, NY, USA, 2nd edition, 2005

[41] F. Ferrero, C. Luxey, G. Jacquemod and R. Starai, "Dual-band circularly polarized microstrip antenna for satellite applications", IEEE antennas and wireless propagation letters, vol. 4, 2005

[42] Asghar Keshtkar, Ahmad Keshtkar and A. R. Dastkhosh, "Circular microstrip patch array antenna for C-band altimeter system", International journal of antennas and propagation, 2008

[43] J. Roberts, "Satellite formation flying for an interferometry mission", Ph.D. thesis, 2005

[44] M. Bentum, C. Verhoeven, A.J. Boonstra, "OLFAR-Orbiting low Frequency antennas for radio astronomy", 20th Annual Workshop on Circuits, Systems and Signal Processing, ProRISC, 2009, Veldhoven, Olanda

[45] http://www.dlr.de/eo/en/desktopdefault.aspx/tabid-5725/9296_read-15979/

[46] G. B. Shaw, "The generalized information network analysis methodology for distributed satellite systems", Ph.D. thesis, 1998

[47] K. Kusza, M. Paluszek, "Lower Layer Protocols for Autonomous Constellations," First Joint Space Internet Workshop, November 2000

[48]   E. Knoblock, V. Konangi, T. Wallett, K. Bhasin,"Network Configuration Analysis For Formation Flying Satellites," Proceedings IEEE Aerospace Conference, 2001

[49]   E.C. Megla, V.K. Konangi, T.M. Wallett, K.B. Bhasin, "Comparison of IEEE 802.11 and wireless 1394 for intersatellite links in formation flying", Dept. of Electr. & Comput. Eng., Cleveland State Univ., OH, USA. Aerospace Conference Proceedings, 2002. IEEE

[50]   L. Clare, E. Jenning, J. Gao, C. Okino, "A Network Architecture for Precision Formation Flying using the IEEE 802.11 MAC Protocol," 2005 IEEE Aerospace Conference Proceedings, March 2005

[51]   T. Vladimirova, K. Sidibeh, "WLAN for Earth Observation Satellite Formations in LEO", bliss, pp.119-124, Bio-inspired, Learning and Intelligent Systems for Security, 2008, IEEE Computer Society

[52]   K. Leung, B. McNair, L. Cimini, J. Winters, "Outdoor IEEE 802.11 Cellular Networks: MAC Protocol Design and Performance", IEEE International Conference on Communication, 2002, NY, USA

[53]   K. T. Alfriend, S. R. Vadali, P. Gurfil, J. P. How, L. S. Breger, "Spacecraft Formation Flying: Dynamics, Control and Navigation," Butterworth-Heinemann Ltd, First Edition, 2010

[54]   W.H. Clohessy and R.S. Wiltshire, "Terminal Guidance System for Satellite Rendez-Vous," The Journal of Aerospace Sciences, Vo.27, No. 9, pp. 653-658, 1960

[55]   Vaddi S. S., Vadali S.R., and Alfriend K.T., "Formation Flying: Accommodating Nonlinearities and eccentricity Perturbations", Journal of Guidance, Control, and Dynamics, Vol. 26, No. 2, pp. 214-223, March-April 2003

[56]   M. Sabatini, G. B. Palmerini, "Linearized Formation-Flying Dynamics in a Perturbed Orbital Environment," IEEE Aerospace Conference, December 2007

[57]   G. B. Palmerini, M. Sabatini, "Dynamics and control of low-altitude formations," Acta Astronautica, Vol. 61, pp. 298-311, April 2007

[58]   D. P. Scharf, F. Y. Hadaegh, S. R. Ploen, "A Survey of Spacecraft Formation Flying Guidance and Control (Part II): Control," American Control Conference, June 30 - July 2, 2004

[59]   P. Müller, " ESA tracking station (ESTRACK) facilities manual (EFM)", September 2008, Darmstadt, Germany

[60]   R. Martin, M. Warhaut, "ESA's 35-Meter Deep Space Antennas at New Norcia/Western Australia and Cebreros/Spain", IEEE Aerospace Conference Proceedings, 2004

[61]   http://www.esa.int/SPECIALS/Operations/SEM8YCSMTWE_0.html

[62]   M. Piera, S.Martì, J. De Vicente, "Improvements in X-Band HPA phase stability through phase compensation – a simulation study", ESOC technical note, March 2008

[63]   S. Martì, J. de Vicente, "Analysis of Ground Station Phase Unstabilities and their effects", ESOC technical note, February 2006

[64]   J.D. Prestage, & G.L. Weaver, "*Atomic Clocks and Oscillators for Deep-Space Navigation and Radio Science*" In: Proceedings of the IEEE, 95, 11, 2235-2247 (2007)

[65]   ESTRACK DSP study final report, February 1997

[66]   IFMS design report, ESA technical note, February 1999

[67]   IFMS users' manual, ESA technical note, January 2010

[68]   Final link budget for CLUSTER mission, ESA technical note, December 1994

Appendices

A. Signal phase variations in RF equipment

A.1 Analysis of filter phase variation

The phase variations of a filter will be produced by the thermal sensitivity. The impact can be calculated from the group delay of the filter. For a signal covering a band, the highest group delay inside the band shall be employed as a worst case.

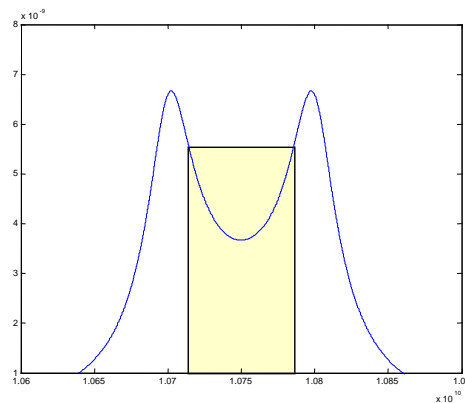The group delay is defined as the phase slope with the frequency:

Figure 102: Group delay of a filter

Eq. (A1)
$$G.D._{n\sec} = \frac{\Delta\phi_{cycles}}{\Delta f_{GHz}}$$

and a more useful equation:

Eq. (A2)
$$\Delta\phi_{cycles} = G.D._{n\sec} * \Delta f_{KHz} * 10^{-6}$$

The filter can be characterised also by his thermal sensitivity. The thermal sensitivity defines how much the filter response moves for a given thermal variation. In the real world, the response of the filter moves and the frequency does not change, but we can simulate this effect by maintaining the filter response unchanged and moving the frequency in the opposite direction. In this case the value of *Δf* is:

Eq. (A3)
$$\Delta f_{KHz} = -\alpha_{ppm/°C} * f_{0\,GHz} * \Delta T_{°C}$$

156

where α is the thermal sensitivity of the filter response in ppm/°C and the change of unit from GHz to KHz compensate the 10^{-6} of the ppm. For mechanical filters, the thermal sensitivity is, in practice, equal to the thermal expansion coefficient of the filter material (with opposite sign).

The relationship between phase and temperature is straightforward (now the phase is in degrees to match the typical units of the phase stability over temperature):

Eq. A(4)

$$\Delta\phi_{\deg} = -G.D._{n\sec} * \alpha_{ppm} * f_{0\,GHz} * \Delta T_{\circ C} * 360 * 10^{-6}$$

$$\frac{\Delta\phi}{\Delta T_{\circ/\circ C}} = -G.D._{n\sec} * \alpha_{ppm} * f_{0\,GHz} * 360 * 10^{-6}$$

With reference to [63], that describes how to calculate the ADEV due to temperature variations, we can write:

Eq. (A5)

$$ADEV_{Filter}(\tau) = \frac{G.D._{n\sec} * |\alpha_{ppm}| * f_{0\,GHz}}{360 * f_{0\,GHz} * 10^9} * ADEV_{\Delta T}(\tau) * 360 * 10^{-6}$$

$$ADEV_{Filter}(\tau) = G.D._{n\sec} * |\alpha_{ppm}| * ADEV_{\Delta T}(\tau) * 10^{-15}$$

A.2 Analysis of mixer phase variation

This appendix shows how to calculate accurately the ADEV of a simple system as a mixer, explaining the critical point of how cascaded Allan deviation adds up.

First of all, it is interesting to recall the definition of the ADEV in terms of fractional frequency (y) or phases (φ):

Eq. (A6)
$$\sigma_y^2(\tau) = \frac{1}{2 \cdot (m-1)} \cdot \sum_{j=2}^{m} \left(\bar{y}_j - \bar{y}_{j-1} \right)^2$$

Eq. (A7)
$$\sigma_y^2(\tau) = \frac{1}{2 \cdot (m-1)} \cdot \sum_{j=2}^{m} \left(\frac{\phi_{j+1} - \phi_j}{f_0 \cdot \tau} - \frac{\phi_j - \phi_{j-1}}{f_0 \cdot \tau} \right)^2$$

Eq. (A8)
$$\sigma_y^2(\tau) = \frac{1}{2 \cdot (m-1)(f_0 \cdot \tau)^2} \cdot \sum_{j=2}^{m} \left(\phi_{j+1} - 2\phi_j + \phi_{j-1} \right)^2$$

Eq. (A9)
$$\sigma_y(\tau) = \frac{1}{f_0 \cdot \tau} \cdot \sqrt{\frac{1}{2 \cdot (m-1)} \cdot \sum_{j=2}^{m} \left(\phi_{j+1} - 2\phi_j + \phi_{j-1} \right)^2}$$

Once the Allan deviation is clearly defined in terms of phases (easier to follow in a system with frequency changes), let's try to analyse the ADEV of a simple system like a mixer.
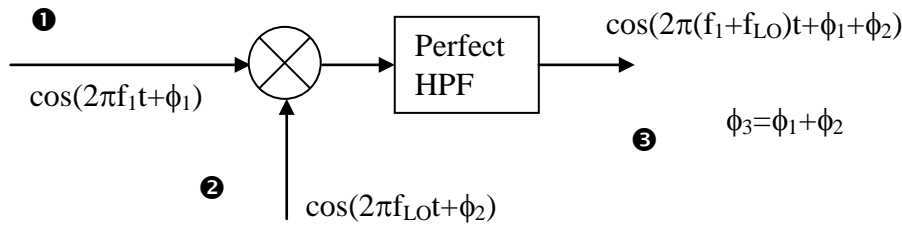

Figure 103: Allan Variance in a mixer

The expressions for the ADEV (referred to $f_1 + f_{LO}$) in the different points are deducted applying Eq. (A9):

Eq. (A10)   In ❶:
$$.\sigma_y(\tau) = \frac{1}{\tau(f_1 + f_{LO})} \cdot \sqrt{\frac{1}{2 \cdot (m-1)} \cdot \sum_{j=2}^{m} \left(\phi_{1\,j+1} - 2\phi_{1\,j} + \phi_{1\,j-1} \right)^2}$$

Eq. (A11)   In ❷: $$\sigma_y(\tau) = \frac{1}{\tau(f_1 + f_{LO})} \cdot \sqrt{\frac{1}{2 \cdot (m-1)} \cdot \sum_{j=2}^{m} \left(\phi_{2\ j+1} - 2\phi_{2\ j} + \phi_{2\ j-1} \right)^2}$$

Eq. (A12)   In ❸: $$\sigma_y(\tau) = \frac{1}{\tau(f_1 + f_{LO})} \cdot \sqrt{\frac{1}{2 \cdot (m-1)} \cdot \sum_{j=2}^{m} \left(\phi_{3\ j+1} - 2\phi_{3\ j} + \phi_{3\ j-1} \right)^2}$$

By expanding the expression of the point ❸ considering that $\phi_3 = \phi_1 + \phi_2$:

Eq. (A13) $$\sigma_y(\tau) = \frac{1}{\tau(f_1 + f_{LO})} \cdot \sqrt{\frac{1}{2 \cdot (m-1)} \cdot \sum_{j=2}^{m} \left[\left(\phi_{1\ j+1} - 2\phi_{1\ j} + \phi_{1\ j-1} \right) + \left(\phi_{2\ j+1} - 2\phi_{2\ j} + \phi_{2\ j-1} \right) \right]^2}$$

Therefore:

Eq. (A14) $$\sigma_y(\tau) = \frac{1}{\tau(f_1 + f_{LO})} \cdot \sqrt{\frac{1}{2 \cdot (m-1)} \cdot \sum_{j=2}^{m} \left(\left(\phi_{1\ j+1} - 2\phi_{1\ j} + \phi_{1\ j-1} \right)^2 + \left(\phi_{2\ j+1} - 2\phi_{2\ j} + \phi_{2\ j-1} \right)^2 + Crossterm \right)}$$

where *Crossterm* equals the following expression:

Eq. (A15) $2\phi_{1\ j+1}\phi_{2\ j+1} - 4\phi_{1\ j+1}\phi_{2\ j} + 2\phi_{1\ j+1}\phi_{2\ j-1} - 4\phi_{1\ j}\phi_{2\ j+1} + 8\phi_{1\ j}\phi_{2\ j} - 4\phi_{1\ j}\phi_{2\ j-1} + 2\phi_{1\ j-1}\phi_{2\ j+1} - 4\phi_{1\ j-1}\phi_{2\ j} + 2\phi_{1\ j-1}\phi_{2\ j}$

In conclusion we can appreciate in Eq. B9 the RSS sum of phase deviations, plus an additional term called Crossterm. Due to the presence of this Crossterm, the total ADEV cannot be calculated only by mean of the RSS. RSS can however be a good approximation depending on which error is tolerable. Sometimes RSS approach is optimistic and sometimes pessimistic because the crossterm can be either positive or negative

A.3 Analysis of waveguides phase variation

The analysis calculates the thermal sensitivity of a rectangular waveguide. The deduction of the thermal sensitivity of a circular waveguide can be derived in a similar way. The absolute phase of a waveguide section is

$$\phi_0 = \frac{L}{\lambda_g}cycles = \frac{L}{\lambda_0}*\sqrt{1-\left(\frac{\lambda_0}{2a}\right)^2}$$

Eq. (A16)
where:

- L is the length of the waveguide section
- λ_g is the group wavelength (same unit than L)
- λ_0 is the vacuum wavelength (same unit than L)
- a is the larger dimension of the rectangular WG

When there is a change in temperature ΔT both, L and λ_g are affected by temperature:

$$\phi' = \frac{L'}{\lambda_g'}cycles = \frac{L*(1+\Delta T\alpha)}{\lambda_g'}$$

$$\lambda_g' = \frac{\lambda_0'}{\sqrt{1-\left(\frac{\lambda_0'}{2a*(1+\Delta T\alpha)}\right)^2}} = \frac{\lambda_0'}{\sqrt{\frac{(1+\Delta T\alpha)^2-(\lambda/2a)^2}{(1+\Delta T\alpha)^2}}} = \frac{(1+\Delta T\alpha)*\lambda_0'}{\sqrt{(1+\Delta T\alpha)^2-(\lambda/2a)^2}}$$

$$\phi' = \frac{L'}{\lambda_g'} = \frac{L*\sqrt{(1+\Delta T\alpha)^2-(\lambda/2a)^2}}{\lambda_0} \approx \frac{L}{\lambda_0}*\sqrt{1-(\lambda/2a)^2+(2\Delta T\alpha)^2}$$

$$\sqrt{a+x} \cong \sqrt{a}+\frac{x}{2\sqrt{a}}; \quad \sqrt{1-(\lambda_0/2a)^2+(2\Delta T\alpha)^2} \cong \sqrt{1-(\lambda_0/2a)^2}+\frac{\alpha*\Delta T}{\sqrt{1-(\lambda_0/2a)^2}}$$

$$\phi' = \frac{L}{\lambda_0}*\left[\sqrt{1-(\lambda_0/2a)^2}+\frac{\alpha*\Delta T}{\sqrt{1-(\lambda_0/2a)^2}}\right]$$

$$\phi' = \frac{L}{\lambda_0}\sqrt{1-(\lambda_0/2a)^2}*\left[1+\frac{\alpha*\Delta T}{1-(\lambda_0/2a)^2}\right] = \phi_0*\left[1+\frac{\alpha*\Delta T}{1-(\lambda_0/2a)^2}\right]$$

So,

Eq. (A17):
$$\frac{\Delta\phi}{\Delta T} = \frac{\phi'-\phi_0}{\Delta T} = \phi_0*\frac{\alpha}{1-(\lambda_0/2a)^2} = \frac{L}{\lambda_0}*\frac{\alpha}{\sqrt{1-(\lambda_0/2a)^2}} \quad \text{cycles/°C} \quad \text{and}$$

Eq. (A18)
$$ADEV(\tau) = \frac{L_m}{c_{m/s}}*\frac{\alpha_{\circ C^{-1}}}{\sqrt{1-(\lambda_0/2a)^2}}*ADEV_{\Delta T}(\tau)$$

160

B. IFMS functional overview

The IFMS is an integrated system which provides ranging, telemetry and telecommand services for both near-earth and deep-space missions. The equipment is essentially a digital radio which can demodulate signals in a bandwidth of ± 7 MHz centered on 70 MHz and which can generate an arbitrary modulated uplink at 230 MHz or 70 MHz using digital waveform synthesis techniques.

In particular the IFMS provides the following system functions:

- Highly accurate and stable integrated Doppler and tone ranging;
- Variable rate telecommand transmission at using different modulation formats and a wide range of bit rates;
- Variable telemetry reception using remnant carrier modulation formats, suppressed carrier PSK and GMSK formats;
- Maximal ratio diversity combination of the co-polar and cross-polar signal components from the antenna, operating with both remnant and suppressed carrier modulation formats;
- Carrier acquisition using FFTs or conventional sweeps;
- Telemetry channel decoding.

A context diagram of the IFMS system is shown in

Figure 104. The IFMS has up to three receive channels at nominal 70 MHz IF frequency. However, a total of nine receive IF input connectors are provided allowing selection between three different groups of three inputs (Y, X and AUX downlink chains).

A block diagram of the IFMS is shown in Figure 105. The IFMS receiver is based on direct digital sampling of an incoming 70 MHz IF followed by digital down-conversion of the wideband spectrum to zero IF. The resulting complex baseband digital stream is then used by all of the receive functions. A high-speed sampling technique is used in the receiver on order to meet the demanding group delay and delay stability requirements which result from the ranging and Doppler data collections functions. Moreover, a generic modulator is based on direct digital synthesis techniques at an IF of 50 MHz followed by subsequent analogue up-conversion to 70 MHz or 230 MHz. All of the receive and codec functions are implemented on a generic DSP car, a hybrid of software and high-speed FPGA. Spectrum analysis using FFT technique is used and in the receivers for signal acquisition and calibration. Digital PLL are used to generate replicas of the incoming signals and provide critical information such as carrier and tone phase. For the ranging demodulator the IFMS

uses a carrier frequency estimate to pre-steer the tone loop frequency. This enables the IFMS to implement extremely narrow loop bandwidth down to mHz.
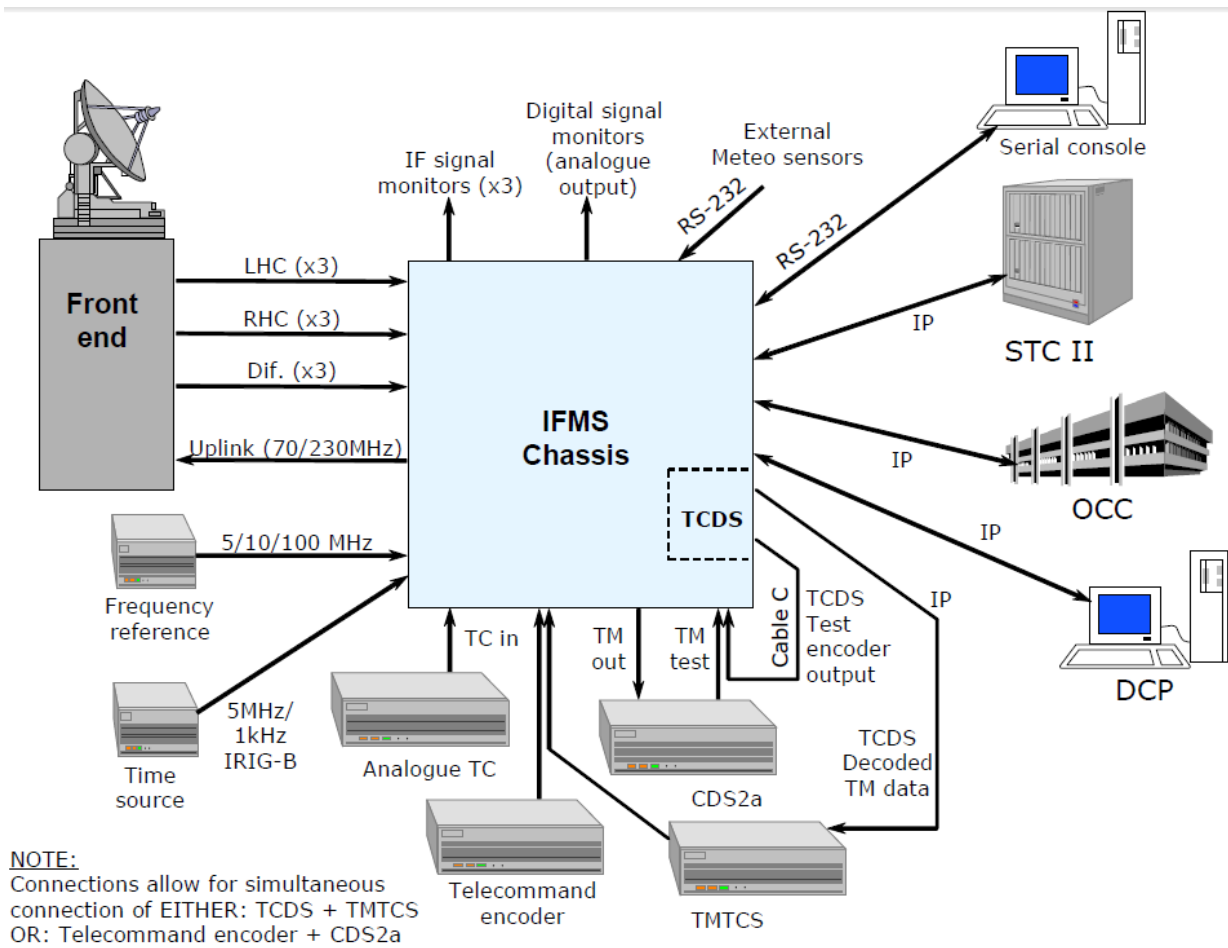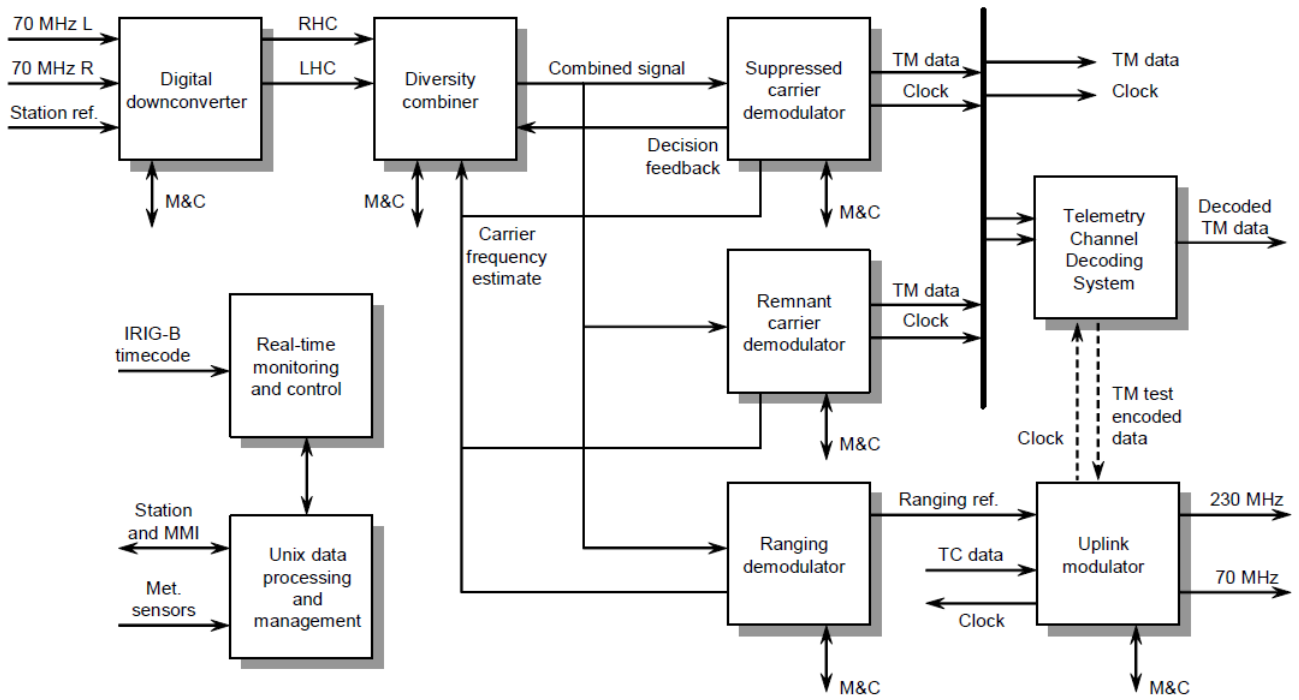

Figure 104: IFMS context diagram

Figure 105: IFMS high-level functional block

C. Ka-band upgrade

Ka-band is a suitable frequency band for RSE data downlink. The total available bandwidth allows high deep space data downlink using up to 500 MHz bandwidth. Considering all the advantage that can be carried out from using an uplink Ka-band for OBRAS application, depicted in this section, a bidirectional Ka-band link is an optimal solution for OBRAS application communication.

Considering ESTRACK DSA, some consideration must be taken into account in order to define a suitable ground station architecture. With respect to New Norcia (DSA-1) station, the introduction of a Ka-band uplink and downlink introduces important consequences on the general structure. Allowing operations at this new frequency band, would imply the impossibility to have at the same time S-band link. A suitable architecture including X- and Ka-band might include:

- A transmission waveguide that routes the RF signal to the X-band feed or Ka-band. The transmitted polarization might be selected with the polarization switch, which routes the RF signal to the uplink arm of one of the two Diplexers, one for each polarization (RCP and LCP) and frequency band (X and Ka);

- A telecommand chains which routes the uplink signal to the X- or KA-band antenna uplink;

- A Doppler predictions coming from Spacecraft Trajectory Data Messages for Telemetry link;

- A dichroic mirror for S- and Ka- band simultaneously;

- a Hydrogen Maser with very long term frequency stability;

With respect to Cebreros (DSA-2) and the under construction DSA-3, the upgrade to Ka-band bidirectional link could be simplified by the absence of S-band uplink or downlink. Different solution for locating a series of dichroic mirrors enabling transmission and reception at both X- and Ka-bands are under evaluation, as the one shown in Figure 106.

The general architecture suitable for DSA-1 could be an optimum choice also for these ground stations. Considering the huge amount of data generated by some RSE, the X-band downlink, affected by ITU limitation on maximum channel bandwidth, could not meet OBRAS application requirements in terms of available final data rate. As a consequence, Ka-band downlink is the preferential band for performing data downlink.
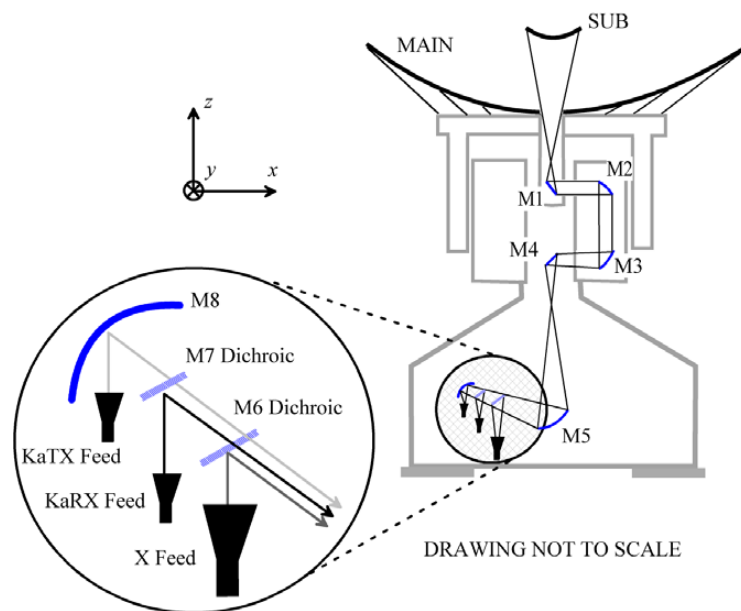
Figure 106: Dichroic mirror equipment for Ka-band in DSA-2 and DSA-3